The R-curve approach for the fracture assessment of an aluminium alloy bridge.

Cheung, C.M.S

The R-Curve Approach for the Fracture Assessment of an Aluminium Alloy Bridge

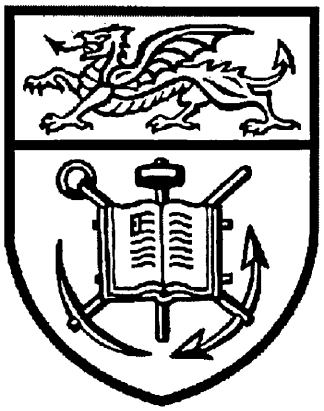

University of Wales Swansea

Department of Civil Engineering

Ph.D. Thesis by

C.M.S. Cheung

B.Eng. (Hons)

Jan., 2001 **C/Ph/242/00**

ProQuest LLC.
789 East Eisenhower Parkway
P.O. Box 1346
Ann Arbor, MI 48106 – 1346

DECLARATION

This work has not previously been accepted in substance for any degree and is not being concurrently submitted in candidature for any degree.

Signed. ..... (candidate)

Date.....12 June 2001.....

STATEMENT 1

This thesis is the result of my own investigations, except where otherwise stated. Other sources are acknowledged by footnotes giving explicit references. A bibliography is appended.

Signed.....(candidate)
Date 12 June 2001

STATEMENT 2

I hereby give consent for my thesis, if accepted, to be available for photocopying and for inter-library loan, and for the title and summary to be made available to outside organisations.

Signed.....(candidate)
Date 12 June 2001

SUMMARY

A result of fatigue testing on a full scale aluminium alloy bridge, which is used by the military for temporary crossings, showed an unexpected increase in fracture resistance, compared with its plane strain K_{IC}. This increase was due to a combination of low constraint and large stable crack extension in the bridge components. Previous work had attributed the increase to the loss of constraint alone, but the present work shows stable cracking is equally important.

The effect of stable cracking in the bridge alloy was first examined experimentally in large 25mm thick 3PB specimens which were analysed numerically using the finite element method. The numerical 2-D results provided a concave J_R-curve showing that dJ_R/da rises increasingly with crack extension. This increase is associated with the transition from flat to slant fracture in the experimental test pieces, due to the loss of plane strain constraint.

Fracture assessment using the R-curve approach showed that long cracks, both in large fracture mechanics specimens and the bridge girder, are stable because, although for a given load, $G=J_R$, $dG/da<dJ_R/da$. Short cracks in standard K_{IC} test specimens are unstable because $dG/da>dJ_R/da$ when $G=J_R$. The J_R-curve for low constraint geometries should be indexed by the T-stress.

The fatigue crack growth rate for the bridge alloy, taken from different sources, was compared. The Paris law index was nearly 4 for large CT and tension specimens, but only about 2 from fatigue tests on a full-scale bridge. For a large tension specimen, the corresponding K_{IC} at the change in index was delayed from 35 (the plane strain K_{IC} value) to 48MPa$\sqrt{m}$, because of the effect of low constraint. A simple model based on the J_R-curve (at initiation) was developed for predicting crack extension under high cyclic load ($K_{max}>K_{IC}$), but with limited success.

ACKNOWLEDGEMENT

I gratefully acknowledge the advice, help and gentle but firm guidance of Mr. A.R. Luxmoore, without whose encouragement and support the project would not have succeeded. His real concern always brings a solution to the problems encountered.

I would like to acknowledge the financial support of the Defence Evaluation and Research Agency (DERA). I am also thankful to my sponsors Mr. D. Webber and Mr. A.J. Stow from DERA, who provide information and experimental test results of the material. I received valuable material test results from Dr. J.D.G. Sumpter. Their support is very much appreciated.

I am greatly indebted to many colleagues in Department of Civil Engineering, University of Wales Swansea, for providing an intellectually stimulating and friendly environment, including Dr. D. Bowness, Dr. E.M. Dexter, Dr. A. Llewelyn-Parry, Dr. D. Boothman, Mr. F. Gazzola, Mr. G. Grewal, Mr. J. Chiravachradej and Mrs. L.J. Jones. System manager Mrs. D.M. Cook deserves special mention for her valuable assistance and help in solving problems arising in the computer network.

I express my gratitude to my girlfriend C. Lebrun for her company and providing joyful breaks from long hours of concentrated work. Last but by no means least I am grateful to my family, specially my parents, in Hong Kong for their devotions and countless sacrifices for the sake of my education.

NOMENCLATURE

Abbreviations

CT	Compact Tension specimen	HRR	Hutchinson-Rice-Rosengren singularity field
CCT	Centre Cracked Tension specimen	LEFM	Linear Elastic Fracture Mechanics
CMOD	Crack Month Opening Displacement	SSY	Small Scale Yielding
COD	Crack Opening Displacement	2-D	Two-dimensional
CTOD	Crack Tip Opening Displacement	3-D	Three-dimensional
EPFM	Elastic Plastic Fracture Mechanics	3PB	Three Point Bend Specimens
FAD	Failure Assessment Diagram		

Notations

A	Crack area	G	Elastic energy release rate
a	Half crack length in centre cracked plates, and the total crack length in edge cracks	G_{eff}	Effective G for a_{eff}
a_{eff}	Effective crack length as plastically corrected	G_{IC}	Plane strain fracture toughness in terms of G
a_o	Initial crack length	J	J-integral
a_f	Critical crack length	J_C	Critical J value at fracture instability
a/W	Crack aspect ratio	J_{eff}	Effective J for a_{eff}
B	Plate thickness	J_{IC}	Plane strain fracture toughness in terms of J
b	Remaining ligament size	J_{max}	Maximum J value in fracture testing
da, Δa	Crack extension	J_R	Fracture resistance, in terms of J
E	Young's modulus	K	Stress intensity factor

K_C	Critical K value at fracture instability	W	Width of test specimen
K_{eff}	Effective K for a_{eff}	Y	The geometry factor for K
K_{max}	Maximum K value in fracture testing	δ	Crack tip opening displacement (CTOD)
N	Numbers of fatigue cycles	ΔK	The range of stress intensity factor, i.e. K_{max}-K_{min} in a load cycle of a fatigue test
n	Strain hardening exponent	ε_i	Strain in the i direction
R	Fracture resistance	γ_s	Surface energy
R-curve	Fracture resistance curve	$\sigma_{applied}$	Applied stress
r	A distance measured from a crack tip	σ_f	Fracture stress
r_y or r_p	Plastic zone size	σ_{flow}	Flow stress, i.e. the average of yield stress and ultimate stress
T	T-stress	σ_i	Stress in the i direction
U_a	Change in the internal elastic strain energy	σ_{re}	Far field (remote) stress
U_0	Elastic energy of an uncracked plate	σ_{ys}	Yield stress
U_γ	Work required to create new surface	ν	Poisson's ratio
u_i	Displacement in the i direction		

CONTENTS

CHAPTER 1. THE BACKGROUND OF CHRISTCHURCH BRIDGE DESIGN FOR DAMAGE TOLERANCE

The Christchurch bridge is a lightweight, transportable bridging utility, see Figure 1.1a, which can be rapidly erected over gaps for emergency or military use. The bridge is fabricated from welded, high strength aluminium sections, which gives it a very high strength/weight ratio. This method of fabrication, when subjected to large live loads, will produce fatigue cracks growing from defects produced by the welding operation. In addition, when used by the military, the bridge may subject to ballistic damage in a component which can also initiate fatigue cracks. Using fracture mechanics analysis, the damage tolerance of the bridge is determined by the size and the position of a crack, whose unstable propagation can cause failure of the section. In either case, fatigue life (corresponding to fatigue crack growth rate) and critical crack length, are the primary concerns in estimating the service life of the bridge. Small scale fracture tests and full scale testing of the bridge were conducted early on in order to examine the fracture behaviour of the material. A simple fracture assessment scheme was developed with the help of these test results. The purpose of the assessment scheme is to provide a measure for determining the maximum residual life before a damaged bridge component has to be withdrawn from service. However, the failure of a structural component is mostly due to rapid (unstable) crack growth, and this will be discussed initially (chapters 4 through 6). In general, fracture prediction is determined by the fracture toughness, which is obtained from the results of standard tests. Conventional safety measures apply to (civil) structures containing no damage so that the strength and stiffness of the structures can withstand any excesses over the design loading. These are not sufficient for the design of the Christchurch bridge, as it is subjected to fatigue damage.

The service life and the critical crack length for the Christchurch bridge was estimated by Webber[1], using the integration of a crack propagation relationship. Assuming an initial surface defect depth of 0.0125 mm, and a typical K_{1C} of 41 MPa$\sqrt{m}$, Webber[1] predicted that the residual life of the bridge would be 11500 crossings for the design vehicle, with the crack extending to 45mm long by 15mm deep.

Despite the estimation using fracture mechanics and existing data for the material properties, an early large scale fatigue test of a single trackway of the bridge conducted by Webber[1] showed

that the residual life of the bridge, after a crack had developed, went far beyond the prediction above. In the fatigue test, the through thickness crack, found in the stem of the tensile T-section chord (Figure 1.1), which developed and caused eventual failure of the section, measured 99mm at 17000 load cycles (vehicle crossings). The crack grew to a length of over 200mm at 22000 cycles and failed at 27000 cycles.

A fatigue test[2] of a ballistic damaged single trackway (25.5m long) showed a long service life of 24446 load cycles (vehicle crossings). After 21000 cycles the test had proved that the service life of the ballistically damaged bridge (which contained seven significant crack growths) was far beyond that expected. A 27mm saw cut was made in the flange in order to observe the effect under severe damage in the high stress section. The crack grew completely through the flange of the section and into the stem, where it grew at an angle to the vertical (the alteration of the crack path could be the result of 'Union Jack' bracing connected between the stems of the chord) until failure. At this stage, the flange (saw cut) crack was over 200mm long while a stem crack was measured at over 80mm. The test stopped after crack growth instability was detected by the monitoring system.

Both the results[1][2] from large scale testing showed that the crack lengths at failure are much longer than that estimated using elastic fracture mechanics analysis. This led to a study of the stress intensity at the crack tip by Henry[3] using elastic-plastic fracture mechanics analysis and a two-parameter approach. Henry et al.[4] showed that low constraint specimens and cracked bridge sections exhibited negative T-stress parallel to the crack surface, and thus increased the critical stress intensity (hence J) at the crack tip. Henry[3][5] suggested that the crack growth instability for the bridge geometry could be predicted by the estimated J and T-stress of a crack. Using this method, instability should occur if the computed J and T-stress for a crack are beyond the J-T fracture toughness loci, produced by Sumpter[6].

The two-parameter approach for the fracture assessment of the damaged bridge component required a Y (the geometry factor in the stress intensity factor, K) solution for a wide range of stem and flange cracks. The Y solution were given from the results of 2-D finite element analysis by Cheung[7]. The seriousness of the crack tip fields in the stem depended on the position of the crack. Hence, three Y solutions were provided for stem cracks depending on the crack tip position.

Despite the advantage of the two-parameter approach, the prolonged service life and the tolerance to severe damage by the bridge still did not agree with the prediction using two-parameter fracture toughness. Although the result[6] of standard fracture tests showed that short cracks failed at initiation, full scale fatigue tests[1][2] produced crack lengths of up to 300mm (see above) before any structural instability was observed. Therefore, further study was focused on the relationship between crack sizes and geometry (i.e. the structural dimensions). Sumpter[6] investigated experimentally the tearing resistance and fracture mode of specimens with square and rectangular (b>>B) ligaments. He suggested that plane strain fracture toughness (K_{1C}) might be over conservative for components with structural dimensions (b>>B). He noticed that the fracture mode changed from flat fracture in specimens with square ligaments to fully slant fracture in rectangular ligaments, and this correlated with the increase of energy dissipation rate.

Using the experimental results, the stable crack growth of 3PB and CCT specimens were simulated numerically, and the resulting resistance curves will be presented in this report. The computed J associated with crack extension (Δa) was represented as the fracture resistance, J_R (hence K_R), of the bridge alloy. Both 3PB and CCT test results showed a rising (concave) R-curve, i.e. the resistance J_R increased with crack extension. The dJ_R/da of the R-curve also increased with crack extension. Hence, for most of the long cracks in the geometries of interest (3PB specimens and bridge girder sections of 25mm thick), the substantial increase in resistance improved the structural safety against unstable crack growth. The numerical plane stress R-curve (from the large ligament 3PB specimen) has been confirmed experimentally by Sumpter[8]. However, a J_C value could not be determined from the data of observed crack extension, either in the numerical or the experimental test results.

As shown by Paris et al., the crack growth rate (da/dN) is related to the range of ΔK ($=K_{max}-K_{min}$) by a power law relationship, $da/dN=C(\Delta K)^m$, known as the Paris law, where $\Delta K=Y\Delta\sigma\sqrt{\pi a}$. The material constants, C and m, are determined from experimental results. The number of cycles for a crack growing from an initial crack length to a critical length can be calculated by integrating the Paris law, provided C, m and Y are known throughout the crack propagation. The results of fatigue tests[9][10][11] on bridge alloy using different specimens and load ratios, shown later in this report, showed a variation of the material constants C and m (m varied from 2 to 4) for the Paris law. Butler and Tutty[10] suggested that data from fatigue

tests of large specimens, which tended to give a low m for the Paris law, was the most appropriate for representing the behaviour of large structural member. The result of a recent fatigue test[8][12] on specimens with large (rectangular) ligaments of bridge alloy by Sumpter showed that the change of crack growth rate coincided with $K_{max}>K_{1C}$ of the material. Sumpter gave $C=2.76\times10^{-08}$ and m=3.7 from his fatigue test results for the Paris law.

The unloading sequences of an R-curve test, using the unloading compliance method, showed that crack extension in subsequent cycles started just prior to achieving the previous maximum load, and crack growth arrested when the specimen was unloaded. If the crack extended due to excessive K in each load cycle, the amount of crack extension should be related to the amount of K in excess of K_R. A simple model, assuming repetitive application of the R-curve approach for explaining fatigue crack growth under constant high cyclic load, has been devised for repetitive crack growth at $K_{max}>K_R$.

A discussion on fracture resistance, i.e. the R-curve of the bridge alloy, and its application to fracture assessment, will be presented in chapters 4, 5 and 6 in this report. Different modes of failure that were observed in plane stress (b>>B) specimens will be discussed in chapter 7. Chapters 8 and 9 will discuss the residual life of the damaged bridge, which is computed using fatigue crack growth rate, and the prediction of crack growth rate, using the information from the R-curve.

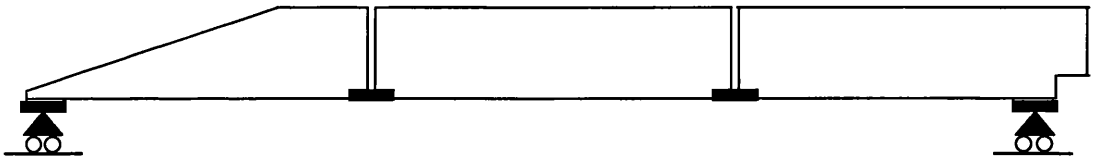

a. A side view of three 8m panels.

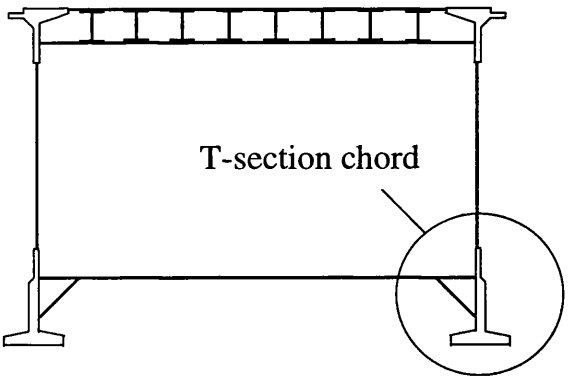

b. A cross section of a trackway.

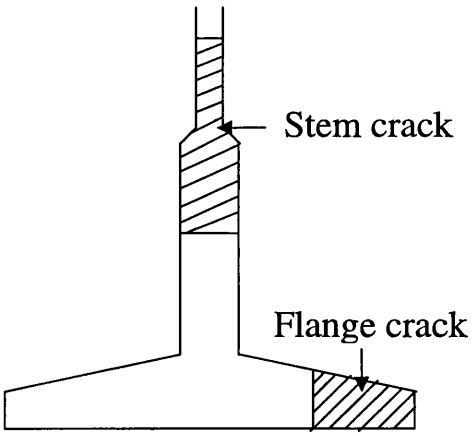

c. Cracks in the stem and flange of a tensile T-section chord.

Figure 1.1 The configuration of Christchurch bridge.

CHAPTER 2. THE FRACTURE MECHANICS APPROACH TO DESIGN

2.1 *History*

Griffith[13] studied the relationship between fracture stress and flaw size, and published his findings in 1920. He formulated a fracture theory based on a simple energy balance. According to this theory, the potential energy of a cracked body must be sufficient to overcome the surface energy of the material, in order to create new surface, i.e. allow fracture. Griffith's model correctly predicted the relationship between strength and flaw size in glass specimens. The Griffith equation only applies to ideally brittle solids. Griffith's model severely underestimates the fracture strength of metals, because it assumes that the fracture resistance comes only from the surface energy of the material.

Irwin[14] recognised that for relatively ductile material the energy required to form new crack surface is generally insignificant compared to the work of plastic deformation. He extended the Griffith approach to metals by including the energy dissipated by local plastic flow. In 1956, Irwin[15] developed the energy release rate concept, which is related to the Griffith theory but is in a form that is more useful for solving engineering problems. Irwin[16] and Williams[17] were among the first to show that the stresses and displacements near the crack tip could be described by a single constant that was related to the energy release rate. This crack tip characterising parameter is known as the stress intensity factor. The stress intensity approach states that fracture occurs when stresses ahead of the crack tip reaches a critical value, i.e. a critical stress intensity factor, K_C. Although corrections for small scale plasticity were proposed for modification of Griffith's approach, these analyses were restricted to structures whose global behaviour is linear elastic.

Wells[18] attempted to measure K_C values in a number of low- and medium-strength structural steels, but he found that these materials were too ductile to be characterised by linear elastic fracture mechanics (LEFM). While examining fracture test specimens, Wells noticed that the crack faces had moved apart prior to fracture, with plastic deformation blunting an initially sharp crack. The degree of crack blunting increased in proportion to the toughness of the

material. This observation led Wells to propose the opening at the crack tip as a measure of fracture toughness. This parameter is known as the crack tip opening displacement (CTOD).

In 1968, Rice[19] showed that a path-independent contour integral, referred to as the J integral, represented the energy release rate of nonlinear materials. Idealising plastic deformation as nonlinear elastic (deformation analysis), Hutchinson[20][21] and Rice and Rosengren[22] related the J integral to crack tip stress fields in nonlinear materials and showed that J can be viewed as a nonlinear stress intensity parameter as well as an energy release rate. Both parameters, namely CTOD and J contour integral, describe crack tip conditions in nonlinear elastic material or elastic-plastic material (provided no unloading occurs), and each can be used as a fracture criterion in elastic-plastic fracture mechanics (EPFM).

LEFM is only valid as long as nonlinear material deformation is confined to a small region surrounding the crack tip (small scale yielding, SSY), while EPFM applies to conditions where the nonlinear material behaviour becomes significant. However, EPFM is strictly valid only for conditions of contained yielding.

2.1.1 *The Griffith Approach*

For many materials, LEFM is not sufficient to characterise behaviour at the crack tip, and so the advanced concepts are necessary for most problems in fracture mechanics. However, all the research on fracture mechanics for nonlinear elastic material behaviour is correlated to the Griffith energy balance. Thus an understanding of the Griffith approach, which forms the fundamentals of LEFM, is essential to the study of advanced fracture mechanics.

Consider a crack of length 2a in a plate of width W (W>>2a) subjected to a constant stress with plane stress conditions prevailing. The Griffith energy balance for an incremental increase in the crack area, dA, under equilibrium conditions can be expressed in the following way:

$$\frac{dE}{dA} = \frac{dU_a}{dA} + \frac{dU_\gamma}{dA} - \frac{dF}{dA} = 0$$

where E = the total energy of an elastic, remotely loaded cracked plate,

U_a = change in the internal elastic strain energy,

U_γ = the work required to create new surfaces,

F = the work performed by external forces.

For the case where no work is done by external forces, the so-called "fixed grip condition", F=0. The change in strain energy U_a, caused by introducing the crack in the plate, is negative. Thus, equation (2.8) can be written as:

$$-\frac{dU_a}{dA}=\frac{dU_\gamma}{dA}.$$

Griffith showed that:

$$U_a=U_0-\frac{\pi\sigma_{apply}^2 a^2 B}{E}$$

where U_0 is the elastic energy of an uncracked plate, B is the plate thickness and E is Young's modulus. Since U_0 is constant, $\frac{dU_0}{dA}$ is zero.

Two surfaces are created when a crack extends, therefore

$$U_\gamma=4aB\gamma_s .$$

where γ_s is the surface energy of the material. Thus,

$$-\frac{dU_a}{dA}=\frac{2\pi\sigma_{apply}^2 a}{E}$$

and

$$\frac{dU_\gamma}{dA}=4\gamma_s .$$

In the case of equilibrium conditions $\sigma_{apply} = \sigma_f$, the fracture stress, and the Griffith energy balance is:

$$\frac{\pi\sigma_f^2 a}{E}=2\gamma_s .$$

Solving for fracture stress gives:

$$\sigma_f=\left(\frac{2E\gamma_s}{\pi a}\right)^{\frac{1}{2}}.$$

2.1.2 *The Energy Release Rate*

Irwin[15] defined an energy release rate G, which is a measure of the energy available for an increment of crack extension:

$$G=\frac{d(F-U_a)}{dA}$$

Thus G is the rate of change in potential energy with crack area, and is also called the crack driving force. This approach is essentially equivalent to the Griffith model. Hence, the energy release rate for a wide plate in plane stress conditions, with a crack length=2a and the change of external force=0, is given by:

$$G=\frac{\pi\sigma_{re}^2 a}{E},$$

and the crack resistance, R, per unit thickness is

$R=2(\gamma_s+\gamma_P)$, where γ_P is the plastic work per unit fracture area.

2.1.3 *The Stress Intensity Approach*

Williams[17] showed that the elastic-stress distribution at the base of a stationary crack could be expressed in the form:

$$\sigma_{ij}=A_{ij}(\theta)r^{-1/2}+B_{ij}(\theta)+C_{ij}(\theta)r^{1/2}+\ldots \qquad (2.1)$$

LEFM is usually based on the assumption that fracture processes occurring close to the crack tip are dominated by the leading term in the series, which is singular at the crack tip and embodies the stress intensity factor K;

$$\sigma_{ij}=\frac{K}{\sqrt{2\pi r}}f_{ij}(\theta)$$

In this case, all the stresses tend to infinity at the crack tip, i.e. r=0, and are products of the geometrical position ($\frac{1}{\sqrt{2\pi r}}f_{ij}(\theta)$) and K, the stress intensity factor. The stress intensity factor is usually denoted as K_I, K_{II} and K_{III} according to the type of loading, see Figure 2.1. Mode I loading corresponds to a force that is applied normal to the crack plane, and tends to open the crack. Mode II is in-plane shear that slides one crack face with respect to the other. Mode III is

out-of-plane shear. Table 2.1 shows the equations describing the stress (σ) and displacement (u) in the singularity dominated zone at the tip of a through crack.

The components of stress, strain and displacement at the crack tip are defined by K. Closed form solutions for K have been derived for a number of geometries, for instance, the specimens used in fracture tests: three point bending test (3PB); compact tension test(CT), and centre crack tensile test (CCP). The K for complex situations are estimated by experiment or numerical analysis.

Table 2.1 *Components of stress and displacement of a crack tip (see Figure 2.2 for details) for Mode I and Mode II loading in isotropic linear elastic material.*

	Mode I	Mode II
σ_{xx}	$\frac{K_I}{\sqrt{2\pi r}}\cos\frac{\theta}{2}(1-\sin\frac{\theta}{2}\sin\frac{3\theta}{2})$	$-\frac{K_{II}}{\sqrt{2\pi r}}\sin\frac{\theta}{2}(2+\cos\frac{\theta}{2}\cos\frac{3\theta}{2})$
σ_{yy}	$\frac{K_I}{\sqrt{2\pi r}}\cos\frac{\theta}{2}(1+\sin\frac{\theta}{2}\sin\frac{3\theta}{2})$	$\frac{K_{II}}{\sqrt{2\pi r}}\sin\frac{\theta}{2}\cos\frac{\theta}{2}\cos\frac{3\theta}{2}$
τ_{xy}	$\frac{K_I}{\sqrt{2\pi r}}\sin\frac{\theta}{2}\cos\frac{\theta}{2}\cos\frac{3\theta}{2}$	$\frac{K_{II}}{\sqrt{2\pi r}}\cos\frac{\theta}{2}(1-\sin\frac{\theta}{2}\sin\frac{3\theta}{2})$
σ_{zz}	0 (Plane stress) $\nu(\sigma_{xx}+\sigma_{yy})$ (Plane strain)	0 (Plane stress) $\nu(\sigma_{xx}+\sigma_{yy})$ (Plane strain)
τ_{xz}, τ_{yz}	0	0
u_x	$2(1+\nu)\frac{K_I}{E}\sqrt{\frac{r}{2\pi}}\cos\frac{\theta}{2}(1-2\nu+\sin^2\frac{\theta}{2})$ (Plane strain) $2\frac{K_I}{E}\sqrt{\frac{r}{2\pi}}\cos\frac{\theta}{2}(1+\sin^2\frac{\theta}{2}-\nu\cos^2\frac{\theta}{2})$ (Plane stress)	$2(1+\nu)\frac{K_{II}}{E}\sqrt{\frac{r}{2\pi}}\sin\frac{\theta}{2}(2-2\nu+\cos^2\frac{\theta}{2})$ (Plane strain) $2\frac{K_{II}}{E}\sqrt{\frac{r}{2\pi}}\sin\frac{\theta}{2}(2+\cos^2\frac{\theta}{2}+\nu\cos^2\frac{\theta}{2})$ (Plane stress)
u_y	$2(1+\nu)\frac{K_I}{E}\sqrt{\frac{r}{2\pi}}\sin\frac{\theta}{2}(2-2\nu-\cos^2\frac{\theta}{2})$ (Plane strain) $2\frac{K_I}{E}\sqrt{\frac{r}{2\pi}}\sin\frac{\theta}{2}(2-\cos^2\frac{\theta}{2}-\nu\cos^2\frac{\theta}{2})$ (Plane stress)	$-2(1+\nu)\frac{K_{II}}{E}\sqrt{\frac{r}{2\pi}}\cos\frac{\theta}{2}(1-2\nu-\sin^2\frac{\theta}{2})$ (Plane strain) $-2\frac{K_{II}}{E}\sqrt{\frac{r}{2\pi}}\cos\frac{\theta}{2}(1-2\nu-\sin^2\frac{\theta}{2}+\nu\cos^2\frac{\theta}{2})$ (Plane stress)

In these equations, E is the Young's modulus, ν is Poisson's ratio and r is the distance from the crack tip.

All stress components in a linear elastic body increase in proportion to the remotely applied force. The geometry of a finite size specimen has an effect on the crack tip stress field, and so the K is modified by a geometry factor:

$$K=Y\sigma_{re}\sqrt{\pi a}$$

where Y is the geometry factor (or correction factor), σ_{re} is the reference stress (generally, the remote stress applied at the crack tip level) and a is the half crack length in centre cracked plates, and the total crack length in edge cracks.

Recall the energy release rate for a crack in a infinite plate:

$$G=-\frac{d(F-U_a)}{dA}=\frac{\pi\sigma_{re}^2 a}{E}$$

and, in this case, Y = 1, thus;

$$K_I=\sigma_{re}\sqrt{\pi a}\ .$$

Combining these two equations shows the relationship between G and K:

$$G=\frac{K_I{}^2}{E} \qquad \text{in plane stress constraints,}$$

or $$G=\frac{K_I{}^2}{E}(1-\nu^2) \text{ in plane strain constraints.}$$

2.1.4 *Plastic Zone Size*

As a first approximation, yielding in a linear elastic material occurs when σ_{yy}, see Table 2.1, along the x-axis is limited to the yield stress (Figure 2.3):

$$\sigma_{yy}=\sigma_{ys}=\frac{K_I}{\sqrt{2\pi r}}$$

Solving the equation for r gives

$$r_{y(\text{plane stress})}=\frac{1}{2\pi}\left(\frac{K_I}{\sigma_{ys}}\right)^2,$$

where r_y denotes the first order estimate of plastic zone size for small scale yielding, assuming a circular plastic zone in plane stress constraint.

In elastic-plastic materials, when yielding occurs, stresses must redistribute in order to satisfy equilibrium, because stresses cannot exceed the current yield surface. The plastic zone must increase in size in order to transmit all stresses. In elastic perfectly plastic material (i.e. where stresses cannot exceed the yield stress), assuming a circular plastic zone shape with diameter r_p, the force balance for the stresses in the redistributed (plastic) area can be written as

$$\sigma_{ys} r_p = \int_0^{r_y} \sigma_{yy} dr = \int_0^{r_y} \frac{K_I}{\sqrt{2\pi r}} dr$$

Integrating and solving for r_p gives

$$r_{p(planestress)} = \frac{1}{\pi}\left(\frac{K_I}{\sigma_{ys}}\right)^2.$$

The result of the plastic zone diameter is twice of that obtained as the first order estimate.

Considering the stresses in terms of principal stresses, the Von Mises yield criterion states that yield will occur when

$$(\sigma_1-\sigma_2)^2+(\sigma_2-\sigma_3)^2+(\sigma_3-\sigma_1)^2 = 2\sigma_{ys}^2,$$

but σ_3 is either 0 (plane stress) or $\nu(\sigma_1+\sigma_2)$ (plane strain), and $\sigma_1 = \sigma_2$ along the x-axis, $\theta = 0$. Thus, if the Poisson's ratio, $\nu = 0.33$,

$$\sigma_1 = \sigma_{yy} \approx 3\sigma_{ys}.$$

in plane strain conditions. Therefore, the plastic zone size along the x-axis for the plane strain condition is

$$r_{y(planestrain)} = \frac{1}{2\pi}\left(\frac{K_I}{3\sigma_{ys}}\right)^2$$

At the plate surface, however, there is a state of plane stress where $\sigma_3=0$, and r_y is the same as the first order estimate, $r_{y(planestress)}$, i.e. nine times as large. The r_y model for plane strain condition must be a considerable underestimate of the overall through-thickness plastic zone size in a plate. For this reason the nominal plane strain plastic zone is,

$$r_{y(planestrain)} = \frac{1}{6\pi}\left(\frac{K_I}{\sigma_{ys}}\right)^2.$$

An effective crack length (Figure 2.4) is defined by Irwin[23] to account for the effect on the K by the occurrence of plasticity at the crack tip,

$$a_{eff}=a+r_y$$

where a is the actual crack length and r_y is the plastic zone radius (for either the nominal plane strain and the plane stress). The K calculation for elastic-plastic material can be evaluated by defining an effective K,

$$K_{eff}=Y_{eff}\sigma_{re}\sqrt{\pi a_{eff}}\ ,$$

where Y_{eff} is the geometry factor corrected for the effective crack length, a_{eff}. Therefore, the a_{eff} and K_{eff} are used as plasticity correction factors that allows LEFM calculations to be extended to cases of limited plasticity at the crack tip.

2.1.5 *The J Integral*

Rice's analysis[19] of a line integral, which he called the integral J, around the tip of a notch in the two-dimensional strain field of an elastic or nonlinear elastic material, has the form of;

$$J=\int_{\Gamma}(Wdy-T_i\frac{\partial u_i}{\partial x}ds)\ ,$$

where W is the strain-energy density which is defined as,

$$W=W(x,y)=W(\varepsilon)=\int_0^{\varepsilon}\sigma_{ij}d\varepsilon_{ij}\ ;$$

Γ is an arbitrary counter-clockwise path around the notch tip; T_i are the components of the traction vector defined according to the outward normal along the contour Γ; u_i are the components of the displacement vector and ds is a length increment along the contour Γ, Figure 2.5. The integral applies to a homogeneous body of linear or nonlinear elastic material, which has a unique relationship between stress and strain, free of body forces and subjected to a two-dimensional deformation field so that all stresses σ_{ij} can be resolved into x and y co-ordinates system.

Consider the integral of any closed contour (Γ^*) enclosing an area (A*) at a notch tip (see figure 2.5) in a two-dimensional field, free of body force. Then

$$\int_{\Gamma^*}(Wdy - T_i\frac{\partial u_i}{\partial x}ds) = \int_{A^*}\left[\frac{\partial W}{\partial x} - \frac{\partial}{\partial x_j}\left(\sigma_{ij}\frac{\partial u_j}{\partial x}\right)\right]dxdy.$$

Rice[19] showed that the integrand in the above equation vanished identically, and thus

$$\int_{\Gamma^*}(Wdy - T\frac{\partial u}{\partial x}ds) = 0$$

for any closed contour Γ^*. The integral of the closed contour is equal to that the sum of each segment, namely Γ_1, Γ_2, Γ_3 and Γ_4. On the crack surface, $T_i = dy = 0$. Thus the integral of Γ_3 and Γ_4 are zero, and $J_1 = -J_2$, where J_1 and J_2 are the integral of contour Γ_1 and Γ_2 respectively. The independence of the J integral is hence proven.

For SSY fields, Rice[19] also showed that

$$J = \frac{1-\nu^2}{E}K_I^2$$

in plane strain deformation field,

and $$J = \frac{K_I^2}{E}$$

in plane stress conditions, which is the same as the energy release rate in linear elastic material. Evidently J = G for linear elastic materials, but the integral J characterises crack tip stresses and strains in nonlinear materials beyond the validity limits of LEFM (Figure 2.6).

Hutchinson[20][21] and Rice and Rosengren[22] analysed the asymptotic stress and strain fields for materials showing a nonlinear stress-strain response such as may be represented by a Ramberg-Osgood power law,

$$\frac{\varepsilon}{\varepsilon_0} = \frac{\sigma}{\sigma_0} + \alpha(\frac{\sigma}{\sigma_0})^n, \text{ for } \sigma \geq \sigma_0,$$

where α is a dimensionless constant, n is the strain hardening exponent and σ_0 and ε_0 are the reference stress and strain respectively, which can be the stress and strain at yield. The solution, known as the HRR model, for Mode I deformation is regarded as a series expansion in which the leading term has the form

$$\sigma_{ij} = \sigma_{ys}\left(\frac{J}{\varepsilon_{ys}\sigma_{ys}\alpha I_n r}\right)^{\frac{1}{n+1}}\tilde{\sigma}_{ij}(\theta, n)$$

$$\varepsilon_{ij} = \frac{\sigma_{ys}\alpha}{E}\left(\frac{J}{\varepsilon_{ys}\sigma_{ys}\alpha I_n r}\right)^{\frac{n}{n+1}} \tilde{\varepsilon}_{ij}(\theta,n)$$

where $\tilde{\sigma}_{ij}(\theta,n)$, $\tilde{\varepsilon}_{ij}(\theta,n)$ and I_n are tabulated functions of the strain hardening exponent n and angle θ. The HRR model is a small geometry change solution and is applied to conditions where the effects of crack tip blunting can be neglected.

The integral J has been used as a fracture characterising parameter for nonlinear materials, but single-parameter fracture mechanics breaks down in a low constraint geometry. Low constraint geometry corresponds to situations where compressive stresses along the crack front reduce the crack tip stresses, and this is discussed in section 2.2.

2.1.6 *The Crack Tip Opening Displacement*

Wells[18] tested structural steels for fracture toughness but failed to obtain valid K_{IC} values. He suggested that the fracture toughness of ductile materials could not be characterised by LEFM. Wells noticed from the specimens that the crack faces moved apart prior to fracture, i.e. plastic deformation blunted an initially sharp crack and he proposed that fracture occurred at a critical crack tip opening. The opening displacement u_y for Mode I loading is given by (see table 2.1)

$$u_y = 2\frac{K_I}{E}\sqrt{\frac{r}{2\pi}}\sin\frac{\theta}{2}\left(2-\cos^2\frac{\theta}{2}-\nu\cos^2\frac{\theta}{2}\right).$$

If plastic deformation occurs at the crack tip, i.e. the effective crack length=a+r_y then, u_y becomes one half of the crack tip opening displacement (CTOD). Solving for the displacement u_y at the edge of the first order estimate of plastic zone size, i.e. $r=r_y$,

$$u_y = 4\frac{K_I}{E}\sqrt{\frac{1}{2\pi}\left(\frac{K_I}{\sigma_{ys}}\right)^2\left(\frac{1}{2\pi}\right)}$$

hence $$u_y = \frac{2}{\pi}\frac{K_I^2}{\sigma_{ys}E} = \frac{2}{\pi}\frac{G}{\sigma_{ys}}.$$

Since the crack tip opening displacement (δ) is $2u_y$, δ is;

$$\delta = \frac{4}{\pi}\frac{G}{\sigma_{ys}}.$$

The actual relationship between CTOD and G (and J for linear elastic materials) depends on stress state and strain hardening. A general form of this relationship is written as

$$\delta = \frac{G}{m\sigma_{ys}},$$

where m is a dimensionless constant. Shih[24] provided further evidence that a unique J-CTOD relationship applies well beyond the validity limits of LEFM. Shih applied the HRR solution to evaluate the displacement at the crack tip in terms of J, so that

$$\delta = \frac{d_n J}{\sigma_{ys}},$$

where d_n is a dimensionless constant and has a strong dependence on the strain exponent. This unique relationship between J and CTOD allows CTOD to be a valid crack tip characterising parameter for nonlinear material behaviour. The fracture toughness of a nonlinear material can be characterised either by a critical value of J or CTOD.

2.1.7 *The T-stress*

The elastic stress distribution around a crack tip has a second term $B_{ij}(\theta)$, referring to Eq. (2.1), which is a constant stress parallel to the crack flank. This stress is geometry dependent, and when it is compressive, it affects the formation of the plastic zones in small scale yielding, reducing the value of the crack tip opening stress for a given J. The loss of J-dominance is most easily observed in shallow cracked test specimens, which give enhanced J_C values at failure[25]. The second term in the William's expansion, which Rice[26] has denoted the T-stress, can be used to expand the two-dimensional near tip elastic stress field to;

$$\begin{bmatrix} \sigma_{xx} & \sigma_{xy} \\ \sigma_{yx} & \sigma_{yy} \end{bmatrix} = \frac{K}{\sqrt{2\pi r}} \begin{bmatrix} f_{xx}(\theta) & f_{xy}(\theta) \\ f_{yx}(\theta) & f_{yy}(\theta) \end{bmatrix} + \begin{bmatrix} T & 0 \\ 0 & 0 \end{bmatrix}.$$

The T-stress forms the second parameter of a two-parameter failure locus which can be used to predict failure for crack tips with different compressive T-stresses. The magnitude of the T-stress is defined through a biaxiality parameter β, introduced by Leevers and Radon[27]

$$\beta = \frac{T\sqrt{\pi a}}{K}.$$

The simplest and most direct method of calculating the T-stress involves inspection of the stress or displacement fields associated with the crack. The displacements can be written in the form

$$u_x = \frac{K}{E}(1+\nu)\sqrt{\frac{r}{2\pi}}f_x(\theta) + (1-\nu^2)\frac{\beta}{E\sqrt{\pi a}}Kr\cos\theta$$

$$u_y = \frac{K}{E}(1+\nu)\sqrt{\frac{r}{2\pi}}f_y(\theta) - \nu(1+\nu)\frac{\beta}{E\sqrt{\alpha a}}Kr\sin\theta$$

On the crack flanks ($\theta=\pi$) and the angular functions $f_i(\theta)$ are zero, allowing the biaxiality parameter to be determined by direct inspection of the asymptotic displacement u_x, given by the above equations.

Anderson et. al.[25] and Betegon and Hancock[28] studied the effect of the compressive stresses on the J-dominated zone. Sumpter[6] conducted fracture tests on high strength aluminium alloys (including the alloy used for the Christchurch fabrication), and indexed the critical values of J for different geometries in terms of the T-stress, Figure 2.7.

2.2 *Fracture Criteria*

Fracture toughness can be characterised by a critical value of a single parameter, namely K_{IC} or J_{IC} for the cases of Mode I loading. The single parameter approach is invalid for low constraint geometry where negative T-stress affects the stresses in the plastic zone (although the plastic zone size must be small compared to all in-plane dimensions for valid K_{IC} and J_{IC} tests). In this case, two-parameter fracture mechanics are required, in which T-stresses are used as a constraint index for a given geometry. Standard fracture toughness testing of materials requires test specimens to be W=2B and $0.45<a/W<0.5$, where W is the width, B is the thickness and a is the crack length. This configuration maintains a triaxial state of stress near the crack tip, i.e. plane strain conditions predominate through the thickness, but plane stress conditions exist on the plate surface where there are no stresses normal to the free surface.

However, for structural components of a ductile material whose in-plane dimensions are much larger than the thickness, a crack in such geometries can fail by crack tunnelling, leading to fully slant crack growth. This type of crack growth can be stable because fracture resistance increases with crack extension, and a rising R-curve is obtained. Fracture tests on a material in plane strain conditions may provide a flat or falling resistance curve (Figure 2.8a), resulting in a critical value of K_{IC} or J_{IC}, whilst a test under plane stress conditions provides a rising resistance curve (Figure 2.8b). For a material exhibiting a rising resistance curve, the failure criteria are:

$$G > J_R$$

and $$\frac{dG}{da} \geq \frac{dJ_R}{da},$$

where G is the driving force, J_R is the resistance in terms of J, and Δa is crack extension.

2.3 *Guides from British Standard Institution*

The standard procedures for material fracture toughness and resistance curve testing are provided by the British Standard Institution (BSI) in BS 7448[29]. The requirements in this guide are provided for plane strain fracture toughness testing. Test results that fall below the requirements are defined as provisional fracture toughness.

An assessment for structural stability using fracture mechanics approach is documented in BS 7910[30]. The assessments in this document are in three levels depending on the available data and the desired accuracy. The assessments in all three levels are presented as failure assessment diagrams (FAD) containing an assessment line. The loading condition is indicated by a load ratio (denoted as S_r for level 1 or L_r for levels 2 and 3) of applied stress to the flow stress (in level 1) or yield stress (in levels 2 and 3). The fracture instability is determined by a fracture ratio (K_r) of the estimated applied K_I to the fracture toughness K_{IC}. The load ratios and fracture ratios are the horizontal axis and vertical axis, respectively, of the FAD.

Two methods are provided for assessment in level 1 in cases where the material information is limited. The methods require the estimates of applied stress and fracture toughness. One of the methods is manual estimation, which does not involve a FAD, but produces an acceptable flaw size. The resulting flaw dimension has to be checked as acceptable for plastic collapse consideration given in the document. The assessment line for the other method is a rectangle and its limits are for $K_r = 1/\sqrt{2}$ and $S_r = 0.8$. The former method is provided for calculating the maximum allowable flaw size using the fracture toughness, either by the stress intensity factor or CTOD method.

There are two methods in level 2 assessment based on a single value of toughness. The fracture ratio (K_r) in the first methods (denoted as Level 2A) is a function of the load ratio (L_r);

$$K_r = (1 - 0.14L_r^2)\{0.3 + 0.7\exp(-0.65L_r^6)\}$$

for $L_r \leq L_{rmax}$; and

$$K_r = 0$$

for $L_r > L_{rmax}$, where $L_{rmax} = \sigma_{flow}/\sigma_{ys}$, i.e. the ratio of flow stress to yield stress.

The second method (Level 2B) requires a specific stress-strain curve. Level 2B applies to materials that exhibit a yield discontinuity in the stress-strain curve. The equations for the assessment line are as follows;

$$K_r = \left(\frac{E\varepsilon_{ref}}{L_r\sigma_y} + \frac{L_r^3\sigma_y}{2E\varepsilon_{ref}} \right)^{-0.5} \qquad \text{for } L_r \leq L_{rmax}; \text{ and}$$

$$K_r = 0 \qquad \text{for } L_r > L_{rmax},$$

where ε_{ref} is the true strain obtained from the uniaxial tensile stress-strain curve at a true stress, $L_r\sigma_y$.

For ductile materials which exhibit stable tearing level 3 assessment should be used. There are three methods in level 3. Two of the methods in level 3, i.e. Level 3A and 3B, are the same as for Level 2A and 2B respectively. Level 3C requires computed elastic and elastic-plastic J integral result, i.e. J_e and J respectively, to produce a FAD specific to a particular material and geometry. The equations for the assessment line are

$$K_r = (J_e/J)^{1/2} \qquad \text{for } L_r \leq L_{rmax}; \text{ and}$$

$$K_r = 0 \qquad \text{for } L_r > L_{rmax};$$

where J_e and J are values corresponding to the same load (same L_r) and K_r is plotted as a function of L_r.

Calculations of load ratio and fracture ratio for a flaw provide an assessment point. The flaw is acceptable where the assessment point is below the assessment line. If a flaw is unacceptable for an initial assessment, a higher assessment level can be applied provided that accurate material information is available.

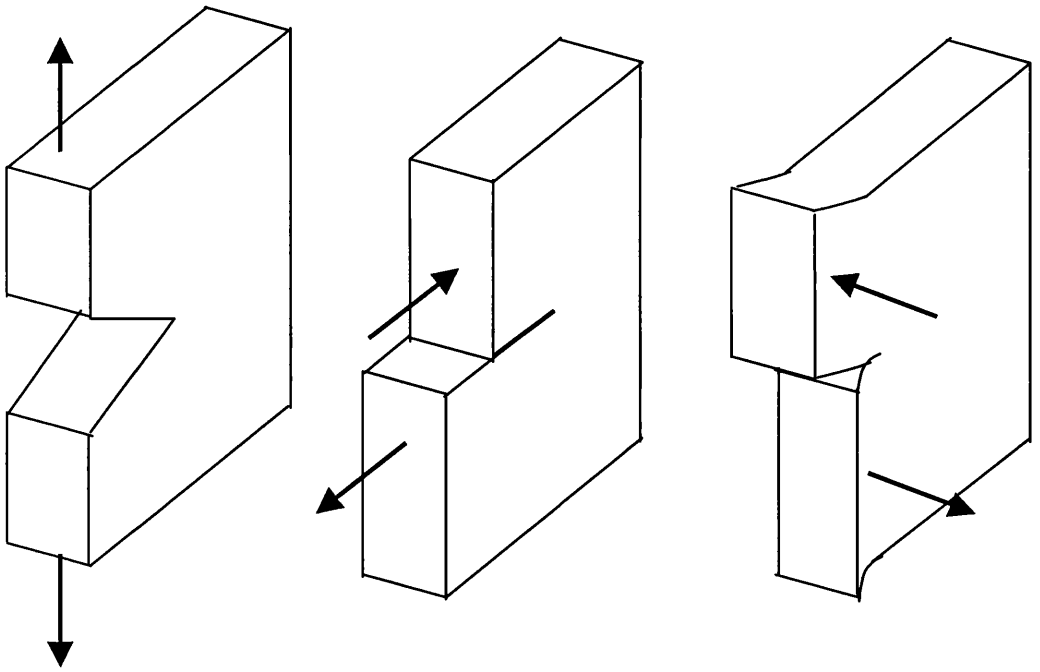

Mode I
Opening mode

Mode II
In-plane shear mode

Mode III
Out-of-plane shear mode

Figure 2.1 The three modes of loading.

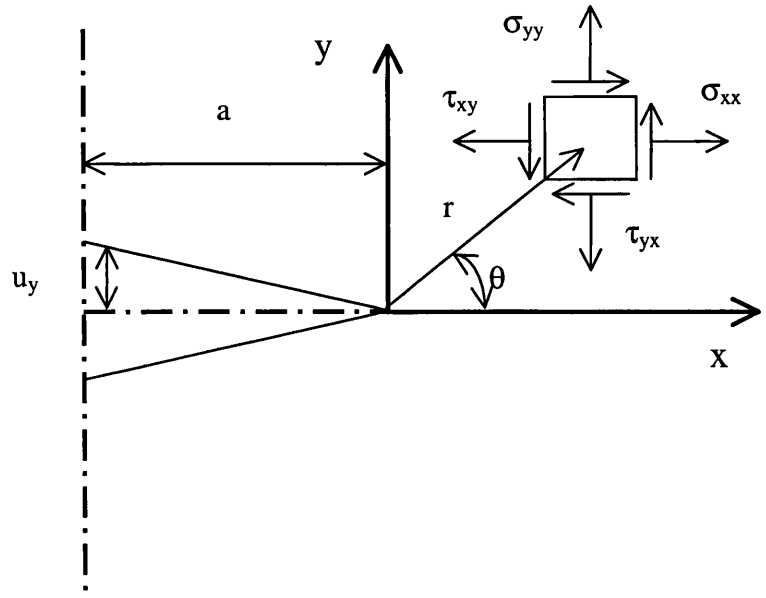

Figure 2.2 Definition of the co-ordinate axis and crack flank displacement of a sharp crack.

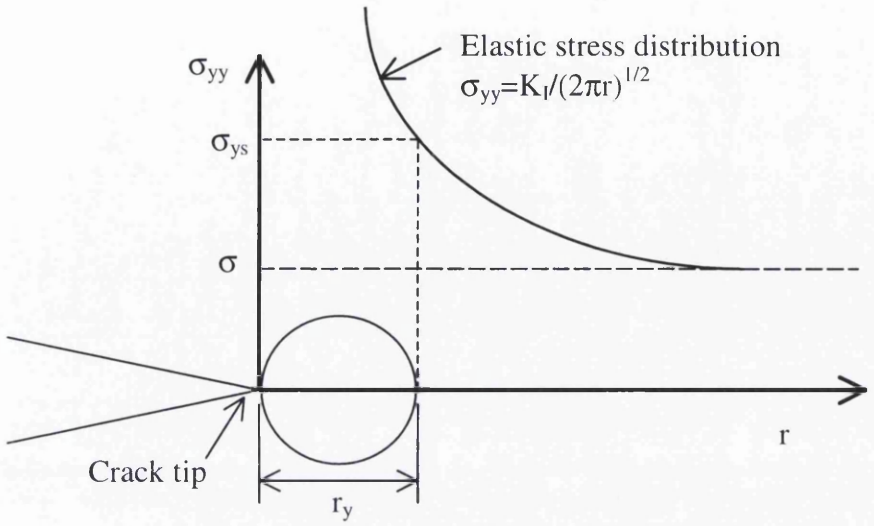

Figure 2.3 The first order estimate of plastic zone size (for plane stress condition).

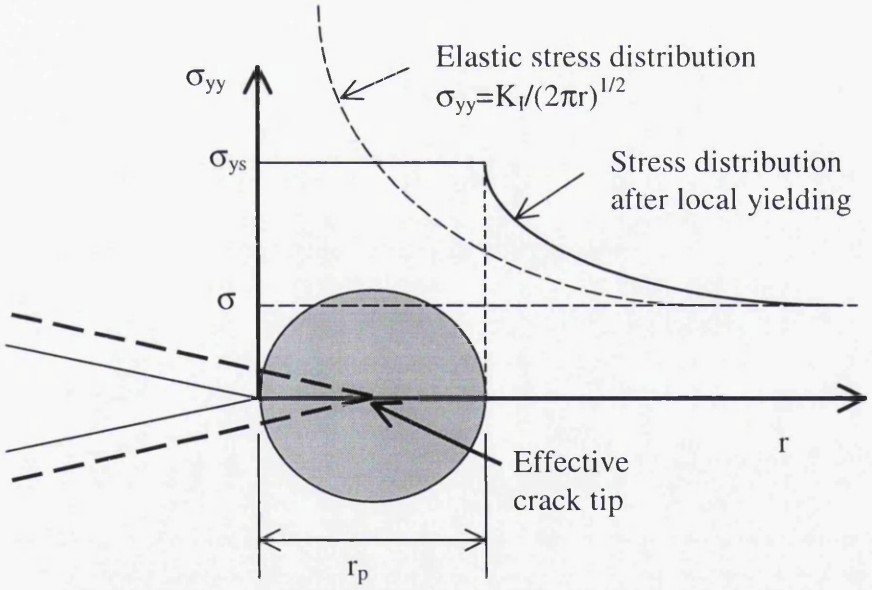

Figure 2.4 The Irwin plastic zone size.

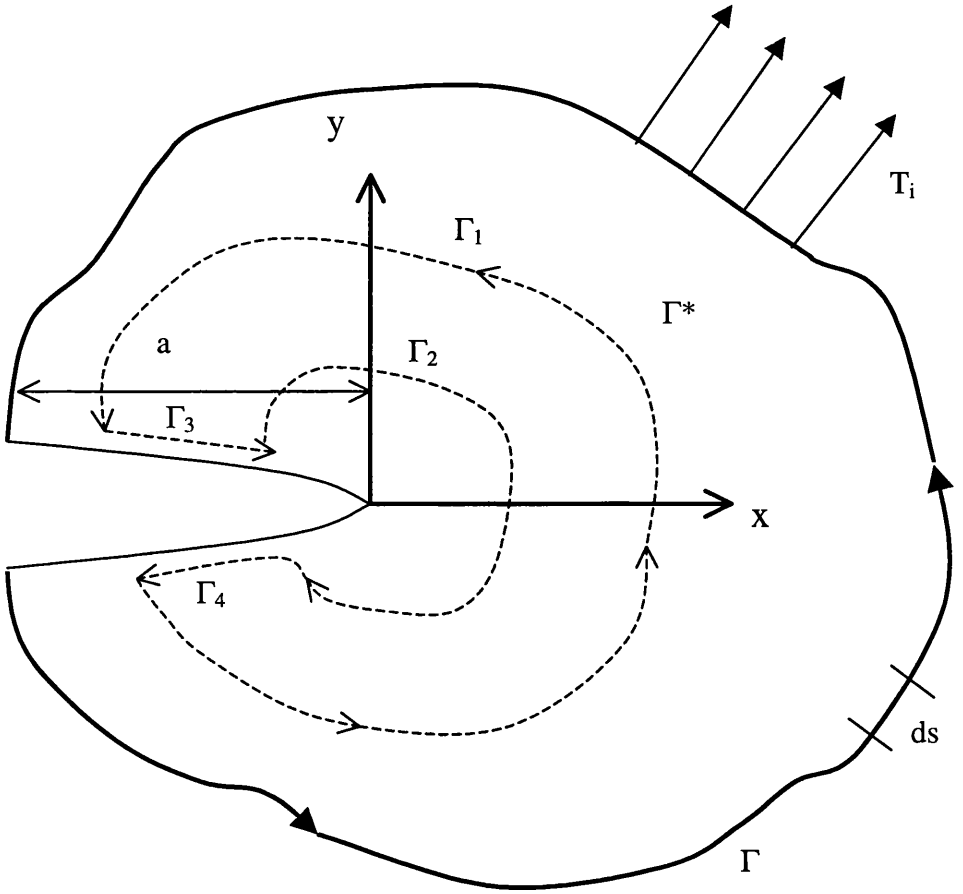

Figure 2.5 An arbitrary contour Γ and an closed contour Γ^* enclosed an area A^*.

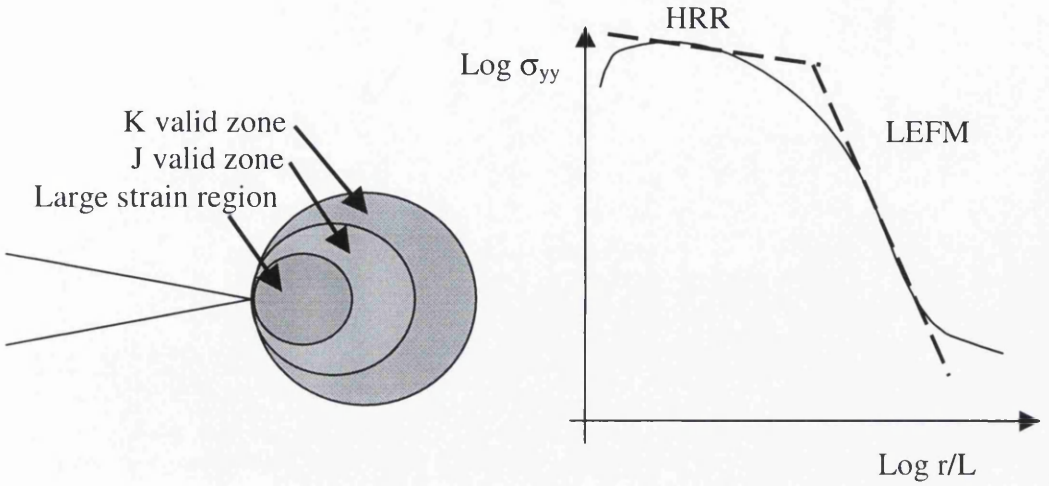

a. Small scale yield

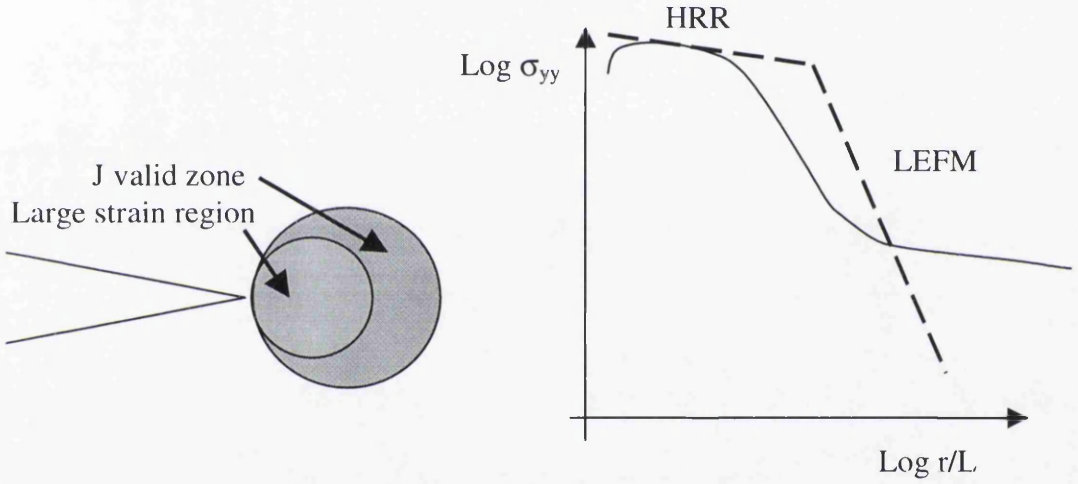

b. Elastic-plastic conditions

Figure 2.6 Effect of plasticity on the crack tip stress field.

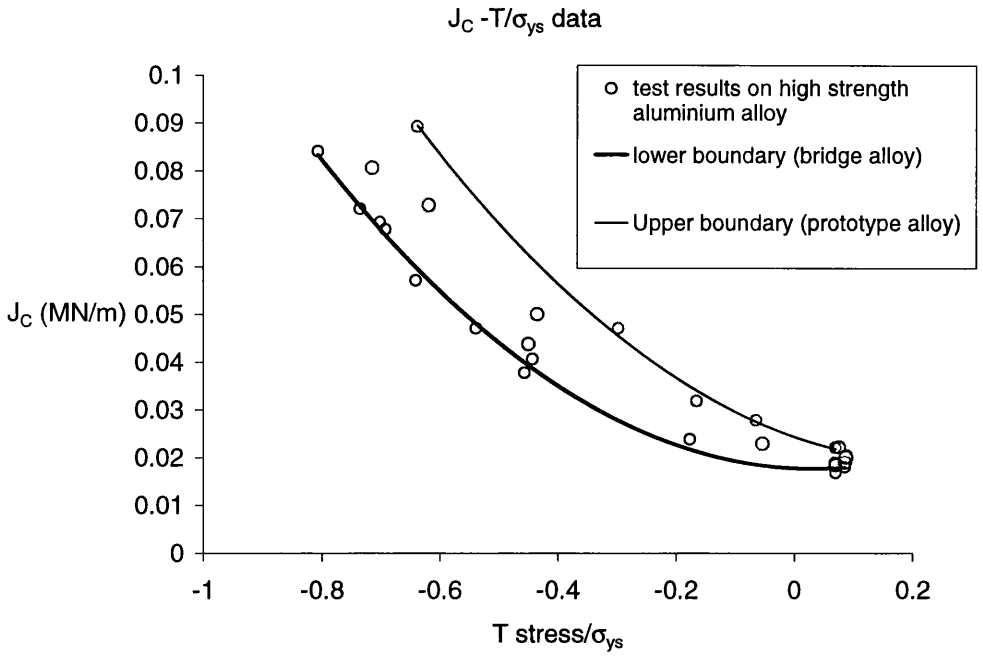

Figure 2.7 The failure loci of J_C versus T/σ_{ys} for high strength aluminium alloy[6].

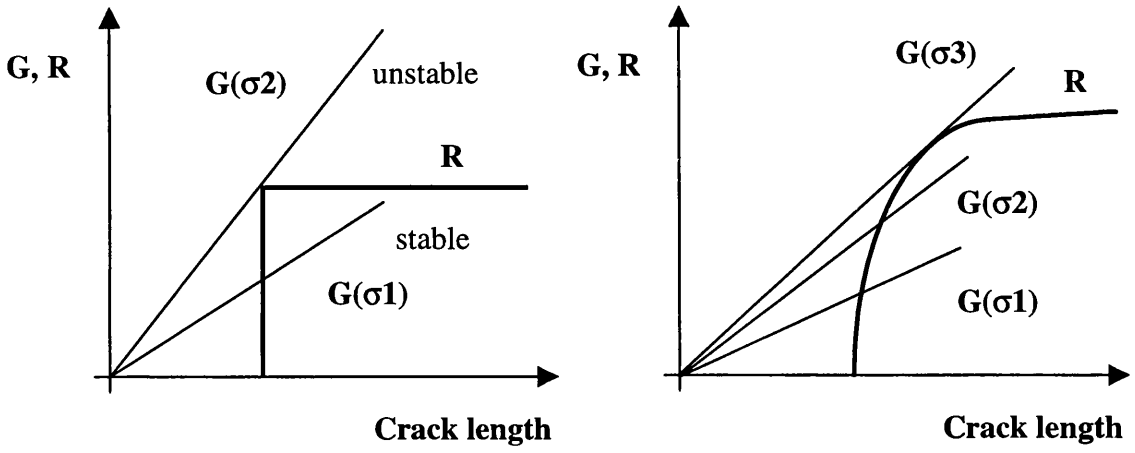

a. A flat or falling R-curve. b. A (conventional) rising R-curve.

Figure 2.8 Schematic driving force G (which is not necessarily linear) and R-curve diagrams.

CHAPTER 3. PREVIOUS FRACTURE ASSESSMENT SCHEMES FOR THE CHRISTCHURCH BRIDGE

3.1 *Summary*

Failure assessment using a fracture mechanics approach has been provided for the damaged Christchurch bridge at different stages of the bridge design. Firstly, Webber[1] applied fracture mechanics to predict a critical size of surface crack, hence the service life. The results were too conservative, compared to a full scale bridge test.

Henry et. al.[4] studied constraint effects on CCT and 3PB specimens using numerical and experimental results from fracture tests on the bridge alloy. The fracture toughness from different geometries were rationalised in terms of the T-stress, so that a fracture toughness loci in the form of J versus T was obtained for the material (see Figure 2.7). Henry's numerical result[3] showed that the constraint at crack tips in the bridge girder is generally low, producing a negative T-stress. Thus, a two-parameter fracture assessment for the damaged bridge was suggested.

Cheung[7] conducted an extensive numerical analysis of the crack tip fields for different crack geometries in the bridge girder. Solutions for the estimation of J or K for various crack tip positions were produced using the numerical results, so that the stress field at a crack tip for a given load could be predicted. Failure assessment for a damaged bridge was performed using the estimated J or K for a known crack in conjunction with the J-T toughness loci.

3.2 *Predicted Services Life*

Webber[1] used the fatigue test results of 9.5mm thick bridge alloy specimens and integrated the crack growth relationship to predict a residual life, using a critical stress intensity factor to calculate the critical crack size. The prediction assumed that a bridge girder failed by a crack grown from a defect in fillet-welded joint. The fatigue test result[9] was presented by a Paris Law:

$$\frac{da}{dN} = C(U\Delta K)^m$$

where $C = 1.7\times10^{-11}$ and 6.9×10^{-12} mm/cycle$(Nmm^{-3/2})^{-3}$, on the scatterband limits;

or $C = 1.08\times10^{-11}$ mm/cycle$(Nmm^{-3/2})^{-3}$, the average between the scatterband limits,

$m = 3$, an approximation for the scatterband trend,

$U\Delta K$ is the effective ΔK; $U=0.4R+0.72$ and R is the ratio of max. and min. applied stress.

However, the data for the geometry factor (Y) in the stress intensity factor was not available. Webber[1] adopted a solution for Y which was obtained from results of a geometrically similar steel joint.;

$$Y = \frac{M_s M_t M_K}{\Phi_0}$$

where $\frac{M_s}{\Phi_0}$, M_t and M_K are correction factors for crack shape, crack depth and shape, and the weld toe stress concentration respectively. In this analysis, Webber[1] adopted a linear crack front shape relationship $2c=6.71+2.58a$ (in mm), where 2c is the width of surface crack and a is its depth.

Using the crack front shape relationship and a typical value $K_{IC}=41MPa\sqrt{m}$ (from material tests made at this time), Webber estimated a critical surface crack size of 45mm(long)×15mm(deep). Assuming an initial crack depth of 0.0125 mm, and keeping the same crack front shape, he predicted that the service life of the bridge was 11500 crossings for the fatigue design load (a stress range of 155 MPa).

However, full scale fatigue tests on structural component showed that long cracks of 100-200mm were regularly sustained by the tension chord in the bridge, and cracks of up to 300mm were observed. In one particular test, a through thickness crack of 99mm length on one side and 57mm on the other was found in the girder after 17000 load cycles. The crack extended to over 200mm and failed at 27000 cycles on the application of the limit load (Figure 3.1). In the test report[1], Webber suggested that an accurate stress analysis and K estimation scheme was necessary for the fracture assessment scheme. This recommendation led to the subsequent numerical analysis of fracture test specimens and cracks in the bridge girder.

3.3 *J-T fracture Toughness Loci*

Fracture tests of the bridge alloy, using CCT and 3PB specimens, were conducted experimentally and numerically by Sumpter[31][32] and Henry[3] respectively. The results[4] showed that constraint effects elevated the fracture toughness, denoted by J_C. These constraints were rationalised in terms of the T-stress, thus a J-T fracture toughness loci was established, see Figure 2.7.

Henry[3][5] showed that a crack in the stem and a shallow crack in the flange of the bridge are low constraint geometries. Henry analysed the crack tip fields for stem cracks (for $0.089<2a/W<0.187$) and flange cracks ($0.021<a/W<0.343$), using the finite element method. The result showed that negative T-stresses existed at the crack front in both stem and flange. The negative T-stresses in the stem cracks were higher than in the flange. The stem and flange cracks were modelled as stationary cracks in 3-D.

Henry[3] provided a framework for a fracture assessment scheme using the J-T fracture toughness loci as the failure criteria. He suggested that the J value for a given geometry can be computed using a J-estimation scheme by Lau[33]. The T-stress could also be estimated according to the crack geometry. Using this fracture assessment scheme, the instability of a given crack geometry subjected to an arbitrary load was determined by whether the estimated J and T were within or beyond the lower bound of the fracture toughness loci. When the applied J (indexed by the T value) exceeded the lower J-T toughness locus, failure would occur.

3.4 *Fracture Assessment for the Christchurch Bridge*

A fracture assessment scheme for the Christchurch bridge was provided by Cheung[7] who estimated the fracture behaviour of a through thickness crack in the bridge. The inspection applies to flange cracks and the lower crack tip of stem cracks where the high tensile stresses are more significant for structural failure. The assessment scheme requires the estimation of the fracture parameter J and the elastic T-stress for a given crack, after which the estimated J and T are checked against the J-T fracture toughness loci in order to assess the stability of the bridge containing the crack.

The J-estimation scheme for evaluating J from elastic parameters Y and r_y has the form:

$$J = \pi\sigma_{ys}\varepsilon_{ys}(a + r_y)Y^2\left(\frac{\varepsilon_{re}}{\varepsilon_{ys}}\right)^2,$$

where σ_{ys} and ε_{ys} are yield stress and strain;

ε_{re} is the reference strain,

Y is the geometry factor, determined by stress analysis,

$a+r_y$ is the effective crack length, accounting for the plasticity at the crack tip,

and $r_y = \frac{1}{6\pi}(\frac{K_I}{\sigma_{ys}})^2$ for plane strain, or for plane stress.

The T-stress is computed from β, the biaxiality factor, see section 2.1.7.

Henry's numerical results[3] of Y and β for flange cracks were used for the fracture assessment scheme. For stem cracks, an intensive analysis for various crack positions was carried out by Cheung[7] in order to study solutions for Y and β for the fracture assessment scheme. Cheung used a 2-D finite element model for the analysis of stem cracks, assuming plane strain conditions at the mid-plane in the thickness direction, because the computation time for 2-D analysis was much less than that for 3-D analysis. Cheung's 2-D results were calibrated for accuracy by comparing them, where possible, to Henry's 3-D result. For the case of a stem crack approaching the flange (crack tip less than 25 mm from the flange, see Figure 3.2 for details) the 2-D result were not sufficiently accurate for fatigue calculation, and a further 3-D analysis was carried out for this thesis (see Appendix A).

The Y solutions for stem cracks are expressed by three polynomial equations depending on the position of the crack. The three categories are namely,

stage I: cracks contained entirely within the stem (thickness=25mm);

stage II: cracks penetrating from the stem to the web (thickness=12.5mm);

stage III: cracks with the same conditions as stage II but with a remaining ligament<25mm from the flange.

The solutions for Y and β in the three stages are shown in Table 3.1.

For flange cracks the critical crack lengths are evaluated for various stress ratios $\sigma_{applied}/\sigma_{ys}$ because the solutions of Y and β for flange cracks are functions of the crack length only. In this

case, the failure criterion is defined in terms of critical crack length for any arbitrary stress, see Figure 3.3.

Table 3.1 The Y and β solutions for stem cracks.

	Y solutions	β solutions
Stage I	$-0.71(a/b)^2+0.59(a/b)+1.06$	$2.85(a/b)^2-3.15(a/b)-0.14$
Stage II	$8.48(s/2a)^5-20.06(s/2a)^4+18.24(s/2a)^3$ $-8.49(s/2a)^2+2.53(s/2a)+0.56$	$22.13(a/b)^4-51.53(a/b)^3$ $+44.74(a/b)^2-17.55(a/b)+1.66$
Stage III	$Y_{(\text{stage II})}$¤$\times 0.049\ \ln(c/25)+1.005$	$1.31(c/25)^3-0.75(c/25)^2$ $-1.27(c/25)-0.15$

The simplification used for flange cracks is not appropriate for the estimation of J and T for stem cracks, whose variables for the Y and β solutions are strongly dependent on the position of the crack. A spreadsheet, which can be set up in a notebook computer, was developed for calculating J and T. This computer code requires the input of applied stress in the bottom flange, and the lower and upper crack tip levels. It is a tool for the inspector's convenience.

Cheung[7] suggested that predictions by the fracture assessment scheme may be too conservative. For instance, the conditions of a 100mm long crack in the stem can be critical according to the assessment scheme, but this crack length is observed to be stable in the bridge test. Therefore, the fracture behaviour of the bridge alloy is investigated further for other factors that can enhance the fracture resistance.

¤ N.B. $Y_{(\text{stage II})}$ is the estimate of Y using the solution for stage II. See Figure 3.2 for notations.

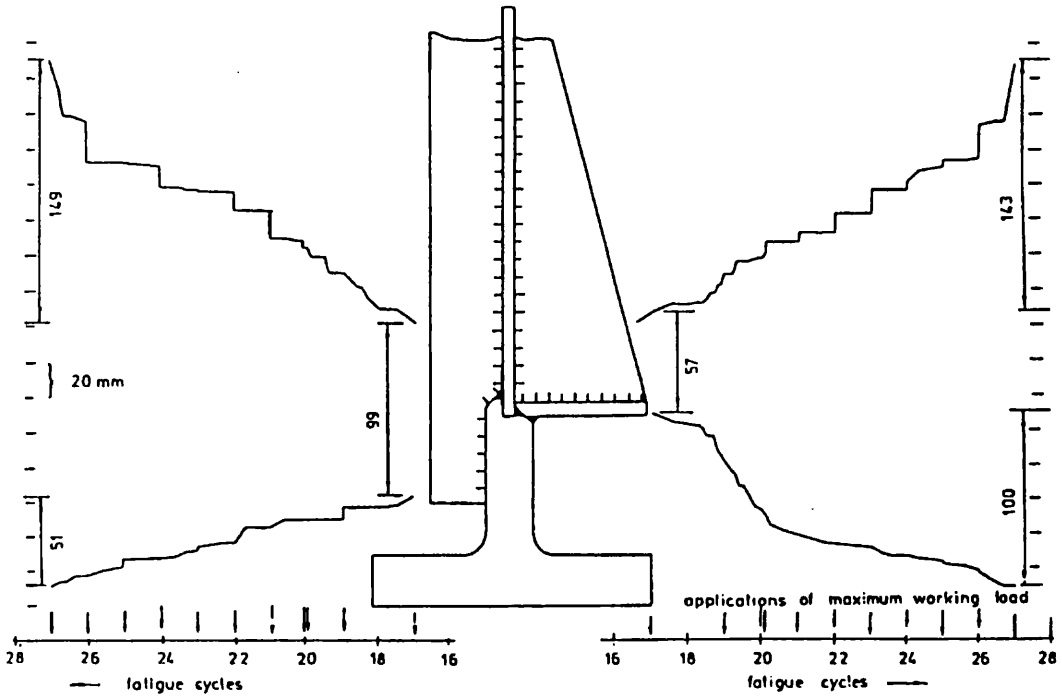

Figure 3.1 Variation of crack growth in the bridge stem with fatigue cycles[1].

a = Half crack length for stem cracks, or the total crack length for flange cracks.

b = Distance from the crack's mid-point to the top of the bottom flange.

W = Flange width.

s = Proportion of the crack length lay within the stem.

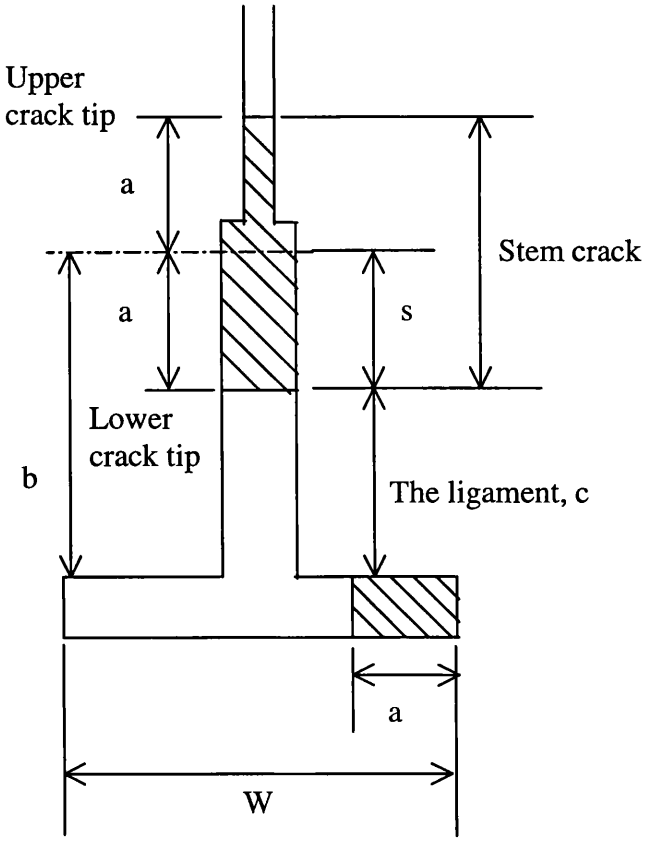

Figure 3.2 Details of crack aspect ratio.

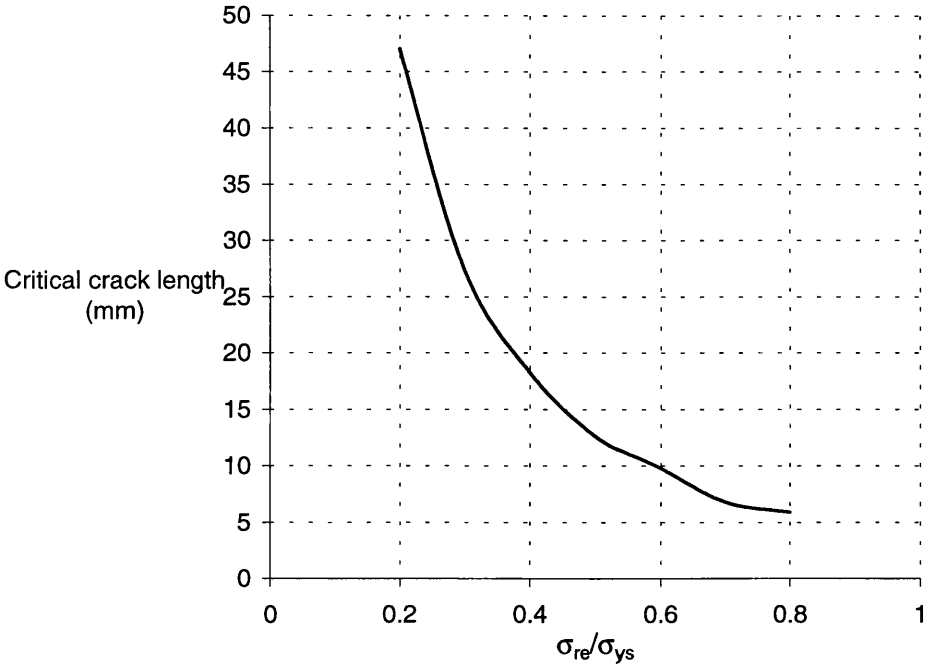

Figure 3.3 Critical crack lengths versus normalised applied stresses for flange cracks (computed for applied $J=J_C$, when J_C is indexed by a given T-stress).

CHAPTER 4. RESISTANCE CURVE DETERMINATION

4.1 *Large Scale Fracture Tests on Aluminium Bridge Alloy*

Sumpter conducted fracture toughness tests[6] on the production version of the bridge alloy using standard (b=B) 3PB specimens (for valid K_{1C} test), with a range of a/W from 0.05 to 0.5. A large 3PB and a large CCT specimen (for the same thickness but b>>B) were also tested and these produced significant stable crack growth. He used the T-stress as the constraint parameter to rationalise the measured J_C for different specimen geometries. He estimated the energy dissipation rate (see section 6.2.2) of a specimen from the slope of the plot of absorbed energy versus crack extension area. The result showed that it increased from 40kJ/m^2 for standard (b=B) 3PB specimens to 1000kJ/m^2 for the large (b>>B) 3PB specimen. Although there was no precise relation between fracture toughness and energy dissipation, this large increase of energy dissipation rate would provide adequate resistance against unstable crack growth. He showed that the G_C and J_C at failure were 0.19 MN/m and 0.33 MN/m respectively for the large 3PB specimen (the test was stopped before instability), but both equalled 0.024MN/m respectively for the standard 3PB specimen. He suggested that the high energy dissipation rate guaranteed structural safety under all possible loading scenarios short of plastic limit load. He noticed that the effect of ligament size was shown as the alteration of the fracture mode, which changed from purely flat fracture in the square ligament (b=B) to slant fracture (in the form of shear lips) in the rectangular ligament (b>>B) for the same thickness. The shear lips developed and caused the flat fracture at the central region of the thickness of the b>>B specimen to taper down, whilst flat fracture was dominant in the b=B specimens[6].

The effect of ligament size on the stress/strain conditions ahead of the crack were studied numerically using the finite element method. The results showed that the differences of opening stress, stress triaxiality, equivalent plastic strain and plastic dissipation at the same J value for different sizes of ligament were insignificant except for the plasticity ahead of the crack tip which varied between different sizes of the 3PB specimens.

The writer simulated stable crack propagation numerically using the DEBOND facility in ABAQUS to provide an R-curve for the bridge alloy. The plasticity, and elastic and plastic energy were also computed as outputs from ABAQUS. The computed energy was calculated

after the load increment within which the crack length had extended, therefore the released energy due to crack extension could not be separated from the energy change under increasing load. As a result the energy release rate could not be calculated accurately from the numerical results, and the J integral was used as the measure of fracture resistance. The numerical result showed a 'concave' (see section 4.6) J_R-curve for the bridge alloy. The dJ_R/da increased with crack extension, i.e. the rate of fracture resistance per unit crack growth was increasing or increasing constantly with crack extension. The results showed an invariant concave R-curve for specimens with square (b=B) and large (b>>B) ligaments. The form of the R-curve was eventually confirmed experimentally by Sumpter[8]. Fracture instability could be predicted by comparing the potential energy rate of a cracked body and its fracture resistance, namely the R-curve approach. Instability prediction (see Chapter 5) using the R-curve approach shows that long cracks with b>>B ligament (in this case, B=25mm) are likely to grow stably under substantial load increases, agreeing with the experimental results of Sumpter.

4.2 *Near Tip Stress and Strain Fields for Small and Large Ligaments*

The aluminium alloy used for the Christchurch bridge fabrication is very similar to AlZnMg-7019. The typical tensile data for the alloy, which were used in the numerical modelling, are summarised in Table 4.1 (fatigue data is given in Chapter 9). The true stress versus true strain curves, parallel and transverse to the extrusion direction, are shown in Figure 4.1.

Table 4.1 Summary of tensile data of the bridge alloy.

E (MPa)	N	σ_{ys} (MPa)	σ_{uts} (MPa)	$\sigma_{failure}$ (MPa)	$\varepsilon_{failure}$
69000	0.33	391	447	603	0.354

Four 3PB specimens, namely a/W=0.2 (for both b=B and b>>B), 0.33 and 0.5, and one centre cracked tension (CCT) specimen, 2a/W=0.52 and b>>B, (see Table 4.2 for details) were analysed as stationary cracks using the finite element method. The finite element meshes were made for 3-D and 2-D analysis. Each 3PB specimen mesh represents only a quarter of the specimen as it is symmetric in the length and thickness directions, while the CCT specimen mesh represents one eighth of the specimen as it is symmetric in all directions (length, thickness and width). Focused meshes (Figure 4.2), consisting of concentric rings of four sided elements

(in 2-D meshes) were used around the crack tip. For elastic-plastic analysis, crack tip blunting can be modelled as the nodes at the crack tip are not tied.

Figure 4.3 compares the numerical load-displacement data between 2-D and 3-D analyses of the four 3PB specimens. The data indicates the global behaviour of each model. The 3-D results of all the small ligament specimens, i.e. specimens with a/W=0.33, 0.5 and 0.2 (b=B), lay between the results of plane stress and plane strain. For the a/W=0.2 specimen with b>>B, where the thickness is much smaller than its in-plane dimensions, the 3-D curve was much closer to the plane stress analysis. The significance of plane stress and plane strain conditions for the numerical modelling of crack extension will be discussed in the next section.

Table 4.2 Details of the 3PB and CCT specimen.

3PB specimens a/W	Uncracked ligament, b (mm)	Crack length, a (mm)	Span, S (mm)	Thickness, B (mm)
0.2(b=B)	25	6.25	125	25
0.33	50	25	300	25
0.5	25	25	200	25
0.2(b>>B)	160	40	800	25
CCT specimen 2a/W				
0.52	62.5	67.5		25

The opening stress and stress triaxiality of the numerical results in the vicinity of the crack tip were compared for the different 3PB crack geometries. Opening stress is the stress normal to the crack growth direction, while stress triaxiality is a measure of constraint, defined as the ratio of hydrostatic stress to effective (Von Mises) stress. High stress triaxiality indicates high hydrostatic stress, which encourages microvoid growth and coalescence. In deeply cracked 3PB specimens, stress triaxiality at the crack tip is high but decreases with increasing distance from the crack tip and with the thickness to the free surface, i.e. higher stress triaxiality at the mid-plane. This results in the tunnelling effect on crack growth and the formation of shear lips accompanying the crack propagation. The stress triaxiality between crack geometries were compared in order to explain the correlation between fracture mode and the geometry effect, because flat and slant fracture respectively were observed in the 3PB specimens with the b=B ligament (flat) and the b>>B ligament (slant).

Figure 4.4 and 4.5 show the opening stress(σ_{yy}) and stress triaxiality respectively, at J=16 and 90kN/m for the four 3PB specimens. These two parameters ahead of the crack tip (plotted against nondimensional distance, $r\sigma_{ys}/J$) are virtually the same for all four specimens. The same conclusion can be drawn for variations across the thickness, Figures 4.6 and 4.7.

Equivalent plastic strain is the total accumulation of plastic strain used to define the yielded area. A contour plot of equivalent plastic strain illustrates the plasticity (the plastic zone) of a numerical finite element model. Figure 4.8 shows the difference in plasticity at the crack tip (on the midplane) between three 3PB specimens, namely a/W=0.5, 0.2 (b=B) and 0.2 (b>>B). The plastic zone at the midplane of specimens with a/W=0.5 and 0.2 (b>>B) are almost identical at lower J. The plastic zone of the 3PB specimen with a/W=0.2 (b=B) is always larger than that of the a/W=0.5 specimen and, at lower J, the a/W=0.2 (b>>B). At a J of about 85kN/m, the a/W=0.2 (b>>B) specimen contains a larger plastic zone at the crack tip (on the midplane) than that of the a/W=0.2 (b=B) specimen.

Figure 4.9 shows the plastic dissipation, i.e. plastic energy, from the numerical results of the three models versus J. Plastic dissipation is defined as the plastic energy dissipated due to non-reversible deformation. The plastic energy increases with increasing J. The plastic energy for specimens with a/W=0.5 and 0.2 (b>>B) are identical at lower J (J<20kN/m), while it is twice as large for the specimen with a/W=0.2 (b=B). The plastic energy for a/W=0.2 (b>>B) specimen starts increasing at a higher rate after J exceeds 20kN/m, and is larger than that for a/W=0.2 (b=B) specimen at J = 34kN/m.

Crack propagation occurs when potential energy change overcomes the fracture resistance. The potential energy is the internal strain energy plus external work, while the fracture resistance is the sum of surface energy and local plastic dissipation. For elastic-plastic material, the plastic energy of a cracked body is always much larger than the surface energy. Figure 4.9 shows that the plastic dissipation for a/W=0.2(b>>B) increases rapidly at J=20kN/m. This may explain the stable crack growth in this specimen because the more rapid increase in plastic work increases the fracture resistance.

4.3 *Numerical Analysis of Stable Crack Extension*

Stable crack growth in the 3PB specimens with a/W=0.5 and 0.2 (b>>B) and the CCT specimen with 2a/W=0.52 (b>>B) was simulated numerically with the ABAQUS' DEBOND process (only available for 2-D meshes). A rectangular finite element mesh at the crack tip region is required for incremental crack extension, Figure 4.10. Crack propagation criteria can be specified in three ways in ABAQUS, namely critical crack opening displacement, critical stress and crack length versus time (which is related to the time period of the analysis). Elements and nodes associated with the two potential crack surfaces are specified in pairs which are initially contacted, but can be separated using one of the prescribed crack propagation criteria, under the DEBOND operation.

The critical crack opening displacement (COD) criterion is typically used for crack propagation in ductile materials, and is used in the present case. For this criterion, the user inputs a relationship between the COD and the crack extension. A fixed distance, measured from the current crack tip, locates the point where the COD is monitored. The crack propagates progressively (from one node to another) as a function of the prescribed crack extension and the ratio of current (computed) COD to the prescribed COD. In the DEBOND process used in the present case, stresses between the two initially contacted elements reduce to zero as a step function when the separation begins. The crack extension versus crack mouth opening displacement (CMOD) had to be estimated on a trial and error basis, because no experimental crack extension data was available at the time of the analysis. The COD was calculated from this estimation. The computation proceeded by dividing the DEBOND process into several steps which allowed the load versus CMOD curve of the numerical result to match the experimental result when satisfactory crack extensions had been selected. Within each load increment there were several increments of crack extension. This procedure was very time consuming, but provided the required results and a good match between the experimental and numerical load-CMOD curves.

Meshes of half of the 3PB specimens and a quarter of the CCT specimen were generated for the 2-D analysis. The three rollers in the 3PB experimental test were also modelled as rigid surfaces, which had no deformation when they contacted with the model of the specimen. The roller positioned above the crack line loaded the model. The use of applied loads was recommended

by ABAQUS for accurate evaluation of the work done to the model. The output of each increment of crack extension from ABAQUS was calculated after the application of load. In this case the released energy due to crack extension could not be separated from the energy change under increasing load. Therefore the fracture resistance was studied in terms of a J (or J_R, where the subscript R indicates values of J on the resistance curve) versus crack extension, Δa .

The experimental fracture testing of the bridge alloy by 3PB specimens used displacement control. Crack growth in both a/W=0.5 (b=B) specimens and the a/W=0.2 (b>>B) specimen was stable[6], but the load behaviour was different after crack initiation. The load for the a/W=0.5 specimens stayed constant within ±10% of the maximum load (Figure 4.11), whilst the load for the a/W=0.2 (b>>B) 3PB specimen rose with increasing CMOD, Figure 4.12. Both types of load behaviour can occur under plane strain and plane stress conditions in the finite element model, and the most appropriate constraint must be decided from other factors. For our analyses, constraint was decided initially by the load-displacement behaviour of the 3D static crack analyses, see Figure 4.3. Where possible, both plane strain and plane stress analyses were carried out.

The large CCT specimen was analysed numerically using plane stress constraint, but the a/W=0.2 (b>>B) and a/W=0.5 (b=B) 3PB specimens (see Table 4.2 for the dimensions of the specimens) were analysed using both plane strain and plane stress constraint. The plane strain J_R-curve of the a/W=0.2 (b>>B) 3PB specimen was not acceptable (Figure 4.12) because the load-CMOD result of the numerical test did not coincide with the experimental record. This was also evident before any crack growth, which started at an applied load of 85kN. In addition, the 3-D analysis of this specimen with a stationary crack, Figure 4.3, showed close agreement between 3-D and plane stress load-displacement curves.

The crack tip plastic zone size (in terms of equivalent plastic strain) increased gradually with the increasing J level, see Figure 4.13 for the plastic zones in the a/W=0.2 (b>>B) 3PB specimen. The size was relatively small compared with the in-plane dimensions, Figure 4.13e (the last load increment), showing small scale yielding predominated. In this case the plastic zone size is about 16mm ahead of the crack tip, Figure 4.13e, where the total crack length is 49mm. Plasticity can also be seen on the model in the top left and bottom right corners at the positions of the rollers. The stress and strain fields ahead of the growing crack tip are discussed in section 6.4.1.

The numerical J_R-curves of the a/W=0.5 (b=B) 3PB specimen for plane stress and plane strain conditions are alike (Figure 4.14). The numerical J_{IC} values (i.e. the value at crack initiation) are 0.018MN/m for the plane stress result and 0.012MN/m for the plane strain result[#], equivalent to 36.2MPa$\sqrt{m}$ and 30.7MPa$\sqrt{m}$ respectively, i.e. the plane strain result is 15% less than that of plane stress. In SSY, the J_R values for the plane strain condition is less than plane stress by 10% (because $G=K_I^2/E'$ where $E'=E$ for plane stress and $E'=E/(1-\nu^2)$ for plane strain). The experimental load-CMOD curve for this specimen is much closer to the numerical plane strain load-CMOD curve (for the initial crack length) than the plane stress curve, Figure 4.11.

The numerical plane stress fracture model of the a/W=0.2 (b>>B) 3PB specimen provides a J_R-curve up to Δa=8mm (Figure 4.15). Within this crack extension, the J_R increases negligibly for the first 4mm of crack extension. After that, the J increases gradually with increasing Δa as the shear lips develop (which is observed in the experimental specimen).

The numerical plane stress K_{IC} for the a/W=0.5(b=B) and a/W=0.2(b>>B) specimens (derived from the J_R values at crack initiation) are 36.2MPa$\sqrt{m}$ and 33.4MPa$\sqrt{m}$ respectively. These values coincide with the plane strain fracture toughness K_{IC} for the bridge alloy of around 35MPa$\sqrt{m}$[8], whereas the plane strain J_R-curve computation gives a significantly lower value, see above.

4.4 *J_R Curve Fracture Assessment*

For materials under elastic behaviour, the driving force (G) defines the change of potential energy (U_e) per unit crack growth (dU_e/da). The crack propagates in a stable fashion when

$$G=R$$

and $$\frac{dG}{da} \leq \frac{dR}{da}$$

but for unstable crack growth;

[#] N.B. The plane strain computation started crack propagation at a load of 15.5kN, just before the load reached its maximum value of 18.1kN.

$$\frac{dG}{da} > \frac{dR}{da}$$

where R is the fracture resistance (see Figure 2.8).

For elastic materials, $R=2\gamma_s$ where γ_s is the surface energy of the material. For an elastic-plastic material, $R=2(\gamma_s+\gamma_p)$, where γ_p, the energy dissipation due to plastic deformation, is typically much larger than γ_s. If the J integral is a measure of the absorbed energy of a growing crack in an elastic-plastic material (which is approximately true for SSY), and the crack growth is stable, J can be viewed as the fracture resistance, R.

A rising J_R curve shows fracture resistance increasing with crack extension. Ductile materials normally exhibit a rising R curve (a conventional rising R curve is a convex curve) because the plasticity at the crack tip increases with crack growth. The G also increases with increasing crack length, giving a positive value of dG/da (providing the load does not decrease) which is the usual case for stable crack growth. For stable crack growth after the maximum load is reached (made possible by displacement control), G can reduce with increasing crack length, giving a negative dG/da. This is the case of the a/W=0.5 3PB specimen in the experimental test[6], where the experimental result showed the crack grew in a stable fashion with the load decreasing.

4.5 *J_{IC} at Meta-instability (Pop-In)*

Sumpter[6] reported that the initial crack propagation in shallow notched standard 3PB specimens, namely $a/W \leq 0.3$, was unstable while the subsequent crack growth in a/W=0.5 3PB specimens (and large ligament specimens) was stable. Although the J_{IC} values for the experimental 3PB specimens (with $0.1 \leq a/W \leq 0.5$) varied between the different crack geometries, the results could be correlated by the T-stress[6], see Figure 2.7 and section 3.3. The T-stresses for $0.1 \leq a/W \leq 0.3$ specimens were negative, but they were positive for a/W=0.5 specimens, which provided the lowest J_{IC} value. The J_{IC} value (or $J_{0.2}$[Ω] value obtained from the a/W=0.2 specimen) obtained experimentally by Sumpter[6] was 0.018MN/m for both a/W=0.5 (b=B) and

Ω N.B. $J_{0.2}$ is defined in BS 7448:Part 4 as the fracture resistance at 0.2mm crack extension. For a valid J_R-curve, $J_{0.2}<J_{max}$ (The evaluation of J_{max} is given in BS 7448:Part 4).

a/W=0.2 (b>>B) 3PB specimens. This also coincided with the typical K_{IC} of 35MPa$\sqrt{m}$[8], see section 4.3.

The numerical plane strain K_{IC} of a/W=0.5(b=B) specimen was 30.7MPa$\sqrt{m}$, see section 4.3. The numerical plane strain K_{IC} was lower than the fracture toughness K_{IC} of 35MPa$\sqrt{m}$, though the load-CMOD curve of the numerical plane strain result agreed with that from the fracture toughness test.

Figure 4.16 shows that the experimental J_R value at initiation of a b>>B CT specimen was in between the values of plane strain and plane stress results, although the experimental J_R curve was computed using plane stress constraint. The J value at initiation from the result of fracture testing on b>>B CT specimens corresponds closely with the K_{IC} from early plane strain fracture toughness test results[8].

Plane strain fracture toughness can be obtained by testing a sufficiently thick plate of alloy. In general, the plane strain fracture toughness G_{IC} (or K_{IC}) is restricted to SSY conditions, and is determined from the load vs. displacement record of a fracture test at pop-in. The G_{IC} (K_{IC}) value is a material property and independent of the specimen dimensions[34], provided that the test result fulfils the requirements of the standard fracture toughness test.

It is clear from both experimental and numerical results described above that crack initiation is associated with SSY (and therefore plane strain) conditions in the near crack tip region, and that different specimen (and hence ligament) sizes do not affect this value. It is, however, affected by the degree of in-plane constraint, as indexed by the T-stress. It is not clear why the use of plane stress finite element analysis of stable crack growth give the same values of K_{IC} as those obtained by plane strain formulae applied to standard test specimens with square ligaments, i.e. b=B.

4.6 *The Form of the R Curve*

The J_R versus Δa curves from both numerical 3PB and CCT test results show a concave R curve for the bridge alloy. The higher J at initiation for the CCT test result (a low constraint geometry) in Figure 4.17 is correlated to a negative T-stress, which is rationalised by Sumpter in the form

of J_C versus T-stresses as a constraint index for the material, Figure 2.7. The J_R-curve of the CCT specimen in Figure 4.17 is a hypothesis which assumes zero T-stress at initiation, see section 4.5. As the R curve rises with crack extension, the curves from the CCT and 3PB (b>>B) specimens converge, because the effects of in-plane constraint becomes insignificant due to increasing amount of slant fracture.

This form of R-curve, i.e. a concave curve, has been confirmed experimentally by Sumpter[8] (Figure 4.16). He used a compliance unloading technique (which gives a measure of the average crack extension) on an a/W=0.23 (b>>B) CT specimen to obtain an R-curve for the material, using plane stress calibrations. He used formulae from ASTM standard[35] (which calculates J-integral for current crack lengths) to obtain J_e and J_p, and hence $J_R=J_e+J_p$. He provided an R-curve for a crack extension up to 18.5mm (the crack tunnelled, and tapered to a point at Δa=18.5mm with a V-shaped cross-section), at which point the specimen failed by unstable V-shaped fracture at 90° to the notch direction. Another fracture test by Sumpter[36] on a a/W=0.5 (b>>B) CT specimen provided a similar J_R-curve for a crack extension of 35mm (Figure 4.18). It is noted that the fracture resistance between the LT[Υ] and TL orientations are different. The former is twice as much as the latter, see Figure 4.18. Only the fracture resistance in the LT direction will be discussed and applied to the instability prediction, because in the full scale test cracks propagated in this direction, see Figure 3.1. The numerical plane stress R-curve from the large ligament 3PB specimen agrees closely with the experimental result from the CT specimen, see Figure 4.16. Both 3PB and CT specimens are high constraint geometries.

The concave R-curve for the material is different from a conventional rising R-curve. The dJ_R/da of a conventional curve decreases with crack extension, and the curve probably approaches a plateau after the instability occurs at J_C. The dJ_R/da of the experimental R-curve for this material showed no sign of decrease with crack extension, even at failure (Figure 4.16). Therefore, J_C values could not be determined from the data over the observed crack extension, although further testing would probably show some form of saturation.

Υ N.B. TL is the extrusion direction, whilst the LT is the direction normal to TL.

4.7 *Plane Stress Crack Propagation*

Plane strain fracture toughness tests are aimed at producing a single K_C value, K_{IC} (or J_{IC}) i.e. the lowest fracture toughness for instability in the material. The K_{IC} (or J_{IC}) is defined only if the specifications for the fracture toughness test are fulfilled, and the test is conducted under predominantly plane strain conditions. Fracture toughness K_{IC} is a measure of crack tip opening stress at the occurrence of crack propagation. If the crack always propagates at a constant K_{IC}, corresponding to an initial applied load, the applied loads for subsequent crack propagation are generally lower because K is a function of applied stress and the crack length (see section 2.1.3), and usually increases with increasing crack length for most test geometries.

For thin plates, the J_C value rises with decreasing specimen thickness[34][37]. This variation of J_C is the result of plastic deformation ahead of the crack front, which allows plane stress conditions to prevail through the thickness. In this case the instability is preceded by stable crack growth (perhaps, with the appearance of shear lips, but limited in width), and J_C is size dependent because it is a measure of the plastic work ahead of the crack tip.

The relationship between the shear lips' width and fracture resistance has been discussed by Kraft[37] and Knott[38] (see Chapter 6). In case of shear lips forming along the crack flanks, Kraft[37] and Knott[38] predicted J values using the width of the shear lips, assuming a constant plastic dissipation energy per unit volume at the crack tip.

4.8 *Plane Strain to Plane Stress Transition*

The fracture surface of b>>B specimens showed flat fracture at initial crack propagation but the crack failed by fully slant fracture. The onset of the shear lips implied that the transition from plane strain to plane stress started at the beginning of the crack extension. In addition, the numerical result from 3-D analysis of static cracks showed that plane strain conditions existed only in the vicinity (about 2mm ahead) of the crack tip. The plane strain conditions rapidly decreased from the crack tip so that the conditions were predominantly plane stress beyond 6mm from the crack tip, Figure 4.19. In this case neither plane strain nor plane stress analysis of crack extension would be appropriate for the calculation of fracture resistance because of the change in out-of-plane constraint. After several millimetres of crack growth, the crack is

subjected to essentially plane stress conditions, and the large specimens (and structure) behave like 'thin-walled' components.

Both the plane strain and plane stress analyses assume consistency of constraint across the thickness, i.e. either $\varepsilon_{33}=0$ or $\sigma_{33}=0$ respectively. In practice, the predominantly plane strain conditions increase towards the central region of the thickness while the plane stress conditions exist on the plate surface. For the J integral in between the centre of the thickness and the plate surface, plane strain analysis could underestimate its value whilst plane stress analysis could overestimate it.

It is unfortunate that at the time of study the numerical crack extension analysis could not be carried out using a 3-D analysis, and the result was only an approximation from either plane strain or plane stress analysis. Figure 4.15 shows that the plane strain and plane stress J_R-curves for the a/W=0.5 3PB specimen (the results of the a/W=0.2 b>>B specimen were not applicable because the plane strain J_R-curve of this specimen geometry was invalid) were alike at the onset of crack extension. The dJ/da of the plane stress results for the first 4mm of crack extension in this specimen was dJ/da=5.2MN/m^2 which coincided with the value of 5MN/m^2 obtained experimentally by Sumpter[6] using a plane strain multi-specimen technique. The J_R-curve, using plane stress calibrations, from fracture testing on a b>>B CT specimen[8] produced an averaged dJ/da of 5.5MN/m^2 for the first 3.5mm crack extension. In addition, the (plane stress) J_R value at initiation for the CT specimen was in between the values of plane strain and plane stress results from numerical J_R-curve testing (see section 4.5 and Figure 4.16).

The numerical plane strain result from the 3PB specimen was dJ/da=3.18MN/m^2, 39% less than that of the plane stress result. The two results diverged with increasing crack extension (Figure 4.15), as the plane stress J_R-curve increased more rapidly with crack growth than the plane strain result. For the b>>B and B=25mm specimens tested, it is certain that flat fracture in the central region of the thickness tapered down to a point where the crack failed by fully slant fracture, i.e. the crack growth was predominantly plane stress after initiation. If the transition from plane strain to plane stress conditions occurred gradually during crack extension, the concave J_R-curve would have been flatter at the onset of the crack extension (Figure 4.20), as obtained in the plane strain J_R-curve where the flat fracture was dominant at the central region of the thickness.

For the a/W=0.5 (b=B) 3PB specimen, the numerical plane strain J_{IC} value of 0.012MN/m was obtained at an applied load of 15.5kN, where crack growth started. The load subsequently increased to a maximum of 18.1kN after 0.7mm of crack extension, giving a J_R value of 0.018MN/m (equivalent to a K value of 37.3MPa$\sqrt{m}$). This small (numerical) crack growth, just prior to maximum applied load, was necessary for the accurate reproduction of the experimental load-CMOD curve, which was the basis of the numerical analysis. However, the increase in numerical J values from 0.012MN/m to 0.018MN/m for a crack extension of only 0.7mm could be due to crack tip blunting in the test piece, which would relax through thickness constraint. On the other hand, the dJ/da of 3.18MN/m^2 from the numerical plane strain result was much lower than the value of 5MN/m^2 obtained by Sumpter[6] using a plane strain multi-specimen technique. The plane strain conditions enforced a constant (plane strain) plastic zone size throughout the thickness at the crack tip in the numerical model, but, experimentally, it was clear that some shear lips developed, so that the plasticity increased at the beginning of the crack propagation, resulting in an increase of dJ/da. Hence, on this basis, plane stress analysis gave a better estimate of the crack tip plastic work in the early stages of crack propagation ($\Delta a<4$mm) rather than the plane strain conditions, which existed around the crack tip prior to propagation.

4.9 *Conclusions*

Short cracks in standard (b=B) 3PB specimens failed at initiation, whilst cracks in b>>B specimens failed after slow crack growth (under increasing load). This discrepancy was observed from experimental testing and was examined initially by comparing the stress/strain conditions ahead of crack tips in 3PB stationary crack geometries using numerical results. It was noticed that the rate of increase in plasticity ahead of the crack tip varied between different sizes of the geometries, but other factors remained the same.

Crack extension was analysed numerically in order to produce J_R-curves for the bridge alloy, and the result provided a concave J_R-curve. In general, it seems that a plane stress J_R-curve gives the best estimate of fracture resistance for the structural components made of 25mm thick sections of bridge alloy. The numerical result of crack extension, namely J_{IC} and dJ/da, using plane stress analysis agrees closely with experimental results using plane strain calibrations. The 3-D numerical result of static cracks in 25mm thick plate shows that plane strain conditions exist at the crack tip within a short distance (<6mm). Therefore a plane strain J_{IC} (or K_{IC}) is valid as a

critical J (or K) at initiation, but the value is correlated with the T-stress due to the effects of in-plane constraint for low constraint geometries. Once crack propagation starts, crack tip plasticity effects, which gives rise to the increase in fracture resistance, are best modelled by plane stress analysis.

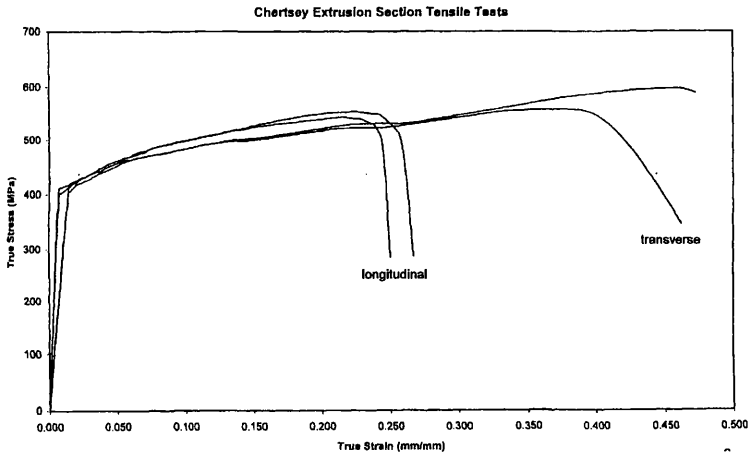

Figure 4.1 The true stress versus true strain curves for the bridge alloy.

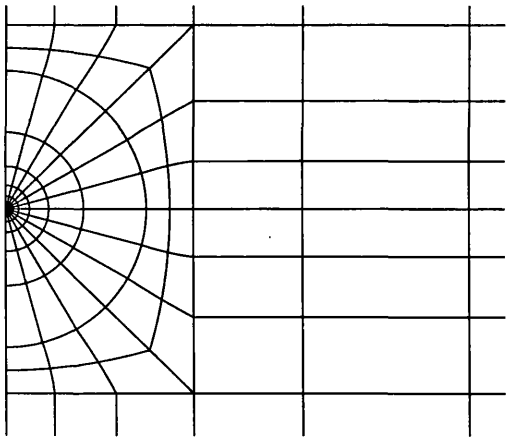

Figure 4.2. Finite element mesh.

a. Focused mesh at the crack tip

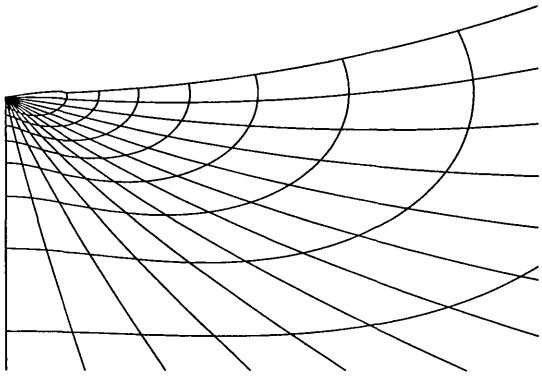

b. The crack tip nodes are tied to enhance the K singularity in LEFM.

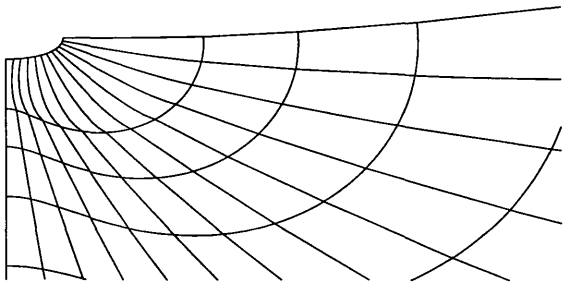

c. Crack tip opening displacement (for EPFM)

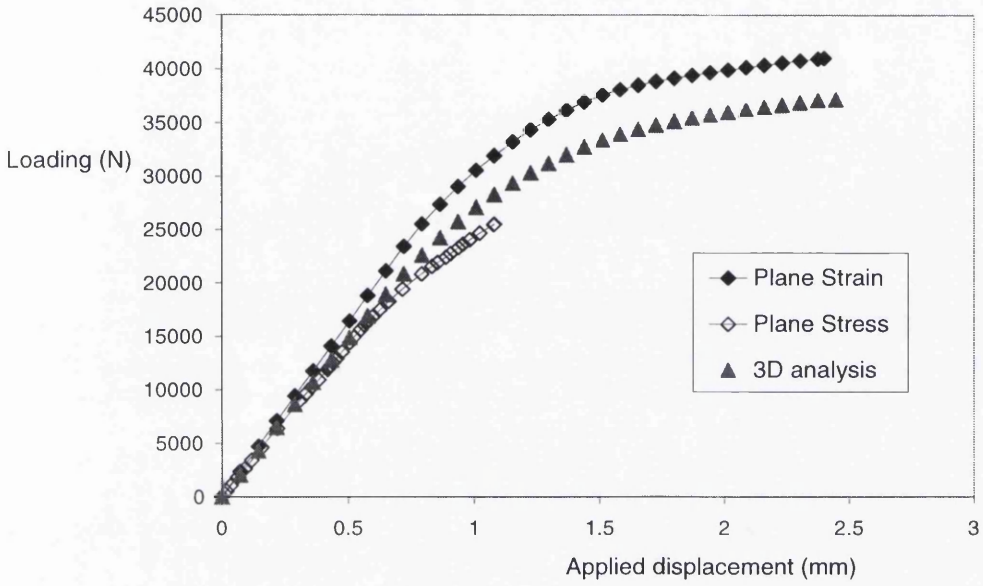

a. a/W=0.2 (b=B)

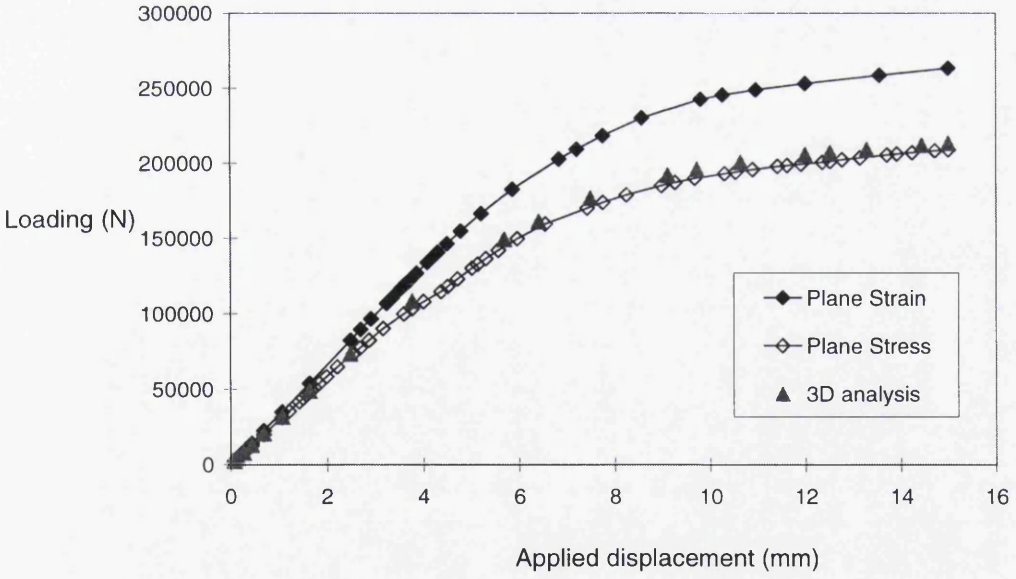

b. a/W=0.2(b>>B)

Figure 4.3 Numerical result of load versus displacement data of 3PB specimens.

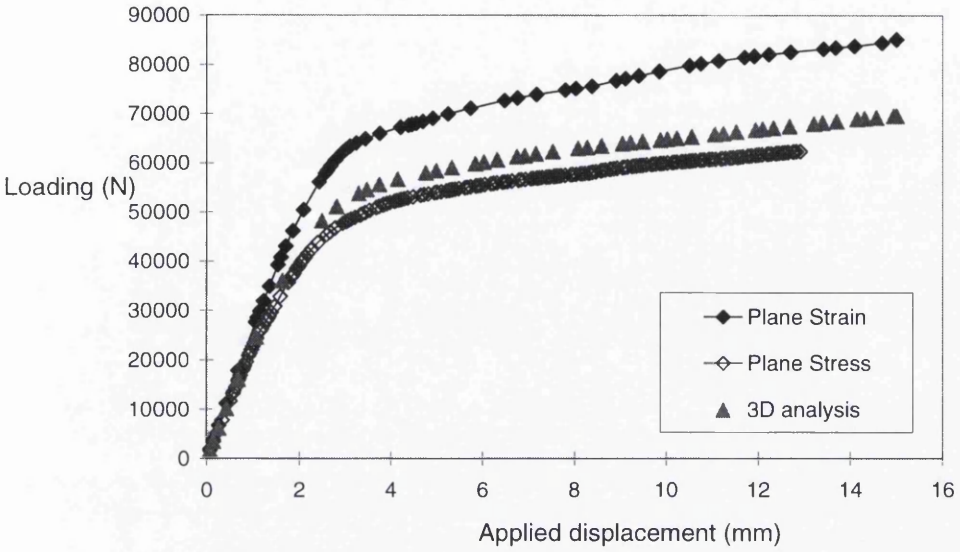

c. a/w=0.33

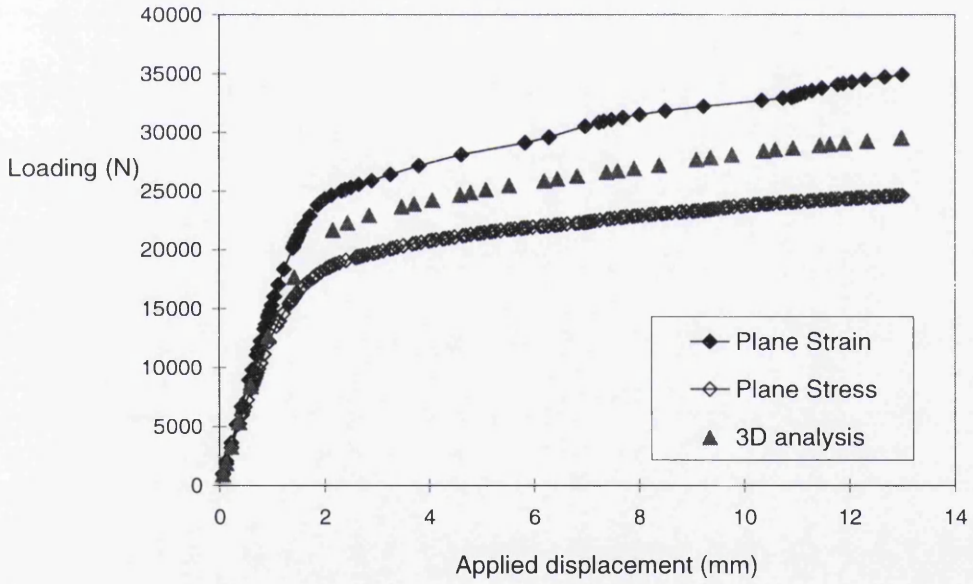

d. a/W=0.5

Figure 4.3(cont.) Numerical result of load versus displacement data of 3PB specimens.

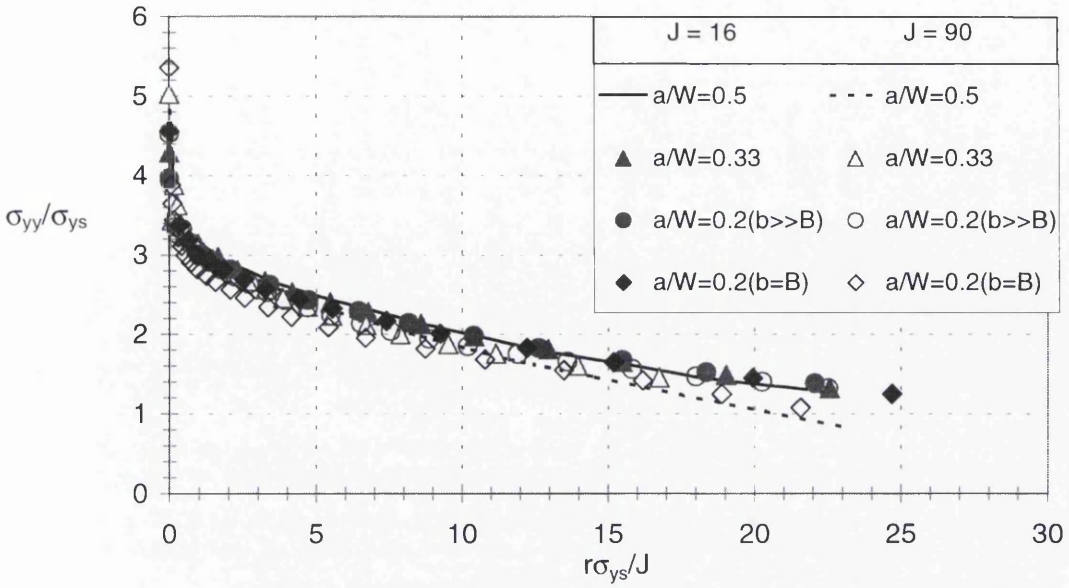

Figure 4.4a normalised opening stress vs. $r\sigma_{ys}/J$ plots (midplane), for J at 0.016 and 0.09MN/m

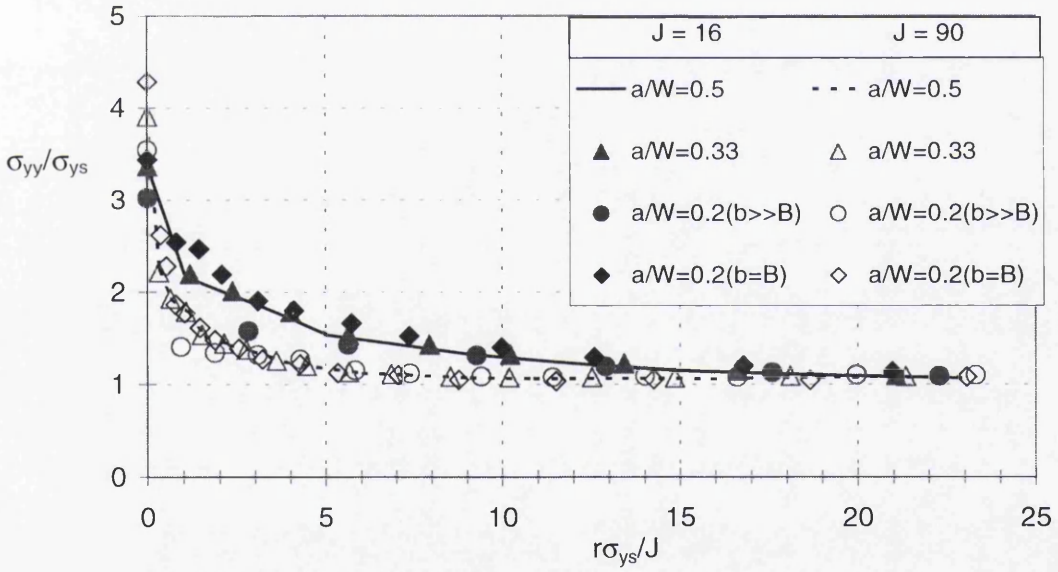

Figure 4.4b normalised opening stress vs. $r\sigma_{ys}/J$ plots (surface), for J at 0.016 and 0.09MN/m

Figure 4.4 Normalised opening stress of 3PB specimens

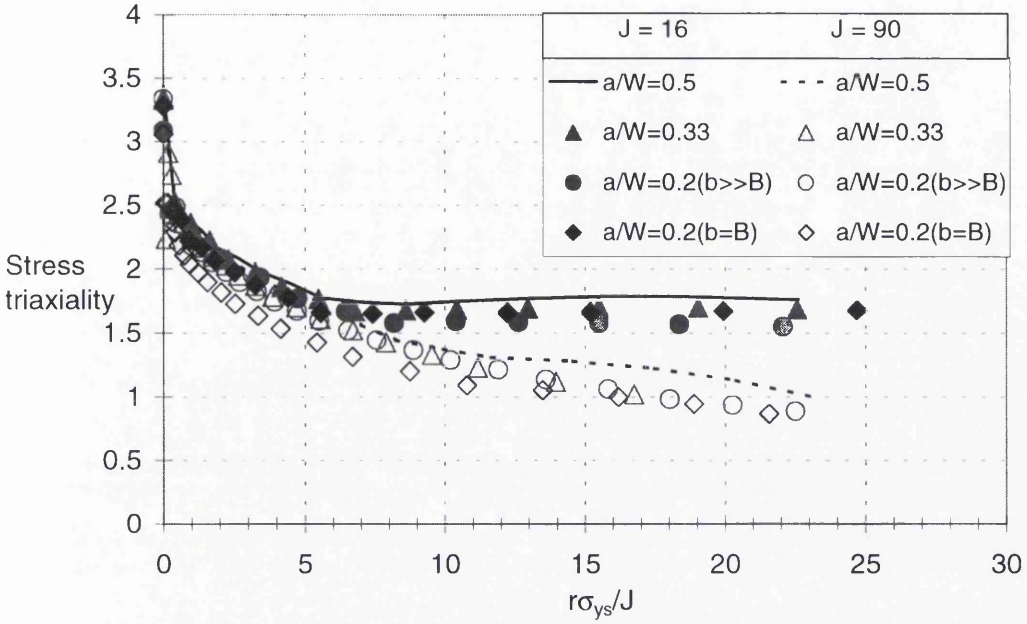

Figure 4.5a Stress triaxiality vs. $r\sigma_{ys}/J$ plots (midplane), for J at 0.016 and 0.09MN/m

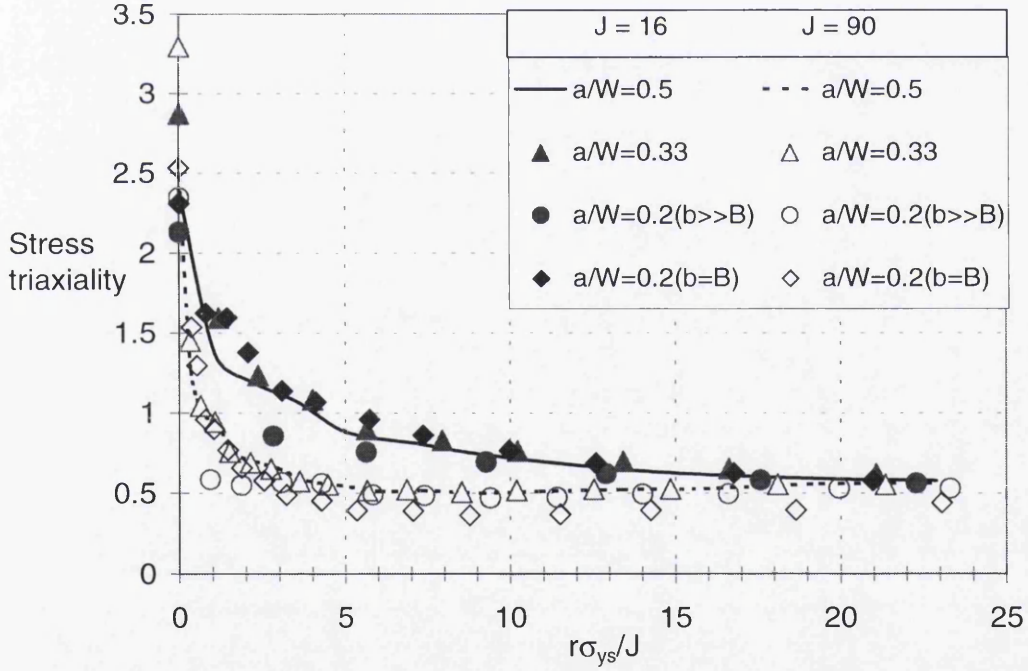

Figure 4.5a normalised opening stress vs. $r\sigma_{ys}/J$ plots (surface), for J at 0.016 and 0.09MN/m

Figure 4.5 Stress triaxiality of 3PB specimens

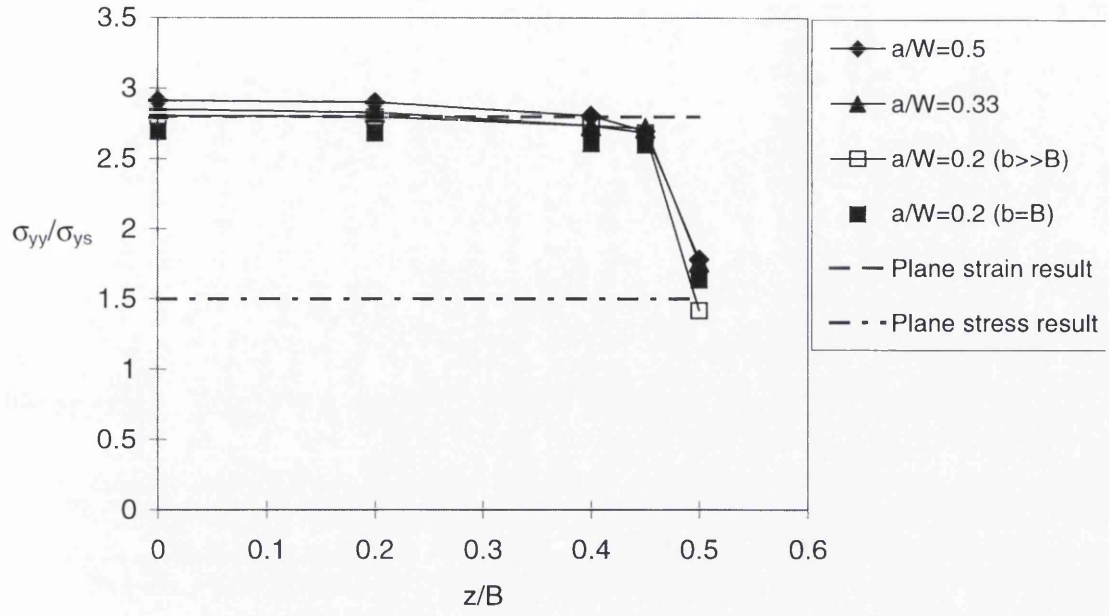

Figure 4.6a Comparison of normalised opening stress across thickness between different sizes of 3PB specimen at distance $r\sigma_{ys}/J=2$

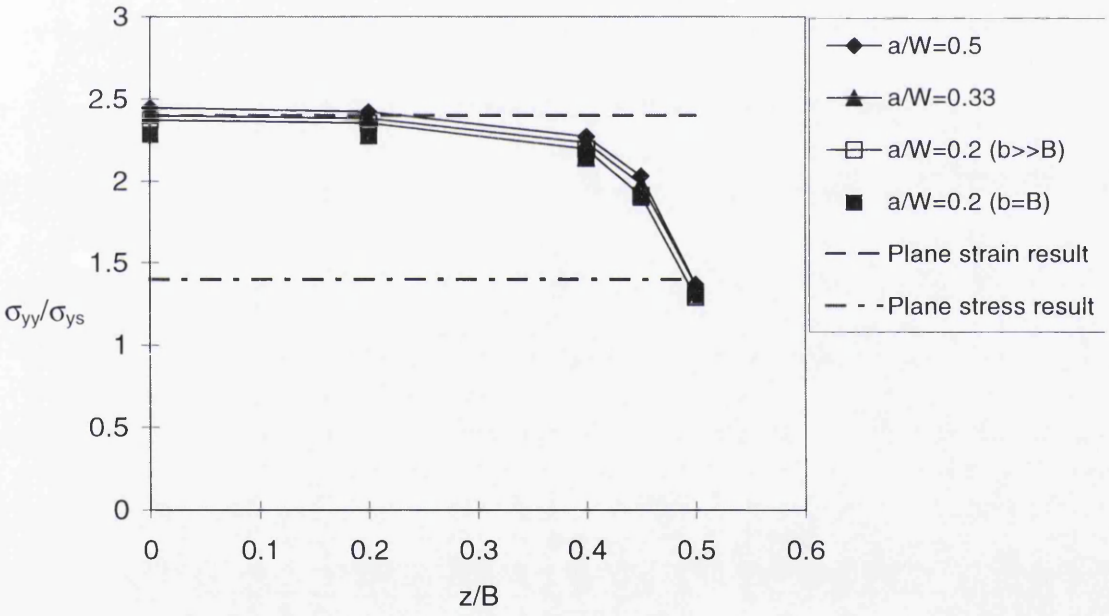

Figure 4.6b Comparison of normalised opening stress across thickness between different sizes of 3PB specimen at distance $r\sigma_{ys}/J=5$

Figure 4.6 Normalised opening stress across thickness of 3PB specimens at J=38 KN/m.

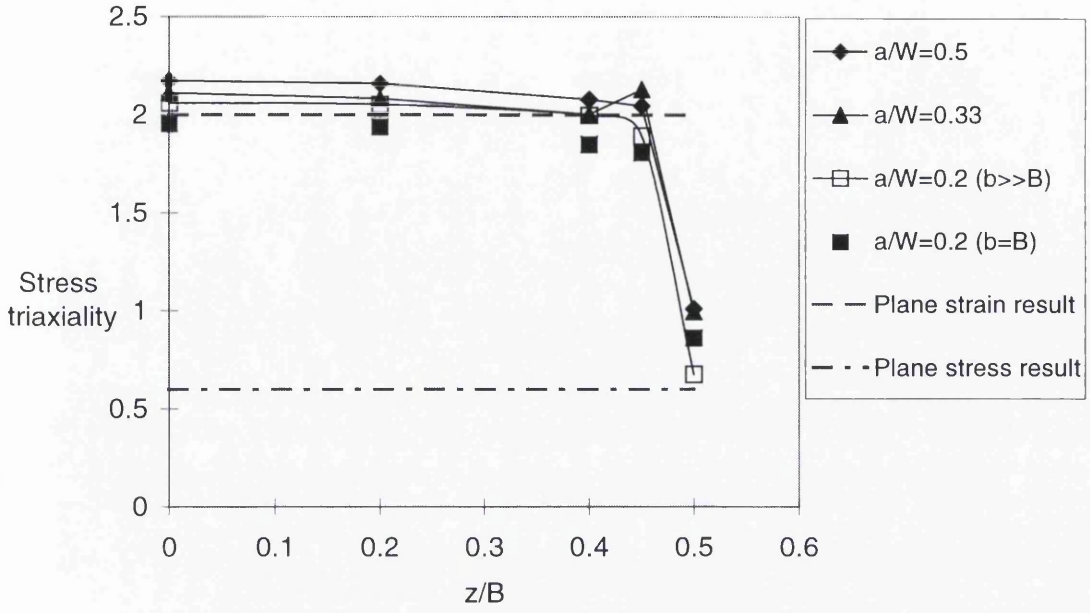

Figure 4.7a Comparison of stress triaxiality across thickness between different sizes of 3PB specimen at distance $r\sigma_{ys}/J=2$

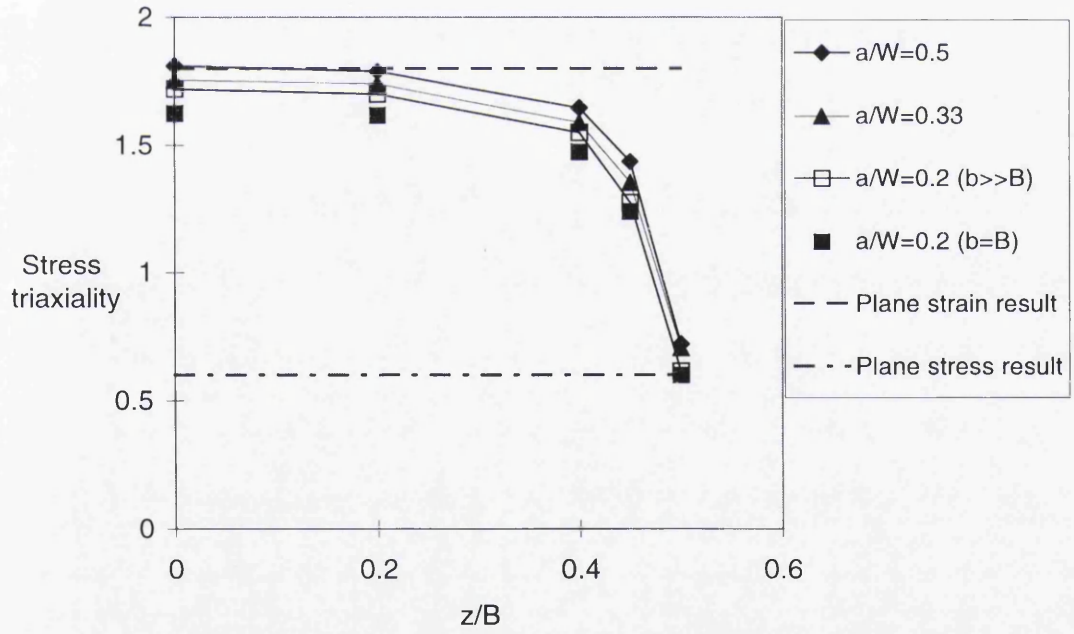

Figure 4.7b Comparison of stress triaxiality across thickness between different sizes of 3PB specimen at distance $r\sigma_{ys}/J=5$

Figure 4.7 Stress triaxiality across thickness of 3PB specimens at J=38 KN/m.

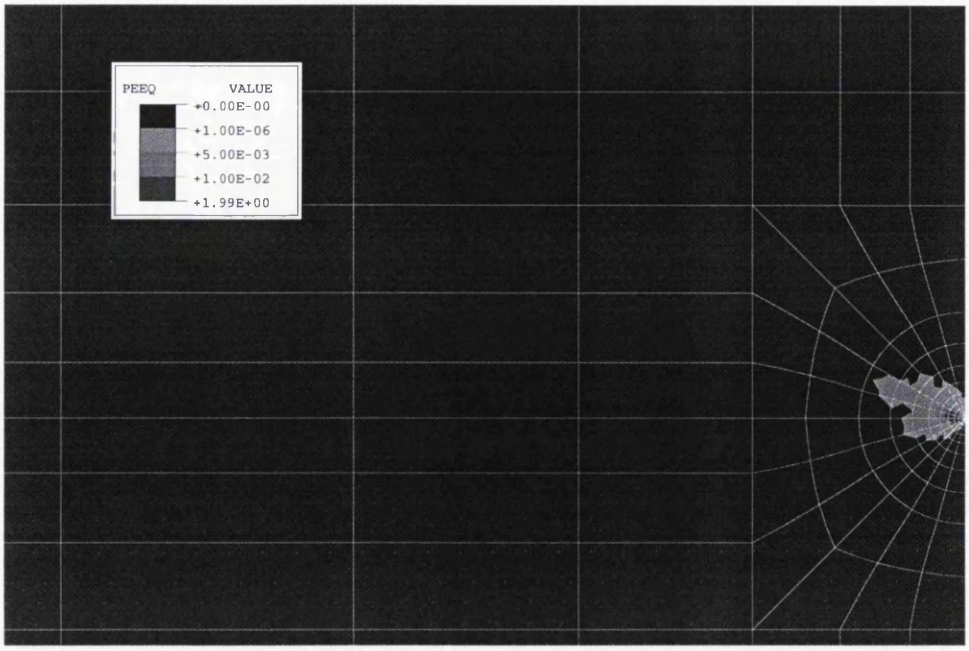

J=18.2 KN/m

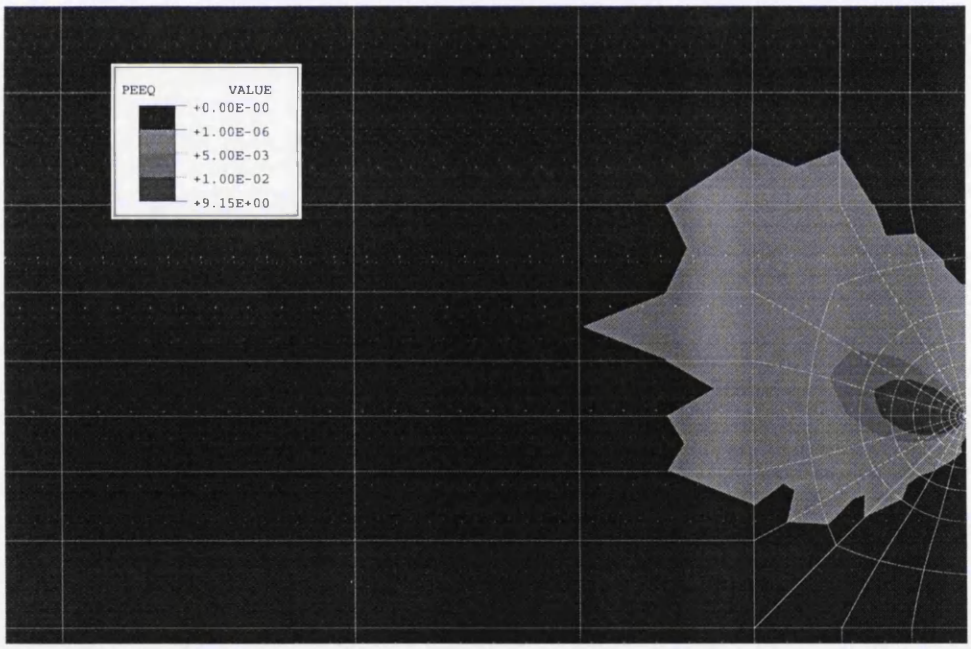

J=83.9 KN/m

scale: 5mm

Figure 4.8a Crack tip equivalent plastic strain (on the midplane) plots of 3PB specimen of a/W=0.5 at given J level.

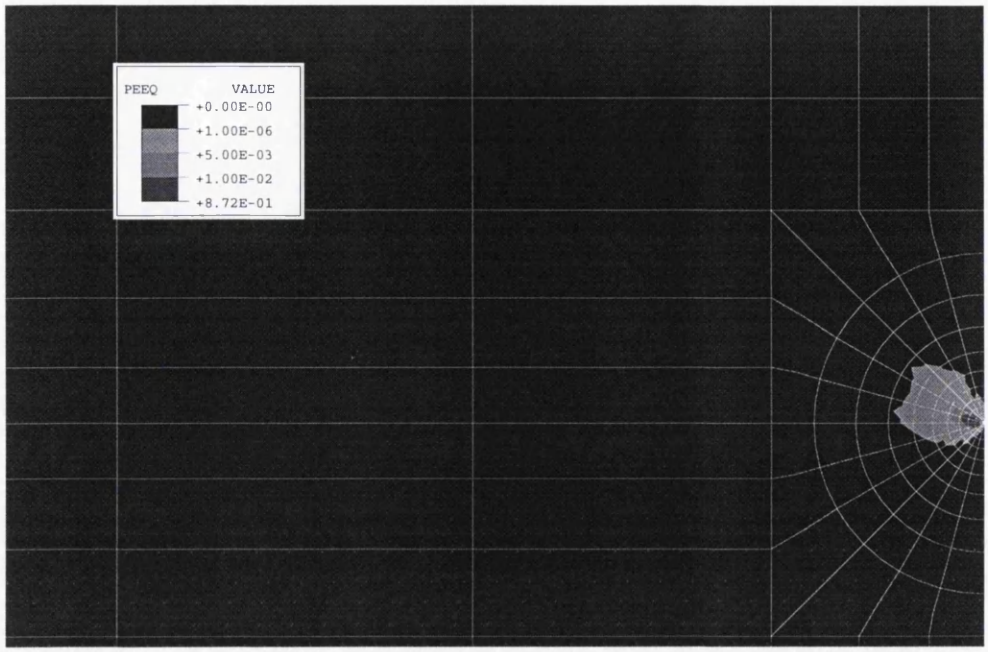

J=18.5 KN/m

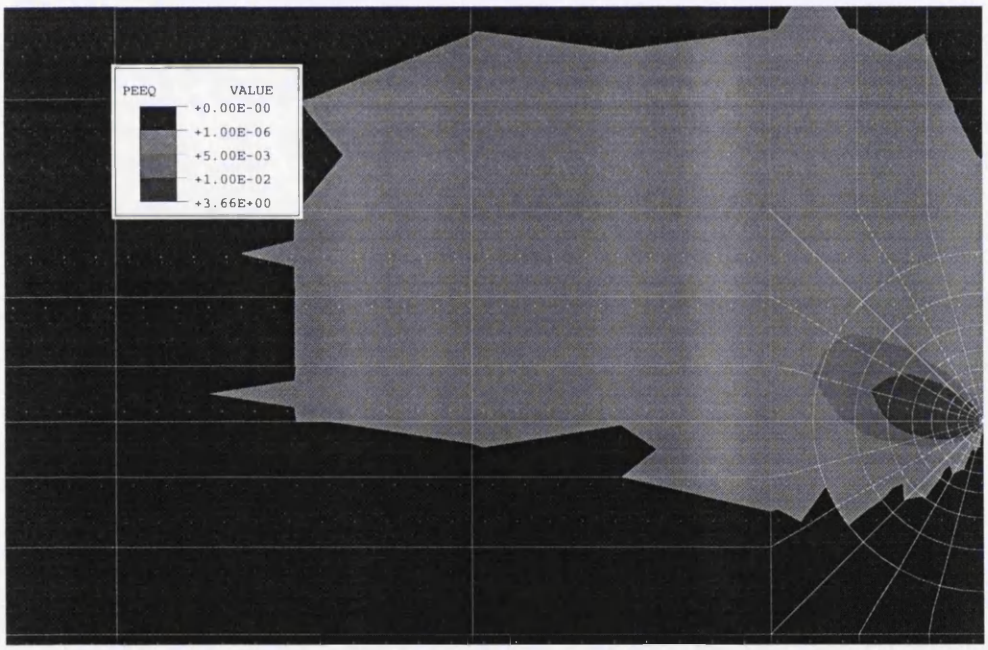

J=86.8 KN/m

scale: 5 mm

Figure 4.8b. Crack tip equivalent plastic strain (on the midplane) plots of 3PB specimen of a/W=0.2(b>>B) at given J level.

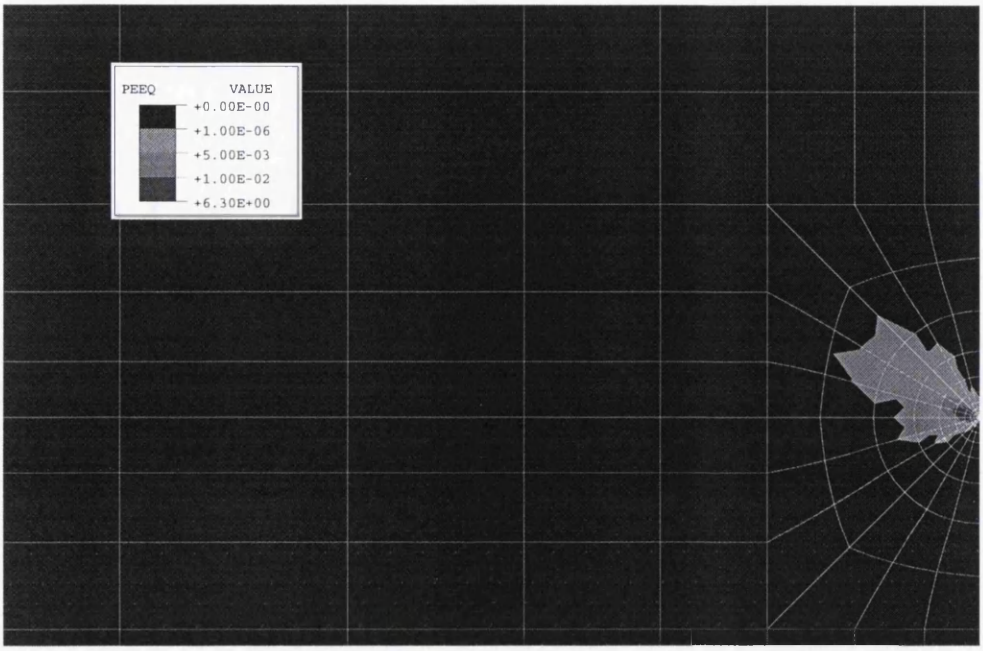

J=20 KN/m

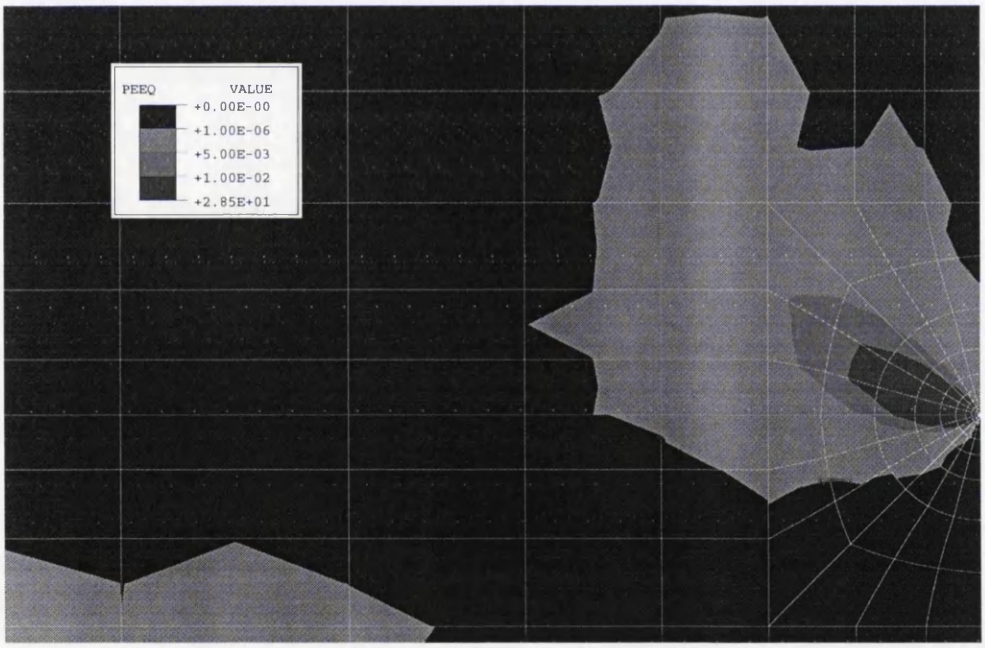

J=83.5 KN/m

scale: 5 mm

Figure 4.8c. Crack tip equivalent plastic strain (on the midplane) plots of 3PB specimen of a/W=0.2(b=B) at given J level.

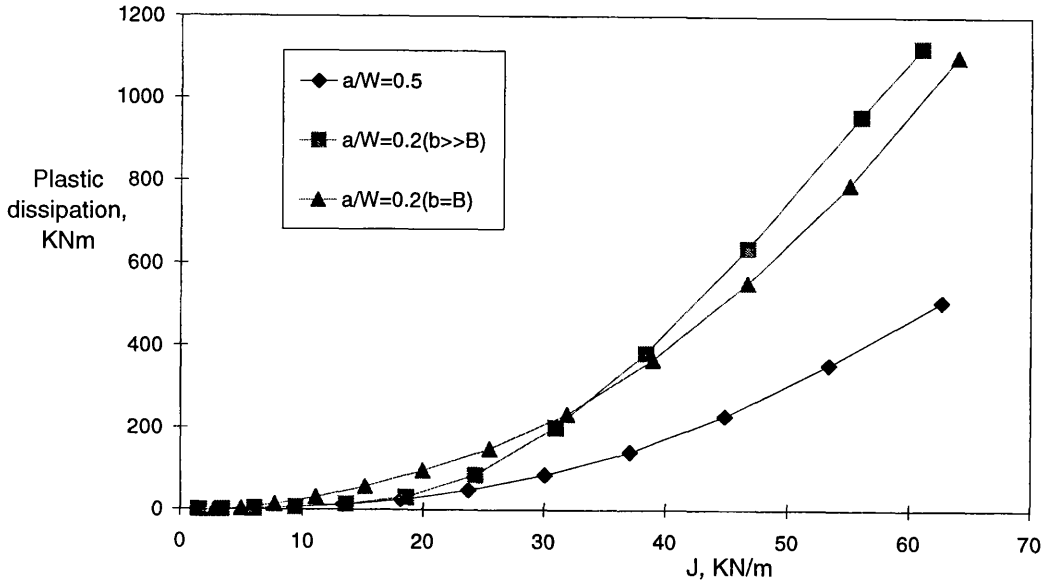

Figure 4.9 Comparison of the change of plastic dissipation with increasing J between 3PB specimens.

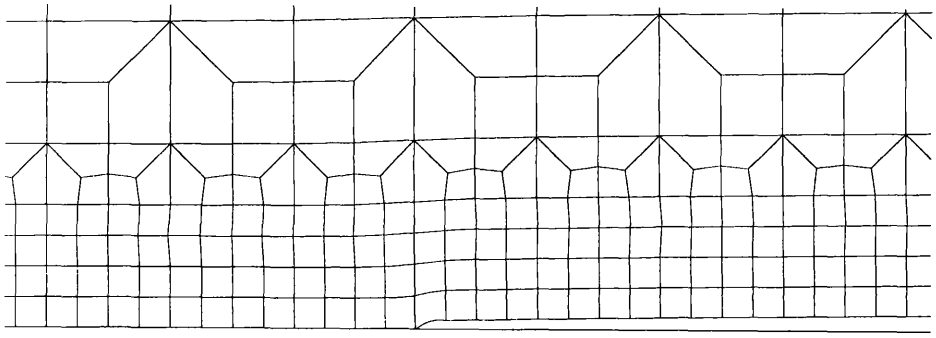

a. Crack blunting

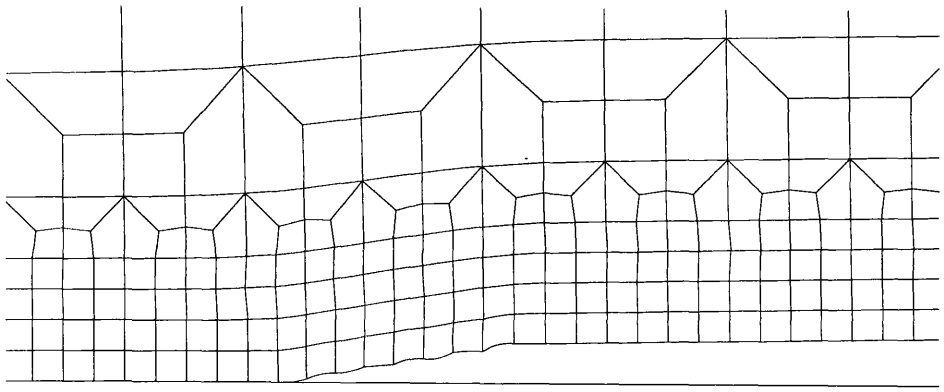

b. Crack propagation.

Figure 4.10 Mesh configuration (at crack tip) for crack extension analysis.

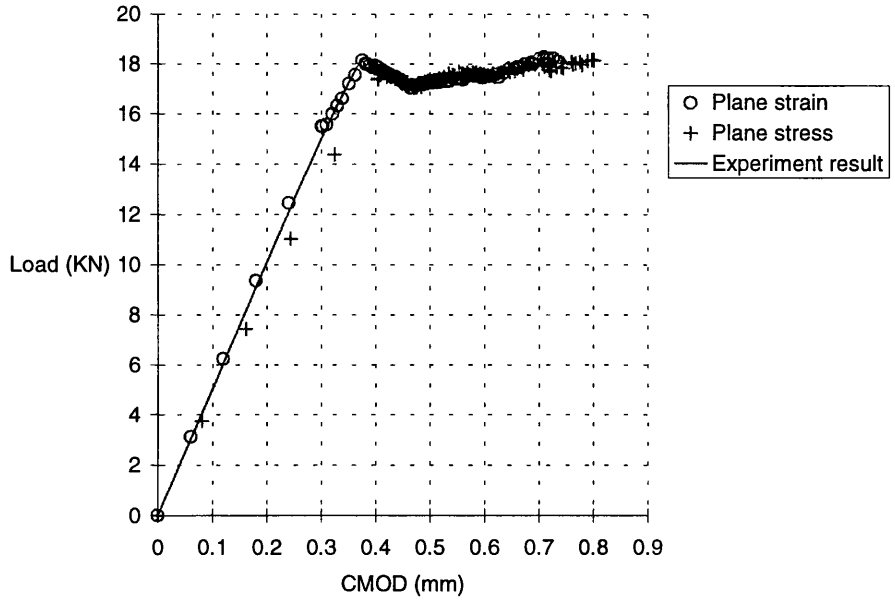

Figure 4.11 The comparison of load vs. CMOD plot between numerical and experimental results of a/W=0.5 3PB specimen.

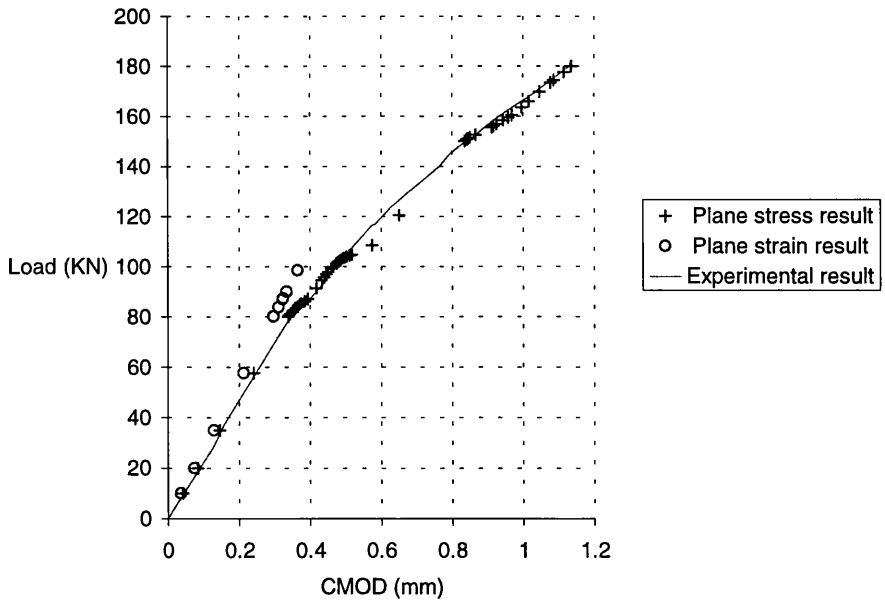

Figure 4.12 The comparison of load vs. CMOD plot between numerical and experimental results of a/W=0.2 (b>>B) 3PB specimen .

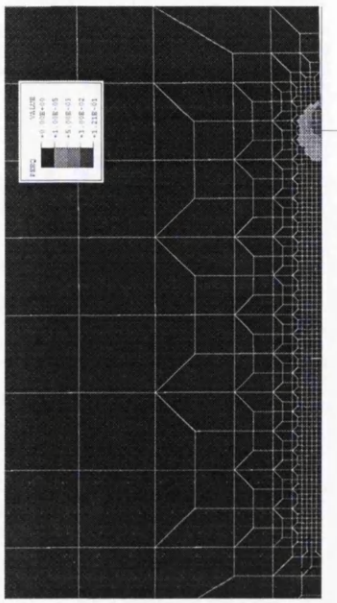

a. Crack initiation at J=0.016MN/m.

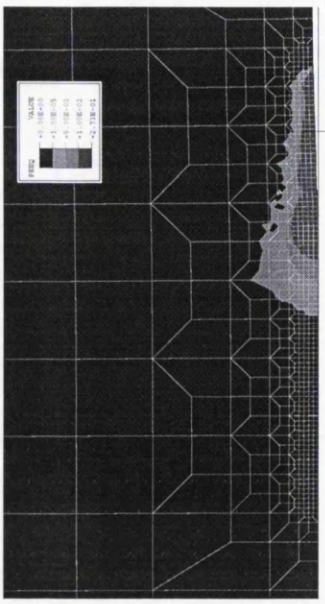

b. $\Delta a \approx 4.5$mm at J=0.043MN/m, $r_y/b_c=0.029$.

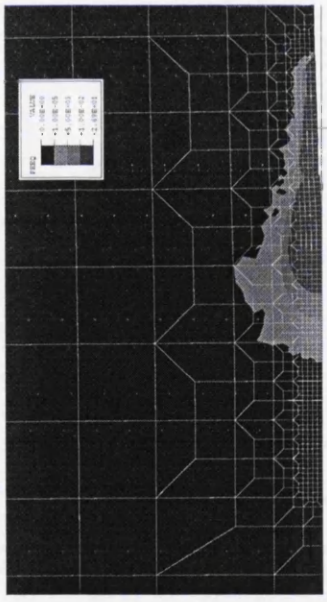

c. $\Delta a \approx 6$mm at J=0.055MN/m, $r_y/b_c=0.046$.

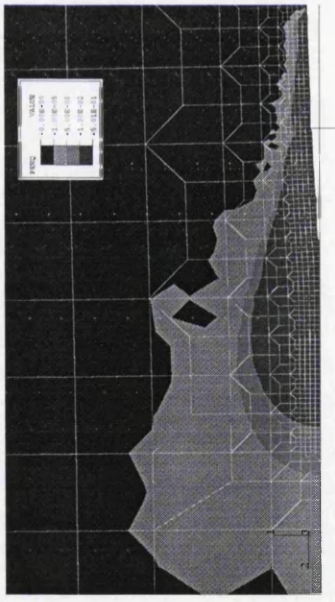

d. $\Delta a \approx 9$mm at J=0.118MN/m ($\sim 7J_{initiation}$), $r_y/b_c=0.106$.

Figure 4.13 The plane stress plastic zone size at the advancing crack tip in the a/W=0.2 (b>>B) 3PB specimen.The size of the element at the crack tip is $2\times2mm^2$. The r_y is the plastic zone size measured along the fracture direction and b_c is the size of remaining ligament.

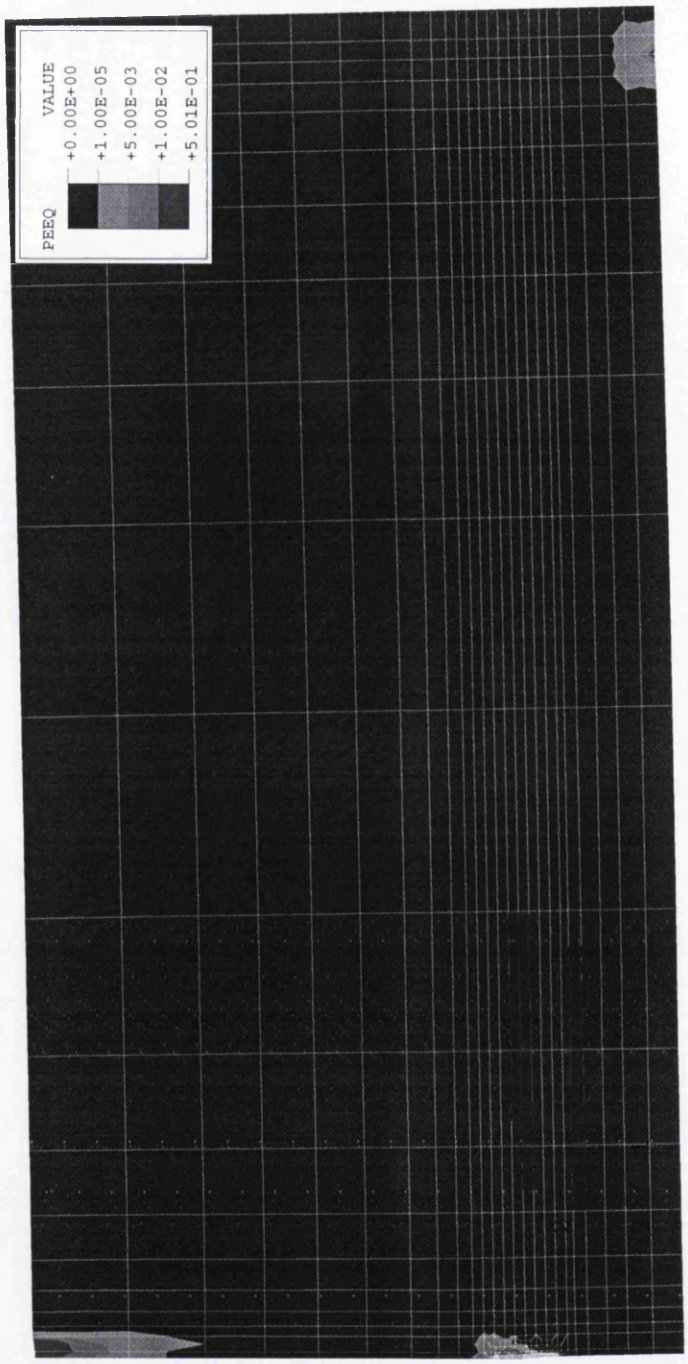

e. A small plastic zone size restricted at the crack tip, see Figure 4.12d for details. Half of the specimen is modelled due to the symmetry of specimen's geometry. The model shown above has been rotated counter-clockwise by 90 degree. The crack tip is located at the bottom right edge of the above diagram.

Figure 4.13(cont.) The plane stress plastic zone size at the advancing crack tip in the a/W=0.2 (b>>B) 3PB specimen.

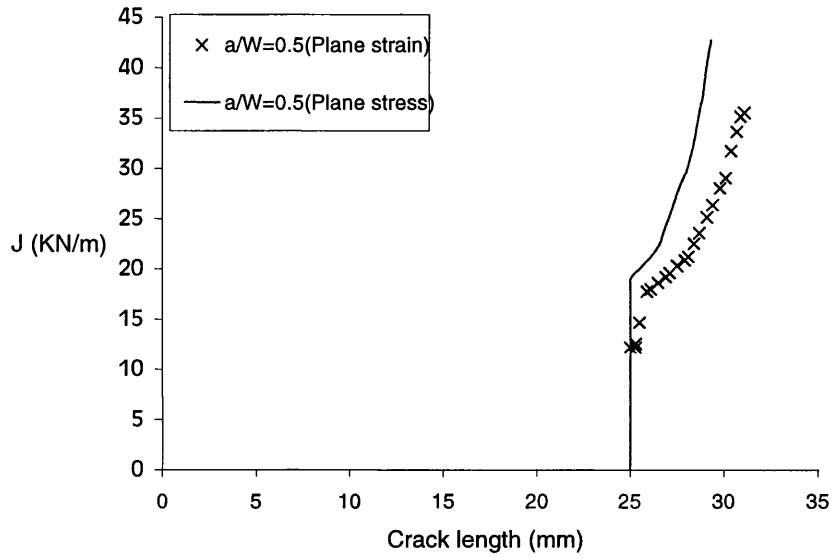

Figure 4.14 Comparison of J_R curve of 3PB a/W=0.5 specimen between plane stress and plane strain analysis.

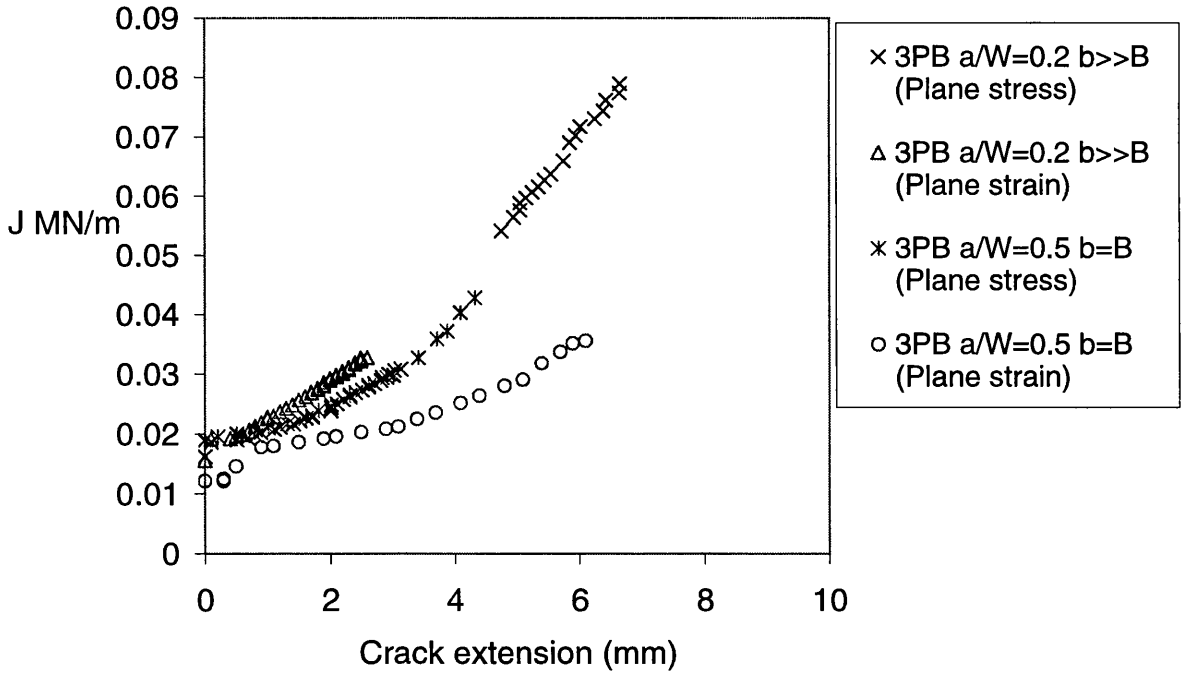

Figure 4.15 The numerical plane stress and plane strain J_R-curves for 3PB specimens.

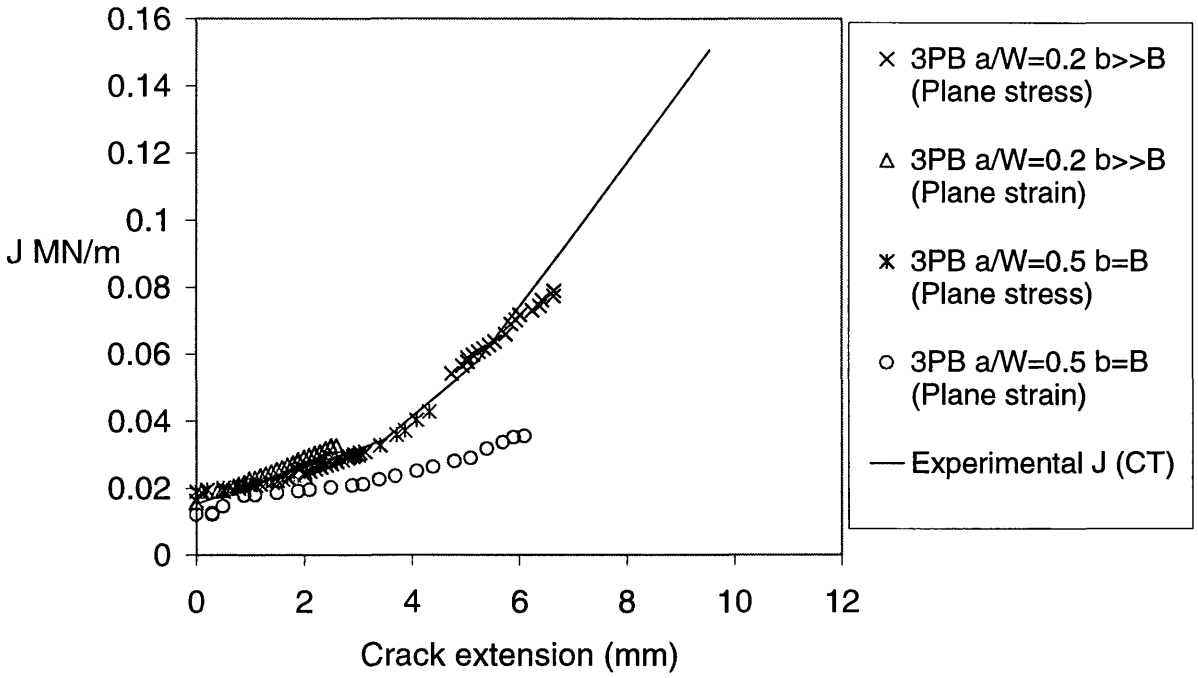

Figure 4.16 The J_R-curves from numerical and experimental results, using 3PB and CT specimens respectively.

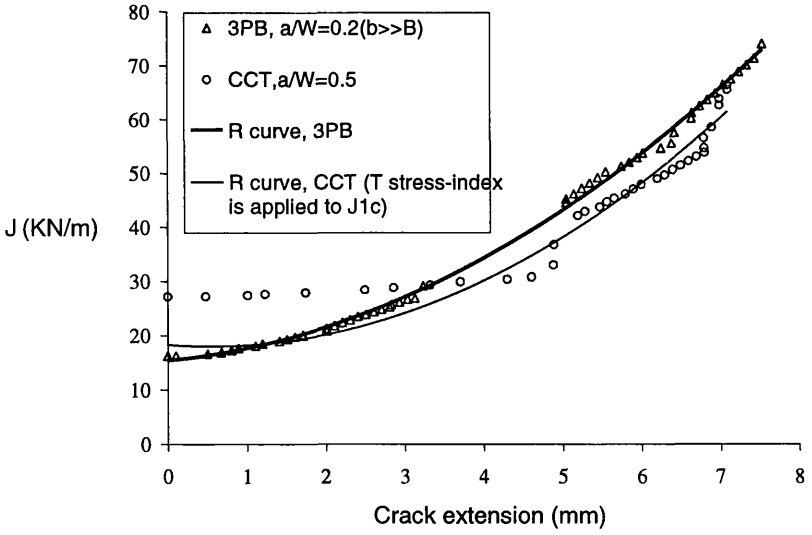

Figure 4.17 Comparison of (plane stress) J_R curve between 3PB and CCT specimens.

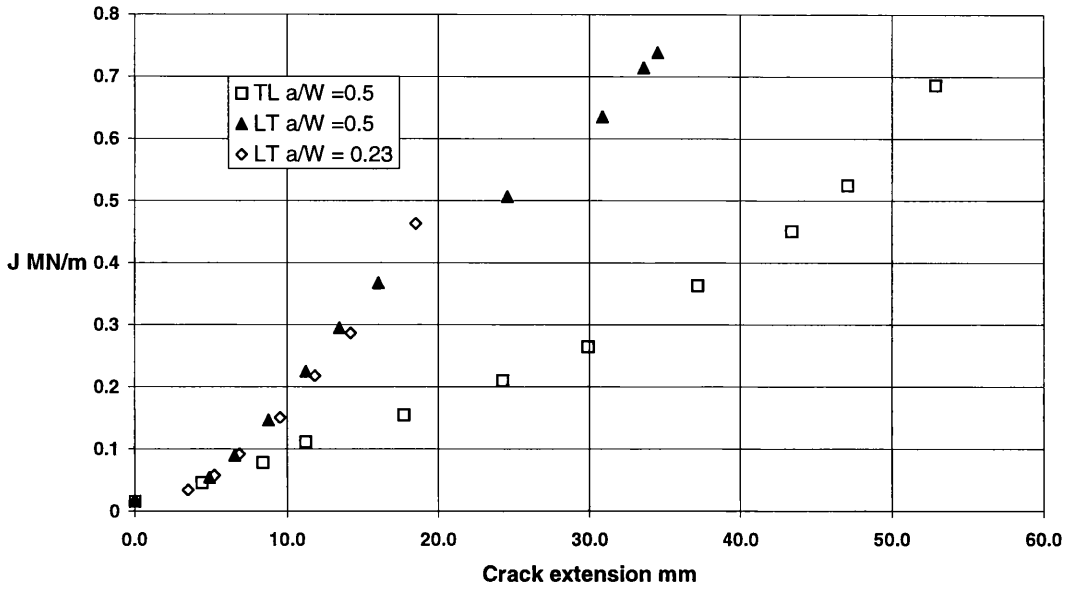

Figure 4.18 Experimental J_R-curves of bridge alloy using CT specimens. Note the difference in fracture resistance between LT and TL directions.

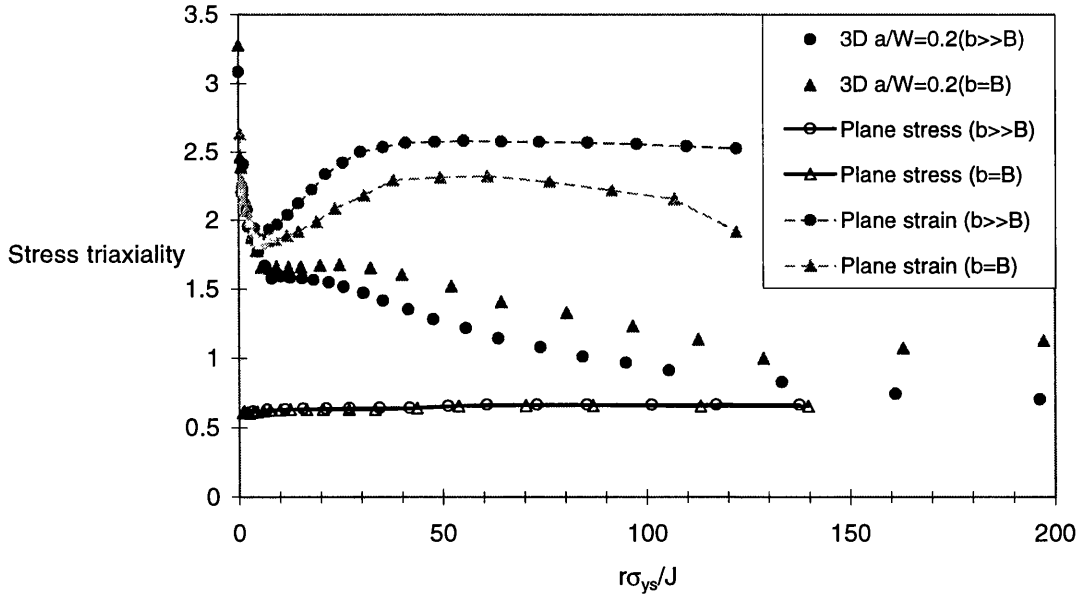

Figure 4.19 Numerical results of static cracks in 3PB specimens at J=0.016MN/m. (In this case, $r\sigma_{ys}/J=150$ is equivalent to a distance of r=6.1mm from the crack tip).

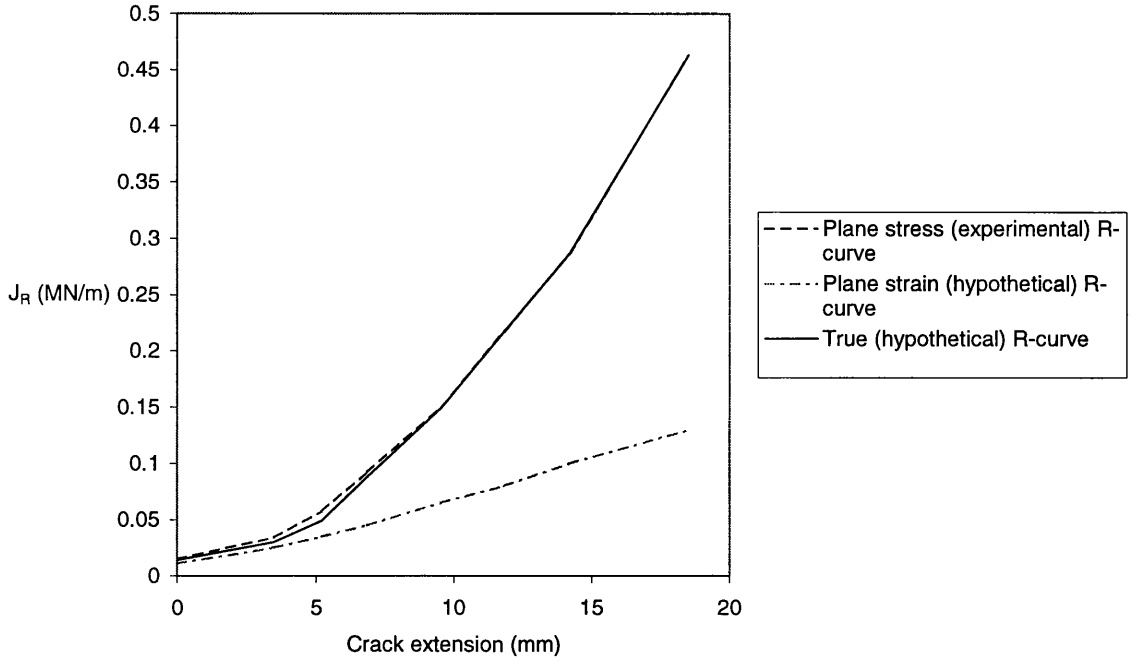

Figure 4.20 A hypothetical 'true' J_R-curve between the plane stress and plane strain J_R-curves.

CHAPTER 5. APPLICATION OF THE R-CURVE

5.1 *Introduction*

Crack propagation in a material that has constant fracture resistance is unstable because the driving force increases with crack growth, but the material resistance remains constant, see Figure 2.8a. In this case the fracture resistance of the material is characterised by a value of K, but, the value of K may be modified by any loss of in-plane constraint inherent in the geometry. If a thick, high constraint, specimen contains a plastic zone at the crack tip which is comparatively small compared to the in-plane dimensions so that plane strain conditions exist in the interior of the plate, the fracture resistance is defined as K_{1C}, the plane strain fracture toughness. This value implies maximum in-plane constraint.

For a material with a rising R-curve, crack growth with increasing driving force is stable until the driving force curve is a tangent to the R-curve, see Figure 2.8b. For a material with a rising R-curve, the fracture resistance cannot be characterised with a single toughness value. However, the point of tangency depends on the shape of the driving force curve (Figure 2.8), which depends on the configuration of the structure. A crack in a thin plate, which is loaded in predominately plane stress conditions, produces a steeper R-curve than that a crack in a thick plate. If instability occurs during an R-curve test, the R-curve cannot be defined beyond the point of ultimate failure.

Materials with rising R-curves can be characterised by a value of K at initiation, corresponding to K_{1C} for high constraint geometry. It can be correlated by the T-stress for low constraint geometry.

Instability prediction using the R-curve approach is determined by comparing the driving force curve and R-curve (see section 4.4). The driving force curve rises with crack extension and should reach a point which is tangential with the conventional R-curve (Figure 2.8b), whose dJ_R/da decreases all the time, i.e. it is convex in shape. The point of tangency, where instability occurs, depends on the shape of the driving force curve, because the R-curve is a material property (although an R-curve in plane stress is steeper than that in plane strain). The R-curve for the bridge alloy rises increasingly with crack extension, i.e. it is concave in shape, and

cannot reach a critical J according to the test results (Figure 4.17). In this case, instability, given by a point of tangency, could not be predicted with the current R-curve for the bridge alloy. The concave R-curve for the bridge alloy showed that crack growth arrested where the R-curve intersected and rose above the driving force curve, see section 5.1.2.

Material tests[6][8] on bridge alloy showed that shallow crack geometries failed at K_{1C}, while in specimens with b>>B ligaments, failure was preceded by stable crack growth. Instability prediction for different crack geometries, i.e. different test pieces, is assessed in this section to demonstrate the method, i.e. the R-curve approach. Assuming the (experimental) plane stress J_R curve and its J_R at initiation are independent of the crack tip condition and specimen geometry (i.e. ignoring the T-stress effects), the invariant J_R curve is reproduced for all crack geometries. The thickness of specimens and the structural components is 25mm, which is also the thickness of specimens for J_R-curve testing (in chapter 4). Instability of a crack geometry is determined graphically by comparing the calculated driving force curve of the geometries and the J_R-curve. If the driving force curve lies above the R-curve, then instability will occur at K_{IC}, and vice-versa. If the two curves cross, then crack stability can be followed by instability, and vice-versa.

The assessments of instability in different crack geometries are produced for 3PB and CT specimens. The (elastic) driving force, G, is calculated using the solution in BS 7448:Part 1. Each curve represents the driving force at constant load (corresponding either to the load necessary to achieve K_{IC}, i.e. at initiation, or the maximum applied load in the experimental test[6][8]) with increasing crack length. The effects of the T-stress on K_{IC} are assessed.

The J_R-curve and G curve, both indexed by the T-stress, are then applied to high constraint 3PB geometries. The results are illustrated in 3-D and will be discussed in section 5.2. In the case of plastic deformation at the crack tip, the driving force G is computed using the effective crack length related to the crack tip plastic zone size. A few examples are shown in section 5.3.

5.1.1 *Instability Prediction for b≤B Ligament Specimens*

Figure 5.1 illustrates the application of the J_R curve approach for shallow crack geometry (see Table 5.1). The driving force curve is evaluated for constant load with increasing crack length,

i.e. increasing a/W ratios. An invariant (high constraint) R-curve is produced for each initial crack length. In Figure 5.1a G versus crack length is calculated for the maximum applied load (53kN). The G at initiation is much larger than the J_R (Figure 5.1a). This high G value is associated with a negative T-stress which raises J_{IC}. In this case, T/σ_{ys}= –0.35[15], corresponding to J_C=0.03MN/m using the constraint index[6], while the computed G is 0.028MN/m. The application of the T-stress constraint index for the R-curve approach will be discussed in section 5.2. The dG/da is larger than dJ_R/da for crack lengths up to 10mm, where the G curve rises up rapidly above the R-curve. This implies that the crack growth is unstable at the constraint corrected K_{IC} value, which agrees with the experimental result.

The driving force curve in Figure 5.1b is calculated using the load (19.3kN) that gives the value of G at initiation, G_{IC}, for the crack length of a/W=0.5(a=25mm). The driving force curve intersects the concave R-curve but does not rise above it for the first 3mm of crack growth. As a result, the crack propagates under the applied load but the crack growth is stable under a constant load: it possibly arrests if the load is removed. Stable crack growth can only continue with increasing specimen's displacement, but constant or decreasing load, Figure 4.11. Instability occurs at a crack length of 40mm where the G curve rises above the R-curve (Figure 5.1b), which represents the resistance associated with the initial crack length. The result coincides with the experimental result that stable crack growth is observed in this geometry, but no experimental crack extension data were available. In the experiment the crack extended and failed at an applied load of 18kN, equivalent to 0.85% of the plane stress limit load (see section 4.3), and close to the calculated G_{IC} load of 19.3kN.

Table 5.1 Details of the 3PB and CT specimen.

3PB specimens a/W	Ligament length, b (mm)	Crack length, a (mm)	Span, S (mm)	Thickness, B (mm)
0.1	25	2.5	110	25
0.5	25	25	200	25
0.2(b>>B)	160	40	800	25
CT specimen a/W				
0.23(b>>B)	115	35		24.5

The prediction of instability at initiation in the a/W=0.1 3PB specimen coincides with the experimental result. For shallow crack geometries the opening stress is affected by compressive

(negative) T-stress (see section 2.1.7). The T-stress indexes the opening stress for both the J_R-curve and G curve, hence the instability prediction including constraint effects will be discussed in section 5.2.

5.1.2 Estimation of Crack Extension in b>>B Ligament Specimens

The test result of large 3PB and compact tension (CT) with b>>B ligament specimens (see Table 5.1 for details) by Sumpter[6][8] showed that the unstable fracture was preceded by stable crack growth. Two driving force curves are produced for each case in order to estimate the amount of crack extension.

For the a/W=0.2 (b>>B) 3PB specimen (see Figure 5.2a), the two driving force curves represent the applied force at 85kN (corresponding to the J_R at initiation) and at 250kN (the maximum applied force in the experimental test[6]). The lower G curve in Figure 5.2a shows $G=J_R$ at the initiation point of the R-curve, where the crack propagates. However, $dG/da<dJ_R/da$ so that the crack growth is stable. The G curve for the maximum force intersects the R-curve (for the initial crack length) at a crack length of 52mm. In this case, the crack extension is 12mm, from 40mm to 52mm (see Figure 5.2a), assuming a single R-curve represents the initial crack length and the applied force rises from 85kN to 250kN. The experimental test was stopped at the final load of 247kN. The experimental crack extension was not available for comparison between that and the analytical result.

An experimental J_R-curve was produced for the bridge alloy using a CT specimen (see Table 5.1 for specimen details) and a compliance unloading technique. This J_R-curve coincided with the numerical result (both used plane stress calibrations, see Figure 4.15), and is used throughout this chapter. Figure 5.2b shows two driving force curves produced for applied forces of 69kN (equivalent to J_R at initiation) and 88kN (as the maximum load of the first load/unloading cycle). The lower G curve shows $G=J_R$ where the crack initiates. However, $dG/da<dJ_R/da$ so that the crack growth is stable. The higher G curve represents the applied force increased from 69kN to 88kN, with which $G=J_R$ at a crack length of 37.5mm (see Figure 5.2b). The further increases of crack length under the given load do not cause unstable crack growth, because $dG/da<dJ_R/da$.

The experimental crack extension in the first load/unloading cycle was 3.5mm, while the estimate was 2.5mm (from 35mm to 37.5mm), see above.

Using the R-curve approach, instability of a shallow crack in a specimen with b=B ligament occurs at G equivalent to J_R at initiation, i.e. at K_{1C}, while stable crack extension in 3PB and CT (b>>B) specimens is predicted. The result shows that the high dJ_R/da of the bridge alloy results in stable crack growth in specimens with b>>B ligament.

5.1.3 *Estimation of Crack Extension in Bridge Components*

Figure 5.3 shows the G curves for a stem crack and a flange crack in the bridge girder. The G values are calculated using the solutions by Cheung[7][39]. The G curve for a stem crack, assuming the crack grows towards the flange but with its lower crack tip more than 25mm away from the flange, is calculated for an applied stress equivalent to $0.43\sigma_{ys}$ (Figure 5.3a). The G curve for the stem crack intersects the R-curves, for an initial crack length of 40mm, at a crack length of 44.5mm. This implies that the crack grows from 40mm to 44.5mm, under the given load, and it arrests where G=R and $dG/da<dJ_R/da$ (Figure 5.3a). The repetition of the R-curve at the initial crack length of 44.5mm, assuming the crack propagates under the same conditions, shows that the G curve intersects the R-curve, i.e. G=R and $dG/da<dJ_R/da$, at a crack length of 49mm. The R-curve for the vicinity of the flange is not known, but is perhaps less steep than the plane stress R-curve because of the change in cross sections, giving an increase in the out-of-plane constraint.

Two G curves are produced for flange cracks from 0 to 78mm subjected to applied loads equivalent to $0.43\sigma_{ys}$ (solid line) and $0.6\sigma_{ys}$ (broken line) in Figure 5.3b. A 5mm flange crack propagates at the J_R value at initiation under an applied load equivalent to $0.6\sigma_{ys}$ (broken line), assuming a constant J_R value at initiation (Figure 5.3b). The crack arrests after initiation because $dG/da<dJ_R/da$, but the crack growth can resume under increasing load. An R-curve is reproduced for a crack length of 60mm. This R-curve intersects the G curve, for a load equivalent to $0.43\sigma_{ys}$ (solid line), at a crack length of 74mm (Figure 5.3b), where G=R and $dG/da<dJ_R/da$. This implies that the crack growth is stable under the applied load at a crack length of 74mm. However, the crack is approaching the joint of the stem to the flange which is

75mm from the edge of the flange. Therefore the R-curve is not so accurate because of the change in the out-of-plane constraint.

5.2 *Interaction of T-Stresses and R-Curve*

Sumpter[6] and Henry[3] showed that cracks in low constraint geometries (namely the CCT and shallow cracks in 3PB specimens) contain negative T-stresses. Henry[3] studied the conditions at crack tips in 3PB and CCT specimens, and the bridge girder, using the finite element method. He showed that negative T-stresses exist at the crack tip. Henry generated solutions using the numerical result for calculating the T-stress for the tested geometries. Sumpter[6], using experimental results, introduced a constraint index in terms of the T-stress (Figure 2.7), which rationalised the geometry effects on J_C for the bridge alloy. According to the index, the increase of J_C is four fold, corresponding to the increase of normalised T-stress (T-stress/σ_{ys}) from 0 to –0.8. The constraint effect is shown in the numerical J_R curve for a CCT specimen (Figure 4.16). The J_R at initiation for the CCT specimen is higher than that for a 3PB specimen, however the constraint effect is negated by the increasing crack length, where the two J_R-curves from 3PB and CCT specimens converge, see Figure 4.16. With the geometry effect, the fracture resistance is a function not only of the crack extension, but also the negative T-stress (positive T-stress has negligible effect on opening stress, thus no effect on J or K). The R-curve rises corresponding to the increase of negative T-stress, Figure 5.4.

Figure 5.4 shows a 3-D diagram of the J_R surface and the (elastic) G curve, both presented in conjunction with the T-stresses, assuming the concave J_R-curve is raised up evenly by a quantity which raises the J_R at initiation caused by a negative T-stress (Figure 2.7). This assumption was made for simplicity in explaining the raised J_R-curve associated with T-stresses. The R-curve results from the CCT and 3PB specimens have already shown that the R-curves merge as Δa increases (Section 4.3). The lowest J_R values along the axis of 'T-stress/Yield stress' in Figure 5.4a represent the J_R at initiation, which increases with the increasing negative T-stresses. Figure 5.4a illustrates that J_R depends on Δa and the T-stress (as a result of the constraint effect) and the construction of a J_R-T surface. The G curve in Figure 5.4b is hypothetical and assumes a decrease in T-stress with increasing crack length, which is often the case. If the G curve stays

above the J_R-T surface, the crack is unstable, but if the curve falls below the surface, only stable cracking can occur.

The J_R-T surface in Figure 5.5a represents the fracture resistance for a 2.5mm long crack in the a/W=0.1 3PB specimen (Table 5.1). The G curve is produced for the 3PB specimen configuration, representing the driving force for the maximum load in the experimental test[6]. The geometry effect is shown in the G curve at the initial crack length, where the T-stress/σ_{ys} is –0.43 and the G curve rises above the J_R-T surface. The geometry effect becomes insignificant as the crack length increases. The T-stress/σ_{ys} is 0 at a/W=0.33, corresponding to a crack length of 9mm.

Figure 5.5b shows the J_R-T surface and the G curve, representing the resistance and the driving force of the maximum applied load for a 25mm crack in the a/W=0.5 3PB specimen (Table 5.1). Figure 5.5b shows that the T-stress has no effect on the J_R-T curve for deep cracks (a/W>0.33) in 3PB specimens. The applied G is less than J_R for the initial crack length, but $\partial G/\partial a > \partial J_R/\partial a$ and the G curve rises above the J_R-T surface at initiation, where the opening stress at the crack tip is not affected by the T-stresses. Although the T-stress is always positive in this crack geometry and has no effect on the J_R-T surface, the G-T curve is shifted with increasing positive T-stress so that $\partial G/\partial a > \partial J_R/\partial a$, resulting in $G > J_R$. As a result, instability is predicted (Figure 5.5b) graphically at crack lengths between approximately 27mm and 30mm, which differs from the result without the T-stress index, see section 5.1.2 and Figure 5.1b. The G curve rises above the J_R-T surface with further increase in crack length, i.e. the increase of a/W ratio.

The above examples show that the interaction of the T-stress with R-curve analysis can be important, but this hypothesis needs thorough testing before it is used in practice. More detailed information on the J_R-T surface is required from experimental testing.

5.3 *G_{eff} for Small Scale Yielding*

The G-curves in sections 5.1 and 5.2 were obtained from elastic K values which were calculated for the given crack length. In the case of plastic deformation at the crack tip, the driving force G

is computed for the effective crack size. Small scale yielding is assumed because the finite element computation of the J_R-curve have only shown this behaviour, Figure 4.7.

Figure 5.6 illustrate instability prediction, using the effective G, G_{eff}, and J_R-curve, for specimens whose configurations are the same as those in Figures 5.1 and 5.2. In these cases the G_{eff} is calculated with respect to a_{eff}, which is $a+f(r_y)$, where $f(r_y)$ is a function of the Irwin plastic zone size (section 2.1.4). The $f(r_y)$ is given, to a first approximation, by[40],

$$f(r_y) = \frac{1}{1+\left(\frac{F}{F_{limit}}\right)^2}\left(\frac{n-1}{n+1}\right)\frac{1}{\beta\pi}\left(\frac{K}{\sigma_{ys}}\right)^2,$$

hence

$$a_{eff} = a + \frac{1}{1+\left(\frac{F}{F_{limit}}\right)^2}\left(\frac{n-1}{n+1}\right)\frac{1}{\beta\pi}\left(\frac{K}{\sigma_{ys}}\right)^2, \qquad (5.1)$$

where a is the crack length;

F is the applied load;

F_{limit} is the limit load with respect to the current ligament width;

n is the strain hardening exponent;

K is the stress intensity factor with respect to the crack length;

β is the factor of plastic zone size, which is 2 for plane stress and 6 for plane strain conditions.

The correction factor for the plastic zone size under plane stress conditions is $\beta=2$, assuming small scale yielding at the crack tip. Iteration is not necessary when applying the above equation to calculate a_{eff} because the equation uses elastic K rather K_{eff}. Although Eq. (5.1) does not have a strict theoretical basis, the effective G using a_{eff} correction agreed closely with the elastic-plastic finite element calculations for small scale yielding[40].

In Figure 5.6 the instability prediction for the geometries under low loads are similar to those in section 5.1, where the G curves are obtained regardless of crack tip plasticity. The difference between G and G_{eff} under low loads is marginal because the plasticity, assumed to be small scale yielding at the crack tip is insignificant. At high load the G_{eff} curve crosses the J_R-curve at a crack length larger than that given by the G curve (Figures 5.6c and 5.6d). Although the estimated crack extension using G_{eff} is longer than that from the G curve, the crack arrests where $dG_{eff}/da < dJ_R/da$. However, the rate of dG_{eff}/da is similar to that of dG/da for a given geometry.

Prediction using both the G and G_{eff} curves suggests that the growth of a long crack in specimen with b>>B ligament is safe because $dG/da<dJ_R/da$.

In section 4.4 the a/W=0.5 (b=B) 3PB specimen failed at a load close to limit load. In the case of a crack tip close to fully plastic conditions, neither the G curve nor the G_{eff} curve is appropriate for the instability prediction because of the larger scale yielding.

5.4 *Conclusions*

The fracture instability of through thickness (25mm) cracks is predicted using the R-curve approach, with a concave R-curve determined from experimental test results. The predictions agree with the experimental results. Standard 3PB specimens with b=B ligaments fracture in an unstable manner (under load control) at a reproducible K_{1C} value, while 3PB and CCT specimen with long cracks and b>>B ligament show $dG/da \leq dJ_R/da$, which prevents unstable fracture, and increases structural safety.

The approach is also applied to cracks in the bridge girder (also 25mm thick). The results, assuming that the form of the concave R-curve is retained at the vicinity of a T-section joint, show that crack growth in stem and flange is stable because of the high dJ_R/da. The result coincides with the experimental results from a full scale test of the bridge which showed high damage tolerance. In the experimental test, a flange crack grew to the stem before the test was stopped. The bridge was subjected to cyclic load, so any stable crack growth might have been spread over all the load cycles that exceeded K_{1C}.

The R-curve approach successfully predicts fracture instability. The opening stress is however affected by the constraints at the crack tip. The driving force and resistance should be presented in conjunction with its (negative) T-stress. In this case the J_R-T surface and the G curve should be displayed in 3-D. This is not, however, convenient for manual assessments.

In case of plastic deformation at the crack tip, the G_{eff} curve (using a_{eff}) is used for instability prediction. The result for crack growth under low load is similar to that using the elastic G curve. At high loads the predicted crack extension using G_{eff} is longer than that from the G

curve. Predictions using both G_{eff} and G curves suggest that crack growth is stable in specimens with b>>B ligament. However, the J_R-curve is not reliable for crack tip conditions which are close to fully plastic. Although the J_R-curve is accepted as a measure of fracture resistance for stable crack growth, the validation for J_R-curve testing confines the result to small scale yielding conditions. The interpretation of the J integral and the validation of the J_R-curve for the bridge alloy is discussed in next section.

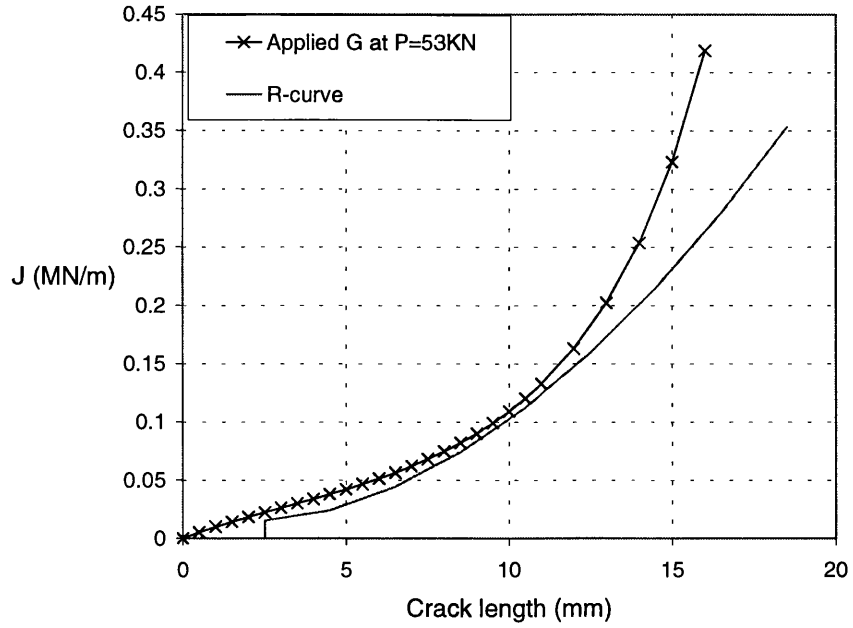

a. 3PB a/W=0.1 (b=B) specimen.

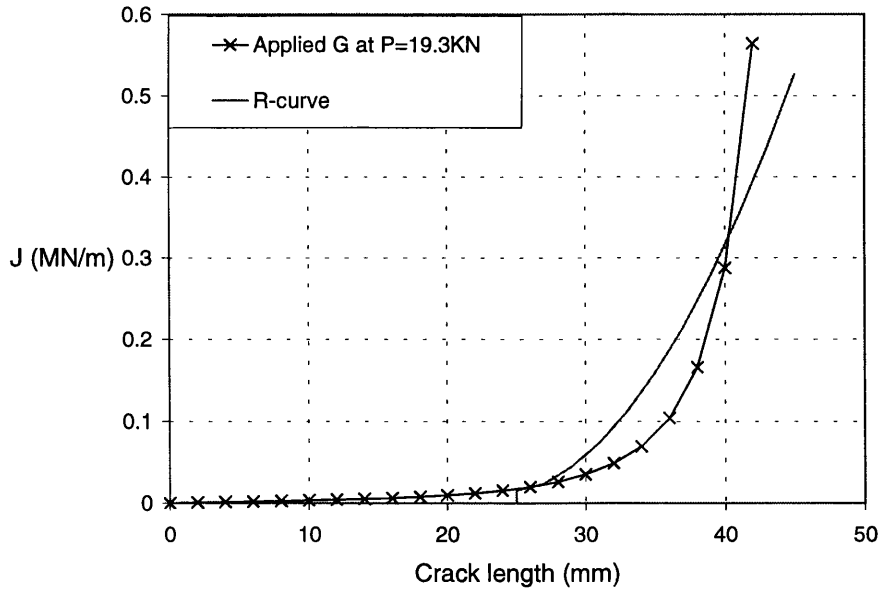

b. 3PB a/W=0.5 (b=B) specimen.

Figure 5.1 Applied G/ J_R curve of b≤B ligament specimens (B=25mm).

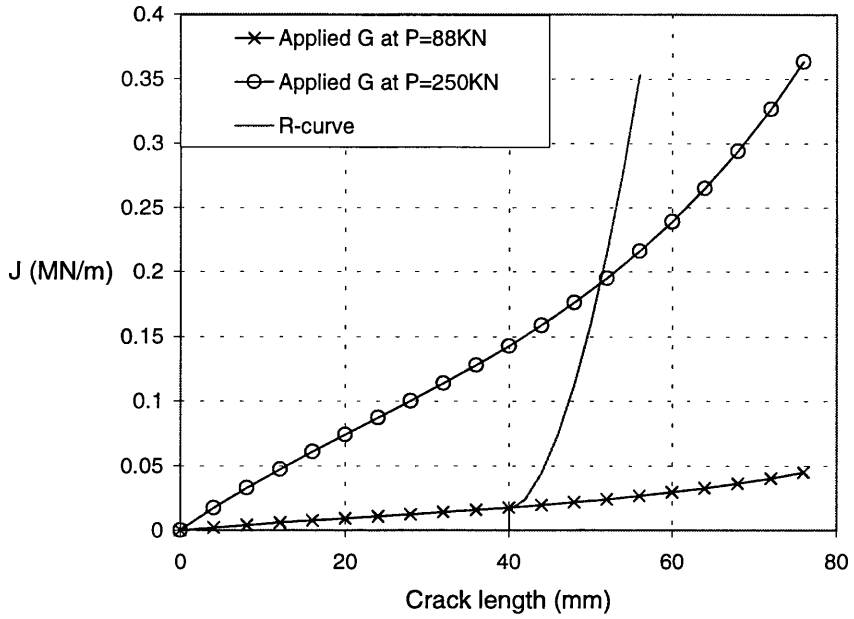

a. 3PB a/W=0.2 (b>>B) specimen (b=160mm).

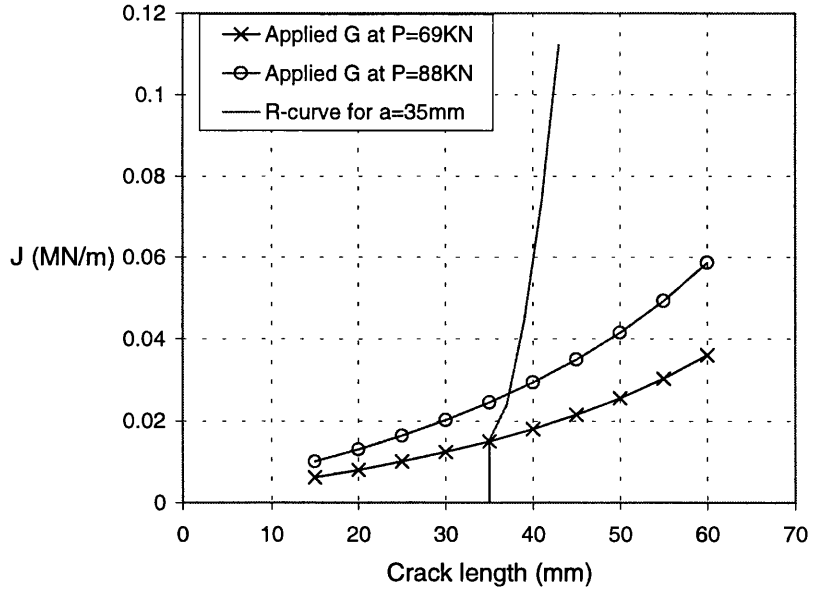

b. CT a/W=0.23 (b>>B) specimen (b=150mm).

Figure 5.2 Applied G/ J_R curve of b>>B ligament specimens (B=25mm).

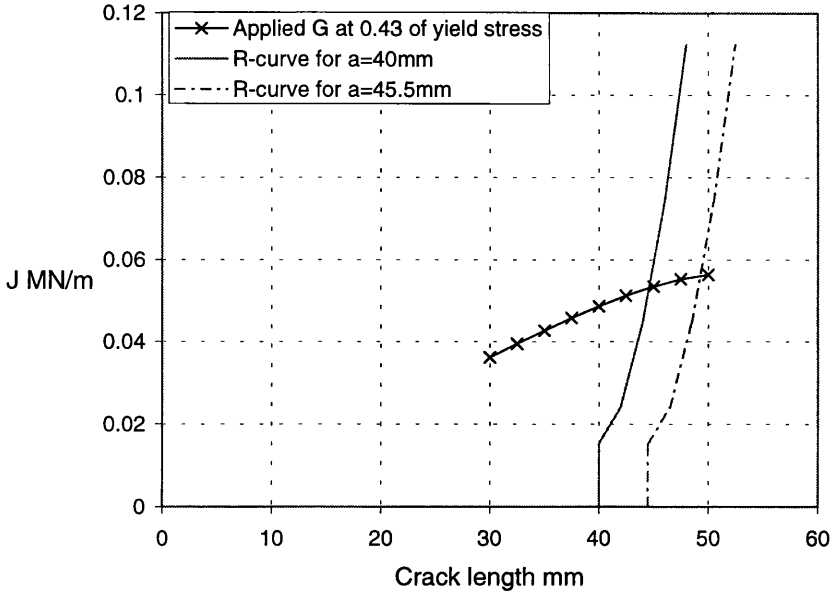

a. Stem crack (assuming 2a=80mm and c=45mm, see Figure3.2 for notations).

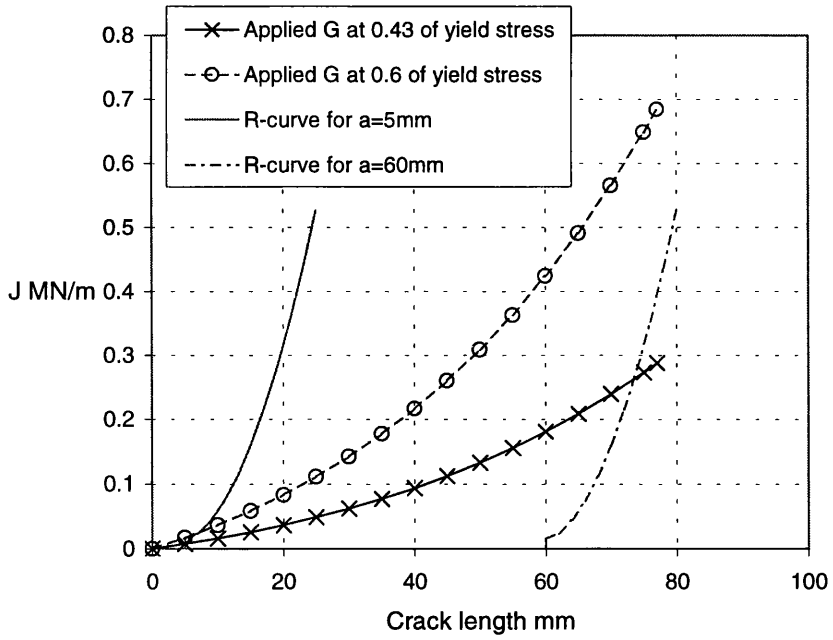

b. Flange crack.

Figure 5.3 Applied G/ J_R curve for cracks in bridge components.

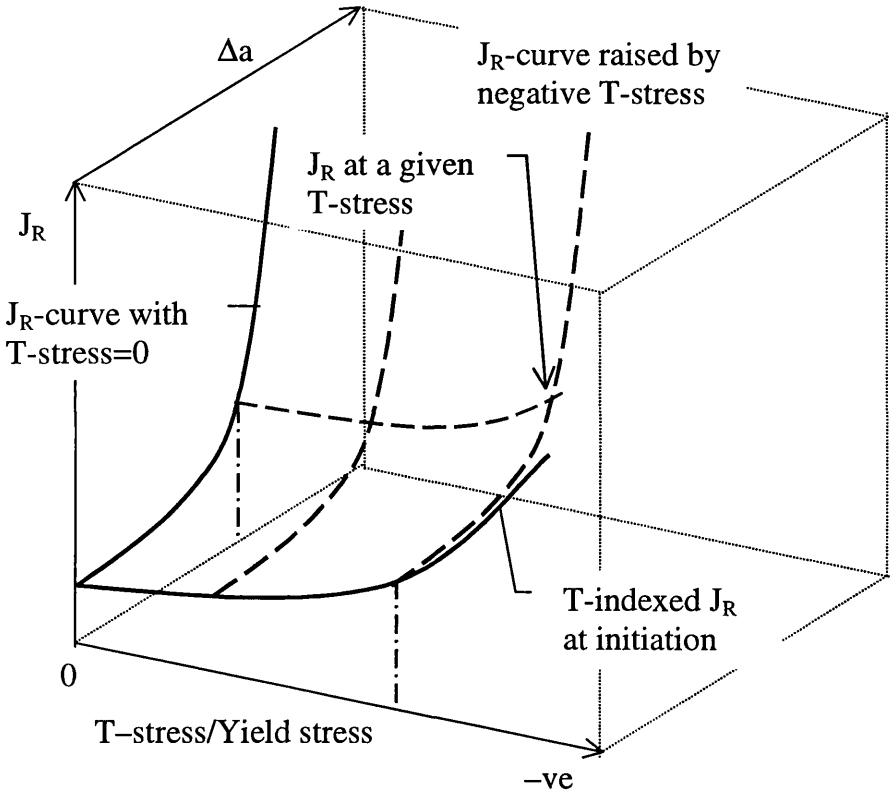

a. The relationship between J_R, Δa and T-stress, and the construction of a J_R-T surface.

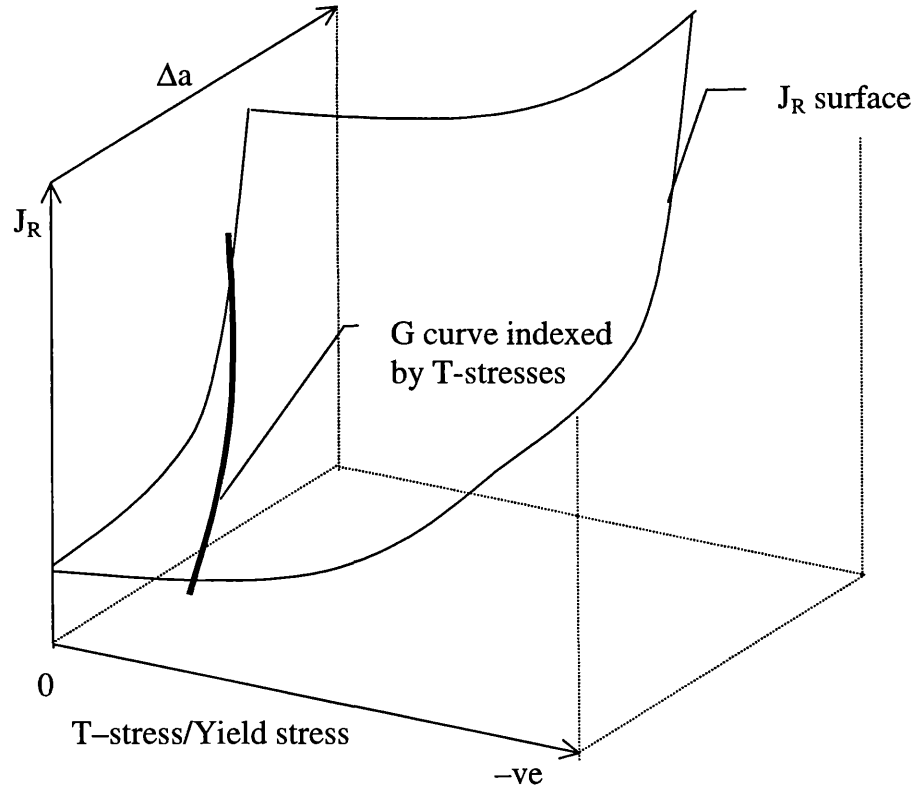

b. Fracture prediction using a J_R-T surface and G curve indexed by negative T-stresses.

Figure 5.4 The construction of J_R-T surface.

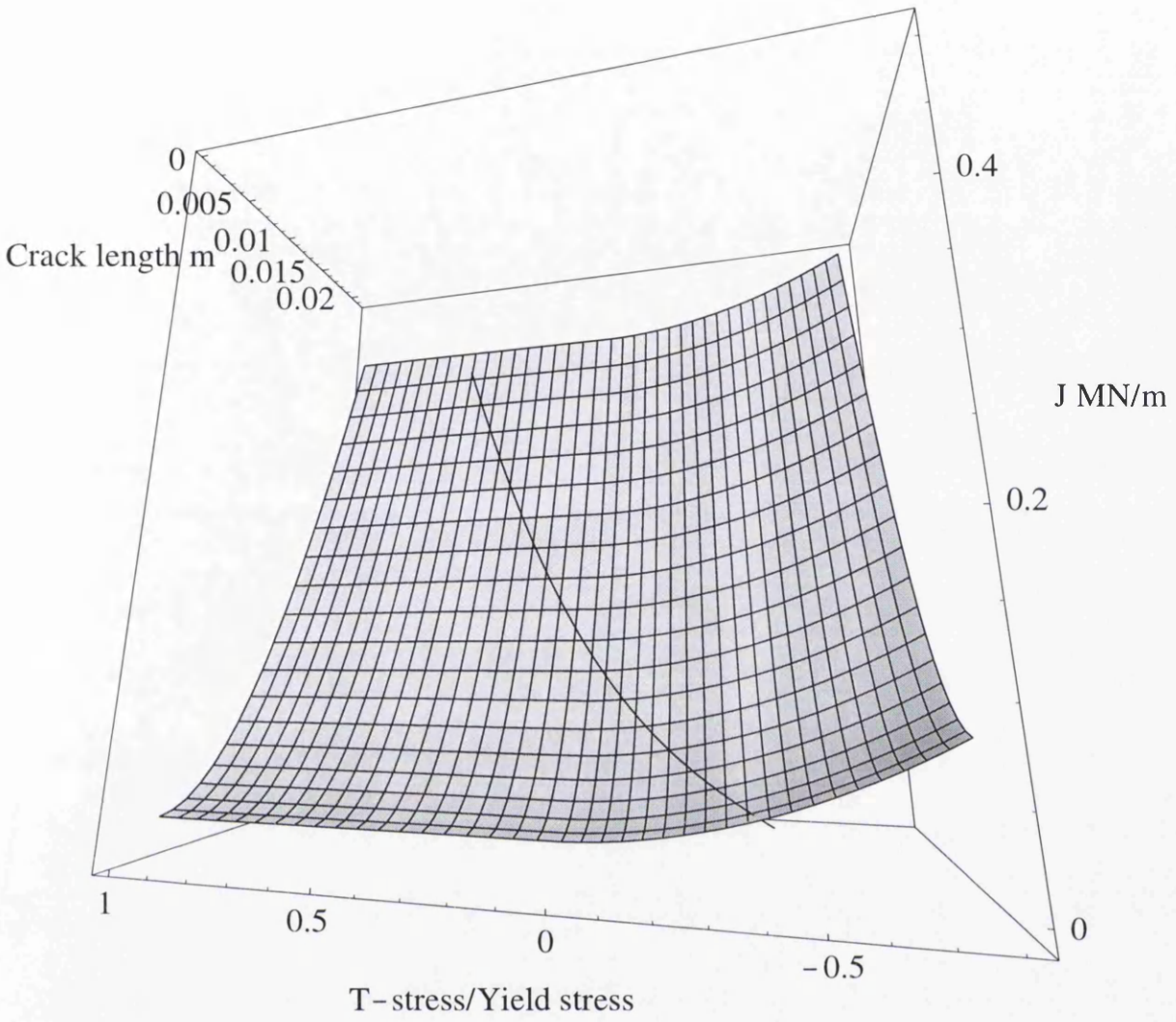

Figure 5.5a 3-D failure surface of 3PB a/W=0.1 (b=B) specimen.

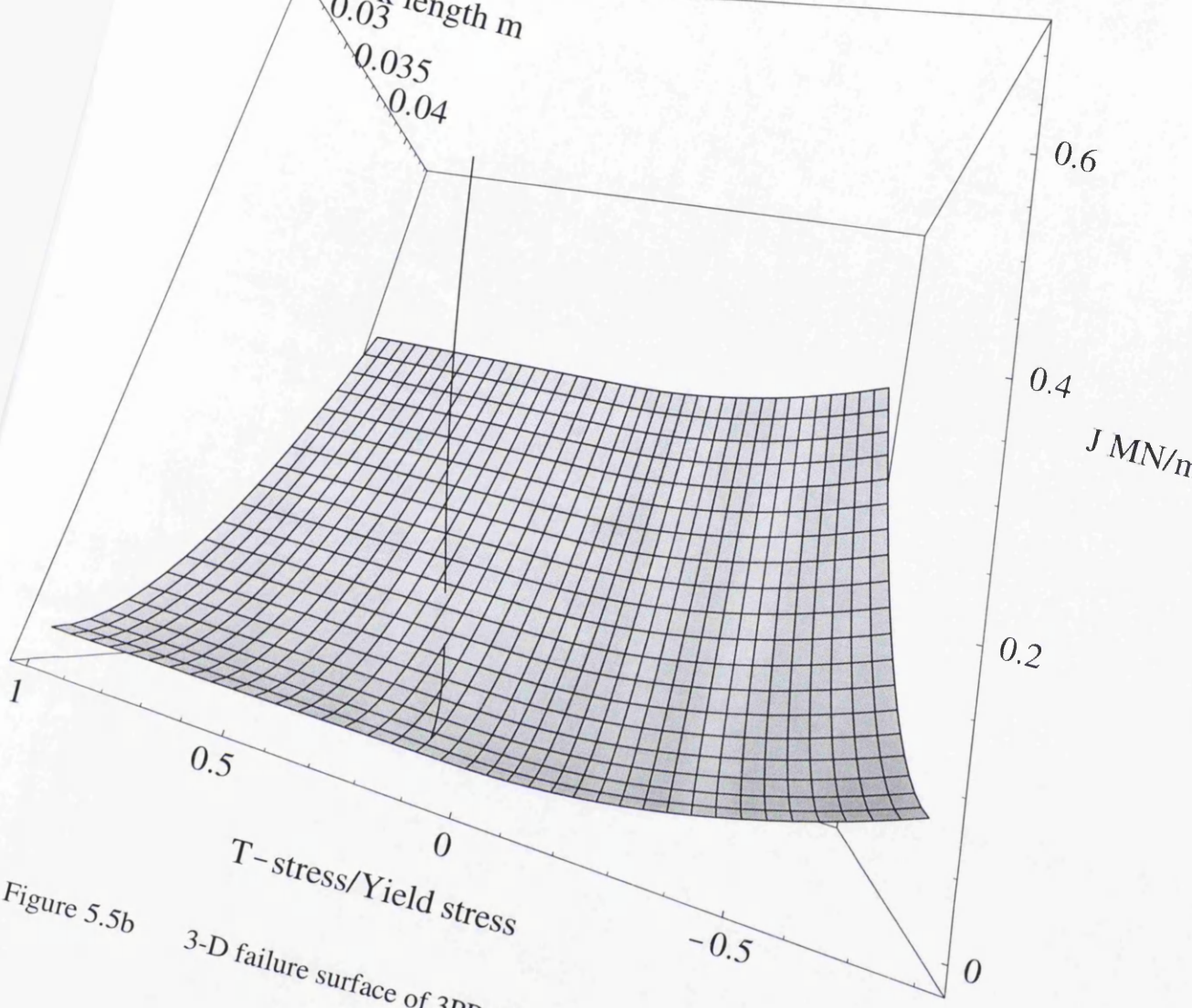

Figure 5.5b 3-D failure surface of 3PB a/W=0.5 (b=B) specimen.

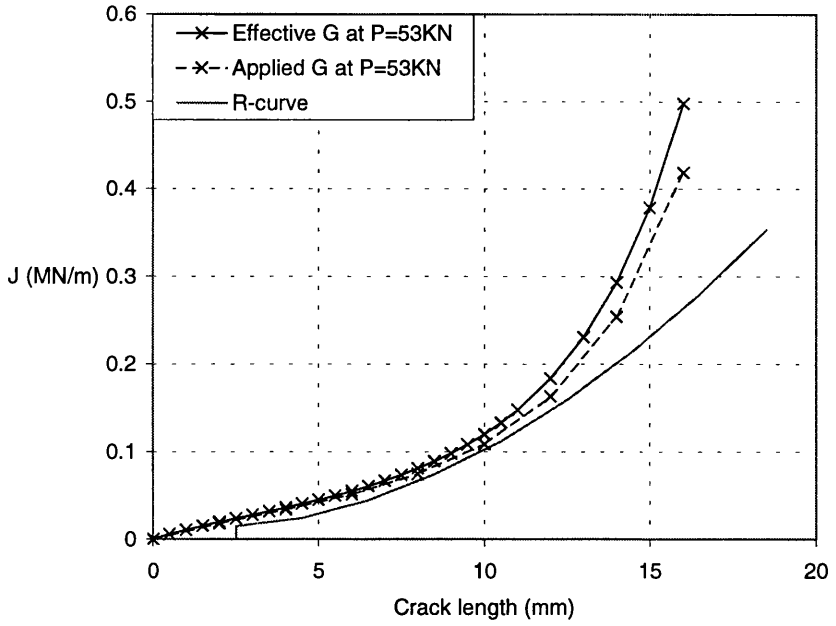

a. a/W=0.1 (b=B) 3PB specimen.

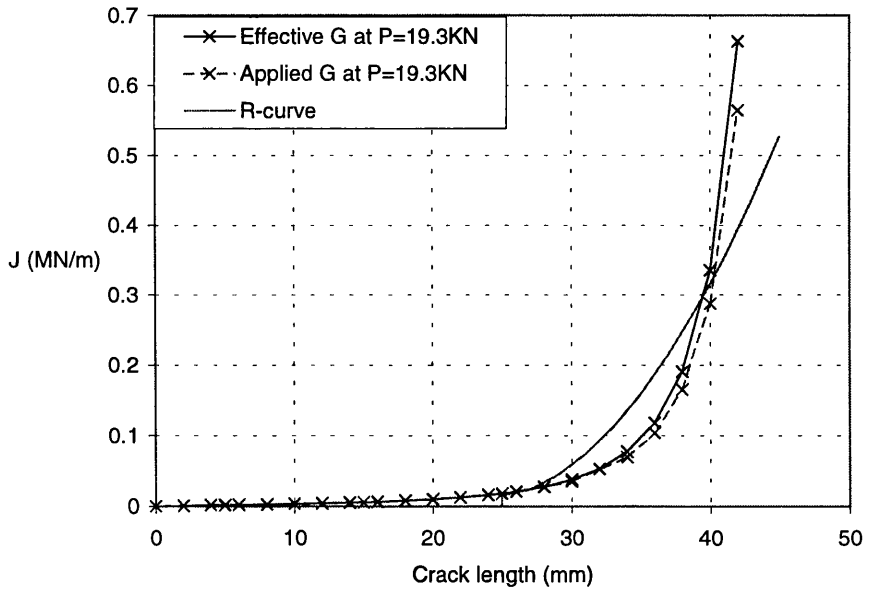

b. a/W=0.5 (b=B) 3PB specimen.

Figure 5.6 Instability prediction for 3PB and CT specimens using G_{eff} (Applied G curve is also given).

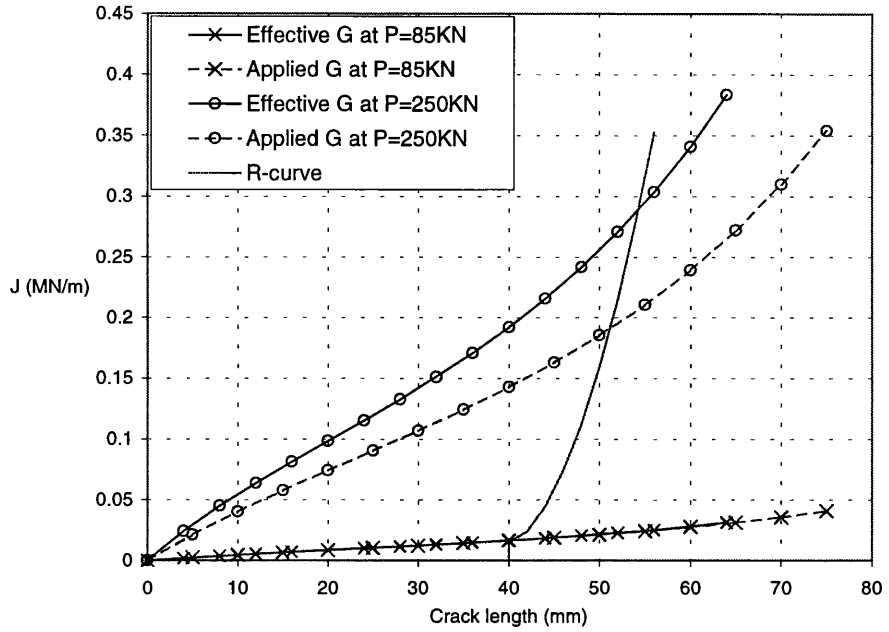

c. a/W=0.2 (b>>B) 3PB specimen.

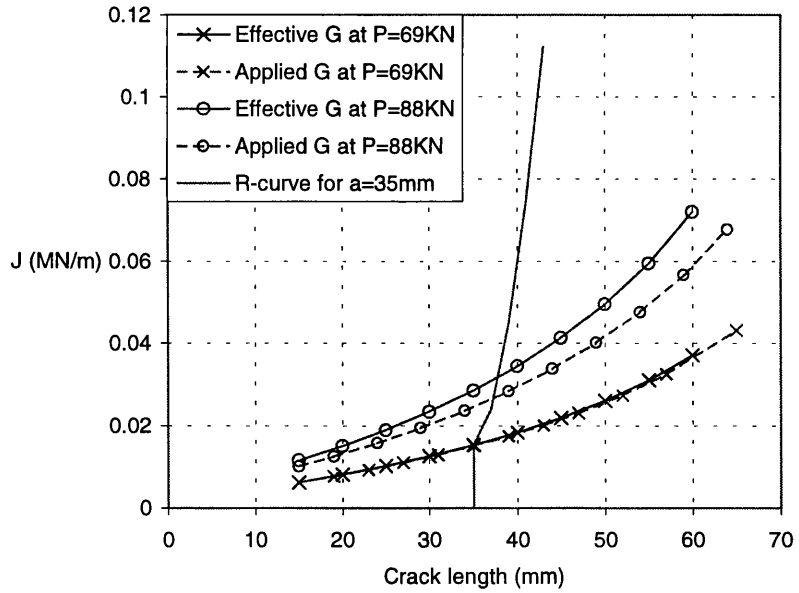

d. a/W=0.23 (b>>B) CT specimen.

Figure 5.6 (cont.) Instability prediction for 3PB and CT specimens using G_{eff} (Applied G curve is also given).

CHAPTER 6. THE INTERPRETATION OF THE J INTEGRAL FOR STABLE CRACK GROWTH

6.1 *Introduction*

Rice[19] showed that the J integral for linear or non-linear elastic material is equivalent to G, i.e. the elastic energy release rate. For elastic material, the energy release rate is the rate of change in potential energy with crack area, because there is no plastic flow in the cracked body. In elastic plastic material, the material around the crack front deforms plastically so that the change of potential energy is the result of changes in plastic dissipation, restored elastic energy and the work of crack propagation. In this case the change of potential energy is not solely for extending the crack length. Rice et al. showed[41] that J can be determined from the load-displacement curve of a fracture test. This method, however, measures available energy in the crack tip and the result gives no indication of the different components of absorbed energy in the cracked body. The physical meaning of J resistance has been studied[42][43][44] in order to determine a precise measure for the absorbed energy. As a result, a modified J integral[44] and a dissipative J-like term[43][45] has been introduced to provide an accurate measure of tearing resistance during the growth of a crack.

Despite the argument about the interpretation of J for elastic plastic material, J_R versus da curves are commonly used as a measure of fracture toughness. The flow (incremental) theory of plasticity is considered a more accurate description of material behaviour, but the deformation theory is capable of producing analytical results, like the HRR field theory. In this case, the conditions for J controlled crack growth are derived[46] to ensure that, within these conditions, the results from both theories are essentially identical.

The interpretation of the J integral and its different modifications for contained plastic dissipation will be discussed in next sections. The validity of the J_R-curve obtained from the fracture tests on the bridge alloy will be examined using currently accepted procedures e.g. BS 7448:Part 4[47]. Most of these procedures assume plane models, and, in section 4.8, it was shown that most of the R-curve, obtained for this study, occurred under plane stress conditions. Hence the use of plane models can still provide valid conclusion. One non-plane model is used in section 6.3 to assess shear lip development.

6.2 *J Based Resistance Curve*

If J is determined from the experimental load-displacement curve of a fracture test on elastic material, it is given by,

$$J = G = -\left(\frac{dU_a}{dA}\right)_F$$

for the results from a load controlled fracture test, while

$$J = G = \left(\frac{dU_a}{dA}\right)_u$$

for the results from a displacement controlled test (see section 2.1.1).

In a fracture test under load control[40], J for unit thickness is given by

$$J = -\int_0^F \left(\frac{\partial u}{\partial a}\right)_F dF = \int_0^F \left(\frac{\partial u}{\partial b}\right)_F dF \qquad (6.1)$$

where u is the loadline displacement, a is the crack length, b is the uncracked ligament size and F is the applied force. For elastic plastic material, u can be separated into elastic and plastic components, i.e. $u=u_e+u_p$, hence,

$$J = \int_0^F \left[\left(\frac{\partial u_e}{\partial b}\right)_F + \left(\frac{\partial u_p}{\partial b}\right)_F\right] dF. \qquad (6.2)$$

The elastic component on the right hand side in Eq. (6.2) is indeed the elastic energy release rate, thus Eq. (6.2) can be written as,

$$J = G + \int_0^F \left(\frac{\partial u_p}{\partial b}\right)_F dF. \qquad (6.3)$$

The above equation indicates that J increases with plastic deformation, as observed from the current experimental results[8][36], which showed that the formation of shear lips caused the flat fracture in the central region to tunnel to a point. It is evident that the rising J_R curve is associated with widening shear lips and the increase of plastic zone size.

For crack initiation under plane strain conditions in high constraint geometries, J or G is the fracture toughness which is geometry independent as long as the plastic zone size is negligible. At the crack front, the material on the specimen side surfaces deforms plastically under

increasing load, because of the plane stress conditions on these surfaces. This plastic flow causes the relaxation of stress through the thickness, so that the plastic zone increases in the in-plane and out-of-plane direction during crack growth. The increase of work done on the cracked body dissipates into plastic flow near the surfaces, while some of the energy provides for crack propagation at the central region of the thickness, where high constraint remains.

Attempts have been made to identify the dissipative energy and fracture work for growing cracks, but this has not yet been successful. Attempts have also been made to correlate rising plastic work with the formation of shear lips, but the prediction[37][38][45] is not precise. The definition of a J-based dissipation rate[43] and the J prediction using the Krafft model[37] will be shown later in this chapter. The modified J integral by Ernst[44] for irreversible process in plasticity is discussed below.

6.2.1 *Modified J integral for Elastic Plastic Material*

Rice[19] introduced the J integral based on deformation theory of plasticity because of the difficulties of using flow theory for crack growth analysis. In this case the applied force, F, is a function of crack length, a, and hence the ligament size, b. Recall that Eq. (6.1), the plastic component of J, J_p, for unit thickness, is given by,

$$J_p = -\int_0^F \left(\frac{\partial u_p}{\partial a}\right)_F dF = \int_0^F \left(\frac{\partial u_p}{\partial b}\right)_F dF.$$

Ernst[44] considered the load history of a fracture test, so that J_p is a function of a and loadline displacement, hence,

$$J_p = \int_{a_0}^{a} \left(\frac{\partial J_p}{\partial a}\right)_{u_p} da + \int_0^{u_p} \left(\frac{\partial J_p}{\partial u_p}\right)_a du_p .$$

or

$$J = G + \int_{a_0}^{a} \left(\frac{\partial J_p}{\partial a}\right)_{u_p} da + \int_0^{u_p} \left(\frac{\partial J_p}{\partial u_p}\right)_a du_p .$$

Ernst[44] introduced J_M as

$$J_M = G + \int_0^{u_p} \left(\frac{\partial J_p}{\partial u_p} \right)_a du_p ,$$

or
$$J_M = G + \frac{1}{B} \int_0^{u_p} \left(\frac{\partial F}{\partial b} \right)_{u_p} du_p .$$

where the second term on the right hand side of the above equations are the plastic component of J_M, and the derivative of this term is with respect to u_p but not the crack length, a. The G is the energy release rate for unit thickness according to the current crack length.

The basis of J_M is that the work done on a cracked body is a function of crack length, a, and loadline displacement, u, so that the elastic strain (recoverable) energy, U_e, is given by,

$$U_e = \int_{a_0}^{a} \left(\frac{\partial U_e}{\partial a} \right)_{u_e} da + \int_0^{u_e} \left(\frac{\partial U_e}{\partial u_e} \right)_a du_e ,$$

hence,
$$U_e = -\int_{a_0}^{a} G da + \int_0^{u_e} F du_e ,$$

where G is the energy release rate for unit thickness.

Ernst suggested that the linear elastic strain energy, U_e, regarding the history-dependence of the load-displacement record is given by,

$$\int_0^{u_e} F du_e = \int_{a_0}^{a} G da + U_e . \qquad (6.4)$$

For a linear elastic body, u_e is the total displacement. For elastic plastic material, total displacement contains elastic and plastic component, i.e. $u=u_e+u_p$. Therefore, the total work done is,

$$\int_0^{u} F du = \int_0^{u_e} F du_e + \int_0^{u_p} F du_p . \qquad (6.5)$$

Combining Eq. (6.4) and Eq. (6.5), Eq. (6.5) can be written as,

$$\int_0^{u} F du = \int_{a_0}^{a} G da + U_e + \int_0^{u_p} F du_p . \qquad (6.6)$$

Eq. (6.6) does not define the different parts of the plastic work done, so that the energy of fracture is not clearly defined. However, Ernst's model emphasises the difference of J between nonlinear elastic material and elastic plastic material. The difference is that the former is based on the current a and u, where the load-displacement path is reversible, whilst the latter is calculated by tracing the load-displacement record of the test to the point of interest.

The effects of using J_M, rather than J, for R-curve analysis have been reported. From experimental results[48] of steel bend specimens, the differences between J and J_M are less than 10%, though J_M characterised crack growth resistance over a wider range of conditions than J. Turner et al.[48] showed that the maximum allowable crack extension for J_M controlled growth is 60% of the current uncracked ligament (based on the results using CCT and DEN specimens). Ernst[49] demonstrated the consistency of the J_M curve using experimental results from tests on steel and aluminium alloys. Ernst[49] also concluded that, for those results, the consistency was sustained in bend specimens for crack growth up to 40-50% of the original uncracked ligament.

6.2.2 *Energy Dissipation Rate*

Turner[43] discussed the dissipative energy and so the meaning of a rising J_R curve. Turner's J_{dis} model for measuring the tearing resistance is a combined elastic and plastic energy, in which the elastic component causes fracture, whilst the plastic component causes damage to the material adjacent to the crack, but may or may not contribute directly to fracture.

The various measures of J for different configurations are based on (c.f. Eq. (6.1))

$$J = \eta U/Bb, \tag{6.7}$$

where η is a dimensionless constant which relates J to work done per unit area, U is the total work done to the cracked body, B is the thickness and b is the size of the original uncracked ligament. After initiation, $J=J_i+\Sigma dJ$, where J_i is the toughness at initiation measured in a fracture test[43][50]. The second term on the right hand side of this equation is given by[45],

$$\Sigma dJ = \Sigma \eta dU/Bb + f[d(\eta U/Bb)].$$

Turner et al.[45][50] argued that dJ should be defined for the material in the increment and that tearing subsequent to initiation is discontinuous in the macro sense, therefore the second

function, i.e. the Δa(or Δb) dependent term, in the above equation can be neglected. As a result, dJ/da is the multiple of a size-dependent factor and the work rate (cf. Eq. (6.7)),

$$dU/Bda = (b/\eta)(dJ/da), \qquad (6.8)$$

where **U** is the external work in a cracked body which has elastic and plastic components, i.e. U_e and U_p respectively.

Turner et al.[45][50] defined the dissipative energy, hence the resistance, $dU_{dis}=d(U - Fu_e/2)$, where $Fu_e/2$ is the internal elastic strain energy. Since $U=U_e+U_p$ where U_e is the sum of initial elastic work prior to tearing plus the change of internal elastic strain energy, $d(Fu_e/2)$, and the elastic component of fracture work, R_G, then dU_e is given by

$$dU_e = d(Fu_e/2)+R_GBda,$$

and $$dU_{dis} = dU_e+dU_p-dFu_e/2 = dU_p+R_GBda.$$

Turner[50] argued that the change of the conventional J integral[19], modified J[44] and J_{dis} (see below) are the same; i.e. $dJ=dJ_M=dJ_{dis}$ if the elastic component in these terms is negligible.

Recalling Eq.(6.1), and rewriting Eq.(6.8) for the energy dissipated in plasticity, Turner et al.[43][45][50] introduced a dissipation rate as,

$$dU_{dis}/Bda = dR/da = (b_i/\eta)(dJ_{dis}/da,)$$

where b_i is the current ligament size.

Turner et al.[45][50] used dU_{dis}/Bda to present the dissipative work rate per unit crack extension for tests on titanium alloy. The results[45][50] showed that dU_{dis}/Bda, J_{dis} and J_M curves could be unified by using an abscissa of $\Delta a/b_0$, where b_0 is the initial size of the uncracked ligament. The plot of dU_{dis}/Bda versus $\Delta a/b_0$ illustrated falling dU_{dis}/da curves. The test results for titanium alloy[50] showed that the use of dU_{dis}/Bda provided a unique R-curve for a given thickness up to $\Delta a = 60\%b_0$, and it was evident that the scatter in the R-curve using J was reduced by using J_{dis}. Turner[45][50] suggested that there was no J-controlled growth for dJ_{dis} versus $\Delta a/b_0$ plots, even for large growth or cases of full plasticity, because the scatter in the test data from different specimen sizes were unified by the scaled abscissa, $\Delta a/b_0$ and the use of dU_{dis}/da brought the results into a more rational basis.

6.3 *The Relation Between Energy Dissipation and Shear Lips*

Stable crack growth accompanying the formation of shear lips has been reported[37][38][48]. The effect of shear lips on the tearing resistance is related to the rising J_R-curve[38][38][48]. Krafft[37] provided an empirical relationship between the growth of shear lips and fracture resistance, on the basis of three assumptions,

i. the shear lips were at 45° to the crack plane and the region bounded by these two lines was a plastic deformation zone;

ii. this plastic zone was subjected to a constant plastic-work density, dW_p/dV, for all thicknesses of shear lips, at any stage of its formation;

iii. the energy to create new surfaces(dW_s/dA) was supplied for the surface of flat fracture in the central region and for the projected surface of slant shear lips, i.e. the surface that was the product of the thickness and the extended crack length.

If S was the ratio of the total width of shear lips to the thickness, the total plastic deformation zone on the crack flanks was $(BS)^2/2$. An increment of work, dW_t, for a growing crack was composed of an areal(flat fracture) and volumetric(plastic deformation) components,

$$\frac{dW_t}{da} = \frac{dW_s}{dA} B + \frac{dW_p}{dV} \frac{(BS)^2}{2}. \qquad (6.9)$$

where $\frac{dW_t}{da}$ = total energy consumption per crack growth ($\frac{dW_t}{Bda}$ is equivalent to J for SSY),

$\frac{dW_s}{dA}$ = energy consumption per unit cracked area,

$\frac{dW_p}{dA}$ = energy consumption per unit volume,

B = specimen thickness,

S = the ratio of the total width of the shear lips to the specimen thickness.

Knott[38] suggested that where a specimen failed by square(flat) fracture and slant shear lips, the fracture of these two modes were independent. Since S was the ratio of the total width of shear lips to the thickness, the proportion of flat fracture in the central region was (1–S) (Figure 6.1). In this case the work done for unit crack extension could be predicted by a solution which was based on Krafft[37], but the energy consumption per unit cracked area was a proportion of (1–S),

$$J_R = \frac{1}{B}\frac{dW}{da} = \frac{dW_s}{dA}(1-S) + \frac{dW_p}{dV}\frac{BS^2}{2} \qquad (6.10)$$

Knott[38] provided the values of $13.5kJm^{-2}$ and $145kJm^{-2}$ for dW_s/dA and $(dW_p/dV)(B/2)$ respectively, for the fracture test results[37] of 7075-T6 alloy (assuming the specimen thickness of 4.5mm). Knott[38] suggested the values of dW_s/dA and $(dW_p/dV)(B/2)$ as $20kJm^{-2}$ and $200KJm^{-2}$ respectively, on the basis of constant total shear lips width of 2mm, in order to predict the critical energy release rate, which he denoted as G_{crit}, for fracture under mixed mode between flat and fully slant. Thus,

$$G_{crit}=200S^2+20(1-S)$$

where S is defined as before. The prediction agreed closely with experimental results[38]. It was noted that Knott[38] assumed that $(dW_p/dV)(B/2)$ was constant for all thicknesses(B).

Turner[45] applied this solution to the results of tests on HY130 steel, which showed that dU_{dis} (the energy dissipation defined by Turner, see above) had a strong response from the volumetric component, i.e. dW_p/dV, with the condition that the width of the shear lips was proportional to the initial uncracked ligament size. Turner[45], however, found that, from the results of tests on a titanium alloy, Eq.(6.10) for dU_{dis} was incomplete, and therefore an extra term was needed to account for the plane strain volumetric work. Eq.(6.10) was rewritten as,

$$J_{dis} = \frac{dW_s}{dA}(1-S) + \frac{dW_p}{dV}\frac{BS^2}{2} + \frac{dW_{p2}}{dV}b_i \qquad (6.11)$$

where dW_{p2} is the plane strain volumetric work, and b_i is the current ligament length. Turner suggested that the third term in Eq.(6.11) is independent of the shear lips width, but proportional to the current ligament size, b_i. However, this solution is restricted to the analysis of test results in [45], which assume dW_s/dA and dW_p/dV are independent of thickness.

Previous test results[38][45][48] reported that the width of the shear lips reached a maximum of between 2 to 3mm. It was also proportional to the initial ligament size, i.e. S/b_0=0.2 and 0.4 in the tests on titanium alloy and HY130 steel respectively[45].

6.3.1 *J Prediction Using Shear Lips Width*

Krafft[37] showed that the dW_s/dA and dW_p/dV could be determined from the plot of G versus $BS^2/2$ data from a test. From the results of their tests on 7075-T6 alloy, they found dW_s/dA and

dW_p/dV to be 68in.lbs/in^2 and 8300in.lbs/in^3 (i.e. 0.012MNm/m^2 and 57.2MNm/m^3) respectively.

In the bridge alloy tests, the region of flat fracture tapered from full thickness to a point where fully slant fracture occurred, section 4.6. The shape of this tapered section was virtually triangular. The projected surface of the shear lip on the crack plane is a simple right-angle triangle (see Figure 6.1), so that S (in Eq.(6.9) and (6.10)) at any increment is equivalent to the ratio of accumulated crack extension (Δa) to maximum flat crack extension, which was 18.5mm[36]. Figure 6.2 shows the relationship between J_R and $BS^2/2$ from the experimental results[36] of the bridge alloy. In this case the dW_s/dA and dW_p/dV are 0.015MNm/m^2 and 36.7MNm/m^3 respectively. There is a small but significant deviation from linearity in the experimental results.

The J for the bridge alloy are predicted using Krafft's model, i.e. Eq.(6.9) of which the component for flat fracture is constant, and Knott's model, Eq.(6.10), with the values of dW_s/dA, dW_p/dV and S shown above, Figure 6.3. The value of dW_p/dV for Knott's model are different from that of Krafft's model, because the value of $dW_s/dA(1-S)$ in Knott's model reduces with the decrease of the flat fracture region. Therefore the value of dW_p/dV in Eq.(6.10) is 37.95MN/m^2 (assuming a linear relationship between J_R and $BS^2/2$ in Figure 6.2 at fully slant fracture). The difference between the two predictions, as a result of the difference in assumptions for dW_s/dA, is marginal, and it is evident that the elastic energy is negligible compared to the increasing plasticity at the crack tip. The predictions by both models underestimate the experimental J. At a crack extension of 7mm, the estimated J is less than the experimental J by 15%. The discrepancy is perhaps due to the simplicity of the shear lips shape and/or other components of dissipative energy, which is proposed by Turner, and discussed previously.

It has been reported[48] that dW_p/dV decreases with increasing shear lips width. In a test[48] on C-Mn steel specimens with thickness between 13mm to 50mm, the dW_p/dV values reached a plateau at a shear lip width of 2.3mm or 40% of its maximum width. The test results, for specimens with width(W) and thickness(B) less than 100mm, and the ratio of b/B equal to unity or above, showed that the shear lip width was proportional to the square root of the ligament size(b) but was independent of the specimens thickness(B).

The dW_p/dV from the results of the bridge alloy reduced with the shear lip width, though the reduction was marginal(Figure 6.4). The dW_p/dV values shown in Figure 6.4 were determined from the experimental J_R–curve. The shear lip width is estimated assuming the same relation with the ratio of instantaneous crack extension to the maximum flat crack extension (see above).

6.4 *J-Controlled Growth*

Although reports of J_M and J_{dis} applications[45][48][49][50] showed that these approaches for measuring tearing resistance were more appropriate than that using conventional J integral, which is computed with respect to the crack length at an increment, the J_M and J_{dis} analyses demanded experimental data that were not available in the present work. Turner[43] suggested that the J_M and J_{dis} resistance curves could be unified by using the abscissa of $\Delta a/b_0$. The J_R-curves in this report were obtained from fracture tests on 3PB (numerical) and CT (experimental) specimens (both high constraint geometry) with different ligament, and they were identical. In this case unification procedures were not essential. Also, this report showed that instability could be predicted graphically using J_R-curve analysis, which is based on the conventional J-integral. Therefore the investigation of the applicability of J_M and J_{dis} for growing cracks is not of interest in this report. The investigation of J-controlled growth, and hence the applicability of the J_R-curve, will be presented in the next section.

The J integral suggested by Rice[19] is based on deformation theory of plasticity, which breaks down when the elastic plastic material is unloaded or the crack tip plasticity becomes a significant fraction of the in-plane dimension. Stationary cracks subjected to monotonic load and restricted crack tip plasticity exhibits J characterisation, or J-T characterisation for low-constraint geometries[3].

Prior history influences the local stress and strain in elastic plastic materials. Large crack growth will produce a region containing elastic unloading behind the crack tip and nonproportional plastic loading at the crack tip. It is obvious that the unloading behaviour between the elastic plastic material and nonlinear elastic material, to which the J integral applies, are different, and this difference violates the assumption of deformation plasticity at the crack tip in the elastic plastic materials. Therefore the J characterisation is valid only if the crack growth is within a J-

dominated zone, so that the stress and strain are proportional to r^{-1} singularity. As a result, an experimental J_R curve is valid as long as the conditions of J-controlled crack growth is satisfied.

Hutchinson and Paris[46] suggested that, for small scale yielding, the wake of elastic unloading and the region of nonproportional plastic loading is of the order Δa, while the size of the singularity region, R, is some fraction of the plastic zone size in small scale yielding, and some fraction of the uncracked ligament in fully yielded specimens. The small scale growth requires $\Delta a << R$. Hutchinson and Paris[46] examined the strain increments using deformation theory under a simultaneous increase in J and crack length, and showed that in order for the predominantly proportional loading to exist in the crack tip singularity region, the condition

$$\frac{da}{r} << \frac{dJ}{J} \tag{6.12}$$

must be satisfied. Let

$$\frac{1}{D} = \frac{dJ}{da}\frac{1}{J},$$

and Eq.(6.12) can be rewritten as

$$D << r.$$

In addition to the conditions of small scale yielding, where $\Delta a << R$, a region in which plastic loading is predominantly proportional and the r^{-1} singularity is dominant exists when

$$D << r << R. \tag{6.13}$$

As a result, if Eq.(6.13) is satisfied, the estimates of strain field, using both deformation and flow(incremental) theories is identical, and hence J characterisation is valid.

In the foregoing argument, R is some fraction of the uncracked ligament (or other characteristic distance from the crack tip to a boundary) in fully yielded specimens. Hence, the condition for J-controlled growth are

$$\omega = \frac{b}{J}\frac{dJ}{da} >> 1$$

together with $\Delta a << R$. In addition[46],

$$\frac{b\sigma_{flow}}{J} >> 1,$$

where σ_{flow} is the flow stress. This condition is required for keeping the crack opening displacement small compared to the ligament size, b.

Reports[48][51] on experimental J-controlled growth have suggested different values for the factors Δa and ω to indicate a J dominant zone. Gibson et al.[48] gave the values as $\Delta a << 0.2b$ and $\omega >> 2.0$, while Jones et al.[51] suggested that

$$\Delta a << 0.2b_0,\ \omega >> 1 \text{ and } \frac{b(\text{or}\,B)\sigma_{flow}}{J} >> 25,$$

where $b\sigma_{flow}/J$ is the specimen size requirement and the minimum value of 25 is to ensure plane strain conditions for geometry dependence, for HY 100 grade steel.

Similar factors for J-controlled growth are also provided for fracture testing in British[47] and ASTM standards[52]. Both of the standards recommend that, for a valid J_R-curve, the conditions of $\Delta a_{max}=0.1b_0$ and $J_{max}=b_0(\sigma_{ys}+\sigma_{ult})/40$ (or $b_0\sigma_{ys}/20$ in[52]) are required, where σ_{ult} is the tensile strength and b_0 can be replaced by B, whichever is smaller. Moreover, test specimens have to fulfil other requirements including,

$$0.8 \le \frac{W}{B} \le 4 \left(\frac{W}{B} = 2 \text{ is preferred}\right) \text{ and } 0.45 \le \frac{a}{W} \le 0.7.$$

6.4.1 *Qualifying The J_R-Curve of The Bridge Alloy*

The stress and strain fields near the crack tip in thin sections, i.e. of predominantly plane stress behaviour, have been studied experimentally[53] and numerically[54]. The experimental results[53] coincided with the HRR estimations (see section 2.1.5), whilst the numerical results[54] showed that the stress and strain distribution are insensitive to specimen geometry. Both of the reports concluded that a J dominant zone existed near the crack tip upon stable crack growth in predominantly plane stress conditions.

Anderson[40] used dimensional analysis to show that

$$\frac{\sigma_{ij}}{\sigma_{ys}} = f_{ij}\left(\frac{EJ}{\sigma_{ys}^2 r}, \theta\right) \qquad (\text{for } 0 \le r \le r_J(\theta))$$

where r_J is the radius of the J-dominated zone. He argues that J characterises the crack tip stress and strain field as long as the product of stresses and strains (the specific work) exhibits a r^{-1} singularity. Also the singularities of the HRR field, namely the $r^{-1/n+1}$ for stresses and $r^{-n/n+1}$ for strains, are special cases for materials exhibiting a Ramberg-Osgood power law, see section

2.1.5. However, the J dominance at the crack tip region does not exist under large scale yielding, because of the different material behaviour between elastic-plastic materials and materials following deformation plasticity, upon which the J integral is based.

The opening stress and equivalent strain near the crack tip from the numerical results of J_R-curve testing on the bridge alloy (see section 4.2) were compared with that of a stationary crack using plane stress analysis. The trend of the distribution for normalised opening stress in a growing and stationary crack is identical, Figure 6.5, although the results of the growing crack at J=17kN/m is less than that of stationary crack. The rate of decreasing σ_{yy}/σ_{ys} against $r\sigma_{ys}/J$ changes at about $r\sigma_{ys}/J=45$ (in the case of the initiation of the stable crack growth, it occurred where $r\sigma_{ys}/J=35$) which coincides with the plastic zone size. Figure 6.6 and 6.7 show the normalised opening stress and equivalent plastic strain ahead of the growing crack. The results at the vicinity of the crack tip increase with crack growth, hence the increasing J level, but the far field results, where $r\sigma_{ys}/J>10$, are converged. However, the opening stress and equivalent plastic strain at initiation are less than that of the subsequent growth of the crack. Figure 6.6 is evidence that J scales the stress/strain field near the crack tip.

Anderson[40] suggested that in small scale yielding and a J dominant zone, the crack tip stress field at crack initiation is given by

$$\frac{\sigma_{ij}}{\sigma_{ys}} = f^1\left(\frac{EJ}{\sigma_{ys}^2 r}, \theta, \frac{\Delta a}{\delta_i}\right), \qquad (6.14)$$

where δ_i is the crack opening displacement(COD) at original crack tip. In this case the J_R-curve depends on crack extension, i.e. $J_R=f(\Delta a)$. The numerical (plane stress) result of crack propagation for J_R-curve testing showed a linear relationship between COD and crack extension(Δa), Figure 6.8, and the ratio of $\Delta a/\delta_{COD}$ for the first 6.2mm crack extension is 26.2. Figure 6.9 shows σ_{ij}/σ_{ys}, from the numerical result of the J_R-curve test, as a function of $(EJ/\sigma_{ys}^2 r)(\Delta a/\delta_{COD})$, where $\Delta a/\delta_{COD}$ is obtained from Figure 6.8, which gives the $\Delta a/\delta_{COD}$ value of 21.1 and 19.8 for crack extensions of 7.7mm and 9.4mm respectively. The σ_{ij}/σ_{ys} is rationalised by $(EJ/\sigma_{ys}^2 r)(\Delta a/\delta_{COD})$ for crack extension from 1.7mm to 6.2mm, Figure 6.9, so that the crack growth is in a J dominant zone.

The numerical J_R-curve provided tearing resistance data for a crack extension of 10mm, and the experimental J_R-curve[8], see Figure 4.15, extended this to 18mm, with both showing good

agreement for Δa up to 10mm. Both analyses used 2-D plane stress representation (experimentally by using plane stress formulae) of the stress and strain fields at the crack tip, giving rise to a global J value. The details of transition from flat to slant fracture are averaged out in these analyses.

The limits of the experimental J_R-curve for the bridge alloy needs to be defined. The current fracture resistance testing procedures[35][47] require the test specimens to be $0.8<W/B<4$ and $0.45<a/W<0.7$. The experimental J_R-curves of the bridge alloy using CT specimens with $a/W=0.23$ and 0.5 are identical. The a/W ratio is within the required range. The W/B value of both specimens is 6, which falls outside the range specified in [35] and [47]. However, specimens as thick as the structural component represent the actual out-of-plane constraint, therefore, in terms of similitude, the experimental results are practical. According to [35] and [47], the limitation of the condition for J-controlled growth in the geometries tested[8] are given by,

$$\Delta a_{max}=0.1b_0, \text{ and hence } \Delta a_{max}=12\text{mm},$$

and

$$J_{max}=B\sigma_{flow}/20=0.525 \text{ MN/m}.$$

From the experimental results, the J_{max} is 0.46MN/m at a crack length of 18.5mm (i.e. $\Delta a_{max}=0.15b_0$). In addition, $\omega=10.2$ at J_{max} which satisfies the recommendation from other researchers. It is evident that the experimental J_R-curve[8] for a crack extension of 12mm is within the requirement for a valid fracture resistance curve to represent stable crack growth.

6.4.2 *J_R and G_{eff} During Crack Extension*

Crack growth in a J dominant zone, i.e. small scale yielding, was shown in the previous section. In addition, Figures 4.13 showed the crack tip plastic zone size for the finite element model of a 3PB specimen. The plastic zone size, in terms of equivalent plastic strain, is only a fraction of the total crack length, and that is limited ahead and behind the crack tip, Figure 4.13d and 4.13e.

In fact, the experimental and numerical J_R values are close to the energy release rate for an effective crack length G_{eff}, as shown below.

Let $G=K^2/E^*$, where $E^*=E$ for plane stress conditions and $E^*=E/(1-\nu^2)$ for plane strain conditions, and $K=Ff(a/W)/(B\sqrt{W})$[29], where $f(a/W)$ can be modified for an effective crack length, $a_{eff}=a+f(r_y)$. The function of $f(r_y)$ is defined as[40],

$$f(r_y)=\frac{1}{1+\left(\frac{F}{F_{limit}}\right)^2}\left(\frac{n-1}{n+1}\right)\frac{1}{\beta\pi}\left(\frac{K}{\sigma_{ys}}\right)^2, \qquad (6.15)$$

which is based on a modified Irwin plastic zone correction (see section 2.1.4), hence

$$a_{eff}=a+\frac{1}{1+\left(\frac{F}{F_{limit}}\right)^2}\left(\frac{n-1}{n+1}\right)\frac{1}{\beta\pi}\left(\frac{K}{\sigma_{ys}}\right)^2,$$

and $K_{eff}=Ff(a_{eff}/W)/(B\sqrt{W})$,

where a is the crack length;

F is the applied load;

F_{limit} is the limit load with respect to the current ligament size;

n is the strain hardening exponent;

K_{eff} is the stress intensity factor with respect to the effective crack length;

β is the factor of plastic zone size, which is 2 for plane stress and 6 for plane strain conditions (see section 2.1.4).

Figure 6.10 shows that, for $\Delta a>10$mm, the values of G_{eff}, using Eq.(6.15) with $\beta=2$ (i.e. assuming plane stress conditions at the crack tip), agree closely with the values of the experimental J_R. Although the actual crack tip field cannot be accurately described by a plane model, being neither plane strain nor plane stress, there is evidence of plane stress dominance at the crack tip after several millimetres of crack growth (see section 4.8). A plastic zone size (r_y) using $\beta=2$ assumes $\sigma_{ij}>\sigma_{ys}$ inside the zone, which is one half of the plastic zone using $\beta=1$ (its size is denoted by r_p in section 2.1.4). For the latter, the stresses at yielding redistribute to remain in equilibrium. In general, the increase of an effective crack length is the size of r_y, i.e. the radius of r_p (see section 2.1.4). In this case the value of G_{eff} at Δa_{max} using $\beta=2$ underestimates the experimental J_R by 15%, Figure 6.10.

6.5 *Discussion*

Numerical results show that, at initiation, the normalised opening stress ahead of the growing crack tip was less than that of a stationary crack, see Figure 6.5. These lower stress values at the growing crack tip reflect the energy released for separation (of elements) in the finite element model. The normalised opening stress, as well as the equivalent plastic strain, ahead of the tip increased with the growth of the crack (Figures 6.6 and 6.7). The increase in plasticity ahead of an advancing crack tip in the experimental tests is observed to be the plastic work absorbed in the specimens side surfaces, resulting in shear lips.

The increase of the shear lips width, with the associated increase in plastic deformation, is evidence that plasticity ahead of a growing crack becomes a significant part of the fracture resistance (for the thickness of 25mm), though the reason for the fully slant fracture in the 25mm thick specimens of the bridge alloy[8] is not clear. The J_R-curve analysis for stable crack growth under plane stress conditions is sound, though the analysis was only possible by 2-D models in the current study.

6.6 *Conclusions*

It is shown for the numerical J_R-curve that J can scale the normalised opening stress and equivalent plastic strain near the tip of a growing crack, and the crack growth is inside a J dominant zone. The conditions of the experimental J_R-curve for J-controlled growth was examined and compared against the recommendations from published standards and reports. It is confirmed that, according to published testing procedures[35][47], the numerical and experimental J_R-curves are valid fracture resistance curves for crack extension of at least 12mm.

Numerical results showed that the plastic deformation at the crack tip was only a fraction of the relative dimension. For the range of Δa in the numerical J_R-curve, the values of J_R agreed closely with the estimates of G_{eff}. It is evident that the J_R values of the present result are equivalent to energy release rates with a plastic zone correction. Therefore the numerical and experimental J_R-curve for stable crack growth is a plausible representation of the tearing resistance of the bridge alloy.

The variation of J_R with Δa is virtually parabolic, and this fact supports the use of analysis based on Krafft's and Knott's models. The elastic and plastic work per fracture surface calculated from these models are in general agreement with the values quoted by Krafft et al. for an aluminium alloy. The result showed that the plastic work rate at the tip of a growing crack is a very significant component of the value of the J-integral, and hence the tearing resistance.

The interpretation of J-integral was reviewed, leading to discussion of modifications such as J_M and J_{dis}. The J_M, J_{dis}, and the scaled abscissa $\Delta a/b_0$ were shown by other researchers to be useful in scaling the R-curve. These parameters could not be evaluated from the numerical results because the evaluation required detailed test records that were not available to the writer. In general, fracture resistance can be represented adequately by a J_R-curve for small scale yielding.

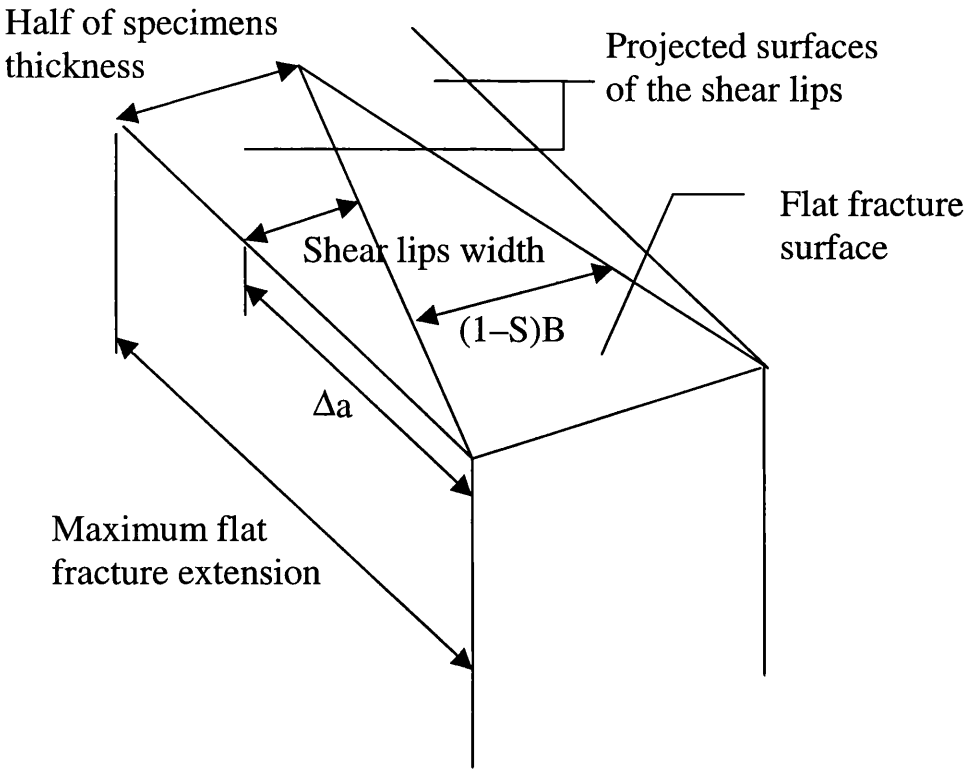

Figure 6.1 The projected surface of the shear lips on large tested specimen[8].

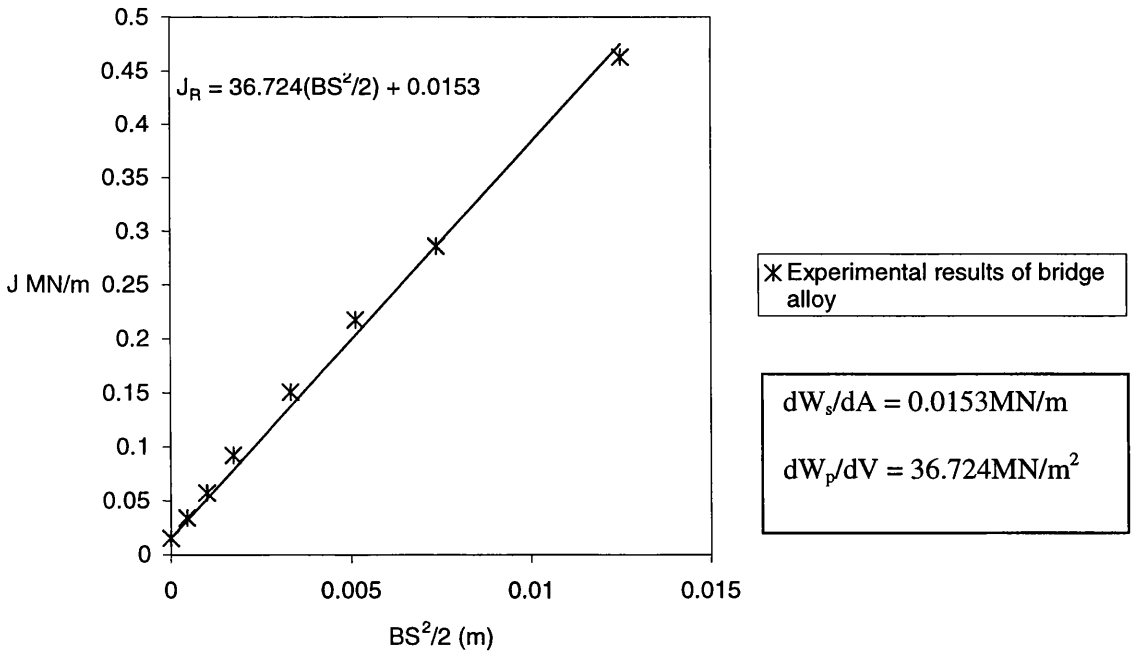

Figure 6.2 Plot of J versus $BS^2/2$ (Eq.(6.9)) to determine dW_s/dA and dW_p/dV.

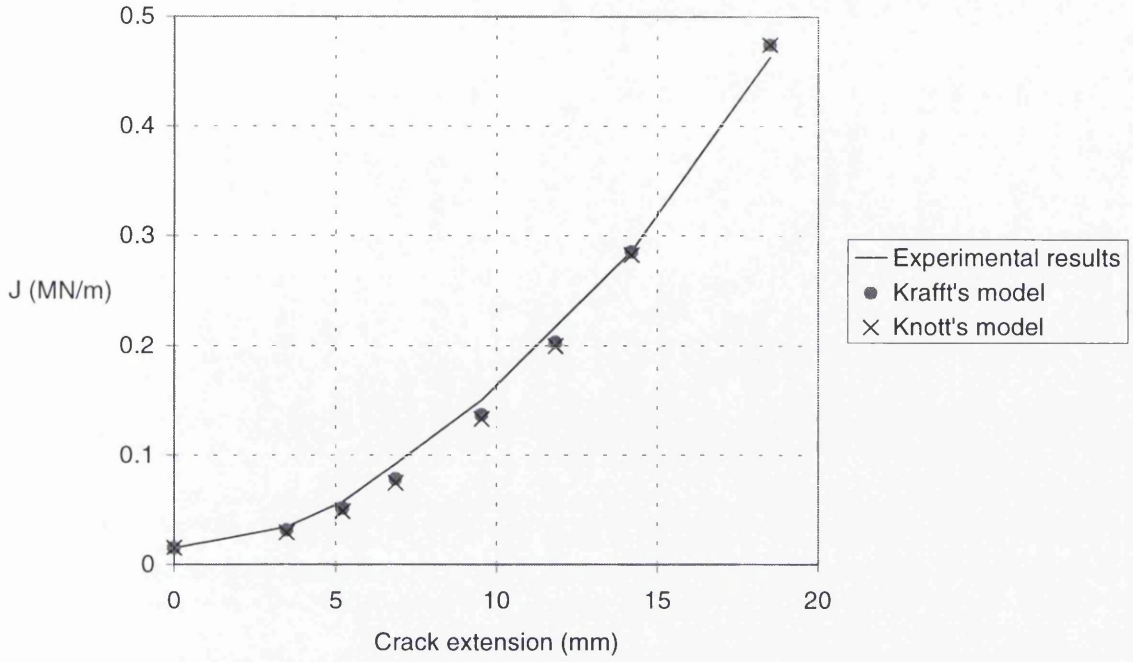

Figure 6.3 The J prediction using the width of shear lip.

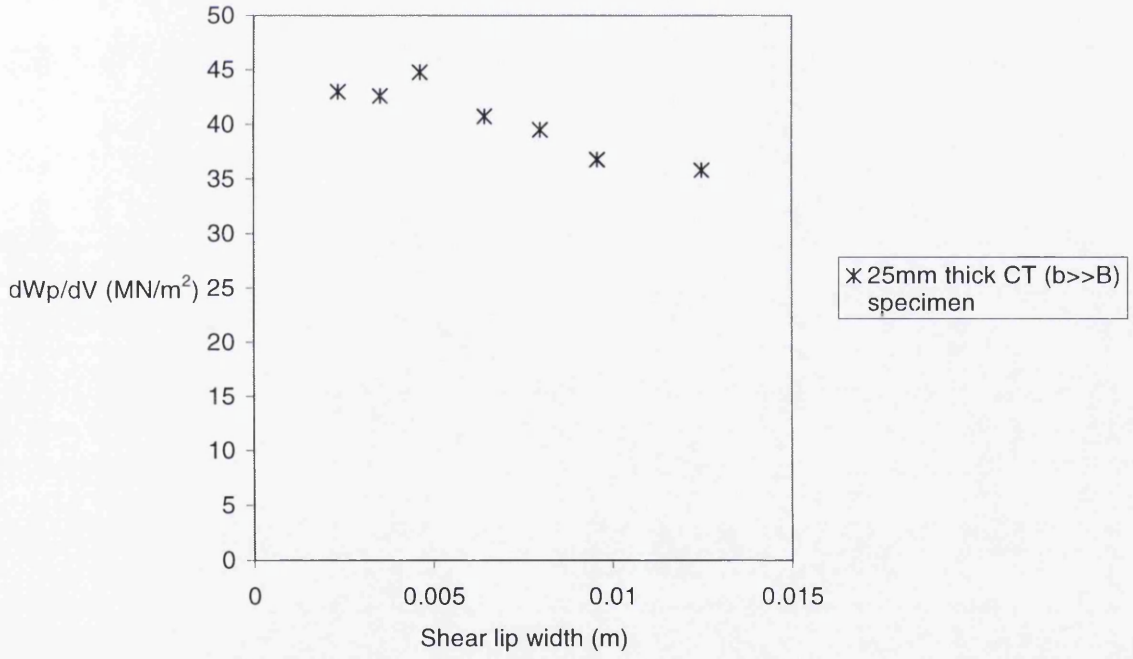

Figure 6.4 The plastic work per unit volume dWp/dV from the result of experimental fracture testing on bridge alloy.

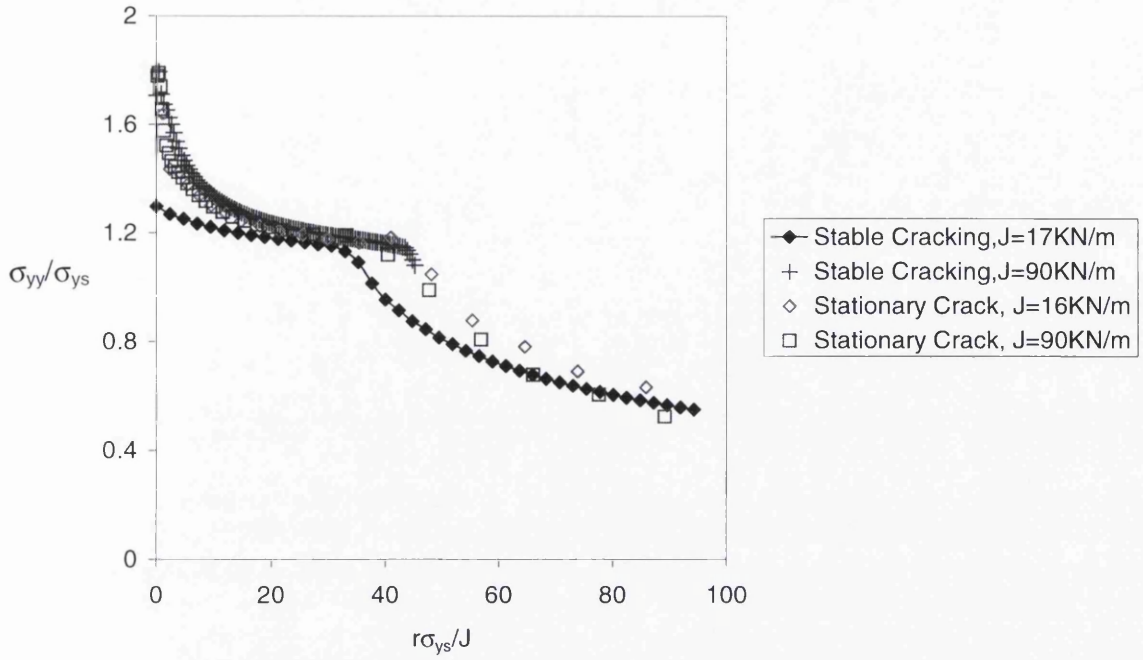

Figure 6.5 The normalised opening stress ahead of the crack tip of a growing and a stationary crack in the a/W=0.2 (b>>B) 3PB specimen.

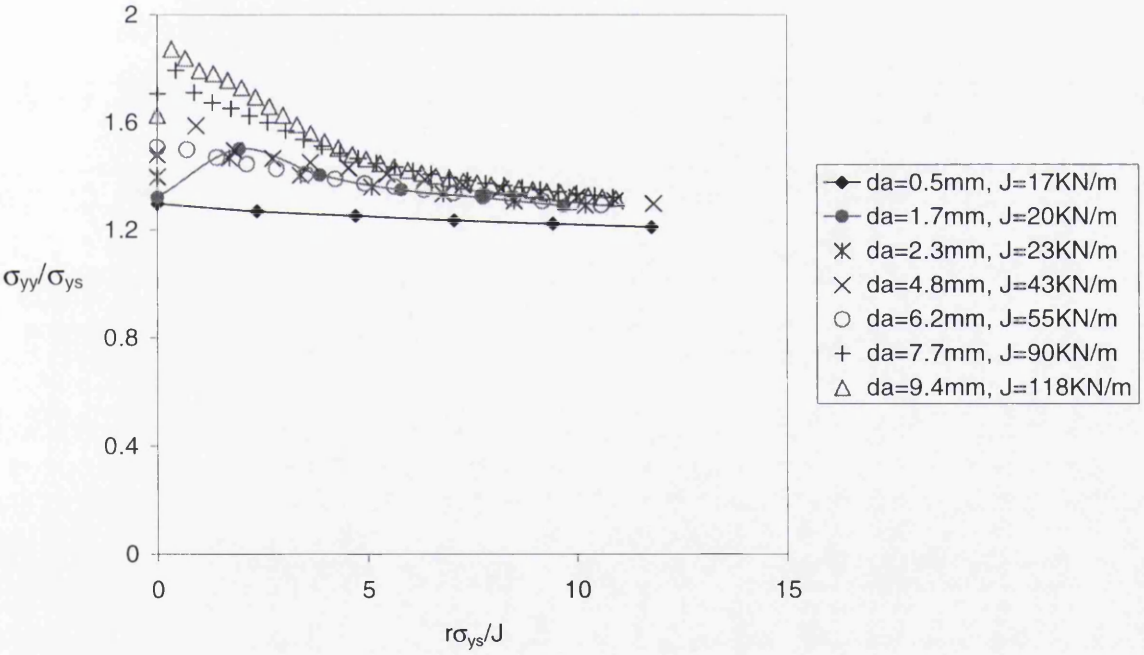

Figure 6.6 The normalised stress ahead of the growing crack tip in the a/W=0.2 (b>>B) specimen at the given J levels.

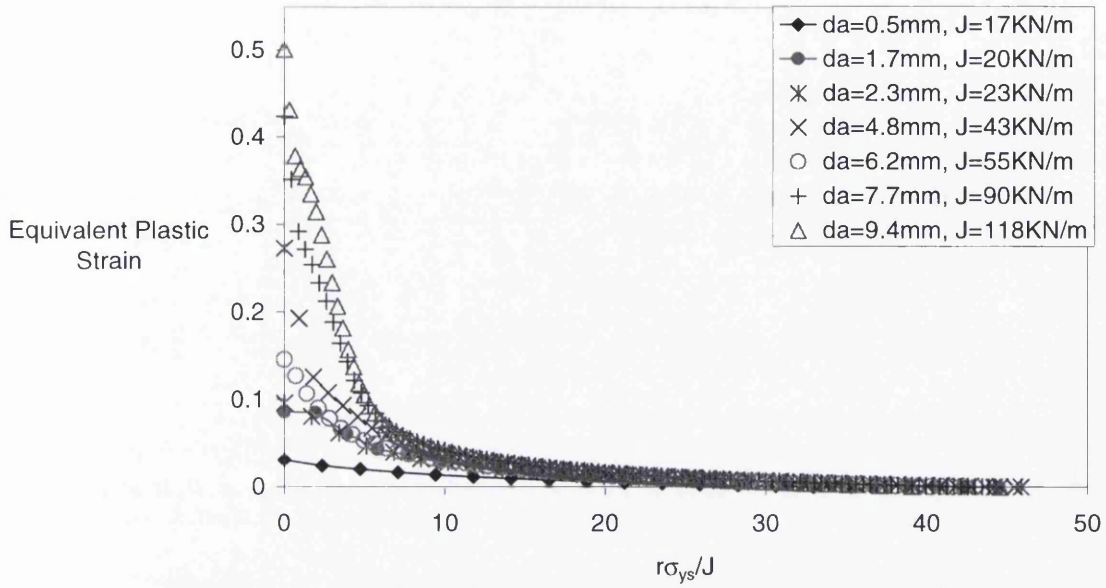

Figure 6.7 The equivalent plastic strain ahead of the growing crack tip in the a/W=0.2 (b>>B) specimen at the given J levels.

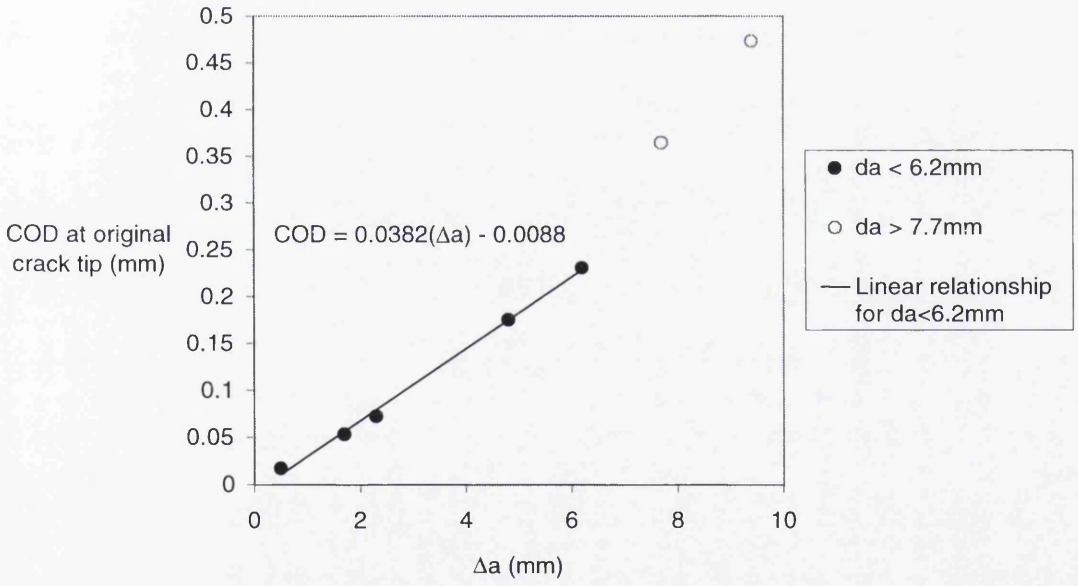

Figure 6.8 The COD versus Δa data from numerical fracture testing on bridge alloy using a 3PB (b>>B) specimen.

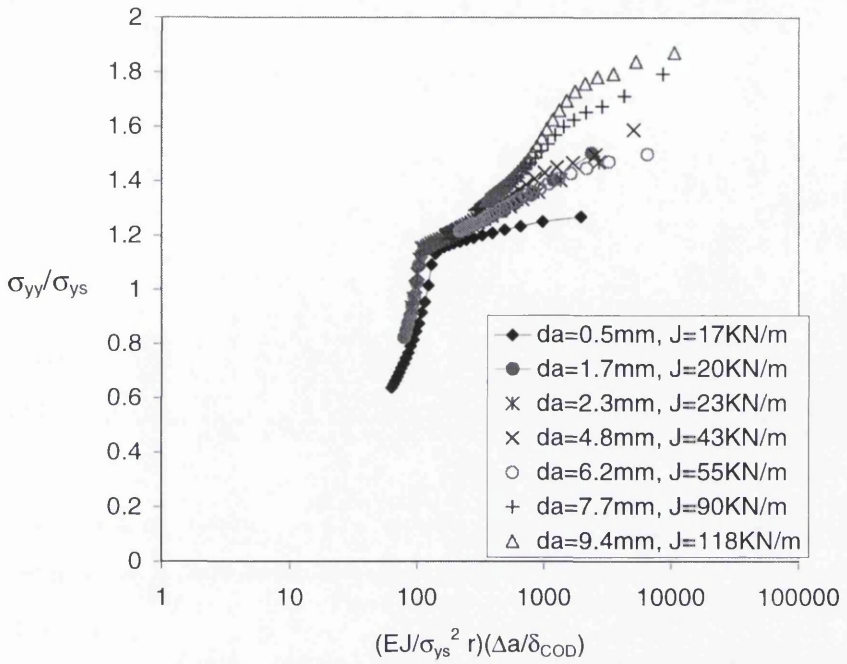

Figure 6.9 In small scale yielding the σ_{yy}/σ_{ys} are rationalised using Eq.(6.14).

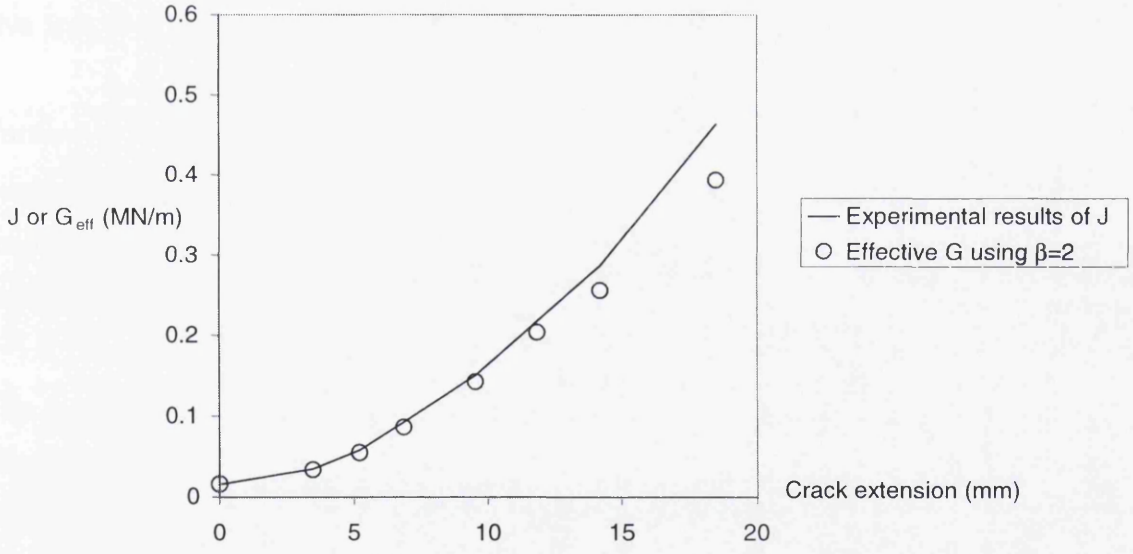

Figure 6.10 The comparison between estimated G_{eff} and experimental J

CHAPTER 7. OTHER MODES OF FAILURE IN LARGE TEST SPECIMENS

7.1 *Tests on Large Tension and Compact Tension Specimens*

Fracture tests on large specimens, equivalent to structural dimensions, for fatigue or fracture were conducted by Sumpter[8]. The results of large CT specimens (W=150mm, B=24.5mm) containing cracks normal to the extrusion direction (LT) showed that cracks favour fracture in the extrusion direction (TL). Three out of five tested specimens showed cracks deviated from the original notch direction. In addition to the plain specimens, one of the CT specimens retained its flange in order to obtain the crack growth rate of a T section. The K_I values for such T section were computed numerically using the finite element method. The results are given in Appendix B. Unfortunately, during the experimental test the crack turned into the direction normal to the original notch direction and failed. The effect of stiffeners on crack growth rate is not substantiated by this test. In general, fracture surface showed either single or double shear lips, i.e. in the form of either fully slant fracture or V-shaped fracture surface. Only one out of five tested specimens failed at a crack length close to the predicted plastic limit load.

Further fracture and fatigue tests on large CT and tension specimens were conducted by Sumpter[12][36] to examine the crack propagation and tearing resistance in the LT direction (using the CT specimens), and crack growth relationship in a large structural element (using the tension specimen).

The results showed that the tearing resistance in the TL direction was well below that in the LT direction, although the values of tearing resistance at initiation (in terms of J_R) in both orientations were the same, $J_i \approx 0.016$MN/m[8]. The tearing resistances in the two orientations began to diverge after between 5 and 10mm of crack extension and, after 20mm of crack extension, the J_R value of the LT tearing resistance was almost twice as high as that in the TL direction.

The fatigue tests on specimens in both orientations produced valuable data. The fatigue crack growth rate in both orientations are identical up to K_{IC}, as defined by the Paris Law,

$$da/dN = 2.76\times10^{-8}\Delta K^{3.74}.$$

It produced a rather high exponent in the Paris law, i.e. m=3.74. The fatigue test results will be discussed in chapter 8.

The crack surfaces in all the tested specimens exhibited the formation of shear lips and the tendency for the propagating crack to turn into the TL direction. Although most of the tested specimens failed below the plastic limit load, a CT specimen with a crack in the LT direction failed close to the limit load. These modes of failure in the test of large specimens are discussed as follow.

7.2 *Failure by Slant Fracture*

During fracture and fatigue testing on large CT specimens[8], most specimens failed by slant fracture. In general, a crack initiated with flat fracture (in plane strain conditions), but shear lips began to develop at the sides of the ligament ahead of the crack. This coincided with the (concave) form of the J_R-curve, which is almost flat at the earlier on of crack extension, but rises increasingly with crack extension (see section 4.7).

Although an exact solution for the transition from flat to slant fracture is not clear, the appearance of the crack surface can be related to the principal stresses in plane strain and plane stress conditions, Figure 7.1. For a fracture mechanics specimen in plane strain conditions and a crack in the plane xz (Figure 7.1a), the principal stresses σ_1 and σ_2 are σ_y and σ_x respectively, and $\sigma_3=\sigma_z=\nu(\sigma_1+\sigma_2)$ with $\varepsilon_3=0$. At the vicinity of a crack tip blunted by plastic deformation, i.e. a crack with finite tip radius, it is clear that $\sigma_1>\sigma_3>\sigma_2$. Thus the maximum shear stress acts along the planes at 45° from the z-axis (Figure 7.1a). As a result, the fracture surfaces are separated along the plane of x-axis and retain in the original crack plane.

For the same specimen but in plane stress conditions, $\sigma_1>\sigma_2>\sigma_3$ because $\sigma_3=\sigma_z=0$. Thus the maximum shear stress acts along the planes at 45° from the x-axis (Figure 7.1b). In this case the fracture surfaces incline to parallel with the plane of maximum shear stress.

If the plane stress conditions prevail near a crack front, the shear lips widen with crack extension and, eventually, cover the entire fracture surface. Ewalds[55] argued that the fracture plane

rotating from flat to slant in monotonic loading is the result of a change from predominantly plane strain to plane stress conditions, while in fatigue, this can be induced by variable amplitude loading. In variable amplitude loading, one or more overloads can induce the formation of shear lips, but the fracture surface reverts to flat under successive lower cyclic loads. Ewalds[55] suggested that the transition from flat to slant fracture can affect the fatigue crack growth rates, because the transition affects the amount of crack growth retardation.

A large a/W=0.23 CT specimen was fatigue tested[8] at a constant cyclic load (between 3 to 30kN), and shear lips began to develop when $K_{max}=0.66K_{IC}$. The value of K_{max} increased and exceeded K_{IC} as the crack continued to grow. The crack failed by fully slant fracture. As the load remained constant, this result suggest that flat-to-slant transition is caused by increasing applied K_I. The fatigue crack growth rate, in terms of the Paris law index, from this specimen was high compared with other results for the bridge alloy (see section 9.1.4).

7.3 *Right-Angle Crack*

The fracture test result on large CT specimens showed that cracks subjected to a higher (6.5-65kN) cyclic load failed where the crack deviated from the original notch (LT) direction, while a crack subjected to a lower (3-30kN) cyclic load failed in the LT direction. The K_{max} in all the tests exceeded the K_{IC} (35MPa$\sqrt{m}$) of the material at some point in the test. The result of fracture tests for crack propagation in the TL direction showed that the fracture resistance (in terms of an R-curve) in the TL direction is about half that in the LT direction (Figure 7.2). The dJ_R/da for the TL direction is also lower than that in the LT direction. Sumpter computed the rate of change of dissipated energy per unit crack area, D, from the test results. The value of D is fairly constant after 16 mm of crack extension: D is 376kJ/m^2 for the LT direction and 155kJ/m^2 for the TL direction. Both parameters showed low fracture resistance in the TL direction of the material. Sumpter[36] suggested that the deviated crack path was the result of the tendency of crack growth towards the weaker orientation.

When the transition from mode I to combined mode I and II occurred in fatigue crack growth at low stress intensity levels, the fracture surfaces were faceted, so that the crack path was a series of microscopic deviated cracks[55] . Gerberich[56] showed that the K_I values for microscopic

deviated cracks are lower than those for pure mode I cracks. Ewalds[55] showed that the blunter the notch the higher the stress required to initiate fracture and the greater the crack branching.

Table 7.1 Crack lengths of the three finite element models.

Model Ref.	Crack length in the LT direction (mm)	Crack length in the TL direction (mm)	Total crack length (mm)
SC1	55		55
RAC1	55	4.45	59.45
RAC2	55	10.45	65.45

The values of K_I and K_{II} for right-angle cracks were evaluated using the finite element method, in order to see if these values could explain the deviation of a LT crack turning into the TL direction. Table 7.1 shows the crack length for the finite element models. Elastic plane stress analyses were used for the computation because time did not allow plasticity effects to be considered. The model SC1 in Table 7.1 contained only a straight crack, for comparison with standard solutions. Although the elastic material properties are the same in any direction in the finite element model, the notations, TL (the weaker orientation) direction for the extrusion direction and the LT direction normal to the TL direction, are adopted for convenience.

Values of G, the total strain energy release rate, were computed using the J-integral routine in ABAQUS, because J = G for elastic analysis. The stress intensity factor K for pure mode I fracture was calculated using equation $K_I^2=EG$ (for plane stress conditions). Note that G_I denotes G for pure mode I. Specimens RAC1 and RAC2 models cracks that turns 90° to the TL direction, so that it is subjected to combined mode I and II fracture. Figure 7.3 shows the model of a CT specimen containing a right-angle crack. In this case, the stress intensity at the crack tip is characterised by K_I and K_{II}. The K_I and K_{II} components are calculated using the displacements that are normal and parallel, respectively, to the crack flank. The G_I and G_{II} values are then calculated assuming $K_i^2=EG_i$, and the total energy release rate is given by $G_{I+II}=G_I + G_{II}$, which can be compared with the total value computed by the J-integral routine.

Computed values of G and K_I for specimens RAC1 and RAC2 are compared with the estimated G_I and K_I from cracks with the same total crack length in only the LT direction (referenced as

specimens SC2 and SC3 respectively). These latter values are calculated from a published solution[40].

7.3.1 *Numerical Results*

Table 7.2 shows the numerical results for the different crack geometries. The K_I and K_{II} are normalised by K_0 and G by an equivalent G_0. The K_0 is given as:

$$\frac{F_{applied}}{2B\sqrt{\pi a_{total}}} \quad .$$

Table 7.2 Normalised G and K for different crack geometries.

Models / Parameters	SC1	SC2	SC3	RAC1	RAC2
G_{I+II}/G_0				73.8	89.7
G_I/G_0	198.7	248.3	339.0	49.9	66.2
K_I/K_0	14.1	15.7	18.4	7.1	8.1
G_{II}/G_0	0	0	0	27.3	27.5
K_{II}/K_0	0	0	0	5.2	5.2

The computed Y factor of K_I for specimen SC1 is 6.61, which agrees with the value of 6.59 from a published solution[40]. The sum of G_I and G_{II}, calculated using the crack opening displacement of the numerical result, is larger than the numerical result of G_{I+II} (calculated via the numerical J-integral) by approximately 5%. The latter is considered the most accurate estimate, and this value is quoted in Table 7.2.

Table 7.2 shows that K_{II} is a very significant proportion of the K_I value for the right-angle cracks, and the K_I for a right-angle crack is just less than half that of the equivalent straight cracks (i.e. SC2 or SC3). Comparing G values instead of K alters these proportions, but there is a simple, fixed relation between these two fracture parameters. It was decided to proceed with the consideration of instability using G for the following reasons:

a) the experimentally measured fracture resistance is expressed in terms of G;

b) both modes I and II can be incorporated into the assessment by using the combined G value, G_{I+II}, and instability can be determined by $G_{applied}$ and G_C (or J_C), see section 7.3.2.

The G_I component is approximately twice the value of G_{II} for the right-angle cracks, with the G_I component increasing with crack length while the G_{II} component remains reasonably constant. In this case, G_I increases by 30% between specimens RAC1 and RAC2, where the difference in crack lengths is 6 mm.

7.3.2 *Prediction of Instability in the TL and LT Direction*

Table 7.2 shows that, for the given crack length, the normalised G of a crack in the LT direction is larger than that of right-angle crack with the crack tip in the TL direction. Instability in either TL or LT direction can be determined by comparing the $G_{applied}$ (i.e. G_I for specimens SC1, 2 and 3, and G_{I+II} for specimens RAC1 and RAC2) and G_C. The comparison between $G_{applied}$ and J_C is given in Table 7.3.

In this section, the G calibrations in the previous section are used to calculate the $G_{applied}$ at the peak load of 0.2 MN in the experimental test, where instability occurred. This is done for the different crack configurations described above (see the model ref. in the first row of Table 7.3). These values are compared with appropriate values of material resistance, J_C, taken from the experimental data[36], to see if crack propagation will occur, i.e. $G_{applied} > J_C$.

Choice of the appropriate value of J_C depends on the crack length. For the straight cracks, we can use the crack extension from the start of stable cracking to enter the R-curve for the LT direction[36], and select the correct J_C for that crack length. For the right-angled cracks, we must use the TL R-curve[36], but the choice of crack length is not so clear. In Table 7.3, we have shown results for two possible crack extensions: the total crack length, including growth in both LT and TL directions, and crack growth in only the TL direction. The latter gives the lowest values of J_C, and is probably the most appropriate.

Table 7.3 Estimates of $G_{applied}$ and J_C for different crack configurations.

Models	SC1	SC2	SC3	RAC1	RAC2
$G_{applied}$[§] MN/m	0.28	0.32	0.4	0.095	0.11
J_C^+ MN/m (estimated using total crack length)	0.43	0.5	0.62	0.21	0.26
J_C^{++} MN/m (estimated using crack length only in the TL direction)				0.046	0.095

The values of estimated $G_{applied}$ in Table 7.3 are rather conservative because they are based on elastic calculations, while the experimental J_C values[36] are calculated from a summation of J_e and J_p. For SC1, $G_{applied}$ should just equal J_C (at the end of stable crack growth), but is, in fact, significantly lower. This underestimate of $G_{applied}$ should apply, in varying degrees, to all cracks. Table 7.3 shows that, for the given geometries, the crack growth in the LT direction, i.e. SC1, 2 and 3, would remain stable because $J_C > G_{applied}$ by a consistent amount (approx. 55%). For the right-angle cracks, i.e. RAC1 and RAC2, the elastic $G_{applied}$ exceeds J_C in the TL direction, resulting in instability in that direction.

The numerical result showed that the stress intensity of pure mode I fracture is larger than that of combined mode I and II. Although the estimate of applied G for the crack configuration of interest could be underestimated, it was larger than the J_C in the TL direction. The instability in the TL direction is hence proven.

§ N.B. Assumed mode I loading for specimens SC1, 2 and 3; and mode I and II loading for RAC1 and RAC2.

7.4 *Limit Load Failure*

Only one out of three fatigue tests on large CT specimens failed close to limit load, when subjected to a low cyclic load (3-30kN). The crack path in this specimen remained more or less in the LT direction. The cracks in the other two specimens, subjected to high cyclic load (6.5-65kN), failed below their limit loads, and their paths turned 90° into the TL (weaker) direction. Fracture test results on specimens with structural dimensions, particularly of the same thickness, showed that high fracture resistance retained the structural safety. The R-curve of the material increases even after 35 mm of crack extension in the LT (tougher) direction[36], Figure 7.2. Sumpter[8][36] provided a criterion based on the fatigue and fracture test results for unstable fracture. He concluded[83] that,

> 'On an empirical basis, for the data obtained so far, cracks may potentially become unstable when their stress intensity exceeds 50 MPa$\sqrt{m}$, or the cracked structure exceeds 60% of its limit load'.

Numerical results of the Y calculation showed that the values of Y reduce as the lower crack tips of the stem cracks approaches the flange (see Figure 7.4). Although fracture may not occur by a long crack in the bridge girder because of the reduced K, failure may occur due to the limit load. Limit load failure in a section results when it reaches net section yielding. As a result, the applied stress in the remaining ligament exceeds the flow stress (the average of yield stress and ultimate tensile stress). The failure can also be examined by means of applied moment.

The load capacity of a cracked bridge girder was examined using numerical results. Three of the most serious crack geometries were examined and the results showed that the limit load was reached at about 70% of yield strain. The details of the cracks in the tensile T-section are shown in Table 7.4. The force carried by the ligament, and the moment at the cracked section, were evaluated for cracks approaching the flange (crack tip to flange distance less than 10 mm). This is where the stress intensity is reduced[7], but failure may occur due to excessive plasticity in the remaining cross-sectional area. The moment is the product of total force and the distance from the neutral axis to the centroid of the cross-sectional area, where the total force acts.

Table 7.4 Details of the geometries for limit load determination.

*s/2a	2a (mm)	S (mm)	C (mm)	C/25
0.488	312.5	152.5	10	0.4
0.497	318.046	158.046	4.454	0.178
0.865	182.646	158.046	4.454	0.178

Figures 7.5 shows the numerical results for the force (F_a) on the remaining ligament and moment (M_a) at the cracked section, which are normalised by limit load (F_L) and yield moment (M_y) respectively. Limit load is the product of the cross-sectional area of the ligament and the flow stress, which is the average of yield stress and ultimate tensile stress. Flow stress is usually used for calculations which assume work hardening effects. In this case the collapse of a remaining ligament is predicted by the normalised load, i.e. $F_a/F_L=1$, see Figure 7.5.

The yield moment, M_y, is defined as the moment corresponding to first yielding at the bottom of the flange of an undamaged bridge girder. The reduction in load capacity of a damaged tensile T-section is indicated by the normalised moment, i.e. M_a/M_y, see Figure 7.5. In Figure 7.5 the normalised forces and moments are plotted against the normalised strain, i.e. the ratio of applied strain(ε) to yield strain(ε_y).

The results of different parameters corresponding to limit load failure, i.e. $F_a/F_L=1$, are shown in Table 7.5. All three damaged T-sections collapse at about $\varepsilon/\varepsilon_y=0.7$, due to the limit load failure in their remaining ligaments, whilst the load carrying capacity of the three sections is reduced by between 30% to 40%. The result shows that the longest crack between the three geometries, whose crack tip is very close to the flange, fails at the lowest $\varepsilon/\varepsilon_y$ level. The shortest crack, although its crack tip is as close to the flange as that of the longest crack in this test, can sustain a higher strain (and stress).

Table 7.5 Different parameters at limit load failure.

s/2a	$\varepsilon/\varepsilon_y$	F_a/F_L	M_a/M_y
0.488	0.69	1	0.63
0.497	0.67	1	0.61
0.865	0.77	1	0.72

* N.B. See figure 3.2 for notations.

These results imply that limit load failure may occur at $\varepsilon/\varepsilon_y \approx 70\%$ for a bridge girder containing a crack which reduces the cross-sectional area by 30% and where the crack tip is 10 mm or less from the flange. This is close to the uncracked load requirement[1] that maximum stress in the tensile chord should not exceed 75% of σ_{ys}. Taking the limiting factor as $F_a/F_L=1$ still leaves an overload margin of 10% (see Figure 7.5). A better margin is obtained by taking $F_a/F_L=0.9$, which can, for convenience, be equated to a strain, at first yield, of $\varepsilon/\varepsilon_y=0.6$ giving $M_a/M_y=0.55$. This would appear to correspond to Sumpter's suggestion, but he used the limit load of the actual cracked test specimens at failure for normalisation, corresponding to $F_a/F_L=0.6$ for the cracked bridge structure. His criterion would give a load carrying capacity of only 40% of M_y (see Figure 7.5) with a corresponding chord strain of $\varepsilon/\varepsilon_y=0.4$.

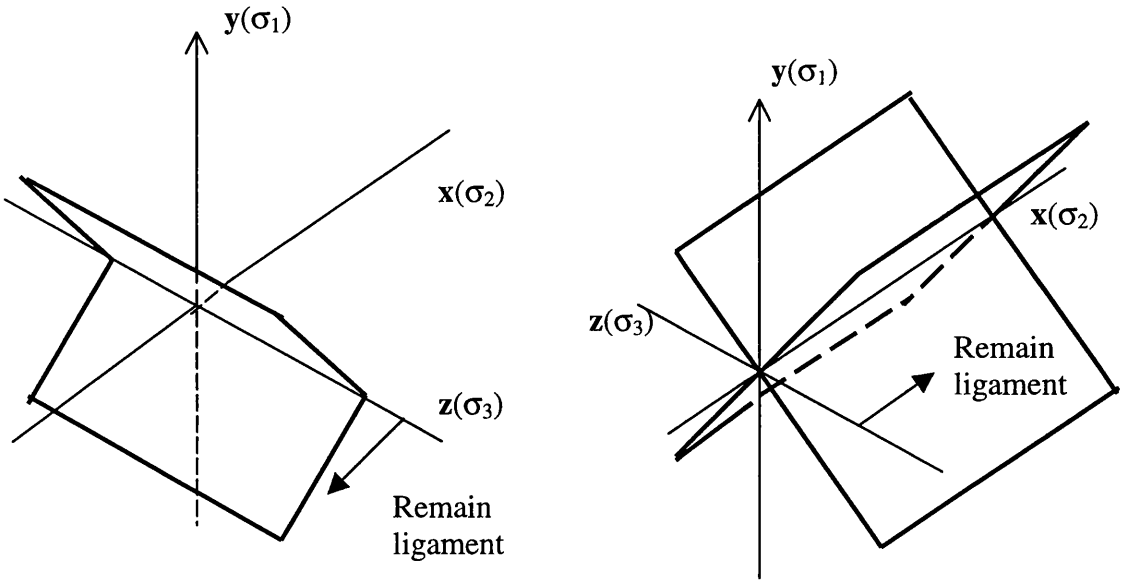

a. Plane strain conditions. b. Plane stress conditions

Figure 7.1 Planes of maximum shear stress acting at the crack tip.

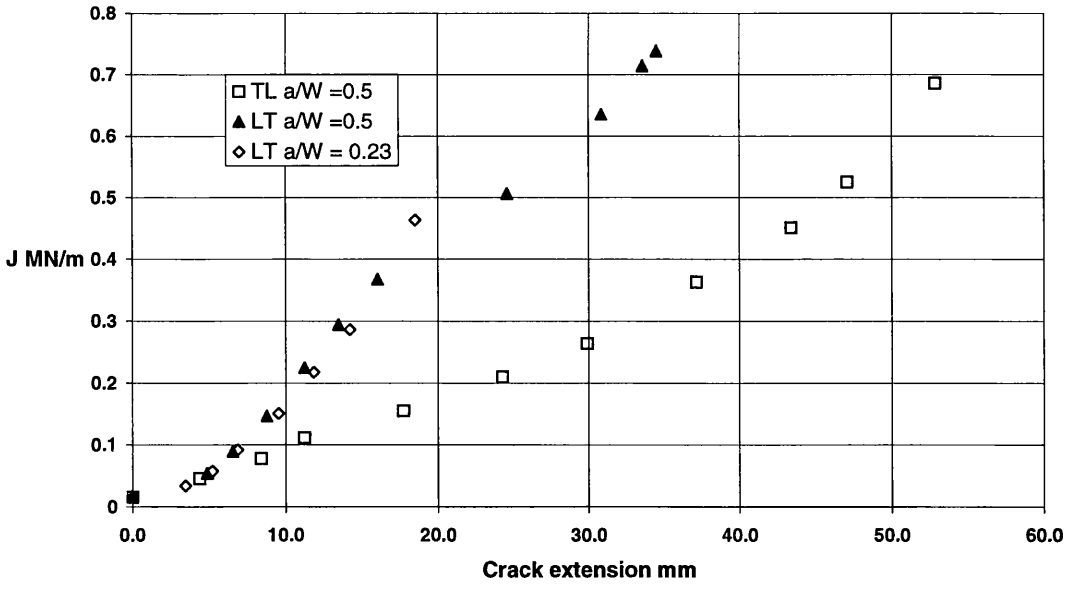

Figure 7.2 Experimental J_R curve [36] in the TL and LT directions of the bridge alloy.

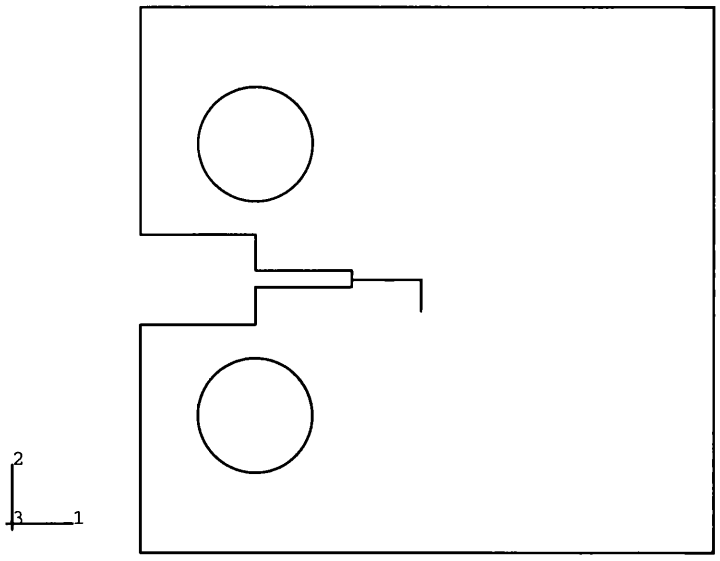

Figure 7.3 Numerical model for RAC1 and RAC2 (see Table 6.1).

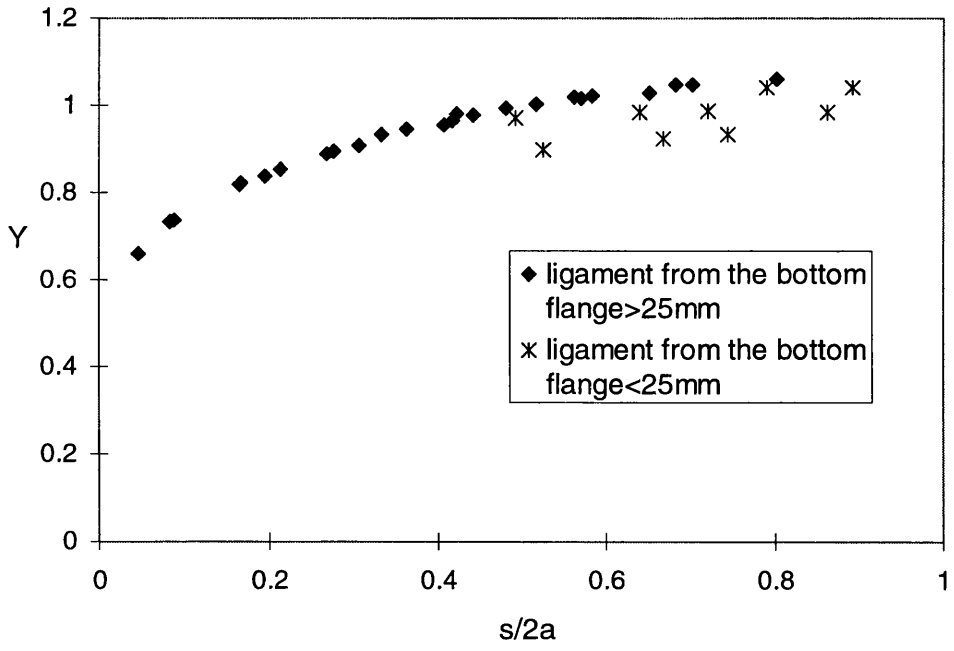

Figure 7.4 Numerical results of Y for stem cracks in the bridge girder. (See Figure 3.2 for notations)

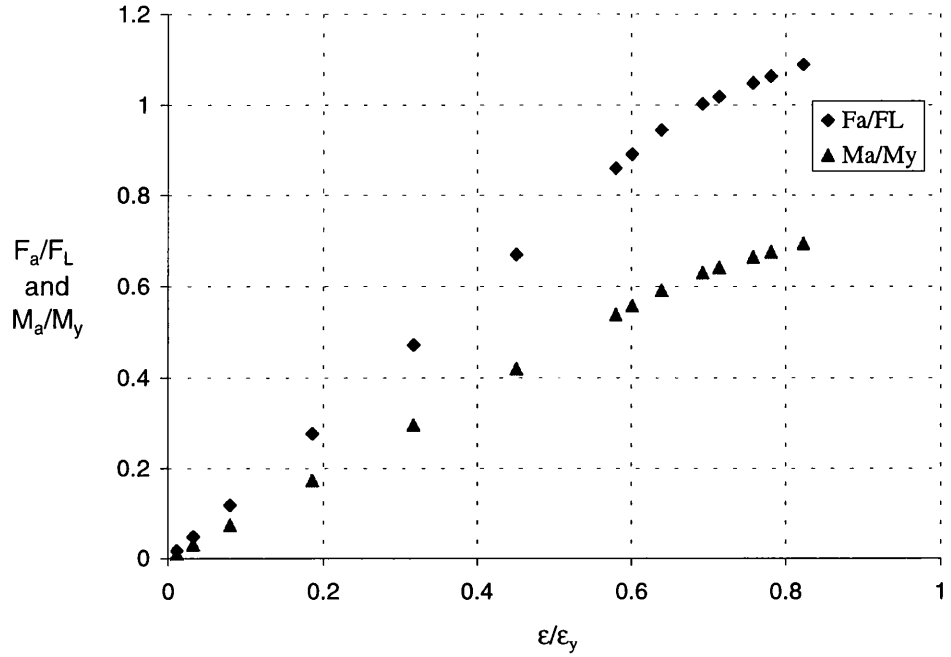

a. s/2a = 0.488

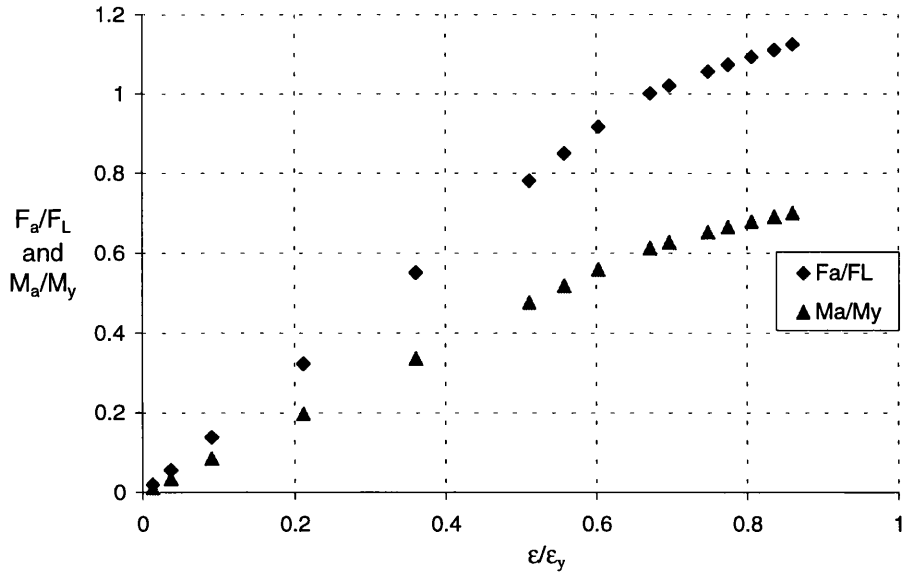

b. s/2a = 0.497

Figure 7.5 Normalised force and moment on the remaining ligament of a damaged bridge component

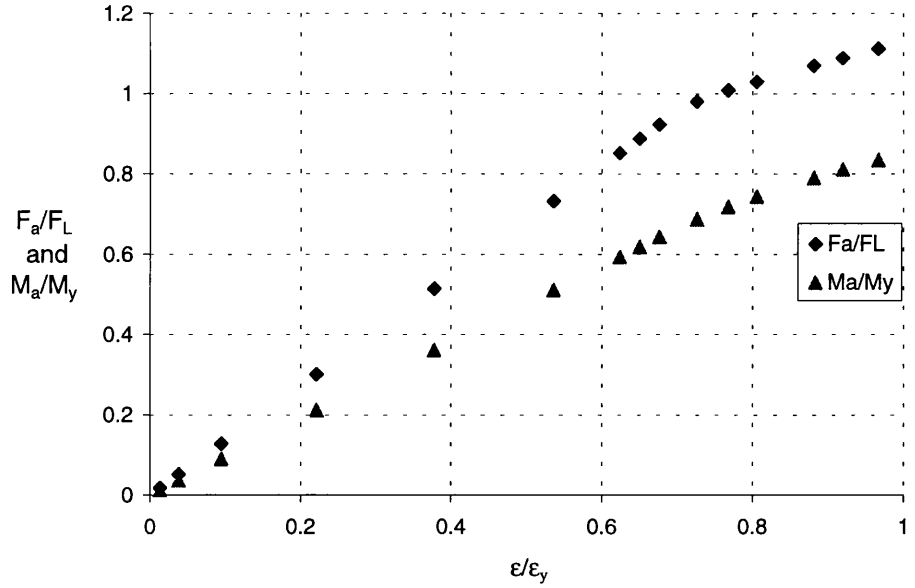

c. s/2a = 0.865

Figure 7.5(cont.) Normalised force and moment on the remaining ligament of a damaged bridge component

CHAPTER 8. A REVIEW OF APPROACHES TO DESIGN FOR FATIGUE

8.1 *Introduction*

There are two different approaches to fatigue design: total-life and damage-tolerant. The total-life approaches, based on nominally defect-free laboratory specimens, measures the combined effect of initiation and propagation. As initiation of cracks is often a much longer phase than the propagation phase, this approach effectively focuses on the resistance to fatigue crack initiation. In total-life approaches, the result of fatigue tests from uncracked specimens shows the number of fatigue cycles to initiate a dominant crack can be as high as 90% of the total fatigue life. In this case, the fatigue life assessment is characterised by the cyclic stress or strain range. In general, there are two categories in the total-life approach: high cycle fatigue, and high strain low cycle fatigue. These depend on the material behaviour under the cyclic load.

The damage-tolerant approach considers the fatigue life of a pre-existing fatigue flaw propagating to a critical size, and deals primarily with the resistance to fatigue crack growth. The fatigue life is then defined as the number of fatigue cycles to propagate the dominant crack from its initial size to some critical dimension. The prediction of crack propagation life using the damage-tolerant approach involves empirical crack growth laws based on fracture mechanics. In terms of the requirements of fracture mechanics, the damage-tolerant approach is applicable under the concept of similitude which implies that the crack tip conditions are uniquely defined by a single characterising parameter, e.g. K or J under conditions of small scale yielding.

8.2 Total-Life Approaches to Fatigue Life

The classical approach for estimating fatigue strength or cyclic life of a component using the intrinsic fatigue curve is defined by the curve obtained in the laboratory from tests on plain specimens, manufactured and polished to a high degree of accuracy, and subjected to completely reversed one-dimensional stresses. The intrinsic fatigue curve is a smoothed curve representing the fatigue data.

When loading conditions are such that only elastic strains are evident, the material behaviour is represented by Hooke's law. However, if the loading is such that local yielding occurs in the component or structure, the material behaviour is no longer linear. It therefore becomes necessary to distinguish between high strain low cycle fatigue (LCF) and high cycle fatigue (HCF). The former are usually obtained by testing specimens under conditions of constant strain (or deformation) and the latter under conditions of constant load.

8.2.1 *High Cycles Fatigue*

High cycle fatigue refers to the combinations of stress (by constant load) and cycles during which macroscopic plasticity or yielding does not occur. In the stress-life approach to fatigue, smooth (unnotched) test specimens are typically machined to provide a waisted (hour-glass) cylindrical gage length and fatigue-tested in uniaxial compression-tension or tension-tension cyclic loading. A stress amplitude-life (S-N) curve is produced from such experimental results, where the stress amplitude, $\sigma_{amp}=(\sigma_{max}-\sigma_{min})/2$, for fully reversed loading is plotted against the number of fatigue cycles to failure, N_f.

If the stress amplitude-life data is drawn on a log-log scale, with the stress amplitude plotted as a function of the number of fatigue cycles or load reversals (a constant amplitude fatigue is composed of two load reversals) to failure, a linear relationship is commonly observed. The resulting expression relating the stress amplitude, in a constant amplitude fatigue test, to the number of load reversals to failure $2N_f$ is

$$\frac{\Delta\sigma}{2}=\frac{(\sigma_{max}-\sigma_{min})}{2}=\sigma_f(2N_f)^b$$

where σ_f is the fatigue strength coefficient (which, to a good approximation, equals the true fracture strength, corrected for necking, in a monotonic tension test for most metals) and b is known as the fatigue strength exponent.

A typical S-N curve (Figure 8.1) exhibits a plateau which is known as the fatigue limit or endurance limit. Below this plateau level the specimen may be cycled indefinitely without causing failure. For many high strength steels, aluminium alloys and other materials which do not strain-age-harden, the stress amplitude continues to decrease with increasing number of

cycles. An endurance limit for such cases is defined as the stress amplitude which the specimen can support for at least 10^7 fatigue cycles.

8.2.2 High Strain Low Cycles Fatigue

Low cycle fatigue refers to the combination of strain (or deformation) and number of cycles during which considerable macroscopic plasticity occurs. In these circumstance, plastic strain energy accumulated each cycle reaches a certain critical value, at which stage a crack may form. Subsequent cycling causes the crack to propagate to critical conditions, and unstable fracture occurs. The fatigue integrity of a component is defined by the sum of the number of cycles to produce an engineering crack, which is typically 0.5mm long, and the subsequent number of cycles needed to grow that crack to some critical conditions.

It is usual to express low cycle fatigue data in terms of total strain amplitude, $\varepsilon_{amp}=(\varepsilon_{max}-\varepsilon_{min})/2$, versus the number of cycles to failure. However, since every value of total strain is made up of an elastic component and a plastic component, $\Delta\varepsilon=\Delta\varepsilon_e+\Delta\varepsilon_p$, it is possible to express cycle life in terms of either the elastic or the plastic strain component.

When the logarithm of the plastic strain amplitude, $\Delta\varepsilon_p/2 = (\varepsilon_{p\,max}-\varepsilon_{p\,min})/2$ was plotted against the logarithm of the number of load reversals to failure, $2N_f$, a linear relationship resulted for metallic materials (Figure 8.2), i.e.

$$\frac{\Delta\varepsilon_p}{2}=\varepsilon_f(2N_f)^c \qquad (8.1)$$

where ε_f is the fatigue ductility coefficient (which is found experimentally to be approximately equal to the true fracture ductility in monotonic tension) and c is the fatigue ductility exponent.

Recalling the expression for the S-N curve in log-log scale:

$$\frac{\Delta\sigma}{2}=\sigma_f(2N_f)^b$$

and noting that

$$\frac{\Delta\varepsilon_e}{2}=\frac{\Delta\sigma}{2E}=\frac{\sigma_{amp}}{E}$$

where E is the Young's modulus; it is found that

$$\frac{\Delta\varepsilon_e}{2} = \frac{\sigma_f}{E}(2N_f)^b \qquad (8.2)$$

Substituting Eqs.(8.1) and (8.2) into $\Delta\varepsilon=\Delta\varepsilon_e+\Delta\varepsilon_p$, gives

$$\frac{\Delta\varepsilon}{2} = \frac{\sigma_f}{E}(2N_f)^b + \varepsilon_f(2N_f)^c$$

In order to examine the implication of 'short' and 'long' fatigue lives, it is useful to consider a transition life, which is defined as the number of reversals to failure $(2N_f)_t$ at which the elastic and plastic strain amplitude are equal (Figure 8.2), i.e.

$$\frac{\Delta\varepsilon_p}{2} = \frac{\Delta\varepsilon_e}{2}$$

or $$\varepsilon_f(2N_f)^c = \frac{\sigma_f}{E}(2N_f)^b$$

This can be rewritten as

$$2N_f = \left(\frac{\varepsilon_f E}{\sigma_f}\right)^{\frac{1}{(b-c)}}.$$

At short fatigue lives, i.e. below the transition life, plastic strain amplitude is more dominant than the elastic strain amplitude and the fatigue life of the material is controlled by ductility. At the long fatigue lives, i.e. cycle lives in excess of the transition life, the elastic strain amplitude is more significant than the plastic strain amplitude and the fatigue life is dictated by the fracture strength.

8.3 *Fracture Mechanics (Damage-Tolerant) Approach to Fatigue Design*

Fatigue tests on notched specimens can provide information about the number of cycles needed to propagate a crack to critical conditions under the given load. If the plastic deformation is limited at the crack tip, i.e. in conditions of small scale yielding, so that the elastic stress field at the crack tip can be fully described by the elastic singularity, fatigue crack growth in such conditions can be characterised by fracture mechanics.

Fatigue of metals by the slow growth of microscopic flaws was first documented in the work of Ewing and Humfrey[57] in the early 1900s. However, the mathematical framework for the quantitative modelling of fatigue crack growth was not available until the evolution of linear

elastic fracture mechanics (LEFM) by Irwin[16]. With the advent of the LEFM approach, attempts were made to characterise the growth of fatigue cracks also in terms of the stress intensity factor. Paris, Gomez and Anderson[58] were the first to suggest that the increment of fatigue crack advance per stress cycle, da/dN, could be related to the range of the stress intensity factor, ΔK, during constant amplitude cyclic loading. With the application of fracture mechanics concepts to fatigue failure, increasingly more attention was paid to the mechanism of subcritical crack growth. Elber[59][60] showed that fatigue cracks could remain closed even when subjected to cyclic tensile loads. In the last two decades, various types of crack closure were investigated that showed that the fatigue crack growth rate is not only affected by the stress intensity factor range, but also by prior loading history and crack size.

8.3.1 *Crack Growth Relationship*

Consider a crack growing under a constant amplitude cyclic stress intensity, so that a cyclic plastic zone forms at the crack tip leaving a plastic wake behind the growing crack. If the plastic zone size is so small that the crack tip conditions are defined by elastic stress intensity, then, the crack growth (da/dN) can be characterised by the combination of applied stress intensity range(ΔK) and crack length(a), in an expression of the form

$$\frac{da}{dN} \propto \Delta K$$

Paris et al.[58][61] showed that the fatigue crack growth increment da/dN is related to the stress intensity factor range by the power law relationship

$$\frac{da}{dN} = C(\Delta K)^m$$

where C and m are material constants that are determined experimentally. The Paris law indicates that the fatigue crack growth rate for any geometry depends only on ΔK.

Paris' equation does not describe fully the relationship between da/dN and ΔK. A log-log plot of da/dN versus ΔK contains three distinct regimes. At the intermediate ΔK values the curve is linear, but the crack growth rate deviates from the linear trend at high and low ΔK levels. In the former case, the crack growth rate accelerates as K_{max} approaches K_{crit}, the fracture toughness of the material. At the other extreme, da/dN approaches zero at a threshold ΔK. The Paris law

applies to fatigue crack growth in the region of intermediate ΔK, where da/dN is insensitive to R, which is defined as

$$R \equiv \frac{K_{min}}{K_{max}}.$$

The enhanced influence of load ratio, R, at high ΔK levels is a consequence of the critical condition that the maximum stress intensity factor value for the fatigue cycle, K_{max}, approaches the fracture toughness of the material, K_{crit}:

$$K_{max} = \frac{\Delta K}{1-R} \rightarrow K_{crit}$$

Forman[62] proposed the following relationship for ΔK at intermediate and high levels:

$$\frac{da}{dN} = \frac{C\Delta K^m}{(1-R)K_{crit} - \Delta K}$$

or

$$\frac{da}{dN} = \frac{C\Delta K^{m-1}}{\frac{K_{crit}}{K_{max}} - 1}$$

Thus the crack growth rate becomes infinite as K_{max} approaches K_{crit}. Erdogan and Roberts[63][64] expressed the crack growth rate relating to the size of the plastic zone, ahead of and in the plane of a propagating crack, by the following equation,

$$\frac{da}{dN} = C(K_{max})^p(\Delta K)^q$$

where C is a material constant and p and q are numerical exponents.

It is argued[65] that there is a significant difference in fatigue crack propagation rates for plane stress and plane strain. Roberts and Kibler[66] modified the Forman equation to incorporate the ideas of Erdogan and Roberts relating to the size of the plastic zone. They have proposed a relationship which, when simplified for plane extension, gives,

$$\frac{da}{dN} = \frac{CK_{max}}{K_{crit} - K_{max}}\Delta K^2$$

Although each of above models are applicable for the particular set of conditions for which they were derived, they each lack generality and not one of them incorporates the conditions of threshold, which defines the ΔK value below which fatigue crack growth does not occur.

A number of equations attempt to describe the entire crack growth curve, taking account of both the threshold and K_{crit}. For example, Priddle proposed the following empirical relationship:

$$\frac{da}{dN} = C\left(\frac{\Delta K - \Delta K_{thre}}{K_{crit} - K_{max}}\right)^m .$$

Duggan[65][67] developed a mathematical model based upon the damage which accumulates at the crack tip as a result of the irreversible process associated with plasticity. Further, the analysis recognises the resistance to fatigue crack propagation caused by prior cyclic loading and the possible existence of basic threshold levels. The original model is written as

$$\frac{da}{dN} = \left(\frac{\pi}{32}\right)^{\frac{1}{2\alpha}} \frac{1}{\alpha}\left\{\frac{2}{\varepsilon_f E(K_{crit} - K_{max})}\left[\left(1+\frac{\Delta K_{thre}}{K_{crit}}\right) - \left(\frac{\Delta K}{K_{crit}} + \frac{\Delta K_{thre}}{\Delta K}\right)\right]\right\}^{\frac{1}{\alpha}} \Delta K^{\frac{2}{\alpha}} \qquad (8.3)$$

where α is the fatigue ductility exponent; ε_f is the fatigue ductility coefficient; E is the Young's modulus; K_{crit} is the critical stress intensity factor (fracture toughness); and ΔK_{thre} is the threshold stress intensity range. If $\Delta K_{thre}/\Delta K$ is small compared with unity and $\Delta K/K_{crit}$, which it might be for practical values of ΔK, Eq.(8.3) reduces to (for zero stress ratio)

$$\frac{da}{dN} = \left(\frac{\pi}{32}\right)^{\frac{1}{2\alpha}} \frac{1}{\alpha}\left(\frac{2}{\varepsilon_f E K_{crit}}\right)^{\frac{1}{\alpha}} \Delta K^{\frac{2}{\alpha}}$$

McEvily[68] developed another equation that can be fitted to the entire crack growth curve:

$$\frac{da}{dN} = C(\Delta K - \Delta K_{thre})^2\left(1+\frac{\Delta K}{K_{crit} - K_{max}}\right)$$

The McEvily equation is based on a simple physical model rather than a purely empirical fit.

With the somewhat confusing and even contradictory array of crack growth relationships, it is important to be able to select one to meet the needs of the fracture analyst.

In practice, integrating the Paris law will give the number of cycles for crack growth, from its initial length to the critical length. This can be complicated because the stress intensity factor, K, hence Y, is usually a function of crack length. It may be simplified by assuming a constant value for Y during fatigue crack propagation.

8.3.2 *Retardation of Fatigue Crack Growth*

Elber[59] noticed an anomaly in the elastic compliance of thin sheets of cracked aluminium alloy. At low loads (which were low but greater than zero), the displacement/load compliance was close to that of uncracked specimens. At high loads, the gradient of the compliance is less steep than was expected from fracture mechanics analysis. Elber believed that the anomaly in compliance was due to the contact between crack surfaces (i.e. crack closure) at low loads. Crack closure decreased the fatigue crack growth rate by reducing the effective stress intensity range.

Consider a growing crack in the presence of a constant amplitude cycle stress intensity. A cyclic plastic zone forms at the crack tip, and the growing crack leaves behind a plastic wake. Elber[59] argued that crack closure resulted from residual tensile deformation in the plastic wake. Elber's work also brought to light the very dependence of fatigue crack growth rates on prior history. Other types of crack closure phenomena have been noticed in other experimental observations. For instance the microscopic roughness of the fatigue fracture surface results in roughness-induced crack closure. Plasticity-induced crack closure is likely to affect the bridge components. Models for this effect, in terms of K_{eff}, will be discussed as follow.

Elber[59] assumed that the portion of the cycle where the crack faces are in contact (below K_{op}, the stress intensity at which the crack opens), does not contribute to fatigue crack growth. He defined an effective stress intensity factor range, ΔK_{eff}, which is responsible for crack growth, as

$$\Delta K_{eff} \equiv K_{max} - K_{op}$$

He also introduced an effective stress intensity ratio for $K_{min} < K_{op}$:

$$U \equiv \frac{\Delta K_{eff}}{\Delta K} = \frac{K_{max} - K_{op}}{K_{max} - K_{min}} \qquad (8.4)$$

When $K_{min} \geq K_{op}$, U=1, and closure does not occur.

Elber then proposed a modified Paris law,

$$\frac{da}{dN} = C(\Delta K_{eff})^m = C(U\Delta K)^m$$

Assuming the opening stress intensity factor, K_{op}, is a material constant, i.e. it is independent of K_{min}, K_{max} and prior history, rewriting Eq.(8.4) in terms of ΔK and R gives

$$U = \frac{1}{1-R} - \frac{K_{op}}{\Delta K}.$$

If there is no intrinsic ΔK_{thre} for the material and da/dN>0, the threshold can be inferred by setting U=0:

$$\Delta K_{thre} = K_{op}(1-R),$$

which applies to the range of ΔK between:

$$K_{op}(1-R) \le \Delta K \le K_{op}\left(\frac{1}{R} - 1\right)$$

Elber measured the closure stress intensity in 2023-T3 aluminium alloy fatigue test (under predominantly plane stress conditions) over a ΔK range of 13 to 40 MPa$\sqrt{m}$ and for variations in load ratio ($-0.1 \le R \le 0.7$), obtaining the following empirical relationship:

$$U = 0.5 + 0.4R$$

or

$$\frac{K_{op}}{K_{max}} = 0.5 + 0.1R + 0.4R^2$$

Elber's equation implies that U depends only on the R ratio.

Shih and Wei[69][70] replotted the experimental data of earlier researchers which showed a definite K_{max} dependence. Hudak and Davidson[71] performed closure measurements on a 7091 aluminium alloy and 304 stainless steel over a wide range of loading variables, for both materials, obtaining a closure relationship of the form:

$$U = 1 - \frac{K_0}{K_{max}} \qquad (8.5a)$$

or

$$U = 1 - \frac{K_0(1-R)}{\Delta K} \qquad (8.5b)$$

Substituting Eq.(8.4) into Eq.(8.5) gives:

$$K_{op} = K_0(1-R) + K_{max}R$$

$$K_{op} = K_0(1-R) + \frac{\Delta K R}{1-R}$$

Thus K_0 is the opening stress intensity for R=0. It is also recognised that, in addition to its dependence on R, U is strongly influenced by the specimen geometry, the stress state, the stress intensity factor range and environment.

8.3.3 *Effective Stress Intensity Factor*

Using experimental results[72][73], the R dependence of da/dN versus ΔK curves can be rationalised by presenting da/dN against ΔK_{eff}, which is the effective stress intensity factor range.

As the effective stress intensity factor is the reduced stress intensity factor resulting from the effect of plasticity-induced closure, it can be estimated using crack tip plasticity analysis. Dugdale's model[74] for the plastic zone size approximates elastic-plastic behaviour by superimposing two elastic solutions: a through crack under remote tension and a through crack with closure stresses at the tip. The model is based on a long, slender plastic zone at the crack tip in a non-hardening material in plane stress. The stress intensity factor resulting from the closure stresses can be expressed:

$$K_{closure} = -2\sigma_{ys}\sqrt{\frac{a+r_p}{\pi}}\cos^{-1}\left(\frac{a}{a+r_p}\right)$$

where r_p is the long, slender plastic zone ahead of the crack tip. The stress intensity factor due to the remote tensile stress, $K=\sigma\sqrt{\pi(a+r_p)}$, must balance with $K_{closure}$, i.e. $K+K_{closure}=0$. Therefore,

$$\frac{a}{a+r_p} = \cos\left(\frac{\pi\sigma}{2\sigma_{ys}}\right)$$

or

$$a\left[\sec\left(\frac{\pi\sigma}{2\sigma_{ys}}\right)-1\right] = r_p .$$

Using Dugdale's model with $\sigma \ll \sigma_{ys}$, and setting the effective crack length equal to $a+r_p$, where r_p is given by the above equation, gives the effective stress intensity factor as[40]:

$$K_{eff} = \sigma\sqrt{\pi a \sec\left(\frac{\pi\sigma}{2\sigma_{ys}}\right)}$$

This is an overestimate, and Burdekin and Stone[75] obtained a more accurate estimate of K_{eff}, giving:

$$K_{eff} = \sigma_{ys}\sqrt{\pi a}\left[\frac{8}{\pi^2} ln\sec\left(\frac{\pi\sigma}{2\sigma_{ys}}\right)\right]^{\frac{1}{2}}$$

Budiansky and Hutchinson[76] provided a comprehensive analysis based on Dugdale's model for using ΔK_{eff} to characterise fatigue crack growth under plasticity-induced crack closure. Although their quantitative predictions do not agree with experimental data[71], this model is useful for demonstrating qualitatively the effect of plasticity on crack closure.

8.3.4 *J Integral for Crack Growth Relationship*

The elastic singularity disappears when there is excessive plasticity at the crack tip, and K characterisation is no longer valid, but J is still an appropriate fracture parameter under certain assumptions. The J integral theory breaks down when the plasticity is significant compared to the in-plane dimensions. Although the J integral applies to nonlinear elastic material i.e. deformation plasticity is employed which assumes no cyclic loading in the material, Dowling and Begley[77] and Lambert et al.[78] successfully correlated ΔJ and experimental data of fatigue crack growth under large scale yielding. In this case, the crack growth relationship was expressed as

$$\frac{da}{dN} = C(\Delta J)^m,$$

where ΔJ is a contour integral for cyclic loading, but $\Delta J \neq J_{max} - J_{min}$. If a material deformation is characterised by $\Delta\sigma_{ij}$ and $\Delta\varepsilon_{ij}$, so that the stresses and strains have initial values σ_{ij}^1 and ε_{ij}^1 and increase to σ_{ij}^2 and ε_{ij}^2, a contour integral around crack tip can be defined as

$$\Delta J = \int_{\Gamma} \left(\Omega(\Delta\varepsilon_{ij})dy - \Delta T_i \frac{\partial \Delta u_i}{\partial x} ds \right)$$

where Γ defines the integration path around the crack tip (Figure 2.5), and ΔT_i and Δu_i are the changes in traction and displacement between points 1 and 2. The quantity Ω is analogous to the strain energy density:

$$\Omega(\varepsilon_V) = \int_0^{\Delta\varepsilon_V} \Delta\sigma_{ij} d(\Delta\varepsilon_{ij})$$

The Ω represents the stress work per unit volume performed during loading, rather than the stress work in a complete cycle, i.e. the area inside the hysteresis loop (see Figure 8.4). If $\sigma_{ij}^1 = \varepsilon_{ij}^1 = 0$, $\Delta J = J$. Thus ΔJ is merely a generalisation of the J integral. If the cyclic stress-strain curve forms a closed loop (Figure 8.4) and the loading and unloading branches are symmetric,

the ΔJ can be defined from the loading and unloading branch. For a given ΔK_I, assuming small scale yielding, ΔJ is defined as

$$\Delta J = \frac{\Delta K_I^2}{E}$$

for plane stress conditions.

8.4 *Assessing Crack Propagation Life*

Since $\Delta K = Y\Delta\sigma\sqrt{\pi a}$, the Paris law can be written

$$\frac{da}{dN} = C\left(Y\Delta\sigma\sqrt{\pi a}\right)^m$$

The number of cycles for a crack growing from an assumed initial size, a_0, to the critical size, a_f, is calculated by integrating the crack growth law, where the applied far field cyclic stresses and geometrical factor Y are assumed constant over the crack propagation

$$\int_{N_1}^{N_2} dN = \frac{1}{CY^m(\Delta\sigma)^m\sqrt{\pi}^m}\int_{a_0}^{a_f}\frac{da}{a^{m/2}}$$

therefore

$$N_f = \frac{2}{(m-2)CY^m(\Delta\sigma)^m\sqrt{\pi}^m}\left\{\frac{1}{a_0^{(m-2)/2}} - \frac{1}{a_f^{(m-2)/2}}\right\}. \qquad (8.6)$$

It is noticed that for $a_0 \ll a_f$, the effect of a_0 on N_f is larger than that of a_f. If the material constants C and m are known or estimated from existing test data for aluminium alloy, N_f can be expressed as a function of stress range $\Delta\sigma$ using Eq.(8.6). In this case, this relationship of $\Delta\sigma$ and N_f can be illustrated in a S–N curve.

8.5 *Design for Fatigue in Aluminium Structures*

A guide to the design for fatigue in aluminium alloy is provided in section 7 of BS 8118[79]. The fatigue failure criterion uses S-N curves. For variable amplitude loading, the summation of all cycles in different stress ranges, using the Miner-Palmgren cumulative law, should not exceed unity.

The classification of details, which depends on the positions of flaws, is given in the document. For constant amplitude loading, the number of fatigue cycles to failure is predicted using a S-N curve corresponding to the classification of the detail. For variable amplitude loading, the stress history at the detail (containing a flaw) is estimated, reduced to an equivalent number of cycles (n) for an equivalent constant stress range (f_r), and then the predicted number of cycles (N) are given by a S-N curve corresponding to the detail. The fatigue design is achieved provided that the summation of n_i/N_i is not greater than unity. In case of $\Sigma(n_i/N_i)>1$, the stress ranges at the detail are reduced.

The S-N curve in BS 8118[79] is described by an equation of the form $\Delta\sigma^b N=A$, and constants A and b provided in the document are computed in such a way to gives 97.5% probability of survival. Constants A and b are factors dependent upon material properties and the stress concentration due to the geometry. BS 8118 gives values of b of between 3 to 4.6, depending on different detail classification, for a range of commercial aluminium alloys, assuming that all alloys have similar fatigue behaviour. For a loading spectrum with occasional overload which can reduce the value of the non-propagation stress range, a more appropriate but less conservative S-N curve could be applied. The modified curve was obtained by altering the gradient from 1/b to 1/(b+2) at $N=5\times10^6$ to 10^8 cycles.

In the draft of Structural Eurocode 9[80] part 2 a layout of fatigue design for aluminium structures is provided. It has common features with BS 8118, although failure assessment for fracture, using the basis of Paris law, is also suggested in cases of structures sustained beyond the predicted service life. For simplicity, the line relation of the Paris law is assumed by

$$\frac{da}{dN} = A(\Delta K)^m.$$

If ΔK has the following form $\Delta K=Y\Delta\sigma\sqrt{a}$, the number of cycles for crack growth from an initial length, a_0, to the critical length, a_f, can be obtained by integrating the Paris law, hence

$$N = \frac{a_f^n - a_0^n}{C\Delta\sigma^m}$$

where $n = -(m-2)/2$ and $C=nAY^m$ for a_0 to a_f.

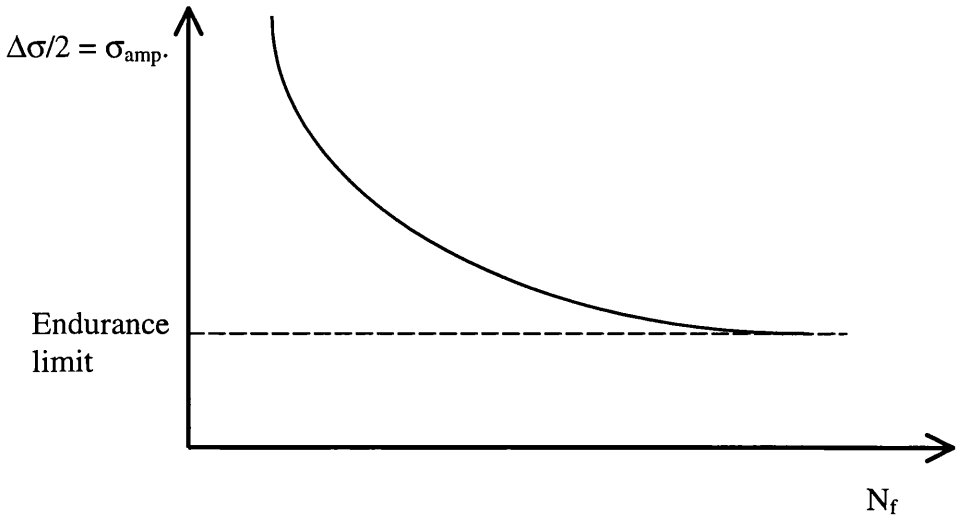

Figure 8.1 Typical S-N curve.

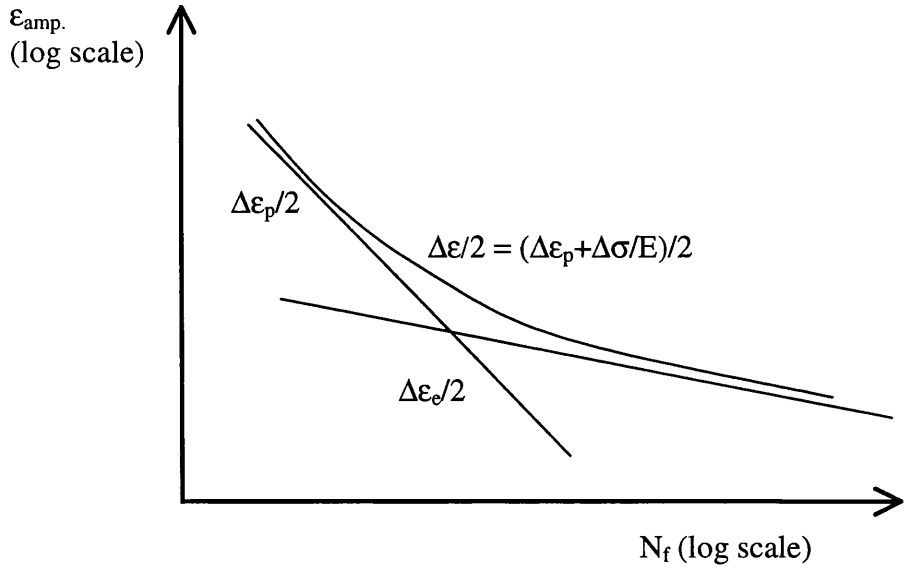

Figure 8.2 A low cycle fatigue curve and the transition life.

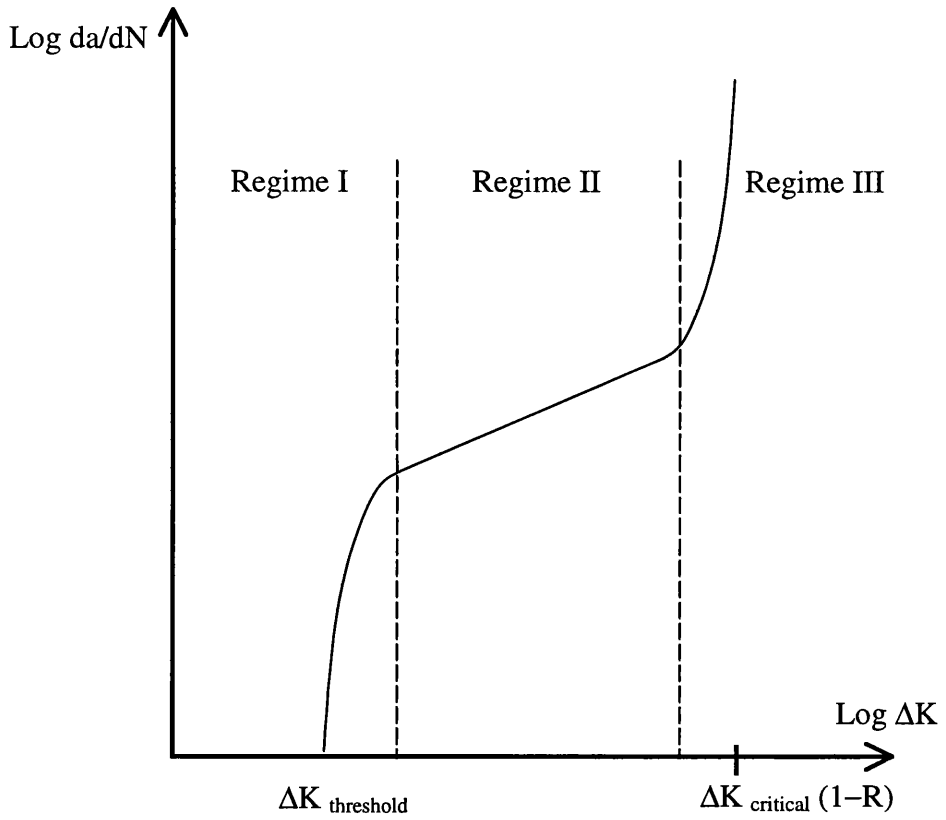

Figure 8.3 Schematic da/dN versus ΔK.

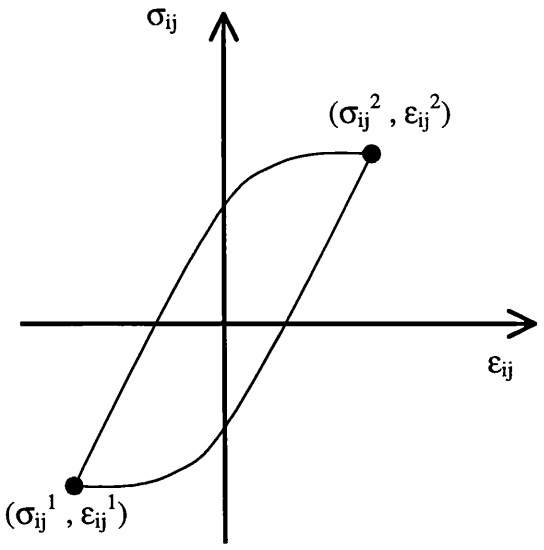

Figure8.4 Schematic cyclic stress-strain behaviour ahead of a growing fatigue crack.

CHAPTER 9. CRACK GROWTH RELATIONSHIP FOR BRIDGE ALLOYS

9.1 *Aluminium Alloy for Christchurch Bridge Fabrication*

The aluminium alloy used for the Christchurch bridge fabrication is similar to 7019 in accordance with the international 4-digit classification system. It is one of the medium strength 7*** series. This heat-treatable alloy contains 4-5% of Zn and 1.0-1.8% of Mg and is readily weldable.

Table 9.1 Fatigue crack growth rate for aluminium bridge alloy.

Author	Test Method	Size of Specimen (mm)	R ratios	Crack growth model	Value of m	Values of C
Maddox and Webber	CCT	162(W)× 9.5(B)	–2 to +0.5	da/dN= $C(U\Delta K)^m$ ΔK in $N/mm^{3/2}$	3	1.08×10^{-11}
Webber (used the result from item 1)	CCT	162(W)× 9.5(B)	–2 to +0.5	da/dN= $C(\Delta K)^m$ ΔK in $MPa\sqrt{m}$	Upper band: 4.77 Lower band: 3.06	Upper band: 1.43×10^{-8} Lower band: 3.38×10^{-7}
Butler and Tutty	3PB	75(W)× 25(B) 150(W)× 25(B)		da/dN= $C(\Delta K)^m$ ΔK in $N/mm^{3/2}$	3 to 4 2.03 to 2.48	2.3 to 6.16×10^{-15} 1.6 to 2.3×10^{-10}
Stow and Webber		Cracks in bridge prototype		da/dN= $C(\Delta K)^m$ ΔK in $N/mm^{3/2}$	Flange cracks: 2.06 Stem cracks: 1.70	Flange cracks: 3×10^{-9} Stem cracks: 1.47×10^{-7}
Sumpter	CT: tension:	CT: 150(W)× 24.5(B) tension: 175(W)× 23aver.(B)× 1000(L)	0.1 (CT) or 0.04 (tension)	da/dN= $C(\Delta K)^m$ ΔK in $MPa\sqrt{m}$	3.7414	2.756×10^{-8}

Fatigue test results for the material have been reported, although some of the tests were carried out on prototype alloys, namely DGFVE 232 and BA 733C, in the early stage of the bridge design. The fatigue crack growth rate of the alloy, namely the constants C and m in the Paris law, from these test results (see Table 9.1) are discussed in the following section.

9.1.1 *Crack Growth Rate of DGFVE 232 alloy*

Maddox and Webber[9] studied the fatigue crack growth of DGFVE 232 alloy by fatigue testing centre-notched plates with a thickness of 9.5 mm. Tests were carried out with a variety of R ($=\sigma_{min}/\sigma_{max}$) values, from –2 to +0.5. Maddox and Webber[9] showed that less scatter occurred using $\Delta K_{eff}=U\Delta K$, than presented using only the Paris law and Forman's equation, see section 7.3.1. They stated that U as the factor of ΔK for ΔK_{eff} was a function of R, and gave $U=0.4R+0.72$ for their test data. Although the value of the exponent (m) for ΔK_{eff} in the crack growth law was not evaluated from the data, they suggested that m=3 was a reasonable value for representing the crack growth rate, from which they computed the constant C. The constants C were

1.7×10^{-11} for the upper limit of the scatterband;

6.9×10^{-12} for the lower limit of the scatterband;

and 1.08×10^{-11} for the average.

Webber[1] reported the exponent (m) on ΔK for the Paris law as:

$$da/dN = 1.428\times10^{-8}\Delta K^{4.771}$$

$$da/dN = 3.384\times10^{-7}\Delta K^{3.056}$$

where da/dN was in mm/cycle and ΔK was in MPa$\sqrt{m}$, and the knee in the da/dN curve is at $\Delta K=6.3$MPa$\sqrt{m}$. The evaluation was based on data reported in reference [9].

Butler and Tutty[10] conducted a series of fatigue tests on test specimens taken from rolled plate and T boom extrusions of DGFVE 232 alloy. The tests included pin jointed tensile tests, cyclic tensile tests on compact tension specimens and beam bending tests. Rolled plate specimens were tested mainly in compact tension, while specimens from T boom extrusions were used for beam bending tests. Butler and Tutty computed m and C for the Paris law using the data from beam bending tests, which tested two types of specimen with depths of 75 mm and 150 mm.

For specimens 75 mm deep × 25 mm thick, m varied from 2.87 to 3.90 for different gross σ_{max} and with specimens taken from different positions on the extruded T boom. The average of this group was 3.33. The results showed m increasing with increasing σ_{max}.

For specimens 150 mm deep × 25 mm thick × over 600 mm long extruded rectangular bar, m varied from 2.04 to 2.80, while specimens of 150 mm deep rectangular section taken from the T boom stem showed that m varied between 1.91 and 2.17. The average was 2.48 for the former group and 2.03 for the latter group.

The results showed that the larger beam specimens gave lower values of m. Butler and Tutty suggested that the result from the larger specimens was the most appropriate for representing the behaviour of the large structural member. They stated that the most realistic mean line for cracks growing through the T boom stem in the long transverse grain direction was the crack growth law with the exponent m=2.5 on ΔK, which gave $C=1.42\times10^{-10}$ at da/dN=0.0045mm/cycle.

9.1.2 *Crack Growth Rate of BA 733C Alloy*

Richardson[11] conducted a series of fatigue tests to demonstrate the crack growth and fracture behaviour of BA 733C alloy, which contains 4.45% of Zn and 1.38% of Mg. Tests were carried out on compact tension and centre-cracked specimens. Specimens had a thickness of 6.5 mm, which did not produce a valid evaluation of K_{IC} in BS 7448[29]. Tests were done for various values of R and $\Delta\sigma$: R varied from 0.1 to 0.5 and gross σ_{max} varied from 17.95 to 44.42 MN/m^2.

Richardson reported that the exponent m on ΔK for the Paris law varied with R. The m values varied from 1.873 to 5.124 on longitudinal specimens and from 1.971 to 4.308 on transverse specimens. The crack growth rate was reproduced from the test data in an attempt to investigate the effect of different crack growth laws. The results showed that m values were inconsistent and, in most cases of test data for the same R values, m increased by over 30% with decreasing gross $\Delta\sigma$. Although tests were done for various R and $\Delta\sigma$, there was no solid conclusion for the variation of m due to R and $\Delta\sigma$.

In an attempt to relate the discrepancy of m with the variations in R, the writer represented the crack growth data (da/dN) in terms of ΔK_{eff}, where $\Delta K_{eff}=U\Delta K$ and $U=0.4R+0.72$ from Maddox[9], and $[(1-R)K_{IC}-\Delta K](da/dN)$ versus ΔK. By applying these conditions the scatterband of the crack growth data was reduced only slightly and the scatter in m was essentially unchanged.

From further examination of Richardson's data, the writer found a link between the exponent m for the Paris law and R, hence $\Delta\sigma$. The linear relationships between m and $\Delta\sigma$ can be written as:

$$m = 6.8846-0.0904(\Delta\sigma) \qquad (9.1)$$

for the case when R=0.1. This equation was taken for the calculation because it gave the most conservative values of m among the data. The constant in Eq.(9.1) is hence correlated with R. The relationship between m and R, which has the form:

$$m = 15.31R^2-13.587R+5.3647$$

The value of m is 4.1591 when R=0.1. Since the constant in Eq.(9.1) varies with R, this equation can be rewritten as:

$$m = \{2.7255+(15.31R^2-13.587R+5.3647)-0.0904(\Delta\sigma)$$

or $$m = 15.31R^2-13.587R-0.0904(\Delta\sigma)+8.09 \qquad (9.2)$$

for $0.1\leq R\leq 0.5$ and $\Delta\sigma<60$MPa.

Table 9.2 Comparison of m between estimation and Richardson's data

	$\Delta\sigma$=29.61MPa		$\Delta\sigma$=44.41MPa	
R	Equation 9.2	Richardson	Equation 9.2	Richardson
0.1	4.16	4.207	2.82	2.848
0.2	3.26	3.130	1.92	1.823
0.3	2.67	2.704	1.33	3.05*
0.5	2.4	2.382		

* Richardson's data for R=0.3 is inconsistent compared to the trend, as m reduces with increasing R.

The estimation of m using equation 9.2 agreed well with Richardson's data, see Table 9.2, but this equation should not be extrapolated outside the limits quoted above.

9.1.3 *Full Scale Fatigue Tests on Christchurch Bridge*

Stow[81] reported the crack growth data from fatigue tests which were carried out by Webber on panels of the Christchurch bridge which were ballistically damaged. The crack growth data was studied using the Paris law.

The calculation of crack growth relationship requires accurate ΔK values. Because of the complex crack shapes generally found on the bridge girder resulting from the ballistic test, only data for three fatigue crack (a flange crack and two stem cracks), whose K values could be calculated using Henry's[3] and Cheung's[7] solutions, were examined. The crack growth relationships are shown in Figure 9.1. The values of m for the first two cases were 2.063 and 1.702 for flange and stem cracks respectively, see Figures 9.1a and 9.1b. These values are lower than those quoted by Maddox[9] and Butler[10], see Table 9.1.

The solution of ΔK for the stem crack was based on the numerical results of a cross-section (for the initial design) whose thickness is larger than that in the experimental test. On the other hand, the numerical model of the bridge girder did not contain cross-bracing, which is added into the latest design. The difference between the configurations might cause an inaccuracy in the calculated ΔK and hence the crack growth rate.

The results for the flange crack, Figure 9.1a, were limited to propagation in the flange only, as K solutions were not available for the crack penetrating through the stem.

9.1.4 *Crack Growth Rate of Large Test specimens*

Sumpter[8][12] conducted a series of fatigue tests to investigate the crack growth rate for applied stress above K_{IC}. Four CT specimens and one tension specimen were fatigue tested for crack growth rate in the extrusion direction (TL) and in the direction normal to the extrusion direction (LT). Published K calculations for the tension specimen were not appropriate for this analysis because of its length (1.32 m) and fixed grips loading. The writer carried out a 2-D finite element analysis to provide an accurate calculation (see Appendix C.).

One of the objectives of the tests was to determine whether the critical crack length is dictated by plastic limit load failure. Large CT specimens (i.e. W>>B) were used in the fatigue tests because results from plane strain fracture tests (for plane strain fracture toughness) were too conservative. In the large specimens, the through thickness constraints ahead of a crack tip should be similar to those of structural dimensions. The test results showed that cracks sometimes failed by turning to the weaker direction (TL) of the material, see section 6.3. No clear link between the critical crack length and limit load failure was observed. The results provided fatigue crack growth rate for the transition of crack tip conditions from plane strain to plane stress, although the cause of the transition could not be substantiated from the results.

Figure 9.2 shows that the crack growth rate for CT specimens in both orientations rises at $\Delta K>35MPa\sqrt{m}$ (the plane strain K_{IC} for the material). The change of the crack growth rate of the TL direction is more noticeable than that in the LT direction. No conclusion was drawn for the rapid increase of the crack growth rate in the TL direction, but Sumpter[83][84] noticed that the fracture surface of the crack growth in the TL direction maintained an element of flat fracture, while that in the LT direction was slant. Sumpter[83][84] showed that, at the same load ratio (i.e. load to limit load), the driving force in the displacement control (fracture) test was higher than that in the load control (fatigue) test, where final failure was unstable.

The crack growth rate of the tension specimen rises at $\Delta K>50MPa\sqrt{m}$, see Figure 9.3. The increase of the growth rate between CT and tension specimens was the result of the elevation of K_{IC} in the tension specimen due to the T stress effect[82]. The large tension specimen was a low constraint geometry, and finite element computation (see Appendix C) showed that, for a crack length of 41mm, the T-stress raised the value of K_{IC} from 35 to $48MPa\sqrt{m}$. When $\Delta K<50MPa\sqrt{m}$ the crack growth rate in this specimen was slightly lower than the CT specimen, but when it exceeded this value, there was a distinct jump in the fatigue crack growth rate. Sumpter[12] showed that the test on the large tension specimen reached a higher stress intensity (Figure 9.4) before failure than any of the CT specimens in the fatigue test.

Sumpter[83][84] suggested values of C and m for the Paris law based on the fatigue test results (excluding the crack growth data for the TL specimen at $\Delta K>K_{IC}$), the crack growth relationship is as follow,

$$da/dN=2.76\times10^{-8}(\Delta K)^{3.7414},$$

where da/dN is in mm/cycle and ΔK is in MPa$\sqrt{m}$.

9.2 *Repetitive Crack Extension Under Excessive K_{max}*

The relationship between fatigue crack growth rate and fracture mechanics is given by the Paris law. Crack growth rate is successfully characterised by the range of stress intensity factors, either by ΔK or ΔJ, where $\Delta J=(K_{max}^2+K_{min}^2-2K_{max}K_{min})/E$. In the case of the Christchurch bridge, the tearing resistance increases with crack extension. Using the R-curve approach for fracture assessment, the crack grows only if the applied driving force, or G, exceeds the tearing resistance corresponding to the crack length.

Fatigue life can be characterised by the number of load cycles, either in high cycle or high strain, low cycle, fatigue. Low cycle fatigue, in general, applies to a component where damage is detected. Crack growth in low cycle fatigue is perhaps governed by the fracture mechanism, i.e. void nucleation, void growth and void coalescence, controlled by the tearing resistance. This would explain the increase in surface roughness observed by Sumpter for fatigue at high ΔK compared to the smooth surface for low ΔK[8].

For material exhibiting a rising R-curve, and tested for crack growth in low cycle fatigue, a high cyclic load producing $K_{max}>K_R$ would be expected to cause the crack to grow continuously until K_{max} reaches a new value of K_R, following the previous crack arrest. Although fatigue cycles of constant applied load may not cause K_{max} to exceed the K_R where the crack arrested previously, continuation of stable crack propagation at $K_{max}>K_R$ can be helped by the increased local damage produced by cyclic loading.

For repetitive crack growth at $K_{max}>K_R$, a simple model is proposed using a cyclic R-curve approach (Figure 9.5) to explain fatigue crack growth under constant cyclic load.

9.2.1 *Estimation of Repetitive Crack Extension*

A J_R curve (Figure 9.5) can be defined as

$$J_{Ri} = f(\Delta a)$$

where J_{Ri} = the J resistance at i th iteration ($J_R=K_R^2/E$) for ΔN cycles.

Hence,

$$J_{R(i+1)} - J_{Ri} = \alpha(\Delta a),$$

Where $J_{R(i+1)}$ = the J resistance at i+Δa iteration (ΔN cycles),

J_{Ri} = the J resistance at i th iteration (ΔN cycles),

α = the ratio of dJ/da,

Δa = the crack extension.

Replacing $J_{R(i+1)}$, by applied J, $J_{(i+1)}$, and substituting $J=K^2/E$ into the above equation, we can rewrite it as

$$K_{i+1}^2 - K_R^2 = E\alpha(\Delta a) \qquad \text{for cycles.}$$

For $K=Y\sigma_{applied}\sqrt{(\pi a)}$,

$$(\sigma_{applied}Y)^2\pi(a_i+\Delta a) - K_{Ri}^2 = E\alpha(\Delta a).$$

Rearrange the 3rd equation to solve for Δa, gives

$$\Delta a = \frac{K_i^2 - K_{Ri}^2}{E\alpha - K_i^2/a_i} \qquad \text{for } \Delta N \text{ cycles.}$$

It is unlikely that the full extent of the R-curve is utilised in any cyclic application, only the initial stage of the R-curve (Figure 9.5), i.e. $dJ/da=\alpha=5MN/m^2$[6], is applied to the calculation. This model was examined using different values for K_{Ri}.

If plane strain conditions are maintained at the crack tip, the crack should propagate at $K_i>35MN/m^{3/2}$, the plane strain fracture toughness.

However, the concave R-curve of the material illustrates that the tearing resistance increases with crack extension. Hence K_{Ri} should be a fraction less than the previous K_{max}, denoted as $K_{max(i-1)}$. The Δa is therefore calculated assuming $K_{Ri} \propto K_{max(i-1)}$. Figure 9.6 shows the results of using $K_{Ri}=K_{IC}$ and $K_{Ri} \propto K_{max(i-1)}$. Although the model for crack extension is based on excessive

K at each load cycle, the results in Figure 9.6 implies that the model overestimates the incremental crack extension, as the estimated Δa rises above the experimental result. It is evident that the calculated Δa represents the crack growth for ΔN cycles. Different combinations of $K_{Ri} \propto K_{max(i-1)}$ and ΔN produce crack growth laws that are comparable to the experimental result, Figure 9.7. A combination of K_{Ri} and ΔN of the model is not unique because the K_R for the model cannot be determined at this stage.

The expression did model the observed fatigue behaviour satisfactorily for cyclic constant loading.

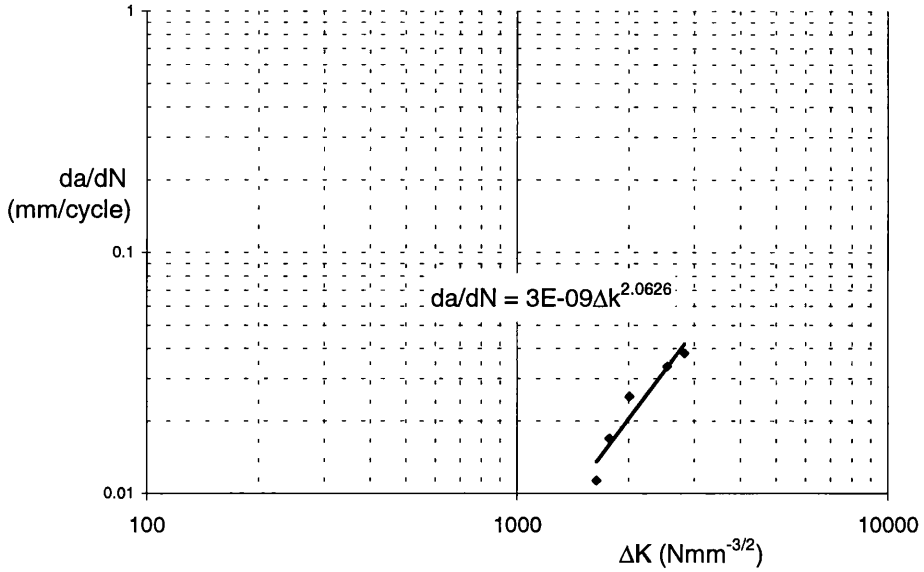

a. A saw cut on the flange of the bridge girder

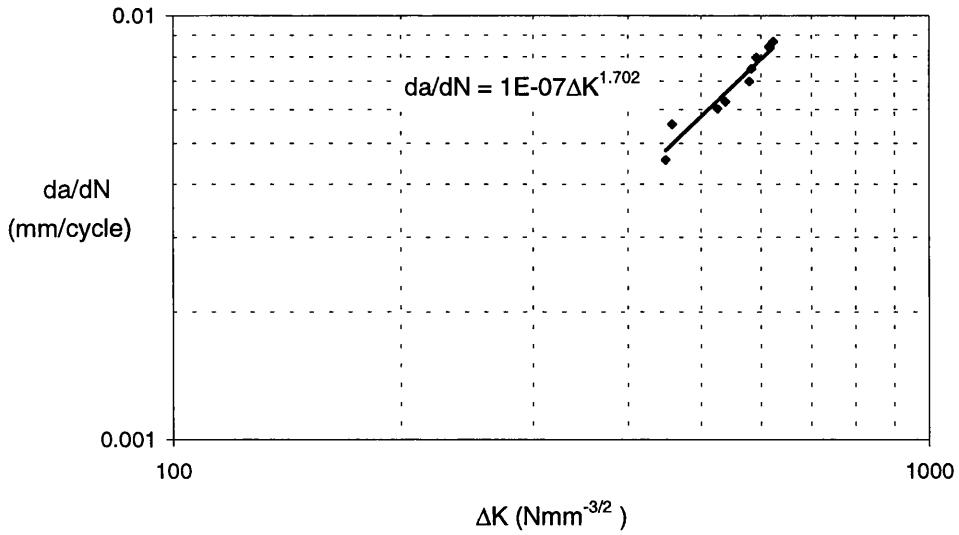

b. A stem crack (measured on the out-side surface), ref. 30 in [82].

Figure 9.1 Crack growth rate from a fatigue test on the damaged bridge.

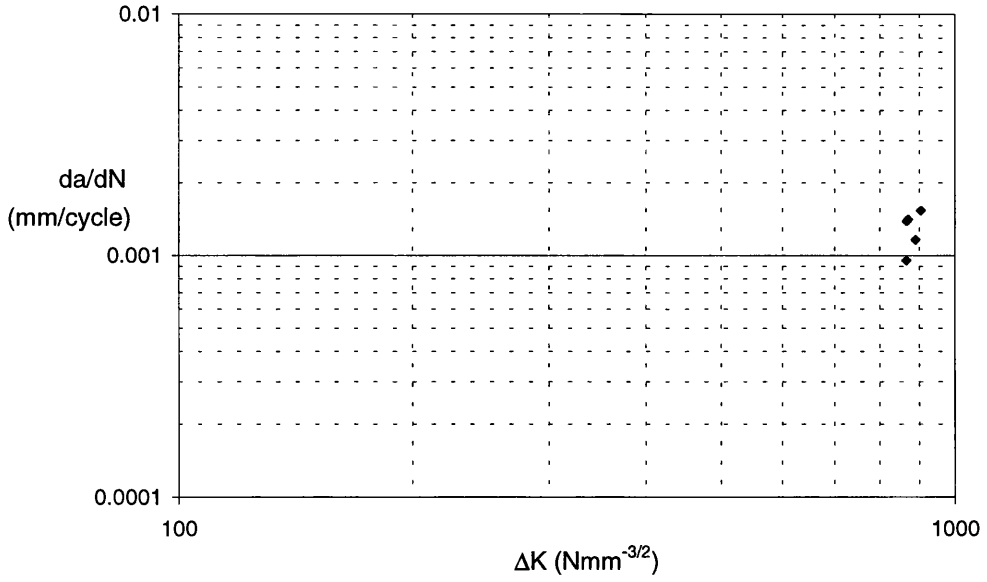

c. A stem crack, ref. 151 in [82].

Figure 9.1 (cont.) Crack growth rate from a fatigue test on the damaged bridge.

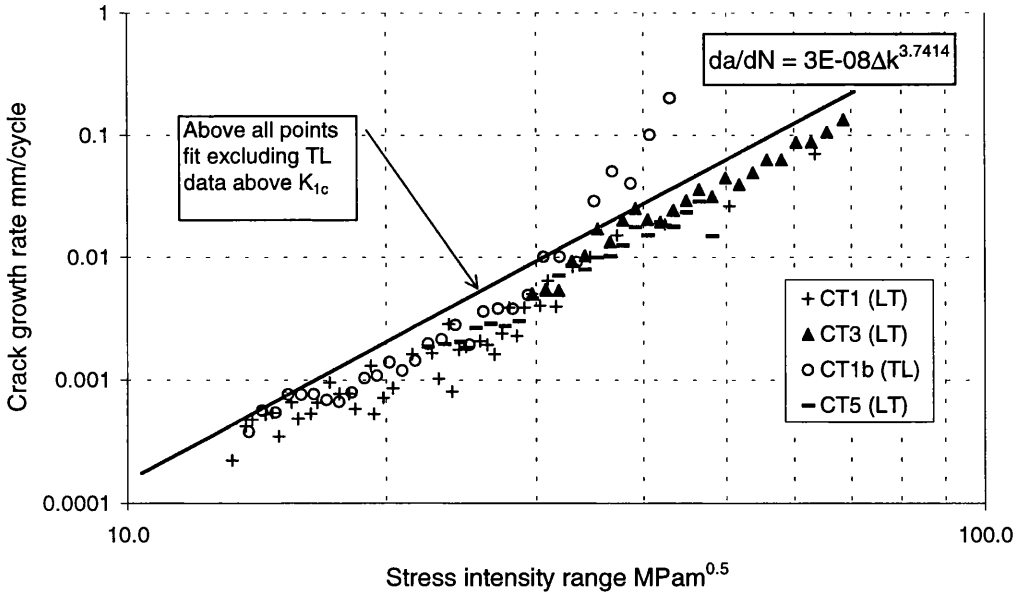

Figure 9.2 Crack growth rate in the LT and TL direction of large ligament CT specimens.

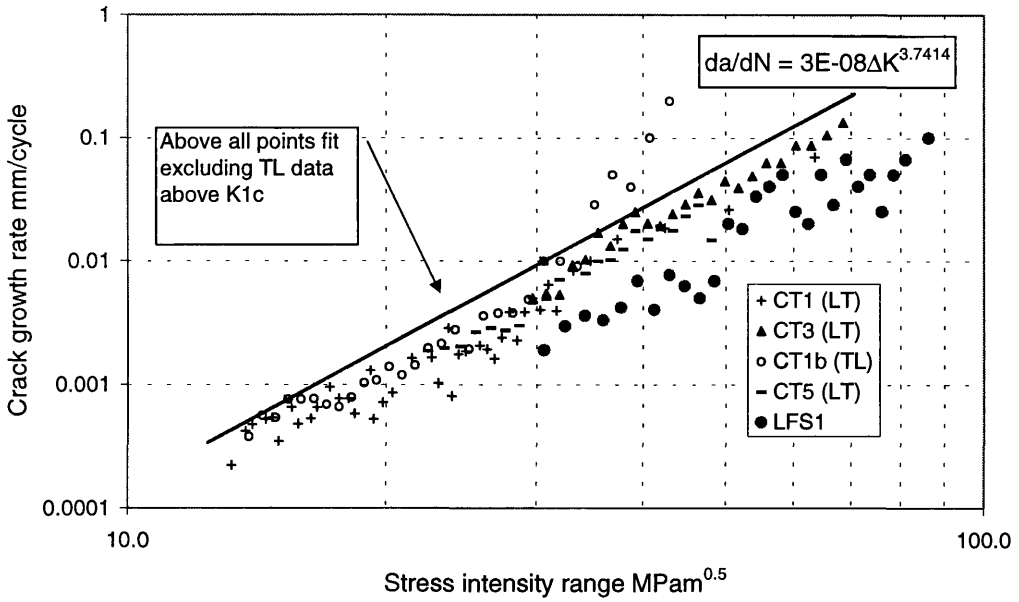

Figure 9.3 Crack growth rate of large ligament CT and tension (LFS1) specimens.

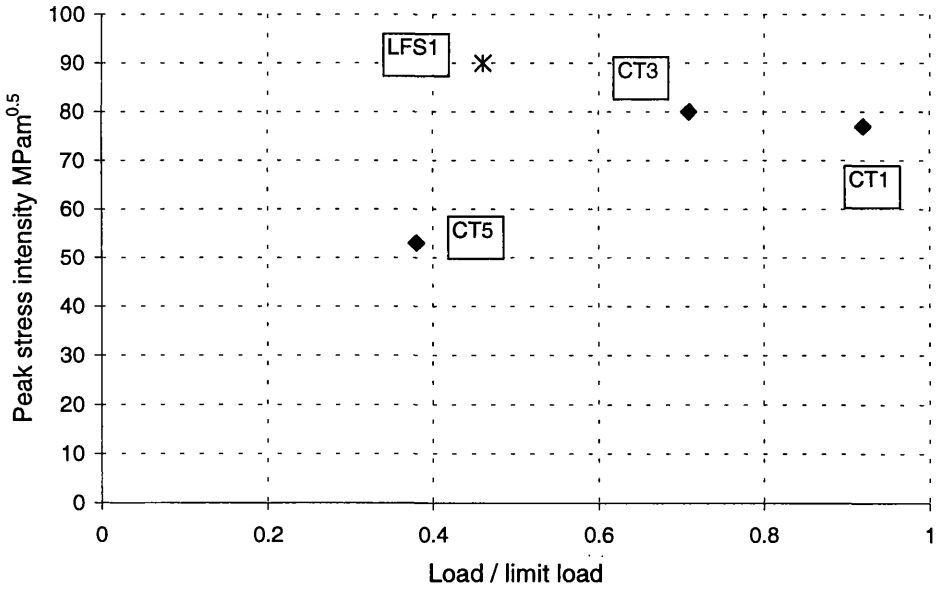

Figure 9.4 Peak stress intensity and load/limit load for fatigue to failure test on CT and tension (LFS1) specimens.

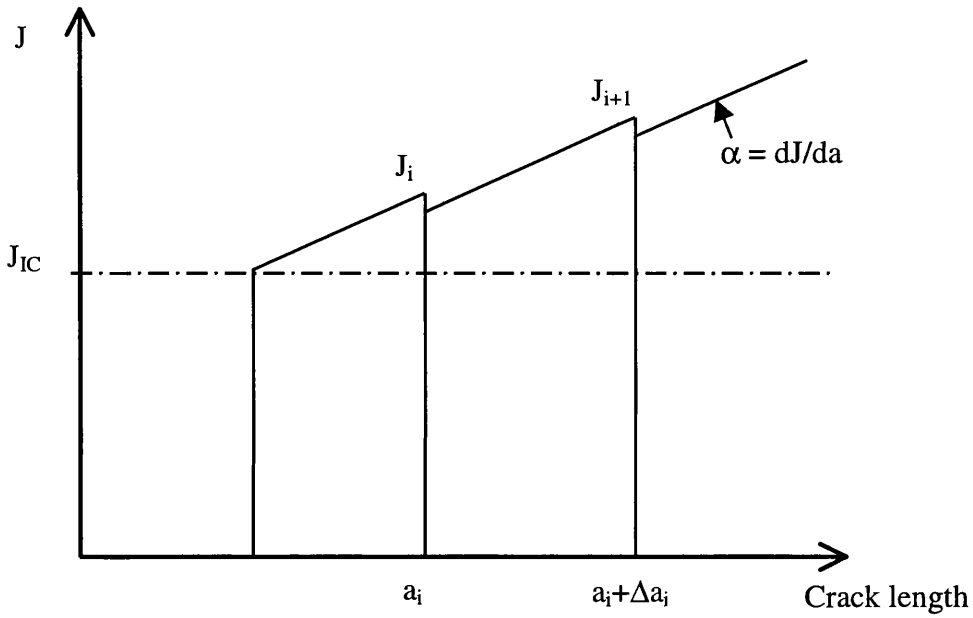

Figure 9.5 Diagrammatic representation of cyclic application of R-curve. (N.B. $J=K^2/E$ is assumed)

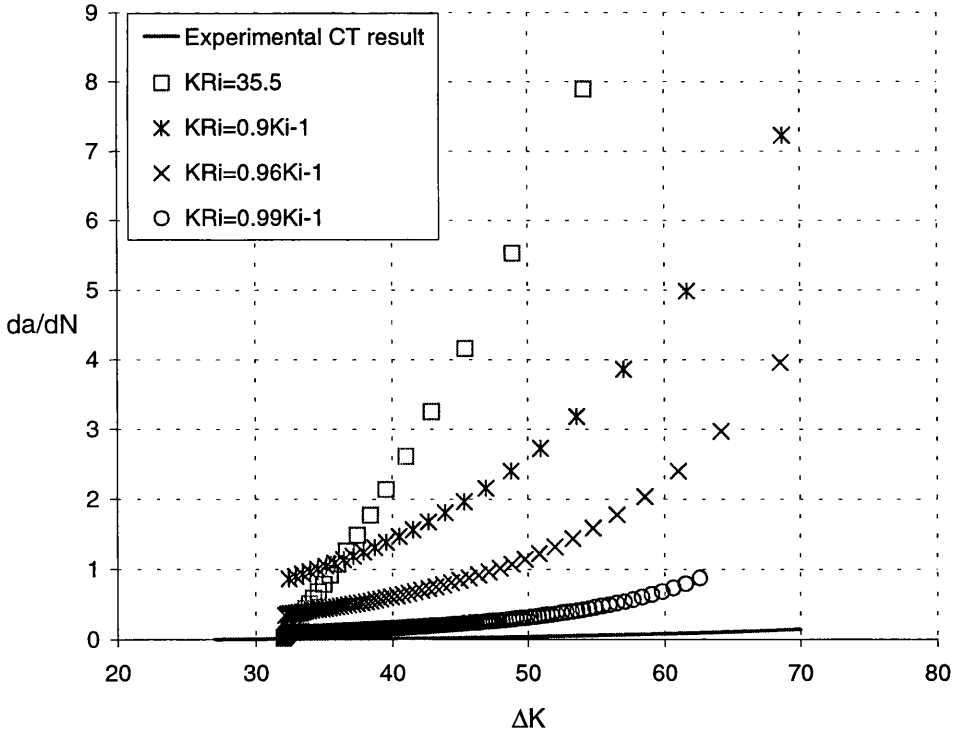

Figure 9.6 Comparison of cyclic R-curve results with experimental fatigue data (N.B. the results severely overestimate the experimental data.).

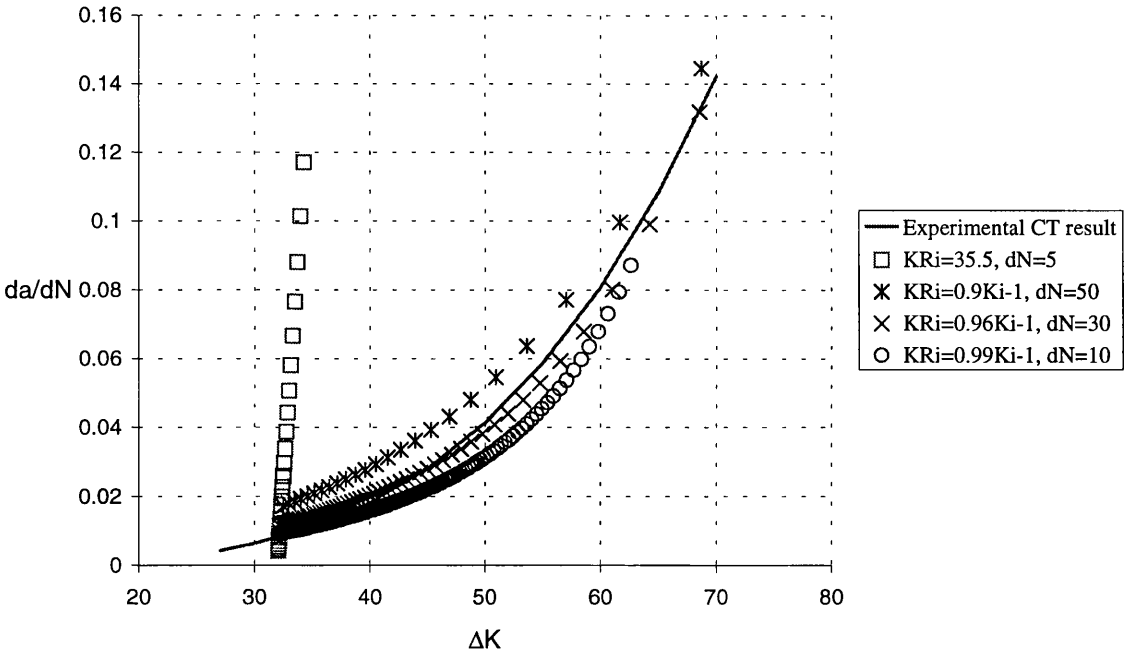

Figure 9.7 Comparison of cyclic R-curve results with experimental fatigue data. (N.B. the cyclic R-curve results are corrected by ΔN.)

CHAPTER 10. CONCLUSIONS AND FUTURE WORK

Numerical and experimental[6][8][36] tests have been carried out on the fracture and fatigue behaviour of the aluminium bridge alloy in order to devise a procedure for assessing the reliability of a damaged bridge component. The prolonged service life of the bridge has been proved by fatigue tests[1][2] on various bridge prototypes, including one subjected to ballistic damage. However, initial fracture mechanics calculations, using data from standard fracture tests, indicated that only short cracks should be tolerated, whereas as cracks up to 300mm long were observed in the structural tests. Subsequent fracture tests on the aluminium alloy revealed that the substantial tearing resistance of the material retards fracture instability in large components (but not in small test pieces). Initially, the study looked for differences between the 3D static crack tip stress and strain fields for small and large 3PB test specimens to explain the division between stable and unstable fracture. Only the plastic strains showed any significant variation, and did not indicate any clear division in specimen behaviour. Attention was then turned to the R-curve concept to explain the difference in behaviour.

The energy for fracture and plastic dissipation cannot be determined accurately from the computational results, so the J values associated with crack propagation are used as the measure of fracture resistance. The plastic zones at the crack tips are small at the beginning of crack growth, allowing the J-integral to be interpreted as a plastically corrected energy release rate. Crack propagation can be analysed numerically using only 2-D analysis at present. Examination of the numerical load versus displacement diagrams for the large 3PB specimens showed that they were very close to the plane stress condition. The dJ/da of the R-curve for the bridge alloy increases with increasing Δa. This form of R-curve covers the transition from flat to slant fracture (for a thickness of 25mm), which is associated with the onset of plane stress conditions near the crack front (there is no reason for the crack plane to change if fully plane strain conditions are maintained). The concave R-curve of the bridge alloy, produced by numerical analysis, coincides with that of the experimental result, with both analyses assuming plane stress conditions. The fracture surface of a large (b>>B) specimen showed flat fracture at the central region of the thickness, indicating plane strain conditions in this region. The flat fracture tapered down to a point where the specimen failed by fully slant fracture. The experimental J_{IC} and dJ/da values (for the first 4mm of crack extension), using plane strain calibration, were close to but slightly lower than the numerical plane stress result. In this case the numerical plane stress result

appeared to be the best approximation for the fracture resistance of the bridge alloy with the geometries tested, and hence for the bridge components.

The use of J-based R-curves allows us to calculate fracture parameters from standard LEFM procedures with well-established plastic correction factors. The use of a J-integral based R-curve is limited when large scale yielding occurs at the crack tip. The discrepancy between J and elastic G increases with increasing crack tip plasticity, but it is insignificant under small scale yielding. The numerical plane stress results showed that the crack propagation was within a J dominant zone. Different modifications of J have been introduced by other researchers in order to obtain an accurate measure of energy per unit crack growth, but were not used in this investigation because the calculations for a modified J value required accurate experimental records which were not available for the numerical analysis.

High and low in-plane constraint effects are observed in the 3PB and CCT specimens respectively. Fracture assessment using the R-curve approach shows that instability is not likely to occur in long cracks subjected to the design load, but short cracks may fail under high design load, as found experimentally in small test pieces. The R-curve approach for fracture assessment must be modified for in-plane constraint by T-stress indexing, but this can only be done approximately at present. The use of R-curves, indexed by the T-stress to correct for different in-plane constraints, provides an adequate predictive tool to explain both the occurrence of unstable fracture in small scale test pieces, and the stable fracture observed in large scale test pieces and structural components.

The disadvantage of the R-curve concept, as used in the present analysis, is the increased complexity of the fracture assessment. In the most commonly used predictions based on stable cracking, the dividing line between stable and unstable fracture is given by the applied dG/da being greater or less than the initial slope of the resistance curve i.e. dJ_R/da (with the concurrent condition that $G=J_R$). An additional simplification is to compare the applied J with the J_R after a small amount of crack growth, say 1-2 mm. For our application, it is necessary to compare the applied G-curve (corrected by the applied T-stress) against the material resistance plotted against both T-stress and crack extension in a 3-dimensional diagram, with a suitable margin of safety (this problem can be solved numerically, without recourse to 3D diagrams). With further investigation, it is highly probable that suitable approximations can be found, similar to those already mentioned.

For certain geometries, such as the T-section stem of the tension chord, it may be sufficient to use a K_{IC} value amended by the appropriate T-stress. This should give an effective K_{IC} of at least double the fully constrained value i.e. 70 MPa$\sqrt{m}$, which may never be reached by the loading imposed on the bridge (the effective K_{IC} must be exceeded for any fracture, stable or unstable, to occur). The extra toughness provided by the R-curve then becomes superfluous. This assessment requires critical areas of the bridge to be identified and assessed. Some advice on the use of R-curves with FAD's is given in BS7910.

The complexity of the R-curve analysis is dictated by the concave shape of the curves (most R-curves reported in the literature are convex in shape). This shape is caused by the change from flat to slant fracture, with the flat fracture tunnelling to a point. This change is associated with the loss of plane strain constraint, which starts at the surface once the flat fracture has progressed by a small distance (4 mm) through existing plastic zones which allow the loss of through-thickness constraint. The large ligaments tested encouraged this plane stress situation to dominate the crack tip, so relatively thick (25 mm) specimens eventually produced slant fracture behaviour. This change occurred in both R-curve and fatigue specimens. Square ligament test pieces produced flat fracture, although not necessarily unstable fracture, as shown by the 3PB a/W=0.5 test piece. The numerical plane strain analysis of this latter specimen produced a similar but lower R-curve than the plane stress analysis, the latter being identical to the plane stress R-curves from the large ligament specimens. It may be sensible to use this 'plane strain' R-curve as a lower bound in any future analysis, because of uncertainties regarding the plane strain to plane stress transition.

From the current work, it is not clear how the fatigue cracks will interact with the material R-curve. An attempt was made to predict the crack growth rate for $K_{max}>K_{IC}$, using a cyclic R-curve approach, but the model did not give unique results. As final failure will be due to either plastic collapse or unstable fracture following fatigue crack growth, this point should be clarified.

Failure by plastic collapse can be estimated to a reasonable precision by simply calculating the area of material remaining under tension, and using a flow stress as the ultimate failure stress. Calculations of damaged bridge components show that, in general, the applied load to remaining

ligaments reaches its limit load at 70% of yield strain. In this case the failure, if it occurs, is due to plastic collapse.

The present study provides important information for the use of the Christchurch bridge. It also provides an explanation for the differences in fracture behaviour between test specimens and structural components of intermediate thickness, which is 25 mm in this case. The conclusions from the present study are itemised as follows:

1. Fracture assessment, using a T-stress indexed fracture toughness alone, underestimates the critical crack length in the bridge components.

2. The numerical analyses of tests exhibiting stable crack growth showed a concave R-curve for the aluminium bridge alloy. These numerical R-curves were later confirmed by experimental results. The form of this rising R-curve coincides with the change to plane stress conditions. (The formation of shear lips and crack tunnelling are evidence that plane stress conditions are dominant). The observed R-curves did not produce a plateau, where the tearing resistance stops increasing with crack extension.

3. Instability with a rising R-curve is defined as G=R and dG/da>dR/da, which gives, for a J_R-curve, G=J_R and dG/da>dJ_R. Material with a conventional rising, i.e. a convex, R-curve (which has high dR/da at the instability point, followed by decreasing values) fails when dG/da=dR/da, i.e. dG/da=dJ_R/da. The concave J_R-curve for the aluminium bridge alloy shows that dJ_R/da increases with Δa. For small ligaments, initial instability leads to final fracture. In large ligament specimens, stable cracking follows crack initiation because of high dJ_R/da.

4. It is evident that the difference of J_R between 3PB (a high constraint geometry) and CCT (a low constraint geometry) specimens at initiation is the result of in-plane constraint. The R-curve for high and low constraint geometries converged after 5 mm or so of crack extension. The R-curve approach must be corrected by the T-stress when it is applied to the bridge component, because the bridge is a low constraint geometry. The J_C value is therefore correlated to Δa and T-stresses, and the failure criterion is defined in terms of a 3-D failure surface.

5. Experimental R-curves parallel (TL) and normal (LT) to the extrusion direction were of similar form, but the value of J_R in the LT direction was larger that in the TL direction.

6. The G_{eff} is computed using a crack length corrected by plastic zone size to predict instability for cracks in small scale yielding. Instability prediction comparing J_R-curves and G_{eff} curves shows a longer crack extension compared with that given by elastic G curves, but the difference is insignificant.

7. The G_{eff} (as defined above) is computed and compared with the J_R from experimental fracture test results. The latter are obtained by using the plastic work from the test record. The G_{eff} values agreed with the experimental J_R. The result supports that the J_R from the fracture testing is equivalent to G corrected for the plastic zone size.

8. The result of opening stresses from the numerical (plane stress) crack propagation analysis shows J characterisation near the crack tip. The validation, using currently accepted procedures, of the J_R-curve from experimental testing of the bridge alloy showed that the curve is valid for the first 12mm of crack extension.

9. For large specimens approaching structural dimensions, the fracture surface in both fracture and fatigue tests was slant at failure. In fact, the experimental results seemed to indicate that slant fracture occurs once the applied K exceeds K_{IC}.

10. Limit load failure appeared to have occurred in the fatigue tests on specimens with large ligament. For cracks in the bridge components, failure at plastic limit load was investigated numerically. Precise solutions of Y (the geometry factor for K) for cracks approaching the flange were therefore obtained using numerical results. The numerical result showed that, for a long crack that reduces the cross-section area by 30%, and with its lower crack tip 4.5 mm from the flange, the crack is likely to fail at a limit load lower than the design load (67% of σ_{ys} or ε_y).

11. The fatigue crack growth rate, i.e. the exponent m in the Paris law, for the aluminium bridge alloy, as measured by different researchers, varies from 2 to 4.7 (see Table 9.1), while the values from full scale tests of bridge panels are close to 2. For large ligament

specimens whose dimensions correspond to structural dimensions, Sumpter showed that the exponent m was 3.74 when $K_{max} > K_{IC}$.

12. A simple model was devised using the R-curve at initiation to predict the fatigue crack extension under excessive K_{max}. The estimate seriously underestimated the fatigue mechanism. The model, $\Delta a = (K_i^2 - K_{Ri}^2)/(E(dJ/da) - (K_i^2/a_i))$ for ΔN cycles, produced a fit to the experimental fatigue crack growth data that was not unique. Different combinations of ΔN and K_{Ri} could give equally valid 'good fits'.

Future Work

The following recommendations for the study of fracture and fatigue behaviour are made on the basis of the numerical and experimental work carried out to date.

1. The transition from predominant plane strain to plane stress condition during crack growth is due to the loss of out-of-plane constraint. For the 25mm thick section of bridge alloy, this transition seems to occur within the first few millimetres of crack extension. The conditions for the change in fracture mode during crack growth can be studied numerically using 3-D analysis.

2. Both plane strain and plane stress calibrations assume constant stress and strain behaviour through the thickness. Both plane strain and plane stress analysis of crack propagation cannot provide accurate J values for the condition between these two constraints. A hypothetical J_R-curve for the bridge alloy with the geometries tested assumes that it is similar to the plane stress result but its dJ_R/da is low at initiation, which is in between the plane stress and plane strain result. A 3-D analysis of crack propagation could clarify the true J values during the changing fracture mode.

3. The in-plane constraint effect on J_{IC} values has been noted, therefore the T-stress indexing is introduced for the elevated J_{IC} of low constraint geometries. As a result the J_R-T surface, i.e. fracture resistance associated with crack length and T-stresses, has been devised, assuming constant elevation at all crack lengths. Numerically, J_R-curves of low constraint

show that the T-stress is significant only at initiation. More information on J_R-curves for low constraint geometries are required to produce the J_R-T surface.

4. The failure assessment diagram (FAD) describes the interaction between fracture and collapse. It is noted that cracks in specimens with large ligament grow stably but are likely to fail by plastic collapse. Providing the R-curve analysis can be simplified, it is possible that the FAD concept, using J_C and limit load, can be applied to the conditions of stable crack growth where $J_C > J_{IC}$.

5. Crack growth in LT specimens with large ligaments tends to propagate from the original notch (LT) plane to the TL plane. The experimental and numerical results show that is due to the tendency of crack growth towards the weaker orientation. The reason that triggers the crack plane to change direction has not been explained. The answer might be found from the interaction between mode I and mode II crack growths.

6. From the fatigue testing of the bridge alloy, it seems that different values of the index in the Paris law are correlated with the crack geometries and K_{max}. There is a difference of m values between the results from full scale bridge testing and large specimens. This discrepancy should be clarified.

7. A simple model using repetition of the J_R-curve for predicting fatigue crack growth rate under high load cycles did not give unique results. However, crack extensions can be predicted using the driving force and J_R curves. Future work on material behaviour under cyclic load should investigate this relationship.

REFERENCES

[1]. Webber, D., 'Fatigue Design and Testing of an AlZnMg Alloy Bridge Girder', Royal Armament Research and Development Establishment, Christchurch, Dorset, 1985; presented at the Third International Conference on Aluminium weldments, Munchen.

[2]. Webber, D., Stow, A.J. and Carson, W., 'Fatigue Test of Ballistically Damaged BR90 Panels (R-COM)', DERA Publication, restricted release, March 1998.

[3]. Henry, B.S., 'Constraint Based Fracture Assessment of Through-Thickness Cracks in a Bridge Girder Structure', Ph.D. Thesis C/PH/194/96, Department of Civil Engineering, University of Wales Swansea, March 1996.

[4]. Henry, B.S., Luxmoore, A.R. and Sumpter, J.D.G., 'Elastic-Plastic Fracture Mechanics Assessment of Low Constraint Aluminium Test Specimens', International Journal of Fracture Vol. 81, 1996, pp.217-234.

[5]. Henry, B.S., and Luxmoore, A.R., 'Two-Parameter Fracture Assessment of Through-Thickness Cracks in an Aluminium Bridge Structure', Eleventh European Conference on Fracture, ECF-11, Futuroscope, France, 1996.

[6]. Sumpter, J.D.G., 'Observations on Tearing Instability in an Aluminium Alloy', Mechanisms and Mechanics of Damage and Failure, ECF-11, Vol. 2, 1996, pp.855-860.

[7]. Cheung, C.M.S., 'Development of a Fracture Assessment Scheme for Through-Thickness Cracks in a Military Bridge Girder', M.Phil. Thesis, C/MPhil/337/97, Department of Civil Engineering, University of Wales Swansea, October 1997.

[8]. Sumpter, J.D.G., 'Summary of Tests on Large Aluminium Compact Tension Specimens', Internal report for DERA, August 1999.

[9]. Maddox, S.J. and Webber, D., 'Fatigue Crack Propagation in Aluminium-Zinc-Magnesium Alloy Fillet-Welded Joints', ASTM STP 648, American Society for Test and Materials, Philadelphia, 1978.

[10]. Bulter, S. and Tutty, N., 'The Damage Tolerance of the Christchurch Bridge', University of Bath, Report no. 3683, 1986.

[11]. Richardson, S.M., 'Fatigue Crack Growth Properties of an Al-Zn-Mg Alloy', Newcastle upon Tyne Polytechnic, M.Sc. thesis, 1983.

[12]. Sumpter, J.D.G., 'Large Tension Fatigue Test on 7019 Aluminium', Internal report for DERA, December 1999.

[13]. Griffith, A.A., 'The Phenomena of Rupture and Flow in Solids', Philosophical Transactions, Series A, Vol. 221, 1920, pp. 163-198.

[14]. Irwin, G.R., 'Fracture Dynamics', Fracturing of Metals, American Society for Metals, Cleveland, 1948, pp. 147-166.

[15]. Irwin, G.R., 'Onset of Fast Crack Propagation in High Strength Steel and Aluminium Alloys', Sagamore Research Conference Proceedings, Vol. 2, 1956, pp. 289-305.

[16]. Irwin, G.R., 'Analysis of Stresses and Strains near the End of a Crack Traversing a Plate', Journal of Applied Mechanics, Vol. 24, 1957, pp. 361-364.

[17]. Williams, M.L., 'On the Stress Distribution at the Base of a Stationary Crack', Journal of Applied Mechanics, Vol. 24, 1957, pp. 109-114.

[18]. Wells, A.A., 'Unstable Crack Propagation in Metals: Cleavage and Fast Fracture', Proceedings of the Crack Propagation Symposium, Vol. 1, Paper 84, Cranfield, U.K., 1961.

[19]. Rice, J.R., 'A Path Independent Integral and the Approximate Analysis of Strain Concentration by Notches and Cracks', Journal of Applied Mechanics, Vol. 35, 1968, pp. 379-386.

[20]. Hutchinson, J.W., 'Singular Behavior at the End of a Tensile Crack in a Hardening Material,' Journal of Mechanics and Physics of Solids, Vol. 16, 1968, pp.13-31.

[21]. Hutchinson, J.W., 'Plastic Stress and Strain Fields at a Crack Tip,' Journal of Mechanics and Physics of Solids, Vol. 16, 1968, pp. 337-347.

[22]. Rice, J.R., and Rosengren, G.F., 'Plane Strain Deformation Near a Crack Tip in a Power Law Hardening Material,' Journal of the Mechanics and Physics of Solids, Vol. 16, 1968, pp. 1-12.

[23]. Irwin, G.R., 'Plastic Zone Near a Crack and Fracture Toughness', Sagamore Research Conference Proceedings, Vol. 4, 1961.

[24]. Shih, C.F., 'Relationship Between The J-integral and The Crack Opening Displacement for Stationary and Extending Cracks', Journal of Mechanics and Physics of Solids, Vol. 29, 1981, pp. 305-326.

[25]. Anderson, T.L., Kirk, M.T. and Dodds, R.H., 'Approximate Techniques for Predicting Size Effects on Cleavage Fracture Toughness', Fracture Mechanics: 24th Volume, ASTM STP 1207, American Society for Testing and Materials, Philadelphia.

[26]. Rice, J.R., 'Limitation to Small Scale Yielding Approximation for Crack Tip Plasticity', Journal of the Mechanics and Physics of Solids, Vol. 22, 1974, pp. 17-26.

[27]. Leever, P.S. and Radon, J.C., 'Inherent Stress Biaxiality in Various Fracture Specimen Geometries', International Journal of fracture, Vol. 19, 1983, pp. 311-325.

[28]. Betegon, C. and Hancock, J.W., 'Two-Parameter Characterisation of Elastic-Plastic Crack -Tip Fields', Journal of Applied Mechanics, Vol. 58, 1991, pp. 104-110.

[29]. BS 7448: Part 1: 1991 Fracture Mechanics Toughness Tests, British Standard Institution.

[30]. BS 7910: 1999 Guide on Methods for Assessing the Acceptability of Flaws in Fusion Welded Structures, British Standard Institution.

[31]. Sumpter, J.D.G., 'Tensile Tests and Experimental Investigation of CCT and 3PB specimens Manufactured from a High Tensile Strength Aluminium Alloy Bridge Girder', Private copy, 1995.

[32]. Sumpter, J.D.G., 'Laboratory Record of Fracture Test of 3PB and CCT Specimens', Private copy, 1996.

[33]. Lau, C.L.L., 'The Development of J-Integral Estimation Schemes for Shallow Cracked Geometries under Large Plastic Deformation', Ph.D. Thesis, C/PH/184/94, Department of Civil Engineering, University of Wales Swansea, 1994.

[34]. Brown, W.F. ,JR., and Srawely, J.B., 'Fracture Toughness Testing Methods', Fracture Toughness Testing and Its Applications, ASTM STP 381, American Society for Testing and Materials, 1965, pp.133-198.

[35]. ASTM E 1820-99a, 'Standard Test Method for Measurement of Fracture Toughness', American Society for Testing and Materials, 2000.

[36]. Sumpter. J.D.G, 'Note on Tearing Resistance in Large Aluminium CT Specimens', Internal report for DERA, December 1999.

[37]. Krafft, J.M., Sullivan, A.M. and Boyle, R.W., 'Effect of Dimensions on Fast Fracture Instability of Notched Sheets', Proceedings of the Crack Propagation Symposium Cranfield, The College of Aeronautics, Vol. 1, 1962, pp. 8-28.

[38]. Green, G. and Knott. J.F., 'On Effects of Thickness on Ductile Crack Growth in Mild Steel', Journal of the Mechanics and Physics of Solids, Vol. 23, 1975, pp. 167-183.

[39]. Cheung, C.M.S, 'Numerical Result for The Y Solution on Stem Cracks in The Bridge Component', Department of Civil Engineering, University of Wales Swansea, A note to DERA, May 1999.

[40]. Anderson, T.L., 'Fracture Mechanics-Fundamentals and Applications', Department of Mechanical Engineering, Texas A&M University, College Station, Texas, CRC Press, Inc., Second Edition, 1995.

[41]. Rice, J.R., Paris, P.C. and Merkle, J.G., 'Some Further Results of J-Integral Analysis and Estimates', Progress in Flaw Growth and Fracture Toughness Testing, ASTM STP 536, American Society For Testing and Materials, Philadelphia, 1973, pp. 231-245.

[42]. Kolednik, O., 'On the Physical Meaning of the J–Δa-Curves', Engineering Fracture Mechanics, Vol. 38, No. 6, 1991, pp. 403-412.

[43]. Turner, C.E., 'A Re-Assessment of Ductile Tearing Resistance.', Fracture Behaviour and Design of Materials and Structures, ECF 8, Vol. 1, 1990, pp. 933-968.

[44]. Ernst, H.A., 'Further Developments on the Modified J-Integral', Nonlinear Fracture Mechanics: Volume 11–Elastic-Plastic Fracture, ASTM STP 995, American Society For Testing and Materials, Philadelphia, 1989, pp.306, 319.

[45]. Turner, C.E. and Braga, L., 'Energy Dissipation Rate and Crack Opening Angle Analyses of Fully Plastic Ductile Tearing', Constraint Effects in Fracture , ASTM STP 1171, American Society For Testing and Materials, Philadelphia, 1993, pp. 158-175.

[46]. Hutchinson, J.W. and Paris, P.C., 'Stability Analysis of J-Controlled Crack Growth', Elastic-Plastic Fracture, ASTM STP 668, American Society For Testing and Materials, 1979, pp. 37-64.

[47]. BS 7448 Part 4:1997, 'Fracture Mechanics Toughness Tests. Method for Determination of Fracture Resistance Curves and Initiation Values for Stable Crack Extension in Metallic Materials', British Standard Institution.

[48]. Gibson, G.P., and Druce, S.G. and Turner, C.E., 'Effect of Specimen Size and Geometry on Ductile Crack Growth Resistance in a C–Mn Steel', International Journal of Fracture, Vol. 32, 1987, pp. 219-240.

[49]. Ernst, H.A., Schwalbe, K.H., Hellmann, D. and McCabe, D.E., 'Modified J, JM, Resistance Curves Under Plane Stress Conditions', International Journal of Fracture, Vol. 37, 1988, pp. 83-100.

[50]. John, S.J. and Turner, C.E., 'Alternative Representations for Scaled R Curves in a Titanium Alloy', Defect Assessment in Components – Fundamentals and Applications, ESIS/EGF9, 1991, pp. 299-318.

[51]. Jones, R.L. and Gordon, J.R., 'The Effect of Specimen Size and Geometry on J-R Curve Behaviour', Defect Assessment in Components – Fundamentals and Applications, ESIS/EGF9, 1991, pp. 271-284.

[52]. ASTM E 1737-96, 'Standard Test Method for J-Integral Characterization of Fracture Toughness', American Society For Testing and Materials.

[53]. Sun, J., Deng, Z. and Tu, M., 'Plane Stress Elastic-Plastic Fracture Criteria and Constraint Intensity in Crack Tip Regions', Engineering Fracture Mechanics, Vol. 37, No. 3, 1990, pp. 675-680.

[54]. Yan, C. and Mai, Y., 'Numerical Investigation on Stable Crack Growth in Plane Stress', International Journal of Fracture, Vol. 91, 1998, pp. 117-130.

[55]. Ewalds, H.L. and Wanhill, R.J.H., 'Fracture Mechanics', Seventh printing 1996, Arnold, section 13.2.

[56]. Gerberich, W.W. and Jatavallabhula, K., 'Quantitative Fractography and Dislocation Interpretations of the Cyclic Cleavage Crack Growth Process', Acta Metallurgica, Vol. 31, 1983, pp. 241-255.

[57]. Ewing, J.A. and Humfery, J.C., 'The Fracture of Metals Under Rapid Alterations of Stress', Philosophical Transactions of the Royal Society, London A200, 1903, pp. 241-250.

[58]. Paris, P.C., Gomez, M.P. and Anderson, W.P., 'A Rational Analytic Theory of Fatigue', The Trend in Engineering, Vol. 13, 1961, pp. 9-14.

[59]. Elber, W., 'Fatigue Crack Closure Under Cyclic Tension', Engineering Fracture Mechanics, Vol. 2, 1970, pp. 37-45.

[60]. Elber, W., 'The Significance of Fatigue Crack Closure', In Damage Tolerance in Aircraft Structures, ASTM STP 486, American Society for Testing and Materials, Philadelphia, 1971, pp. 230-242.

[61]. Paris, P.C. and Erdogan, F., 'A Critical Analysis of Crack Propagation Laws', Journal of Basic Engineering, Vol. 85, 1960, pp. 528-534.

[62]. Foreman, R.G., 'V.E. Keary and R.M. Engle, "Numerical Analysis of Crack Propagation in Cyclic-Loaded Structures', Journal of Basic Engineering, Vol. 89, 1967, pp. 459-464.

[63]. Erdogan, F. and Roberts, R., 'The Effect of Mean Stress on Fatigue Crack Propagation in Plates Under Extension and Bending', Transaction of the American Society of Mechanical Engineers, Journal of Basic Engineering, Vol. 89, 1967, pp. 885.

[64]. Erdogan, F. and Roberts, R., 'A Comparative Study of Crack Propagation in Plates Under Extension and Bending', Process of International Conference on Fracture, 1965, Sendian, Japan.

[65]. Duggan, T.V., 'Application of Fatigue Data to Design-Crack Propagation in a Simulated Component Under Cyclic Loading Conditions', Ph.D Thesis, Portsmouth, 1973.

[66]. Roberts, R. and Kibler, J.J., 'Some Aspects of Fatigue Crack Propagation', Engineering of Fracture Mechanics, Vol. 2, 1971, pp. 243.

[67]. Duggan, T.V., 'A Theory for Fatigue Crack Propagation' Symposium of Mechanical Behaviour of Materials, 1974, Kyoto, Japan.

[68]. McEvily, A.J., 'On Closure in Fatigue Crack Growth', ASTM STP 982, American Society of Testing and Materials, Philadelphia, 1988, pp. 35-43.

[69]. Shih, T.T. and Wei, R.P., 'A Study of Crack Closure in Fatigue', Engineering Fracture Mechanics, Vol. 6, 1974, pp. 19-32.

[70]. Shih, T.T. and Wei, R.P., 'Discussion.' International Journal of Fracture , Vol. 13, 1977, pp.105-106.

[71]. Hudak, S.J. ,JR. and Davidson, D.L., 'The Dependence of Crack Closure on Fatigue Loading Variables', ASTM STP 982, American Society for Testing and Materials, Philadelphia, 1988, pp. 121-138.

[72]. Tanaka, K., ' Mechanics and Micromechanics of Fatigue Crack Propagation', ASTM STP 1020, American Society for Testing and Materials, Philadelphia, 1989, pp. 151-183.

[73]. Tanaka, K. and Nakai, Y., 'Propagation and Non-Propagation of Short Fatigue Cracks at a Sharp Notch',Fatigue of Engineering Materials and Structures 6, 1983, pp.315-327.

[74]. Dugdale, D.S., 'Yielding of Steel Sheets Containing Slits', Journal of the Mechanics and Physics of Solids 8, 1960, pp. 100-108.

[75]. Burdekin, F.M. and Stone, D.E.W., 'The Crack Opening Displacement Approach to Fracture Mechanics in Yielding Materials', Journal of Strain Analysis 1, 1966, pp. 145-153.

[76]. Budiansky, B. and Hutchinson, J.W., 'Analysis of Closure in Fatigue Crack Growth', Journal of Applied Mechanics, Vol. 45, 1978, pp. 267-276.

[77]. Dowling, N.E. and Begley, J.A., 'Fatigue Crack Growth During Gross Plasticity and the J Integral', ASTM STP 590, American Society for Testing and Materials, Philadelphia, 1976, pp. 82-103.

[78]. Lambert, Y., Saillard, P. and Bathias, C., 'Application of the J Concept to Fatigue Crack Growth in Large-Scale Yielding', ASTM STP 969, American Society for Testing and Materials, Philadelphia, 1988, pp. 318-329.

[79]. BS 8118 Part 1: 1991, ' Structural Use of Aluminium', British Standard Institution.

[80]. Jaccard, R and Ogle, M.H., 'Aluminium Eurocode – Design for Fatigue', WRC Proceedings IIW. BSI document No. 97/107503.

[81]. Stow, A., 'Fatigue Tests on Ballistically Damaged BR90 Panels', Test data, Gap Crossing, DERA.

[82]. Cheung, C.M.S, 'The J and T of Large SENT Specimen of Bridge Alloy', Department of Civil Engineering, University of Wales Swansea, A note to DERA, December 1999.

[83]. Sumpter, J.D.G., 'TL (Low Toughness) Direction Fatigue Test on 7019 Aluminium', Internal report for DERA, December 1999.

[84]. Sumpter, J.D.G., 'Large Tension Fatigue Test on 7019 Aluminium', Internal Report for DERA, December, 1999.

APPENDIX A. Y SOLUTION FOR K CALCULATION (STEM CRACKS)

A1 *Objective*

2D numerical results showed that Y , hence K, of the lower crack tip in the T-section stem reduces with decreasing ligament size as it is less than 25 mm from the flange (see Figure A1). This was confirmed by the 3-D result. The Y solution for the ligaments>25mm was obtained using 2-D result. However, for the ligament is less than 25mm, the Y solution should be modified by f(c/25) (see below).

A2 *Summary*

For a crack with its uncracked ligament longer than 25mm above the flange, Y (for the lower crack tip) is calculated by,

$$f(s/2a) = 8.4803(s/2a)^5-20.056(s/2a)^4+a8.243(s/2a)^3 -8.4935(s/2a)^2+2.5338(s/2a)+0.5639 \quad \text{(A1)}$$

This Y solution is based on 2-D result ($Y_{(2\text{-D solution})}$).

However, in cases where the ligaments are less than 25mm, the Y solution can be obtained by modifying the 2-D solution,

$$Y_{(numerical)} = Y_{(2\text{-D solution})} \times f(c/25)$$

where $$f(c/25) = 0.04921\ln(c/25)+1.0051 \quad \text{(A2)}$$

This solution is based on a 3-D result.

A3 *Details of models*

For the cases of ligament > 25mm

s/2a	2a (mm)	s (mm)	c (mm)
0.1	400	40	125
0.2	200	40	125
0.3	328.3	98.5	66.5
0.5	197	98.5	66.5
0.8	123.1	98.5	66.5

For the cases of ligament < 25mm

s/2a	2a (mm)	S (mm)	C (mm)	C/25
0.462	297.5	137.5	25	1.0
0.471	302.5	142.5	20	0.8
0.480	307.5	147.5	15	0.6
0.488	312.5	152.5	10	0.4
0.497	318.046	158.046	4.454	0.178
0.848	162.1	137.5	25	1.0
0.853	167.1	142.5	20	0.8
0.857	172.1	147.5	15	0.6
0.861	177.1	152.5	10	0.4
0.865	182.646	158.046	4.454	0.178
0.7	215	150.5	12	0.48
0.62	240	149.1	13.4	0.54
0.631	215	135.7	26.8	1.07
0.768	182	139.7	22.8	0.912

A4 *Results*

For the cases of ligament > 25mm

Figure A2 shows that the 3-D results agree well with the 2-D Y solution, Eq. (A1). The discrepancy between the results of 2-D and 3-D is less than 5%.

For the cases of ligament < 25mm

Figure A3 illustrates the numerical Y (3-D results) versus s/2a. These can be rationalised by f(c/25) Eq. (A2), see Figure A4.

Figure A5 illustrates a plot of normalised Y (i.e. $Y_{(\text{numerical results})}/Y_{(\text{2-D solutions})}$) versus c/25. The discrepancy of normalised Y between 2-D and 3-D is less than 5%.

A5 *Conclusions*

1. 2-D simplification in the finite element method can be employed for the analysis only when the conditions at the crack front are not influenced by the stiffener.
2. The effect of the stiffener cannot be represented reliably by using 2-D analysis.
3. The crack tip behaviour is affected by the stiffener when the ligament shape is square, which, in this case, is $25\times25mm^2$.
4. The Y solutions for stem cracks in the bridge girder with ligaments <25mm and >25mm were obtained numerically.

a = Half crack length for stem cracks, or the total crack length for flange cracks.

b = Distance from the crack's mid-point to the top of the bottom flange.

W = Flange width.

s = Proportion of the crack length lay within the stem.

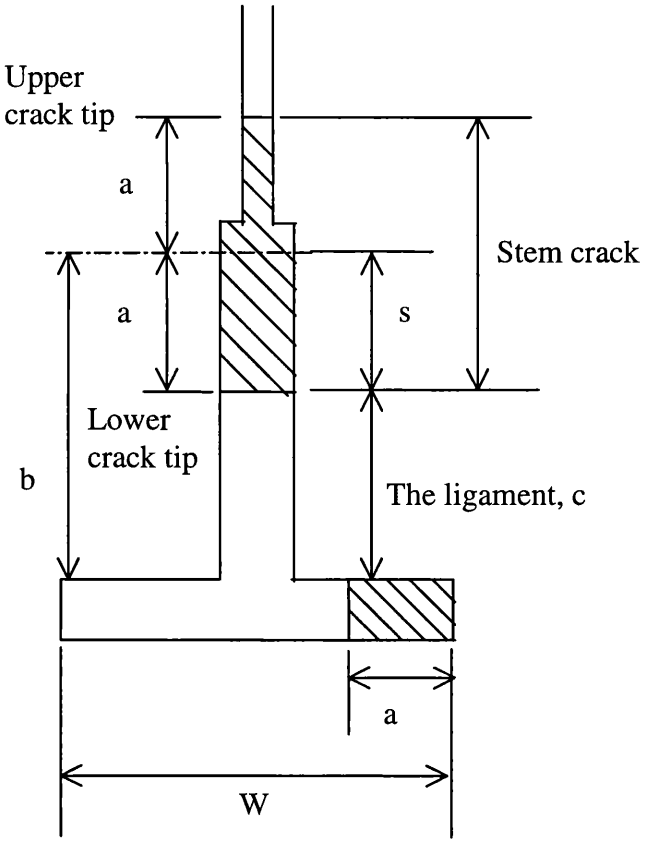

Figure A1 Details of crack aspect ratio.

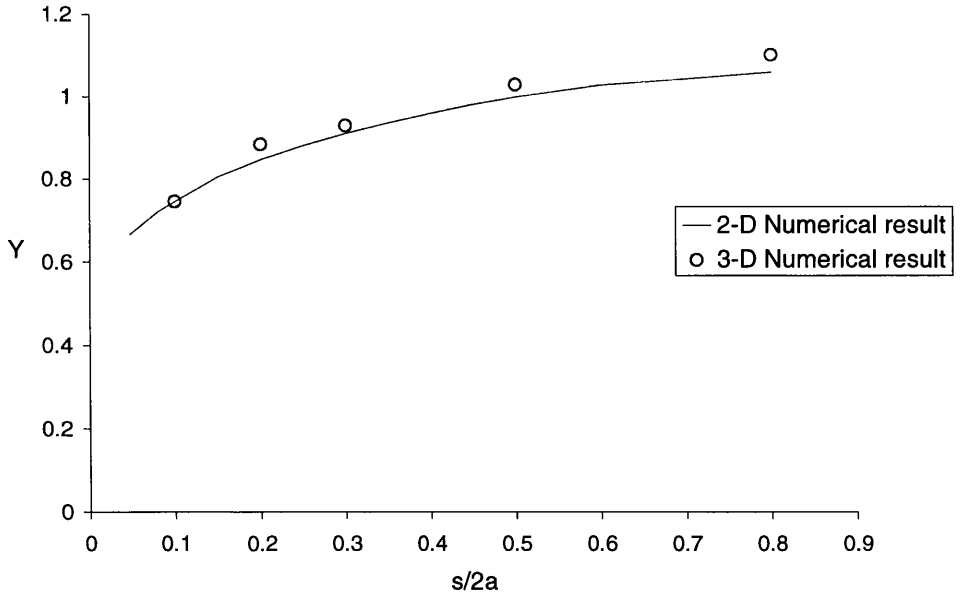

Figure A2 Comparison of numerical Y between 2-D and 3-D results.

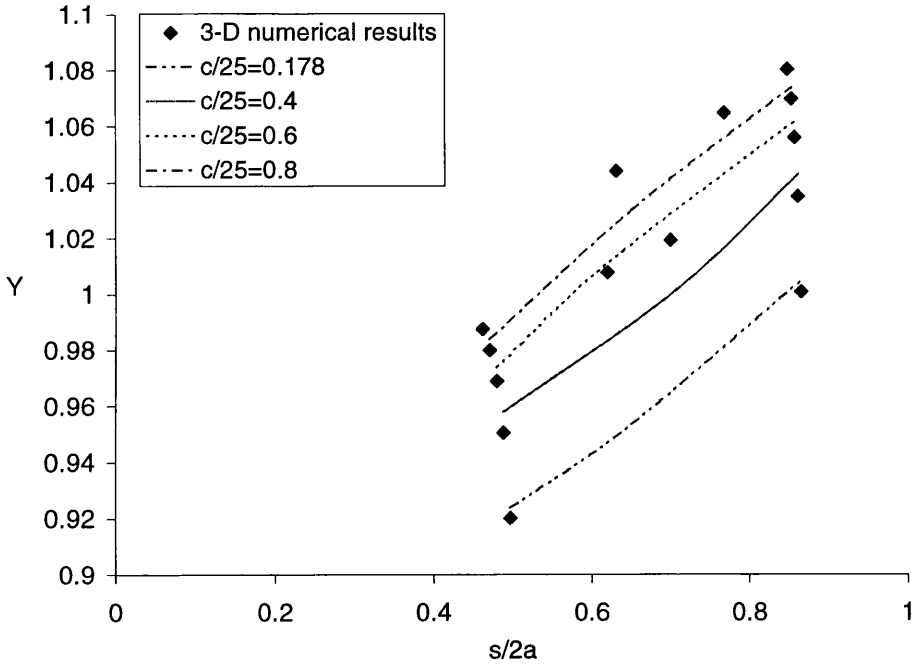

Figure A3 Numerical Y as functions of s/2a factor.

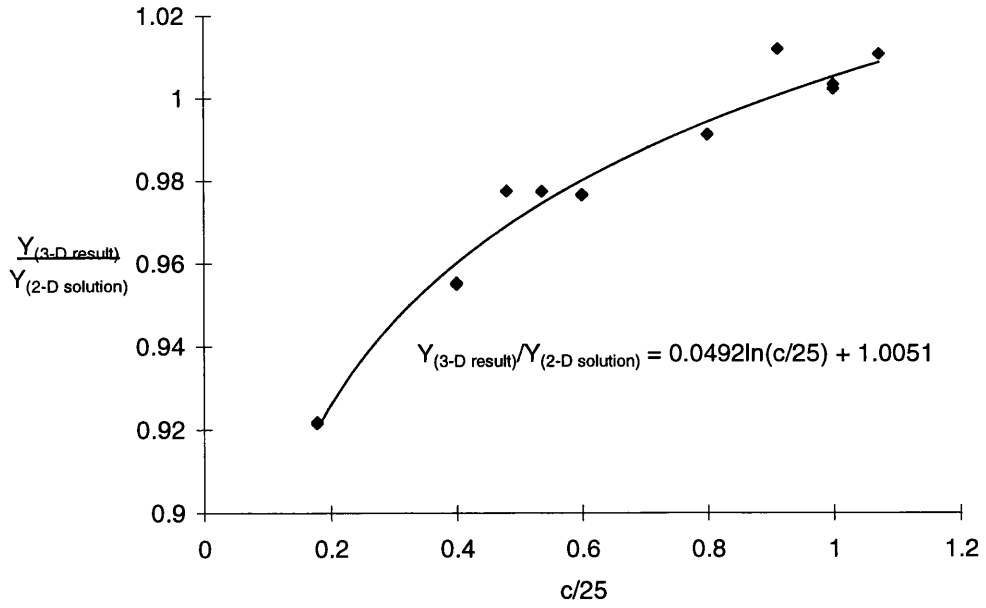

Figure A4 Normalised Y as a function of c/25 factor.

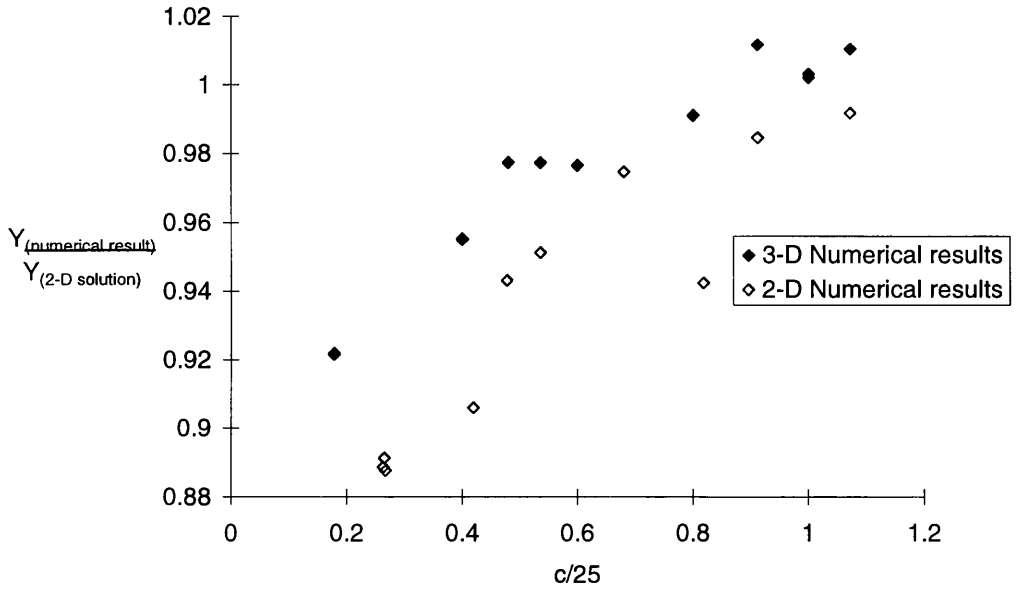

Figure A5 Comparison of normalised Y between 2-D and 3-D results.

APPENDIX B. NUMERICAL RESULTS OF K FOR T-SECTION CT SPECIMENS

B1 *Summary*

Four plane CT test specimens and seven T-section CT test specimens (see Figure B1) were modelled using the finite element method. The K is determined from J, which is calculated using elastic analysis. The correction factor of K for the T-section specimens, f(a/b), is computed using $K=f(a/b)F/(W^{1/2}t)$. Elastic-plastic analysis was performed for assessing the limit load of the T-section models.

B2 *Modelling*

The details of the test specimens are shown in Table B1. As a result of symmetry on planes y and z only a quarter of a specimen was modelled, see Figure B1.

TABLE B1. DETAILS OF SPECIMENS.

Plane CT test specimen (t=24.5mm, W=152mm and depth=180mm)							
a (mm)	36.5	60.5	91.5	122.5			
a/W	0.24	0.4	0.6	0.81			
T-section CT test specimen (t=24.5mm, W=152mm, depth=180mm, b=127mm and width of flange =175mm)							
a (mm)	36.5	60.5	91.5	101.5	106.5	114.4	122.5
a/W	0.24	0.4	0.6	0.67	0.7	0.75	0.8
a/b	0.29	0.48	0.72	0.8	0.84	0.9	0.97

In the test, displacement was applied to two elements at the top of the pin hole. The model would be overconstrained when the prescribed displacement was assigned to more elements along the hole, because that would restrict the rotation of the pinhole.

The meshes were generated with elements concentrated towards the crack tip, see Figure B1c.

B3 *Finite Element Results*

The stress intensity factor K is calculated using the elastic result, while the elastic-plastic result is used for assessing the limit load.

B3.1 *The Correction Factor*

The stress intensity factor K is calculated using $K^2=E'J$, where E' is the Young's modulus for plane stress conditions whilst $E'=E/(1-\nu^2)$ for plane strain conditions, and J is the J integral from the numerical result. The correction factor of K, f(a/W) for the plane CT specimen is calculated using $K=f(a/W)F/(W^{1/2}t)$, where F is the applied force, t is the thickness and W is the width. The comparison of f(a/W) between the F.E. result and the solution used in BS 7448, where $f(a/W)=(2+a/W)(0.886+4.64(a/W)-13.32(a/W)^2+14.72(a/W)^3-5.6(a/W)^4)/(1-a/W)^{3/2}$, is shown in Figure B2.

Table B2 shows the calculated correction factor, f(a/W), for plane CT test specimens and the T-section specimens. The correction factor of K for the T-section specimens (a/W=0.81) reduces by one half due to the effect of the stiffener, see Figure B3. For the T-section specimens, the correction factor is rationalised by a/b (see Figure B1 for notations), i.e. f(a/b), see Table B2. This is the usual way to present results for stiffened specimens in literatures.

TABLE B2. CORRECTION FACTOR OF TESTED SPECIMENS.

Plane CT test specimen							
a/W	0.24	0.4	0.6	0.81			
f(a/W)	5.15	7.79	14.62	42.8			
T-section CT test specimen							
a/W	0.24	0.4	0.6	0.67	0.7	0.75	0.81
a/b	0.29	0.48	0.72	0.8	0.84	0.9	0.97
$\frac{Kt(W)^{1/2}}{F}$ i.e. f(a/W)	4.91	7.41	12.24	14.29	15.9	18.87	21.27

Figure B4 shows the correction factor for T-section CT specimens as a function of a/b. The solution in Figure B4 applies to 0.48<(a/b)<0.97. For 0.48>(a/b) , or 0.4>a/W, stiffener (the flange) has no significant effect to K, see Figure B3.

B3.2 *The Limit Load*

The load versus load-line displacement data are shown in Figure B5.

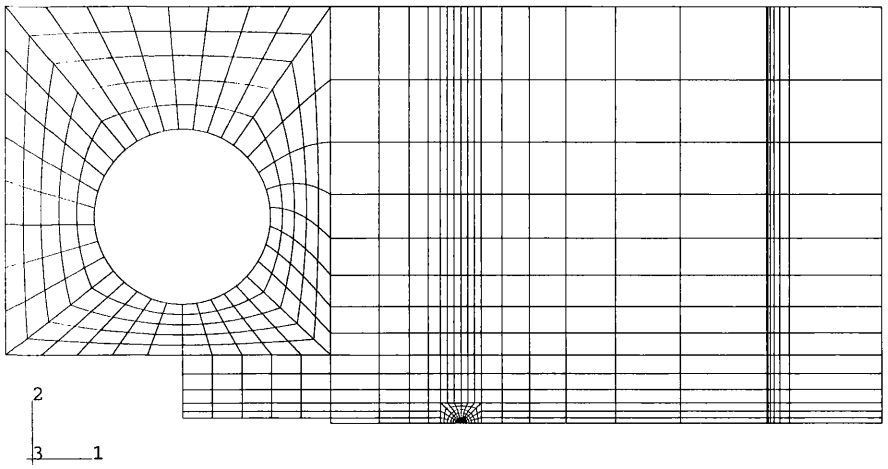

a. Front view.

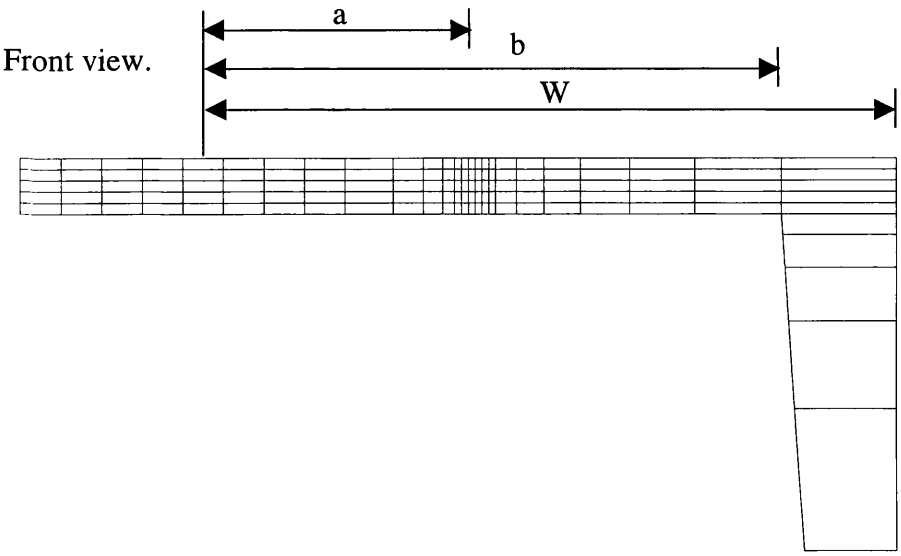

b. Plan view

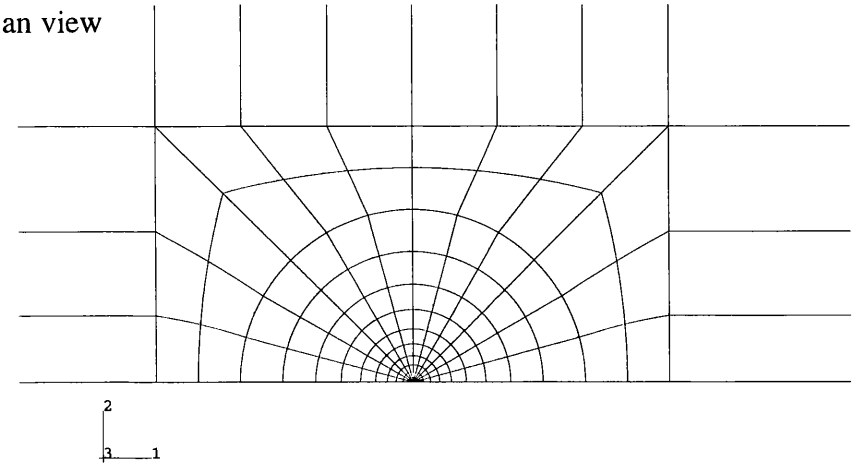

c. The mesh configuration at crack tip.

Figure B1 Details of the model and mesh configuration.

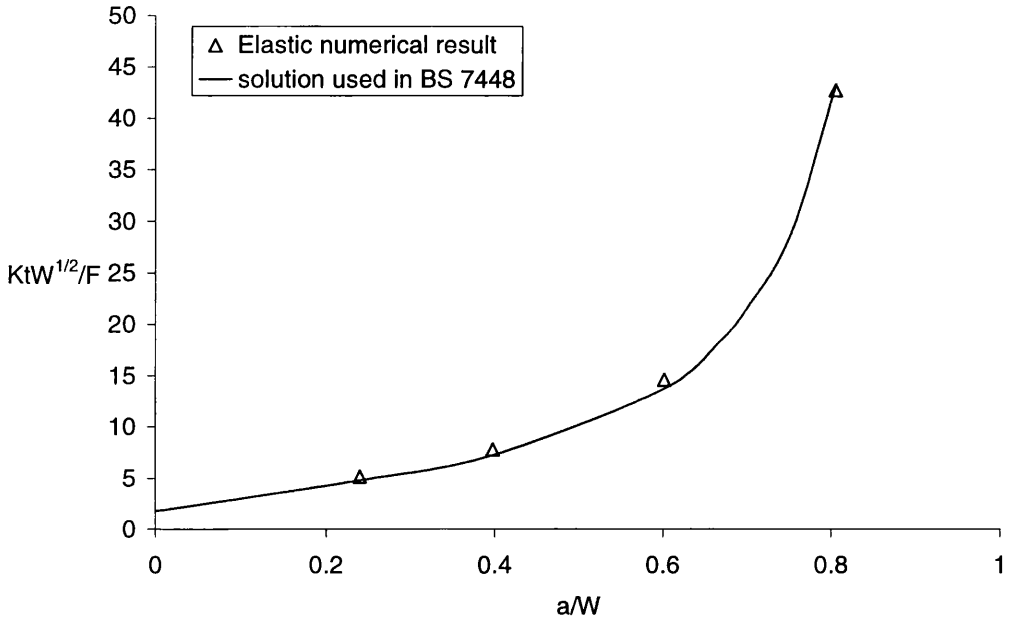

Figure B2 The comparison of the correction factor for K between numerical results and calculated K from published solution (as shown).

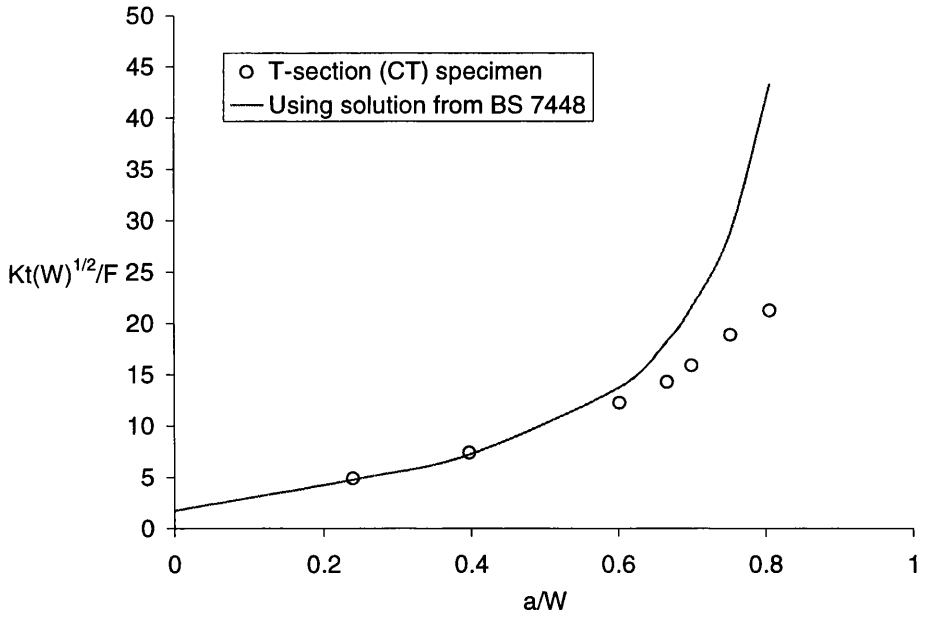

Figure B3 The comparison of the correction factor for K between T-section CT specimens (numerical results) and calculated K for plain CT specimens from published solution (as shown).

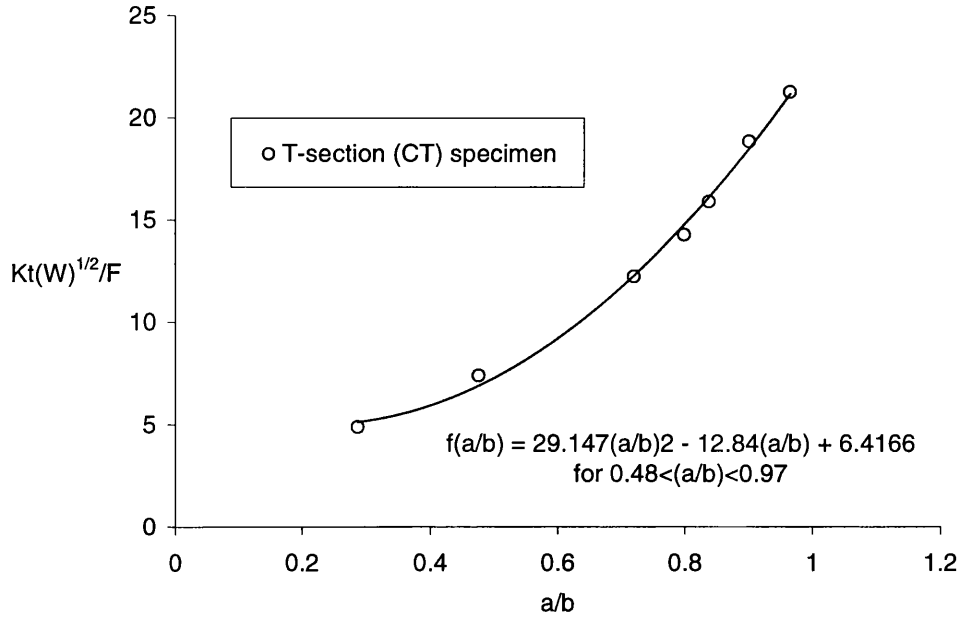

Figure B4 The correction factor of K versus (a/b).

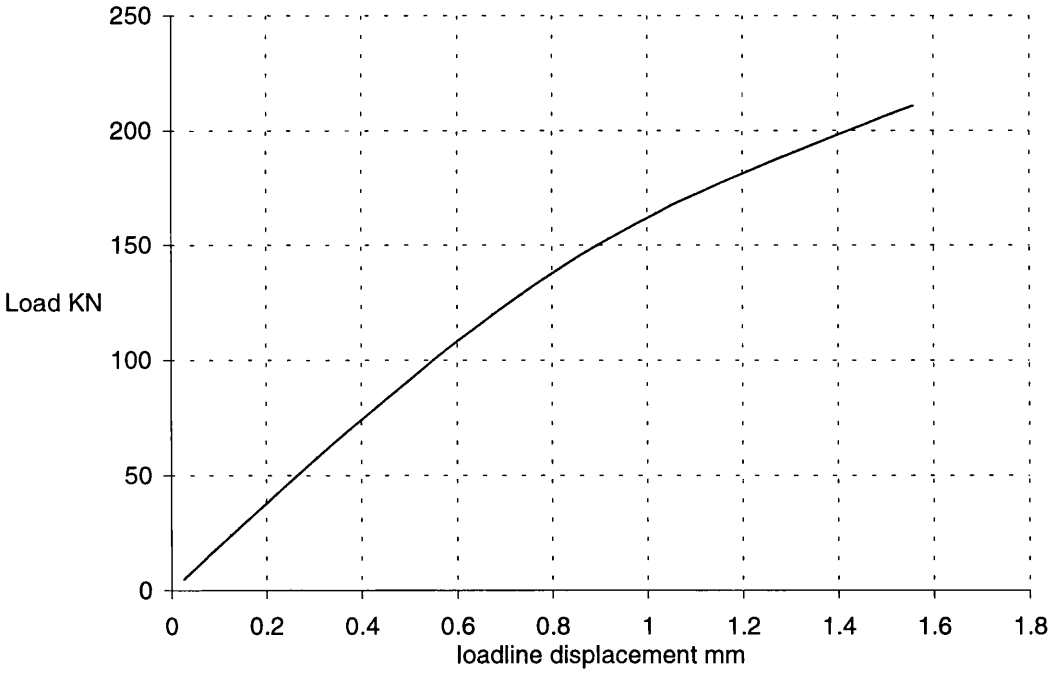

a. a/W=0.24

Figure B5 A plot of load versus loadline displacement the numerical result of T-section (CT) specimens.

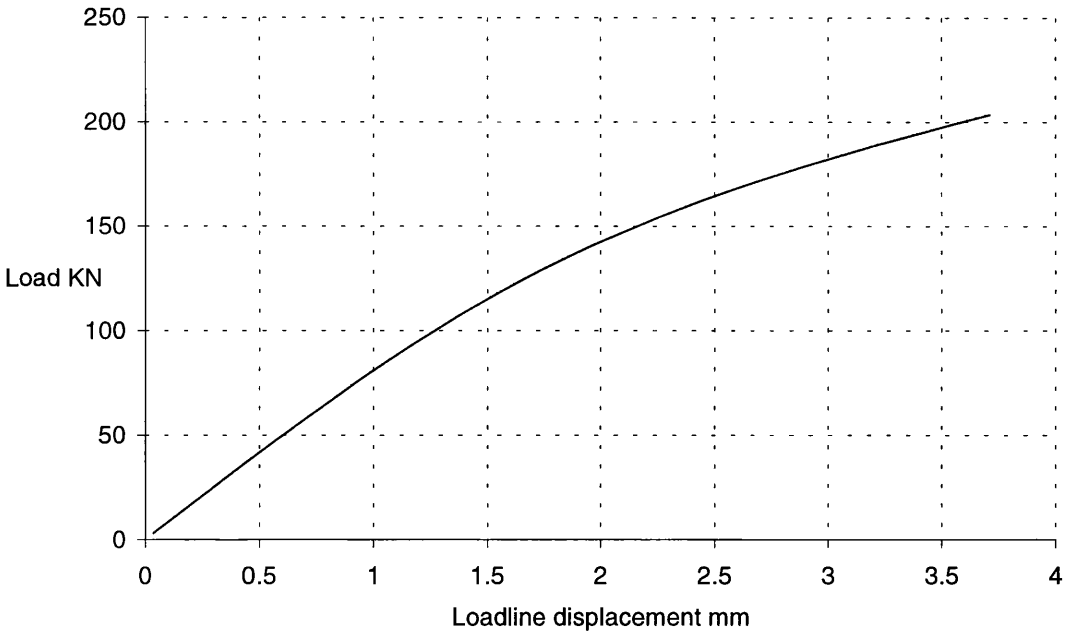

b. a/W=0.4

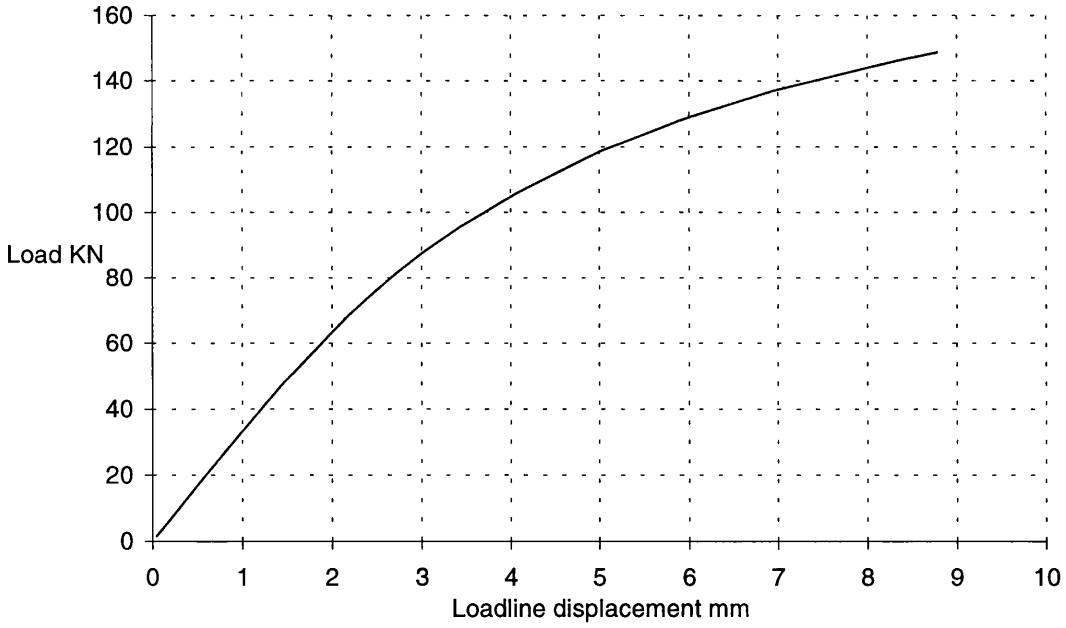

c. a/W=0.6

Figure B5 (cont.) A plot of load versus loadline displacement the numerical results of T-section (CT) specimens.

APPENDIX C NUMERICAL RESULTS FOR LARGE TENSION SPECIMEN

C1 *Introduction*

A large tension specimen (175(W)×1320(L) mm) of the bridge alloy was tested by Sumpter [C1]. The result showed that there was a sharp increase of the fatigue crack growth rate at a crack length of 41mm. The initial notch was 17mm deep, i.e. a/W=0.1. The crack was extended to 20mm by cyclic loading, with a peak load of 234kN and ΔK=15 MPa$\sqrt{m}$. Thereafter, a higher cyclic load between 420 and 16.5kN was applied. The fatigue crack growth data were measured at 2mm intervals of crack extension.

The elastic J (J_e) and T-stresses for the large tension specimen are computed numerically. The numerical results showed that the increase of Y (and hence J_e) with crack growth is less than that from the standard SENT solution. It also showed that the negative T-stress and J_e at the crack length of 41mm, where the experimental crack growth rate increased rapidly, closely agrees with previous experimental data for the J_C versus T-stress failure locus [C2].

C2 *Numerical Results of J_e and T-stresses*

Table C1 shows the crack lengths used for the finite element models. The crack lengths of the finite element models correspond to those quoted in the experiment, assuming a flat and straight crack path from the original notch direction. The T-stresses are computed using 2-D elastic analysis in plane strain conditions. The elastic material properties are as follow: E=69000MPa and σ_{ys}=391MPa.

The relationship between T-stress and K_I is defined as,

$$T = \frac{\beta K_I}{\sqrt{\pi a}}$$

where β = the biaxiality factor, which can be calculated from the following equation [C3]:

$$u_x = \left(1-\nu^2\right)\frac{\beta}{E\sqrt{a}} K_I r\cos\theta \qquad \text{(see Figure C1 for notations)}$$

where u_x= the deformation of the cracked surface in the crack growth direction,

θ = the cylindrical co-ordinate system;

and ν = the Poisson's ratio.

The K_I is calculated as where

$$K_I = \sqrt{\frac{EJ_e}{(1-\nu^2)}}$$

J_e is the output from ABAQUS. The results for Y and β are shown in Table C1.

TABLE C1 Details and results of numerical models for the large SENT specimen of bridge alloy.

Finite element models	SENT_f1	SENT_f2	SENT_f3	SENT_f4	SENT_f5
a/W	0.1	0.18	0.28	0.43	0.5
Crack length (mm)	17	31	50	76.2	87
Y	0.645	0.939	1.364	2.096	2.468
β (biaxiality factor)	-0.42	-0.42	-0.39	-0.34	-0.32
T-stress/σ_{ys} (at peak load)	-0.12	-0.13	-0.14	-0.15	-0.16

The comparison of Y and B between the numerical results and published solutions [C3][C4] are shown in Figures C2 and C3. The J_e for the large tension specimen is less than that of the published solution [C4]. This is associated with the restriction of rotation at the clamped ends of the test specimen. The β values for the large tension specimen remain negative in the numerical test (a/W=0.1 to 0.5). The negative β values of the numerical results are lower than the calculated β (published solution) [C3] for short cracks (a/W=0.1 to 0.28), but much high for longer cracks. The ratio of T-stress/σ_{ys} varies from –0.12 to –0.16 for a/W=0.1 to 0.5.

C3 *The J_C and T-stress Index*

Sumpter showed [C1] that the fatigue crack growth rate increased sharply after about 5000 cycles of the high cyclic load (between 420 and 16.5kN). The increase of the crack growth rate occurred when the stress intensity range reached 48MPa$\sqrt{m}$ at a crack length of 41mm. In

fatigue tests of CT specimens, the crack growth rate increased at the critical K_{1C} value. Sumpter [C1] suggested that the K_{1C} might have been elevated (48MPa$\sqrt{m}$>35MPa$\sqrt{m}$) as a result of the T-stresses effect.

The estimated J_e and T-stress for the 41mm crack length are 0.029MN/m (equivalent to K_I=47.1MPa$\sqrt{m}$) and 52.5MPa respectively, which are calculated from the numerical results. These results agree with the previous published data for this alloy [C2], see Figure C4.

C4 *Conclusions*

The sharp increase in the fatigue crack growth rate of the large tension specimen was observed at $K_{max}>K_{1C}$ [C1]. The J_e and T-stresses for the large SENT specimen are calculated using the finite element method. The numerical results show that the J_e for a crack length=41mm, at which the fatigue crack growth rate increases sharply, is elevated by the negative T-stress.

The numerical results show that the large tension specimen is a low constraint geometry. The ratio of T-stress(at peak load)/σ_{ys} decreases by 30%, from –0.12 to –0.16, for a/W=0.1 to 0.5.

C5 *References*

[C1] Sumpter, J.D.G., 'Large Tension Fatigue Test on 7019 Aluminium', Internal report for DERA, December 1999.

[C2] Sumpter, J.D.G., 'Observations on Tearing Instability in an Aluminium Alloy', Mechanisms and Mechanics of Damage and Failure, ECF-11.

[C3] AM Al-Ani and JW Hancock, 'J-Dominance of Short Cracks in Tension and Bending', J. Mech. Phys. Solids. Vol. 39, No. 1, pp. 23-43, 1991.

[C4] Anderson, T.L., 'Fracture Mechanics-Fundamentals and Applications', Department of Mechanical Engineering, Texas A&M University, College Station, Texas, CRC Press, Inc., Second Edition, 1995.

[C5] DP Rooke and DJ Cartwright, 'Compendium of Stress Intensity Factor', 1976. Her Majesty's Stationary Office, London.

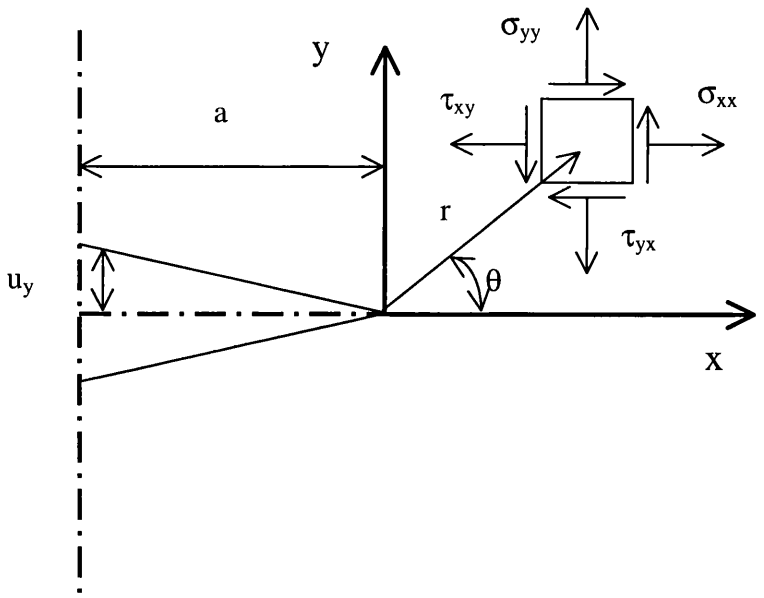

Figure C1 Definition of the co-ordinate axis and crack flank displacement of a sharp crack

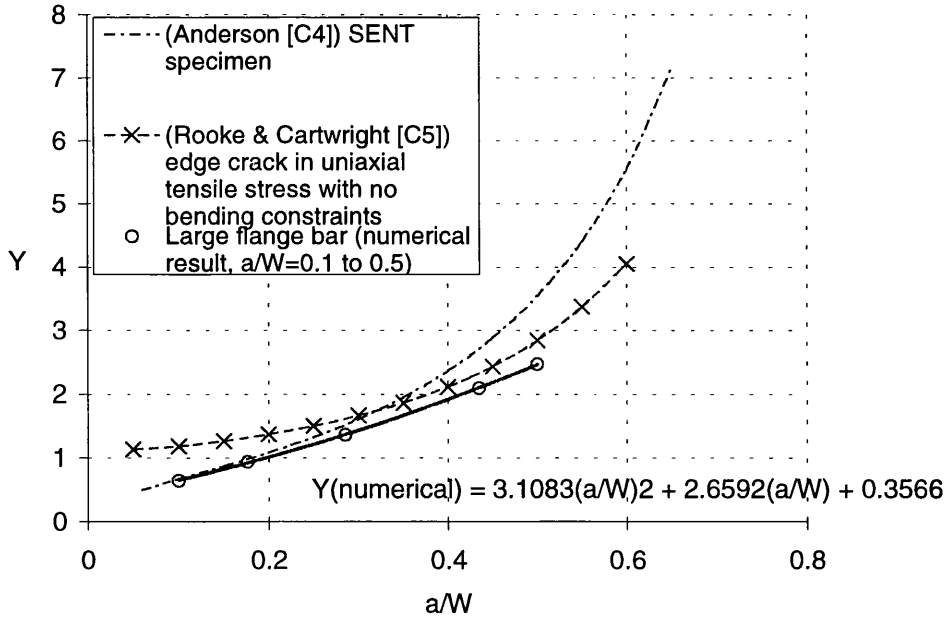

Figure C2 Comparison of Y between numerical results and published solution (as shown).

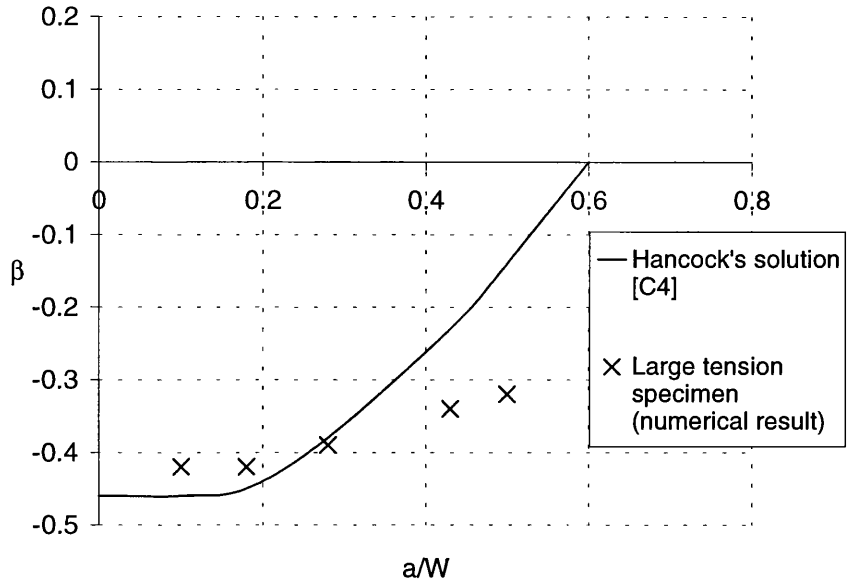

Figure C3 Comparison of b between numerical results and published solution (as shown)

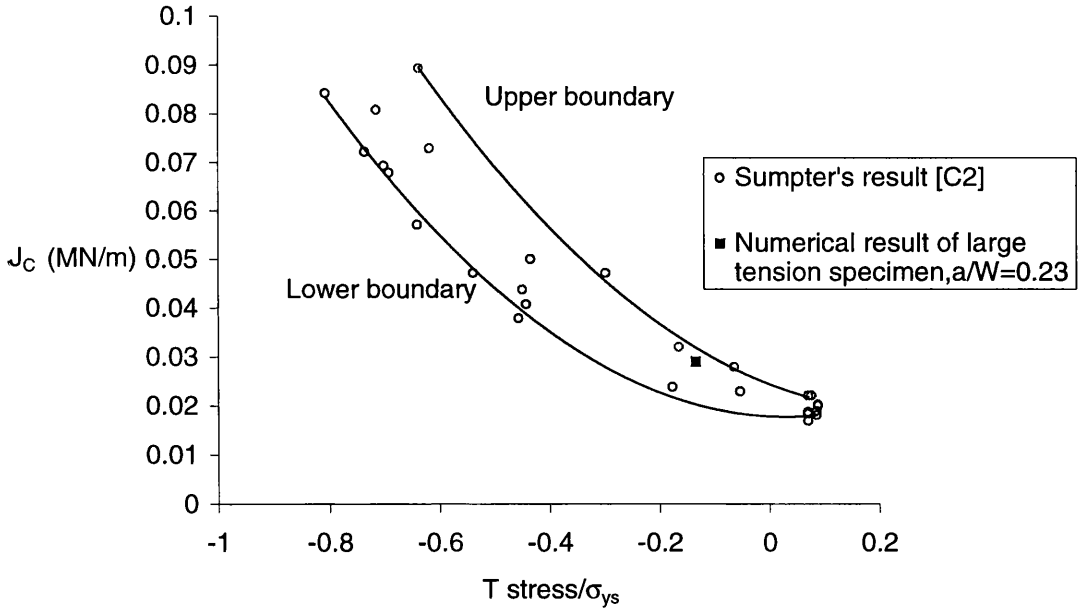

Figure C4 Elevated J and T-stress indexing.